2018

Customizable heterogeneous catalysts: From 3D printed designs to mesoporous materials

Juan Sebastian Manzano Davila
Iowa State University

Customizable heterogeneous catalysts: From 3D printed designs to mesoporous materials

by

J. Sebastián Manzano Dávila

A dissertation submitted to the graduate faculty

in partial fulfillment of the requirements for the degree of

DOCTOR OF PHILOSOPHY

Major: Chemistry

Program of Study Committee:
Igor I. Slowing, Co-major Professor
Aaron D. Sadow, Co-major Professor
Marek Pruski
Wenyu Huang
Young-Jin Lee

The student author, whose presentation of the scholarship herein was approved by the program of study committee, is solely responsible for the content of this dissertation. The Graduate College will ensure this dissertation is globally accessible and will not permit alterations after a degree is conferred.

Iowa State University

Ames, Iowa

2018

TABLE OF CONTENTS

Page

ACKNOWLEDGMENTS

I would like to thank Dr. Igor I. Slowing for providing me the opportunity to work in his research group. Your guidance, constant criticism, and patience in dealing with me for all these years showed me how to be a good mentor. I would not be here writing this today if it weren't for you. I would also like to thank my committee members, Drs. Aaron D. Sadow, Marek Pruski, Wenyu Huang and Young-Jin Lee for their valuable time, support, and collaborations.

I would like to thank the Slowing group for all the support through all these years. I would like to especially thank Dr. Nelson for all the scientific discussions, but more importantly for his friendship. I would also like to thank Dilini, who I considered my big sister, for all the patience and the fun we had these years. I would also like to especially thank Cindy for all the help and for her friendship, the food provided, and for all the talks about life, science, and future (PS. You are going to kill it in grad school).

I would like to thank Maria, for all her love and support during this time in Ames. We both went through the same program; I just hope I was as supportive as you were with me. You have always been there for me and I appreciate that very much. Last, but not least, I would like to thank my family for all the support throughout the years that allowed me to get to this point.

I would like to thank the U.S. Department of Energy, Office of Basic Energy Sciences, Division of Chemical Sciences, Geosciences, and Biosciences, through the Ames Laboratory Catalysis Science program at the Ames Laboratory under contract number DE-AC02-07CH11358.

ABSTRACT

This dissertation describes the author's efforts in developing new heterogeneous catalytic systems. The work is focused on controlling the structure of heterogeneous catalysts at the macroscale (using 3D printing methods) and at the nanoscale (using Mesoporous Silica Nanoparticles). The first chapter consists of a general introduction to 3D printing and its applications in chemistry laboratories and heterogeneous catalysis.

The second chapter presents the 3D printing process of materials with active functional groups using a commercial stereolithographic 3D printer. Controlling the composition of the 3D printable resin, different organic/inorganic catalytic groups were incorporated into the 3D architectures. The active sites, part of the 3D structure, did not require any post-printing treatment for activation and they were used directly after printing. The incorporated functionalities were accessible and catalytically active for the Mannich, aldol, and Huisgen cycloaddition reactions. As a proof of concept, custom-made catalysts were printed and used for studying the kinetics of a heterogeneously catalyzed reaction in a conventional solution spectrophotometer. In addition, we used 3D printed millifluidic devices containing catalytic sites on their walls to promote azide-alkyne cycloadditions. We showed that 3D printing allows controlling the morphology of the active materials, resulting in enhancing catalytic activity upon increasing complexity of the 3D architectures.

The third chapter presents a study of the effect of macroscopic catalyst morphology on the performance of batch reactions. A series of catalytically active magnetic stir-bar compartments (SBC) with different architectures were 3D printed and used to promote the hydrolysis of sucrose. Fixing the surface area and the number of accessible catalytic sites of the 3D printed SBC allowed exploring the effect of subtle changes in morphology on the

fluid dynamics of the reaction systems, and consequently on the efficiency of the catalytic conversion. Moreover, varying the ratios between acrylic acid (AA) and 1,6-hexandieoldiacrylate (HDDA) in the SBC allowed tuning cooperativity between acidic sites and hydrophobic domains to control the rate of sucrose hydrolysis. This work demonstrates that 3D printing catalytic materials enables optimizing their performance by simultaneously controlling their macroscopic and molecular structures.

The fourth chapter presents a new method for high-throughput screening of 3D printable catalytic resins. While, stereolithography (SLA) is a popular 3D printing technique, large volumes of resins (~150 mL) are required in each printing cycle. Thus, developing materials with different chemical or physical properties can be expensive and time consuming. To address this problem, we designed matrices of miniaturized resin tanks and adapted them to a commercial 3D printer. The resin tanks with smaller volumes (2 mL) were used for fast and efficient discovery of new 3D printable materials, allowing to simultaneously print up to 16 compositions. Using this approach, we screened for resins that can produce 3D objects with different degrees of surface hydrophilicty/hydrophobicity and catalytic activities. The optimized 3D printed catalytic materials with the largest area were used for oxidation of benzyl alcohol into benzaldehyde. The capacity of screening multiple materials simultaneously allowed us to combine the best properties to manufacture an optimized 3D printed catalyst (i.e. highest hydrophobicity, highest catalytic activity and highest geometrical surface area).

In chapter five, we studied the functionalization (grafting) kinetics of mesoporous silica nanoparticles with organo-substituted trimethoxysilanes (R-TMS). Controlling and understanding the functionalization of silicas is necessary to enable a rational design of

hierarchical MSN-based hybrid materials. We observed that the grafting process involves an adsorption/desorption equilibrium of R-TMS with the silica surface prior to its reaction with the surface silanols. Monitoring the changes in 3-aminopropyltrimethoxysilane (AP-TMS) grafting rates as a function of its concentration revealed a substrate-inhibition of the kinetics. Analysis of methanol production rates showed a significantly higher grafting rate for AP-TMS compared to other R-TMS, due to a catalytic effect of the amino group. This effect was used to control the grafting rates of other R-TMS by adding amines with different pK_a values. Solid-state NMR (SSNMR) studies revealed that the amine additives can also control the distribution of the grafted R-TMS on the surface of MSN.

In chapter six, phenyl-functionalized mesoporous silica materials were used to explore the effect of non-covalent interactions on the release of Ibuprofen into simulated body fluid. To this end, phenyl groups with different orientations and conformational mobilities were introduced onto mesoporous silica surfaces. The Ibuprofen release profiles from the materials were analyzed using an adsorption-diffusion model. All phenyl-containing mesoporous materials showed lower initial release rates than the bare silica. Comparing the different orientations of the phenyl groups, we observed that locked phenyl conformations provide stronger interactions with the drug than flexible phenethyl groups. The differences in adsorption interactions were consistent with DFT calculations. These results show how fine-tuning the orientation of groups can control drug release profiles.

CHAPTER 1. INTRODUCTION

Conventional methods to manufacture 3D objects include injection molding, and plastic forming and joining. However, in this digital era, computer aided design (CAD) provides increased flexibility to produce unique, custom-made objects in a single-step.[1] Two technologies that implement digital designs to manufacture objects are 3D printing and computer numerical control (CNC). CNC is a subtractive method based on removing material from a larger bulk and can be considered as a "top down" approach. Contrarily, 3D printing is an additive method that builds materials in a layer by layer fashion using a "bottom up" approach, therefore it is also known as additive manufacturing.[1] 3D printing technologies offer the advantage of reducing material waste and enabling the production of complex geometries that are hardly accessible by CNC methods. The ability to produce intricate structures and functional devices in a single step has stimulated the recent adoption of 3D printing technologies by several industries and scientific fields.

3D printing has been implemented in many fields including education, physics, biology and medicine.[2-35] The increasing interest in this technology is driven by its ability to produce custom devices, its simplicity, speed, and the low-cost of 3D printers. Nonetheless, its application to heterogeneous catalysis remains fairly limited, mainly due to the lack of printable materials that are catalytically active and can preserve their activity after 3D printing. One of the potential benefits of implementing 3D printing technologies in catalysis is that it may facilitate the on site and on demand production of chemicals. Such a personalized chemistry approach is a convenient way to respond to the increasing interest in locally processing distributed resources like waste or feedstocks that are hard to transport. 3D printing can enable manufacturing catalytic systems with characteristics precisely tailored to

match any type of feedstock, scale, and process one may need at a specific time and location. Importantly, directly printing heterogeneous catalysts can place the control of the full experimental set-up in hands of the end-user, allowing the reactor and catalyst design to become a part of the same experimental layout. Finally, there is currently little understanding of the role that the macroscale geometry of catalysts (i.e. arrays of catalytic sites) plays on controlling overall reaction performance. 3D printing offers the opportunity to explore this new area of inquiry in a controlled manner, and therefore should be a valuable tool to merge our understanding of the molecular and nanoscale features of catalysts with their behavior at the macroscopic scale.

3D printing technologies

A 3D printing process starts by creating a virtual design of the target object using CAD software. The file is then converted into a STL (Standard Tessellation Language) format, where only the surface geometry of the object is described, ignoring other attributes from the CAD file such as color or texture. This file is then converted to a G-code file by slicing the 3D model into printable layers. Finally, the printing conditions (e.g. temperature, positioning, extrusion rate, laser passes, etc.) are added to the file before transferring to the 3D printer. The most common 3D printing methods include: fused deposition modeling (FDM), stereolithography (SLA), selective laser sintering (SLS), and robocasting or direct ink writing (DIW).

Fused deposition modeling (FDM)

FDM was initially introduced by Scott Crump in 1989 and was commercialized by Stratasys.[36] After the patent expired, this technology was commercialized by many other companies, making it more affordable and accessible. Nowadays FDM printers can be even purchased in retail stores. This technology is based on feeding thermoplastic filaments

(diameters ranging from 1.75 mm to 3.00 mm) into a hot nozzle and extruding them onto a build platform. The extruder can move horizontally in the X and Y directions, while the platform moves vertically along the Z axis. Using the sliced 3D model, the object is produced by depositing the molten filament in a layer by layer fashion. There is a wide range of filaments available with different properties including color, flexibility, strength, etc. The most common materials are polylactic acid (PLA), acrylonitrile/butadiene/styrene (ABS), high impact polystyrene (HIPS), nylon and polypropylene. More specialized filament materials include composites that possess electrical conductivity, fluorescence, magnetism, etc.[37]

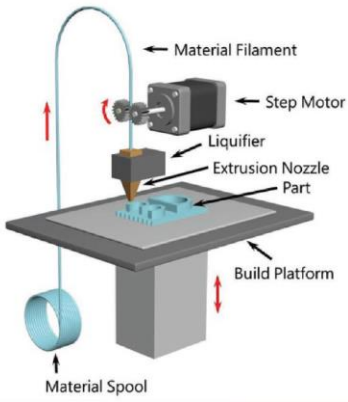

Figure 1. Fused Deposition Modeling (FDM) printing process. Reproduced with permission from Zhou et al.[38]

Stereolithography (SLA)

SLA, developed in 1984, is the oldest 3D printing technology.[39] It is based on the photo-polymerization of a suitable resin. A laser (usually 405 nm), guided by galvo mirrors, is focused on a resin tank to induce the polymerization on the spot and form the 3D object in a layer by layer fashion. The advantages of this technology compared to FDM include a higher resolution (ca. 150 µM for XY details compared to 400 µM of FDM) and faster building speeds (the laser moves in each layer instead of an extruder like in FDM). The type

of materials used in SLA varies depending on the photo-polymerization chemistry,[37] and includes radical polymerization (using type I, type II photo-initiators, or thiol-ene),[40-42] or cationic photo-initiators[43] (using epoxides,[44] polyols,[45] or oxetenes.[46]). Recently, an updated version of SLA called continuous interface liquid production (CLIP) was developed by DeSimone et al.[47] This approach involves the use of an oxygen permeable resin tank which creates a "dead zone" where the polymerization is inhibited by the high concentration of oxygen. This "dead zone" converts the layer-by-layer process in a continuous process, increasing printing speeds up to 100 times.

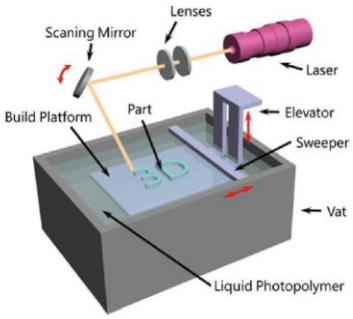

Figure 2. Stereolithography (SLA) printing process. Reproduced with permission from Zhou et al.[48]

Selective laser sintering (SLS)

SLS was developed by Deckard and Beaman in 1986.[49] This process is analogous to SLA, but involves a powder bed instead of a photo-curable resin. A high-power laser selectively sinters the powder in a layer-by-layer fashion to form the 3D object. The laser heats the powder just under its melting point in each layer. After each layer is sintered, the powder bed is lowered, and new powder is deposited on top. These steps are repeated until the final 3D architecture is formed.

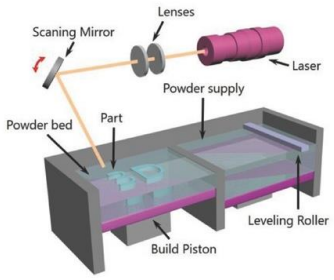

Figure 3. Selective laser sintering (SLS) printing process. Reproduced with permission from Zhou et al.[38]

Direct ink writing (DIW)

This technique is also known as robocasting and is based on the direct extrusion of a semifluid.[50] The ink viscosity must be low before printing, but should increase after being extruded to keep its shape on the build platform. To tune the ink consistency, usually organic binders and plasticizers are used. Considering the ink composition, in theory, any powdered material can be printed, as long as it possesses the right rheological properties. The extruded materials are usually fragile and need an additional high temperature treatment to sinter and burn the organic materials. This post-printing treatment causes shrinkage of the 3D object, affecting the dimensionality of the original design. The brittleness of the printed structure limits the production of complex geometries.

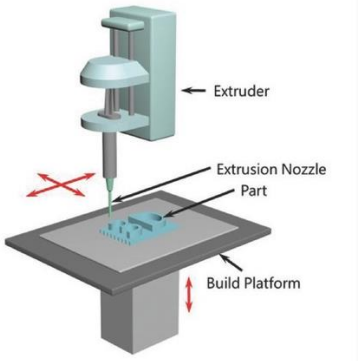

Figure 4. Robocasting or direct ink writing printing process. Reproduced with permission from Zhou et al.[48]

3D printing in chemistry

3D printing reactors

The first application of 3D printing in chemistry was in producing laboratory equipment. Currently, there are many open source sites that make labware designs readily available to the community.[51, 52] The most common technology used for this purpose is FDM due to its relatively low cost and the chemical resistance of the materials. Gordeev et al. produced typical chemistry labware with this method and studied its stability in different solvents (e.g. acetone, water, hexane, toluene, dimethylsulfoxide, ethanol, dichloromethane, diethyl ether, acetonitrile and tetrahydrofuran) at various pressures.[53] In general, the observed stability trend was: PP (polypropylene) > PLA (polylactic acid) > ABS (acrylonitrile/butadiene/styrene) > PETG (polyethylene terephthalate glycol). Nonetheless, the choice of printing material should ultimately depend on the specific target application and conditions.

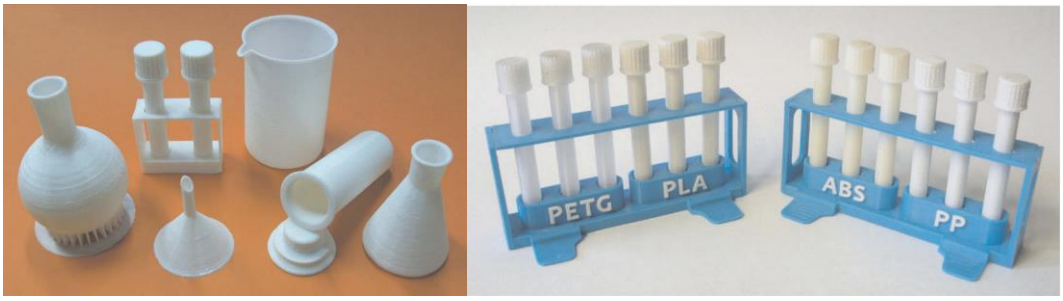

Figure 5. a) Examples of labware typically used in chemistry laboratories printed by an FDM 3D printer b) test tubes produced with different filaments. Reproduced with permission from Ananikov et al.[53]

Cronin and co-workers introduced the concept of "reactionware" (i.e. bespoke chemical reactors) in a series of papers. In their first work, they used acetoxysilicone robocasting to 3D print a vessel composed of two injection antechambers and one reaction

chamber with an opening to fit indium-tin oxide windows. They loaded a solution of 5-(2-bromoethyl)phenanthridium bromide into one of the antechambers and a solution of Et_3N and 4-methoxyaniline on the other one. Mixing of both solutions in the reaction chamber led to formation of the product **3** in 90% yield. However, by mixing the solutions in a new 3D printed vessel with a smaller reaction chamber the selectivity was reversed to give mainly product **4** (80% yield).

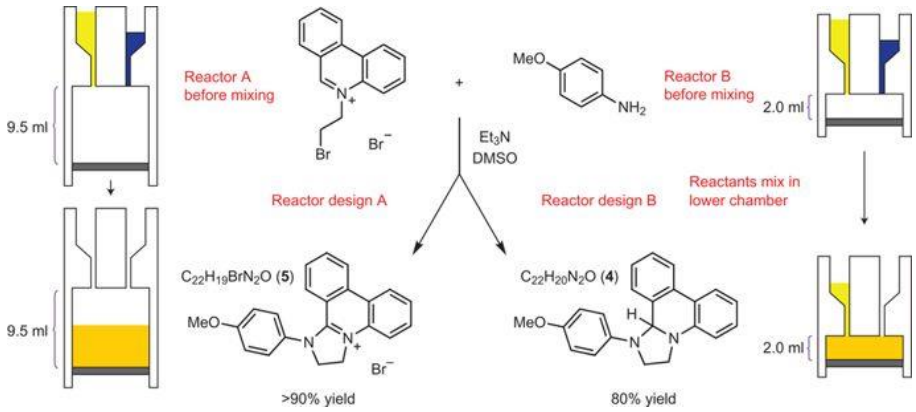

Figure 6. The 3D-printed reactionware-assisted selective syntheses of $C_{22}H_{20}N_2O$ and $C_{22}H_{19}BrN_2O$. Reproduced with permission from Symes et al.[54]

In another example, the same group 3D printed arrays of sealed monolithic hydrothermal reactors for the high throughput synthesis of metal organic frameworks (MOF).[55] The production of the reactors was temporarily paused after 3D printing their bottom parts to add the MOF precursors and then continued to seal the reactors. This sealed reactionware enabled the discovery of two new coordination polymers. The concept of 3D printing sealed reactionware was also used to conduct multi-stage hydrothermal reactions, and led to the discovery of polyoxometalate-containing MOF.[56]

The same group also 3D printed a self-contained plastic reactionware device to conduct the multistep synthesis of (±)-baclofen.[57] Importantly, the digital production of reactionware allows storing blueprints, for downloading and implementing when required.

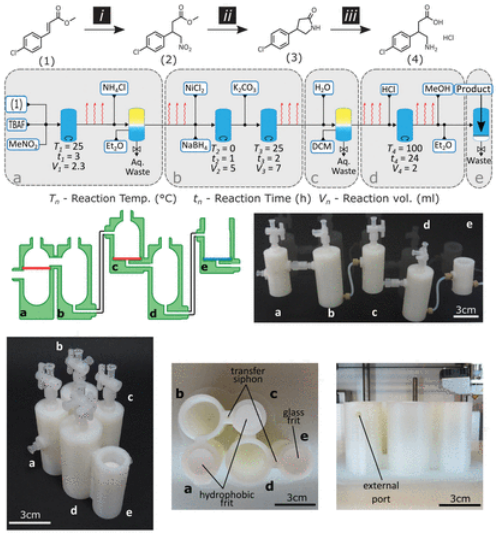

Figure 7. Synthesis of (±)-baclofen in a series of reaction cartridges. Reproduced with permission from Kitson et al.[57, 58]

In 2017, Lederle et al. used FDM to 3D print an NMR tube/spinner combination and study the Sonogashira coupling between aryl halides and arylpropiolic acids.[59] The printed reaction vessels were used to measure reaction rates and correlate them to the donor capacities of different aryl bromides. The vessels were printed using polyamide, which is compatible with a wide range of organic solvents and completely invisible in ^{1}H NMR spectroscopy. The printing was carried out inside a glovebox to prevent reagent degradation. Similarly, Zalesskiy, et al. 3D printed a photoreactor to promote a visible light thiol-ene click reaction for the synthesis of sulfur containing products.[60] The 3D printed reactor consisted of a custom-made cover containing the LED source.

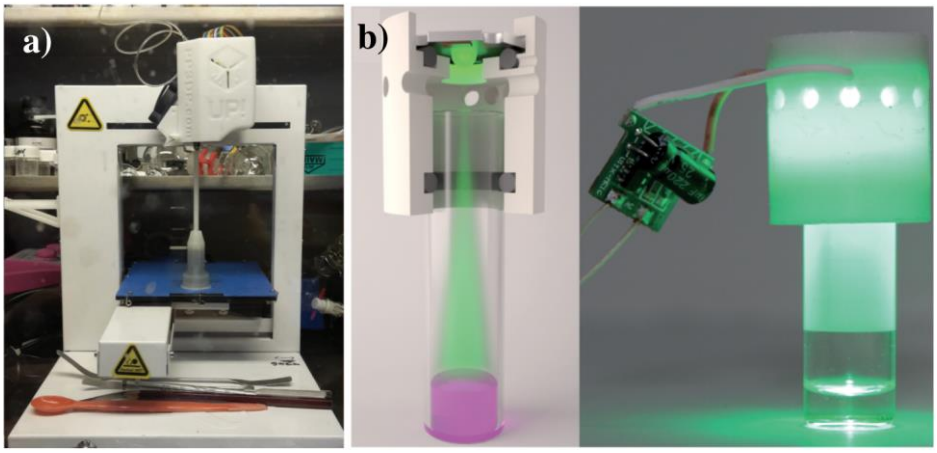

Figure 8. a) 3D printing of NMR/spinner combination for Sonogashira couplings and b) 3D printed photo-reactor. Reproduced with permission from Zalesskiy et al.[60] and Lederle et al.[59]

3D printing catalytic materials

The next level of complexity in this realm is 3D printing catalytically active materials.[38, 61-63] The major concern in printing catalytic materials is the incorporation of active components into a printable matrix. The immobilization of catalysts into 3D printed matrices not only enables the recyclability of active species, but also gives the control over the morphological structure of the catalysts. Two different strategies have been used to incorporate catalytic materials in 3D printed architectures. The most common strategy involves a *physical mixing* where the catalyst is dispersed into a matrix (i.e. printable material) to produce a composite that is then 3D printed. An alternative approach is to integrate the catalytic moieties via *chemical binding*. This can be accomplished either by using 3D printing precursors that possess the active component as part of their own molecular structure, or by covalently modifying the surface chemistry of the materials after 3D printing.

Physical incorporation of catalysts

In one of the first attempts to incorporate catalysts into a 3D printing process Kitson, et al. used robocasting to deposit an acetoxy-silicone matrix containing Pd/C and K10 Montmorillonite onto the walls of a 3D printed multichamber reactor.[64] The reactor was then used to conduct a sequence of Diels-Alder and reductive amination reactions controlled by a series of manual rotations. Nonetheless, in this work two different equipment were used to incorporate the catalysts, and no control over the shape or accessibility of the catalyst was shown.

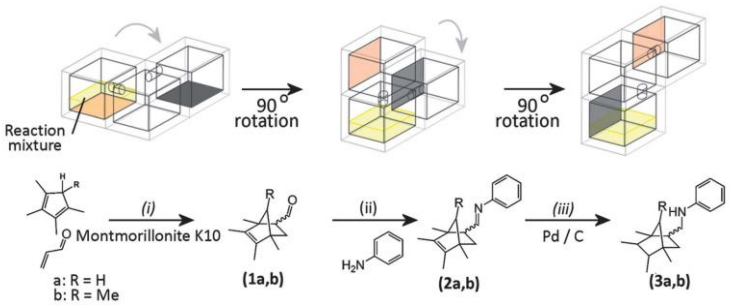

Figure 9. Multi-step reaction sequence in both open and sealed reactionware. In each step Reproduced with permission from Kitson et al.[64]

The physical mixing approach has been mainly employed with the FDM technique. To ensure an efficient mixing, the catalyst particles are dispersed in a solution of the polymeric precursor and thoroughly homogenized. The solvent is then evaporated leaving a solid polymer that is extruded to form a filament. In one of the first examples, Skorski et al. incorporated TiO_2 nanoparticles into an ABS filament to 3D print a composite that was an active catalyst for the photodegradation of Rhodamine 6G.[65] Similarly, Bible et al. incorporated HKUST-1metal organic frameworks (MOF) into an ABS filament by dispersing the nanoparticles in a solution of the polymer and studied the gas storage properties of the 3D

printed composite.[66] Nonetheless, the amount of MOF included within the polymer filament could only be 10 wt%. Higher amounts would produce filaments too brittle to print.

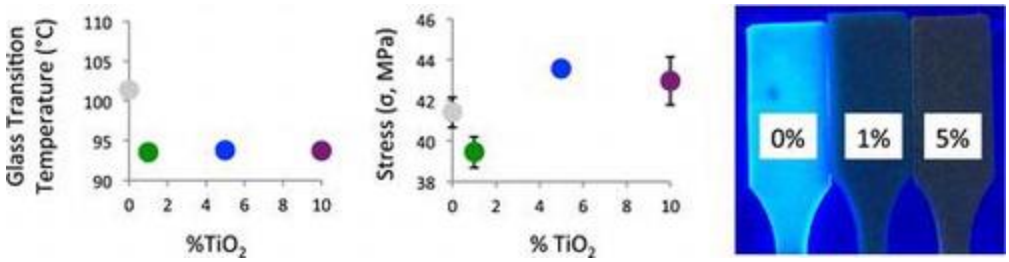

Figure 7. 3D printing of TiO2/ABS composites and their catalytic activity in the degradation of Rhodamine 6G. Reproduced with permission from Skorski et al.[65]

Recently, Sun et al. used of an iron-containing PLA filament to print active impellers capable of catalyzing the Fenton oxidation of aromatic molecules.[67] Because the iron was not accessible in the printed impellers, the printed polymer was etched with base and hydrogen peroxide to expose the active sites and display catalytic activity.

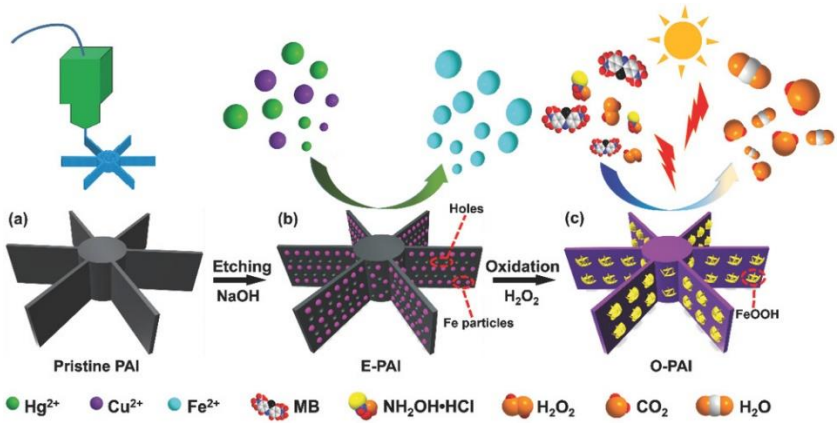

Figure 8. 3D printing catalytic impellers. The catalytic sites are first exposed and oxidized prior use in the Fenton reaction. Reproduced with permission from Sun et al.[67]

On a different approach, incorporating catalytic supports into a printable matrix has been performed via robocasting, where a concentrated colloidal suspension (ink) is extruded through a nozzle.[68-73] In the first demonstration of printing heterogeneous catalysts, Tubío, et al. developed an ink containing Al_2O_3 dispersed in a mixture of $Cu(NO_3)_2$, hydroxypropyl methylcellulose, and poly(ethylenimine).[74] The woodpile-like structure created, with an open, porous and high surface area to volume ratio, was catalytically active for the Ullman reaction.

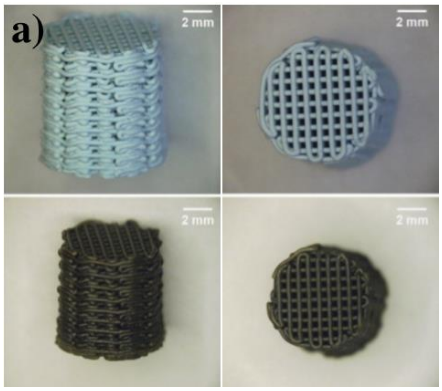

Figure 12. Photographs of alumina supports with embedded Cu-based catalysts, after low-temperature drying (top) and high-temperature sintering (bottom). Reprinted with permission from Tubío et al.[74]

More recently, Zhu et al. reported the 3D printing of hierarchical nanoporous gold using the same robocasting technique.[75] The ink composition consisted of Ag and Au clays along with organic binders. The porous gold materials, after a process of sintering and dealloying, exhibited three distinct structural length scales ranging from the macroscale to the nanoscale. Catalytic measurements on the methanol oxidation revealed that the 3D printed structures improve mass transport and reaction rates compared to non-porous gold catalysts.

Surface modification for active sites

Differently, to add catalytic materials or active sites, post-treatments to 3D printed materials can be used. In this way, Wang et al. functionalized an ABS 3D printed number skeletons by coating of porous Cu-metal-organic frameworks on it using a step-by-step in situ growth.[76] The nanoparticles formed on the surface of the 3D architecture ranged from 200 nm to 900 nm. This composite was used in the adsorption of methylene blue in aqueous solutions.

Combining a physical mixture of catalytic materials with post-printing addition of catalytic materials, Diaz-Marta et. Al. demonstrated the compartmentalization of Cu and Pd catalytic sites in two different 3D printed SiO_2 monoliths.[77] This was done by functionalizing the monoliths with different amino silanes. The multicatalytic system was used in the assembly of different 1,2,3-triazoles using tBuOH/H_2O as solvent. The catalysts showed good recyclability up to 10 times without sign of leaching.

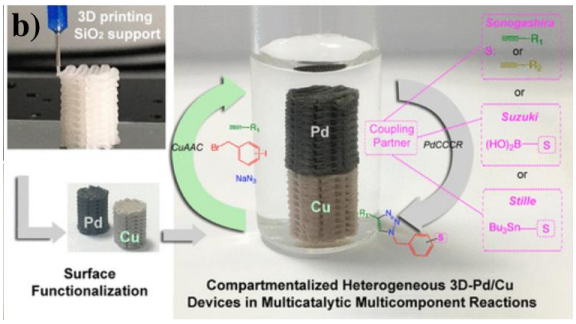

Figure 93. Two 3D-hybrid monolithic catalysts containing immobilized copper and palladium species. Reprinted with permission from Diaz-Marta et al.[77]

On a similar approach, Stassi, et al. used acrylic acid to control the amount of acidic sites and 3D printed microcantilevers using an SLA approach.[78] These microarrays were then functionalized with enzymatic sites and used in a standard immunoassay protocols and

demonstrated their suitability for biological applications. Similarly, Wang et al. incorporated a Br-containing vinyl monomer into a photo-curable resin.[79] The resin was 3D printed via SLA to give a lattice structure with pendant Br atoms that were subsequently used as ATRP initiators to create polymer brushes with different hydrophobic/hydrophilic properties. They denominated this approach as print 3D initiator integrated objects or i3DP. In a different work, the same group reported the use of this methodology to incorporate Pd, Cu or Ni nanoparticles on the surface of the 3D architecture containing poly[(2-(methacryloyloxy)ethyl)trimethylammonium chloride] polymer.[80]

Chemical binding

In this method the active sites are part of the building blocks used during 3D printing and their chemistry can be tuned prior manufacturing the 3D geometries. In this way, there is no need of post-treatment methods to modify, access or strengthen the 3D structure. Based on this method, Yee et. al demonstrated the fabrication of chemically functionalized 3D structures by first modifying the acrylate monomers via the thiol-Michael reaction and then polymerizing it using two-photon lithography.[81] The resulting geometries had different targeted surface properties.

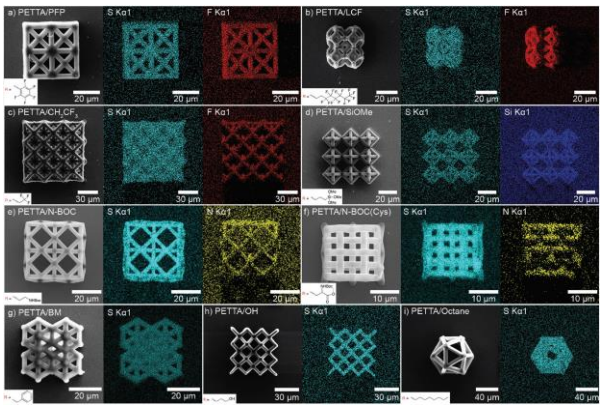

Figure 14. Energy-dispersive X-ray spectroscopy elemental maps for 3D architectures with different surface properties. Reprinted with permission from Yee et al.[81]

Later, the same group demonstrated a printing process to manufacture self-supporting 3D photocatalytic titania architectures. To this end, titanium(IV)ethoxide ligands were exchanged with acrylic acid and then printed using a commercially available SLA 3D printer. The final structure was pyrolyzed to remove the organic material and produce the titania architectures. Controlling the molecular structure of the monomers allowed the tuning of catalytic properties of the final architectures.

In this thesis, we will describe an approach for tuning the chemical composition of photo-curable resins in an SLA 3D printer. Varying the chemical composition can enable the modification of the chemical and geometrical properties simultaneously. The 3D printed architectures were tested as catalysts in multiple acid-, base-, and metal-catalyzed reactions. Controlling the chemical composition of the photo-curable resin allowed us to tune the local environments and induce cooperativity between functional groups or domains with different surface properties (hydrophobicity/hydrophilicity). To complement the control over the chemical properties, 3D printing was used to study the effects of macroscopic features in the catalytic activity.

References

1. Gibson, I.; Rosen, D.; Stucker, B., Additive manufacturing technologies: 3D printing, Rapid Prototyping, and Direct Digital Manufacturing. 2 ed.; Springer-Verlag New York: 2015.

2. Tabassum, T.; Iloska, M.; Scuereb, D.; Taira, N.; Jin, C.; Zaitsev, V.; Afshar, F.; Kim, T., Development and Application of 3D Printed Mesoreactors in Chemical Engineering Education. Journal of Chemical Education **2018,** 95 (5), 783-790.

3. Smiar, K.; Mendez, J. D., Creating and Using Interactive, 3D-Printed Models to Improve Student Comprehension of the Bohr Model of the Atom, Bond Polarity, and Hybridization. Journal of Chemical Education **2016,** 93 (9), 1591-1594.

4. Kosenkov, D.; Shaw, J.; Zuczek, J.; Kholod, Y., Transient-Absorption Spectroscopy of Cis–Trans Isomerization of N,N-Dimethyl-4,4′-azodianiline with 3D-Printed

Temperature-Controlled Sample Holder. Journal of Chemical Education **2016,** 93 (7), 1299-1304.

5. Davis, E. J.; Jones, M.; Thiel, D. A.; Pauls, S., Using Open-Source, 3D Printable Optical Hardware To Enhance Student Learning in the Instrumental Analysis Laboratory. Journal of Chemical Education **2018,** 95 (4), 672-677.

6. Porter, L. A.; Washer, B. M.; Hakim, M. H.; Dallinger, R. F., User-Friendly 3D Printed Colorimeter Models for Student Exploration of Instrument Design and Performance. Journal of Chemical Education **2016,** 93 (7), 1305-1309.

7. Kaliakin, D. S.; Zaari, R. R.; Varganov, S. A., 3D Printed Potential and Free Energy Surfaces for Teaching Fundamental Concepts in Physical Chemistry. Journal of Chemical Education **2015,** 92 (12), 2106-2112.

8. Lu, Y.; Santino, L. M.; Acharya, S.; Anandarajah, H.; D'Arcy, J. M., Studying Electrical Conductivity Using a 3D Printed Four-Point Probe Station. Journal of Chemical Education **2017,** 94 (7), 950-955.

9. Carroll, F. A.; Blauch, D. N., Using the Force: Three-Dimensional Printing a π-Bonding Model with Embedded Magnets. Journal of Chemical Education **2018,** 95 (9), 1607-1611.

10. Muskin, J.; Ragusa, M.; Gelsthorpe, T., Three-Dimensional Printing Using a Photoinitiated Polymer. Journal of Chemical Education **2010,** 87 (5), 512-514.

11. Piunno, P. A. E., Teaching the Operating Principles of a Diffraction Grating Using a 3D-Printable Demonstration Kit. Journal of Chemical Education **2017,** 94 (5), 615-620.

12. Blauch, D. N.; Carroll, F. A., 3D Printers Can Provide an Added Dimension for Teaching Structure–Energy Relationships. Journal of Chemical Education **2014,** 91 (8), 1254-1256.

13. Grasse, E. K.; Torcasio, M. H.; Smith, A. W., Teaching UV–Vis Spectroscopy with a 3D-Printable Smartphone Spectrophotometer. Journal of Chemical Education **2016,** 93 (1), 146-151.

14. Scalfani, V. F.; Vaid, T. P., 3D Printed Molecules and Extended Solid Models for Teaching Symmetry and Point Groups. Journal of Chemical Education **2014,** 91 (8), 1174-1180.

15. Lolur, P.; Dawes, R., 3D Printing of Molecular Potential Energy Surface Models. Journal of Chemical Education **2014,** 91 (8), 1181-1184.

16. Griffith, K. M.; Cataldo, R. d.; Fogarty, K. H., Do-It-Yourself: 3D Models of Hydrogenic Orbitals through 3D Printing. Journal of Chemical Education **2016,** 93 (9), 1586-1590.

17. Meyer, S. C., 3D Printing of Protein Models in an Undergraduate Laboratory: Leucine Zippers. Journal of Chemical Education **2015,** 92 (12), 2120-2125.

18. Dean, N. L.; Ewan, C.; McIndoe, J. S., Applying Hand-Held 3D Printing Technology to the Teaching of VSEPR Theory. Journal of Chemical Education **2016,** 93 (9), 1660-1662.

19. Jones, O. A. H.; Spencer, M. J. S., A Simplified Method for the 3D Printing of Molecular Models for Chemical Education. Journal of Chemical Education **2018,** 95 (1), 88-96.

20. Higman, C. S.; Situ, H.; Blacklin, P.; Hein, J. E., Hands-On Data Analysis: Using 3D Printing To Visualize Reaction Progress Surfaces. Journal of Chemical Education **2017,** 94 (9), 1367-1371.

21. Carroll, F. A.; Blauch, D. N., 3D Printing of Molecular Models with Calculated Geometries and p Orbital Isosurfaces. Journal of Chemical Education **2017,** 94 (7), 886-891.

22. Rodenbough, P. P.; Vanti, W. B.; Chan, S.-W., 3D-Printing Crystallographic Unit Cells for Learning Materials Science and Engineering. Journal of Chemical Education **2015,** 92 (11), 1960-1962.

23. Paukstelis, P. J., MolPrint3D: Enhanced 3D Printing of Ball-and-Stick Molecular Models. Journal of Chemical Education **2018,** 95 (1), 169-172.

24. Rossi, S.; Benaglia, M.; Brenna, D.; Porta, R.; Orlandi, M., Three Dimensional (3D) Printing: A Straightforward, User-Friendly Protocol To Convert Virtual Chemical Models to Real-Life Objects. Journal of Chemical Education **2015,** 92 (8), 1398-1401.

25. de Cataldo, R.; Griffith, K. M.; Fogarty, K. H., Hands-On Hybridization: 3D-Printed Models of Hybrid Orbitals. Journal of Chemical Education **2018,** 95 (9), 1601-1606.

26. Penny, M. R.; Cao, Z. J.; Patel, B.; Sil dos Santos, B.; Asquith, C. R. M.; Szulc, B. R.; Rao, Z. X.; Muwaffak, Z.; Malkinson, J. P.; Hilton, S. T., Three-Dimensional Printing of a Scalable Molecular Model and Orbital Kit for Organic Chemistry Teaching and Learning. Journal of Chemical Education **2017,** 94 (9), 1265-1271.

27. Scalfani, V. F.; Turner, C. H.; Rupar, P. A.; Jenkins, A. H.; Bara, J. E., 3D Printed Block Copolymer Nanostructures. Journal of Chemical Education **2015,** 92 (11), 1866-1870.

28. Robertson, M. J.; Jorgensen, W. L., Illustrating Concepts in Physical Organic Chemistry with 3D Printed Orbitals. Journal of Chemical Education **2015,** 92 (12), 2113-2116.

29. Kitson, P. J.; Macdonell, A.; Tsuda, S.; Zang, H.; Long, D.-L.; Cronin, L., Bringing Crystal Structures to Reality by Three-Dimensional Printing. Crystal Growth & Design **2014,** 14 (6), 2720-2724.

30. Chen, T.-H.; Lee, S.; Flood, A. H.; Miljanić, O. Š., How to print a crystal structure model in 3D. CrystEngComm **2014,** 16 (25), 5488-5493.

31. Wang, K.; Ho, C.-C.; Zhang, C.; Wang, B., A Review on the 3D Printing of Functional Structures for Medical Phantoms and Regenerated Tissue and Organ Applications. Engineering **2017,** 3 (5), 653-662.

32. Munaz, A.; Vadivelu, R. K.; St. John, J.; Barton, M.; Kamble, H.; Nguyen, N.-T., Three-dimensional printing of biological matters. Journal of Science: Advanced Materials and Devices **2016,** 1 (1), 1-17.

33. Bose, S.; Vahabzadeh, S.; Bandyopadhyay, A., Bone tissue engineering using 3D printing. Materials Today **2013,** 16 (12), 496-504.

34. Jungst, T.; Smolan, W.; Schacht, K.; Scheibel, T.; Groll, J., Strategies and Molecular Design Criteria for 3D Printable Hydrogels. Chemical Reviews **2016,** 116 (3), 1496-1539.

35. Studart, A. R., Additive manufacturing of biologically-inspired materials. Chemical Society Reviews **2016,** 45 (2), 359-376.

36. Crump, S. S. Apparatus and method for creating three-dimensional objects. 1989.

37. Ligon, S. C.; Liska, R.; Stampfl, J.; Gurr, M.; Mülhaupt, R., Polymers for 3D Printing and Customized Additive Manufacturing. Chemical Reviews **2017,** 117 (15), 10212-10290.

38. Zhou, X.; Liu, C.-j. C., Three-dimensional Printing for Catalytic Applications: Current Status and Perspectives. Advanced Functional Materials **2017,** 27 (30), 1701134-n/a.

39. Bartolo, P., Stereolithography Materials, Processes and Applications. Springer: 2011.

40. Green, W., Industrial Photoinitiators. CRC Press: Boca Raton, 2010.

41. Wayner, D. D. M.; Clark, K. B.; Rauk, A.; Yu, D.; Armstrong, D. A., C−H Bond Dissociation Energies of Alkyl Amines: Radical Structures and Stabilization Energies. Journal of the American Chemical Society **1997,** 119 (38), 8925-8932.

42. Husár, B.; Ligon, S. C.; Wutzel, H.; Hoffmann, H.; Liska, R., The formulator's guide to anti-oxygen inhibition additives. Progress in Organic Coatings **2014,** 77 (11), 1789-1798.

43. Jenkins, A. D., Photoinitiators for free radical cationic and anionic photopolymerisation, 2nd edition J V Crivello and K Dietliker Edited by G Bradley John Wiley & Sons, Chichester 1998. pp ix + 586, £ 90.00 ISBN 0-471-97892-2. Polymer International **2000,** 49 (12), 1729-1729.

44. Lapin, S. C.; Snyder, J. R.; Sitzmann, E. V.; Barnes, D. K.; Green, G. D. Stereolithography Using Vinyl EtherEpoxide Polymers. 1995.

45. Lapin, S. C.; Brautigam, R. J. Stereolithography Using Vinyl Ether Based Polymers. 1996.

46. Xu, J. Photo-Curable Resin Composition. 2015.

47. Tumbleston, J. R.; Shirvanyants, D.; Ermoshkin, N.; Janusziewicz, R.; Johnson, A. R.; Kelly, D.; Chen, K.; Pinschmidt, R.; Rolland, J. P.; Ermoshkin, A.; Samulski, E. T.;

DeSimone, J. M., Continuous liquid interface production of 3D objects. Science **2015,** 347 (6228), 1349-1352.

48. Zhou, X.; Liu, C.-j., Three-dimensional Printing for Catalytic Applications: Current Status and Perspectives. Advanced Functional Materials **2017,** 27 (30), 1701134.

49. Deckard, C. Method and apparatus for producing parts by selective sintering. 1986.

50. Lewis, J. A., Direct Ink Writing of 3D Functional Materials. Advanced Functional Materials **2006,** 16 (17), 2193-2204.

51. Stratasys Grabcad. https://grabcad.com.

52. MakerBot MakerBot Thingiverse. https://www.thingiverse.com/.

53. Gordeev, E. G.; Degtyareva, E. S.; Ananikov, V. P., Analysis of 3D printing possibilities for the development of practical applications in synthetic organic chemistry. Russian Chemical Bulletin **2016,** 65 (6), 1637-1643.

54. Symes, M. D.; Kitson, P. J.; Yan, J.; Richmond, C. J.; Cooper, G. J. T.; Bowman, R. W.; Vilbrandt, T.; Cronin, L., Integrated 3D-printed reactionware for chemical synthesis and analysis. Nat Chem **2012,** 4 (5), 349-354.

55. Kitson, P. J.; Marshall, R. J.; Long, D.; Forgan, R. S.; Cronin, L., 3D Printed High-Throughput Hydrothermal Reactionware for Discovery, Optimization, and Scale-Up. Angewandte Chemie International Edition **2014,** 53 (47), 12723-12728.

56. Lin, C.-G.; Zhou, W.; Xiong, X.-T.; Xuan, W.; Kitson, P. J.; Long, D.-L.; Chen, W.; Song, Y.; Cronin, L., Digital Control of Multistep Hydrothermal Synthesis via 3D Printed Reactionware. Angewandte Chemie International Edition **2018,** 0 (ja).

57. Kitson, P. J.; Marie, G.; Francoia, J.-P.; Zalesskiy, S. S.; Sigerson, R. C.; Mathieson, J. S.; Cronin, L., Digitization of multistep organic synthesis in reactionware for on-demand pharmaceuticals. Science **2018,** 359 (6373), 314.

58. Kitson, P. J.; Glatzel, S.; Cronin, L., The digital code driven autonomous synthesis of ibuprofen automated in a 3D-printer-based robot. Beilstein journal of organic chemistry **2016,** 12, 2776-2783.

59. Lederle, F.; Meyer, F.; Kaldun, C.; Namyslo, J. C.; Hübner, E. G., Sonogashira coupling in 3D-printed NMR cuvettes: synthesis and properties of arylnaphthylalkynes. New Journal of Chemistry **2017,** 41 (5), 1925-1932.

60. Zalesskiy, S. S.; Shlapakov, N. S.; Ananikov, V. P., Visible light mediated metal-free thiol–yne click reaction. Chemical Science **2016,** 7 (11), 6740-6745.

61. Parra-Cabrera, C.; Achille, C.; Kuhn, S.; Ameloot, R., 3D printing in chemical engineering and catalytic technology: structured catalysts, mixers and reactors. Chemical Society Reviews **2018,** 47 (1), 209-230.

62. Hurt, C.; Brandt, M.; Priya, S. S.; Bhatelia, T.; Patel, J.; Selvakannan, P. R.; Bhargava, S., Combining additive manufacturing and catalysis: a review. Catalysis Science & Technology **2017,** 7 (16), 3421-3439.

63. Rossi, S.; Puglisi, A.; Benaglia, M., Additive Manufacturing Technologies: 3D Printing in Organic Synthesis. ChemCatChem **2017,** 10 (7), 1512-1525.

64. Kitson, P. J.; Symes, M. D.; Dragone, V.; Cronin, L., Combining 3D printing and liquid handling to produce user-friendly reactionware for chemical synthesis and purification. Chemical Science **2013,** 4 (8), 3099-3103.

65. Skorski, M. R.; Esenther, J. M.; Ahmed, Z.; Miller, A. E.; Hartings, M. R., The chemical, mechanical, and physical properties of 3D printed materials composed of TiO2-ABS nanocomposites. Science and Technology of Advanced Materials **2016,** 17 (1), 89-97.

66. Bible, M.; Sefa, M.; Fedchak, J. A.; Scherschligt, J.; Natarajan, B.; Ahmed, Z.; Hartings, M. R., 3D-Printed Acrylonitrile Butadiene Styrene-Metal Organic Framework Composite Materials and Their Gas Storage Properties. 3D Printing and Additive Manufacturing **2018,** 5 (1), 63-72.

67. Sun, X.; Yan, Y.; Zhang, L.; Ma, G.; Liu, Y.; Yu, Y.; An, Q.; Tao, S., Direct 3D Printing of Reactive Agitating Impellers for the Convenient Treatment of Various Pollutants in Water. Advanced Materials Interfaces **2018,** 5 (8).

68. Azuaje, J.; Tubío, C. R.; Escalante, L.; Gómez, M.; Guitián, F.; Coelho, A.; Caamaño, O.; Gil, A.; Sotelo, E., An efficient and recyclable 3D printed α-Al2O3 catalyst for the multicomponent assembly of bioactive heterocycles. Applied Catalysis A: General **2017,** 530, 203-210.

69. Thakkar, H.; Eastman, S.; Al-Naddaf, Q.; Rownaghi, A. A.; Rezaei, F., 3D-Printed Metal–Organic Framework Monoliths for Gas Adsorption Processes. ACS Applied Materials & Interfaces **2017,** 9 (41), 35908-35916.

70. Li, X.; Rezaei, F.; Rownaghi, A. A., Methanol-to-olefin conversion on 3D-printed ZSM-5 monolith catalysts: Effects of metal doping, mesoporosity and acid strength. Microporous and Mesoporous Materials **2019,** 276, 1-12.

71. Li, X.; Li, W.; Rezaei, F.; Rownaghi, A., Catalytic cracking of n-hexane for producing light olefins on 3D-printed monoliths of MFI and FAU zeolites. Chemical Engineering Journal **2018,** 333, 545-553.

72. Li, X.; Alwakwak, A.-A.; Rezaei, F.; Rownaghi, A. A., Synthesis of Cr, Cu, Ni, and Y-Doped 3D-Printed ZSM-5 Monoliths and Their Catalytic Performance for n-Hexane Cracking. ACS Applied Energy Materials **2018,** 1 (6), 2740-2748.

73. Lefevere, J.; Mullens, S.; Meynen, V., The impact of formulation and 3D-printing on the catalytic properties of ZSM-5 zeolite. Chemical Engineering Journal **2018,** 349, 260-268.

74. Tubío, C. R.; Azuaje, J.; Escalante, L.; Coelho, A.; Guitián, F.; Sotelo, E.; Gil, A., 3D printing of a heterogeneous copper-based catalyst. Journal of Catalysis **2016,** 334, 110-115.

75. Zhu, C.; Qi, Z.; Beck, V. A.; Luneau, M.; Lattimer, J.; Chen, W.; Worsley, M. A.; Ye, J.; Duoss, E. B.; Spadaccini, C. M.; Friend, C. M.; Biener, J., Toward digitally controlled catalyst architectures: Hierarchical nanoporous gold via 3D printing. Science Advances **2018,** 4 (8).

76. Wang, Z.; Wang, J.; Li, M.; Sun, K.; Liu, C.-j., Three-dimensional Printed Acrylonitrile Butadiene Styrene Framework Coated with Cu-BTC Metal-organic Frameworks for the Removal of Methylene Blue. Scientific Reports **2014,** 4, 5939.

77. Díaz-Marta, A. S.; Tubío, C. R.; Carbajales, C.; Fernández, C.; Escalante, L.; Sotelo, E.; Guitián, F.; Barrio, V. L.; Gil, A.; Coelho, A., Three-Dimensional Printing in Catalysis: Combining 3D Heterogeneous Copper and Palladium Catalysts for Multicatalytic Multicomponent Reactions. ACS Catalysis **2018,** 8 (1), 392-404.

78. Stassi, S.; Fantino, E.; Calmo, R.; Chiappone, A.; Gillono, M.; Scaiola, D.; Pirri, C. F.; Ricciardi, C.; Chiadò, A.; Roppolo, I., Polymeric 3D Printed Functional Microcantilevers for Biosensing Applications. ACS Applied Materials & Interfaces **2017,** 9 (22), 19193-19201.

79. Wang, X.; Cai, X.; Guo, Q.; Zhang, T.; Kobe, B.; Yang, J., i3DP, a robust 3D printing approach enabling genetic post-printing surface modification. Chemical Communications **2013,** 49 (86), 10064-10066.

80. Wang, X.; Guo, Q.; Cai, X.; Zhou, S.; Kobe, B.; Yang, J., Initiator-Integrated 3D Printing Enables the Formation of Complex Metallic Architectures. ACS Applied Materials & Interfaces **2014,** 6 (4), 2583-2587.

81. Yee, D. W.; Schulz, M. D.; Grubbs, R. H.; Greer, J. R., Functionalized 3D Architected Materials via Thiol-Michael Addition and Two-Photon Lithography. Advanced Materials **2017,** 29 (16), 1605293.

CHAPTER 2. DIRECT 3D PRINTING OF CATALYTICALLY ACTIVE STRUCTURES

Reprinted with permission from *ACS. Catal*., **2017**, *7*,7567-7577. Copyright (2017) American Chemical Society

J. Sebastián Manzano1[,2], Zachary B. Weinstein[1,2], Aaron D. Sadow[1,2], Igor I. Slowing[1,2]

[1]US DOE Ames Laboratory, Ames, Iowa 50011, United States

[2]Department of Chemistry, Iowa State University, Ames, Iowa 50011, United States

Abstract

3D printing of materials with active functional groups can provide custom-designed structures that promote chemical conversions. Herein, catalytically active architectures were produced by photopolymerizing bifunctional molecules using a commercial stereolithographic 3D printer. Functionalities in the monomers included a polymerizable vinyl group to assemble the 3D structures and a secondary group to provide them with active sites. The 3D-printed architectures containing accessible carboxylic acid, amine, and copper carboxylate functionalities were catalytically active for the Mannich, aldol, and Huisgen cycloaddition reactions, respectively. The functional groups in the 3D-printed structures were also amenable to post-printing chemical modification. As proof of principle, chemically active cuvette adaptors were 3D printed and used to measure in situ the kinetics of a heterogeneously catalyzed Mannich reaction in a conventional solution spectrophotometer. In addition, 3D-printed millifluidic devices with catalytically active copper carboxylate complexes were used to promote azide-alkyne cycloaddition under flow conditions. The importance of controlling the 3D architecture of the millifluidic devices was evidenced by enhancing reaction conversion upon increasing the complexity of the 3D prints

Introduction

3D printing, also known as additive manufacturing, is a "bottom-up" technique for assembling materials layer-by-layer to produce three-dimensional objects.[1] The process is typically guided by a model created through computer–aided design. Although this technology was developed in the 1980s, its applications have only started to grow significantly in the past decade.[2] 3D printing has been used to produce functional architectures in the biomedical field,[3-6] as well as electronics,[7] mechanical devices,[8-16] periodic microstructures,[17, 18] and ceramics.[17, 19-22]

In contrast to the above applications, the use of additive manufacturing to control chemical processes is fairly recent, the first example being Cronin group's 3D printing of inert reactors with controlled architectures.[23, 24] Incorporation of chemical activity to 3D-printed objects has been achieved by post-printing deposition of catalysts,[25, 26] or by adding atom-transfer radical polymerization initiators to commercial resins, which then act as covalent binding sites on the printed solids.[27] Chemically active 3D-printed structures have also been produced by dispersion of reactive nanoparticles into printable matrices,[28, 29] or by extruding alumina inks followed by high temperature sintering.[30, 31]

To further expand the possibilities of using additive manufacturing for controlling chemical reactions, this work introduces a general concept that involves direct 3D printing of molecules with catalytically active functional groups. This strategy provides additional control to existing approaches as it allows directly positioning chemically active sites in intricate geometries (e.g. the interior walls of catalytic millifluidic devices, or small components of spectrophotometer cells that enable real time monitoring catalytic conversions). This new approach is still compatible with post-print chemical transformations of the active sites or introduction of orthogonal catalytic functionalities, which provides the

additional opportunity of producing multifunctional architectures by using sub-stoichiometric amounts of modifiers. The concept is based on using bifunctional molecules as building blocks, where one functional group serves to assemble 3D objects via polymerization and a second functionality with orthogonal reactivity provides the printed architectures with the chemical activity of interest. Additive manufacturing technologies based on spatially resolved photopolymerization such as stereolithography (SLA) or Continuous Liquid Interface Production (CLIP)[1, 32] are well suited to this approach because they typically use reactive acrylate and bis(acrylate) esters as monomers and crosslinkers respectively. These reactive monomers fit the proposed design as they are functionalized alkenes in which the double bond yields the 3D objects upon polymerization and possess an additional functional group that can deliver the target chemical activity. In this work, replacement of the ester moiety with other functional groups was explored as a means to produce catalytically active architectures (Figure 1). Importantly, this approach involves covalent immobilization of active sites on the prints which prevents catalyst leaching and consequent loss of activity. A second functional alkene monomer can also be added to the resin formulation to 3D print co-polymers and produce bifunctional architectures. Therefore, this approach can directly produce multifunctional objects with simultaneous control of structure and chemical activity.

Herein, formulations of functional group-containing monomers were 3D printed into catalytically active architectures via SLA (Figure 1b). The formulations were based on acrylic acid to give monofunctional structures and on mixtures of acrylic acid with allylamine, diallylamine or copper acrylate to print bifunctional structures. Additional components of the formulations included a cross-linker and a photoinitiator. The 3D-printed architectures were tested as catalysts in a three component Mannich reaction, an aldol

condensation that benefits from cooperativity between neighboring acid and amine functionalities, and a copper-catalyzed Huisgen cycloaddition reaction. In addition, as proof of concept, custom catalytic devices were 3D printed and used to study the kinetics of individual steps of the Mannich reaction and to perform continuous flow azide-alkyne cycloadditions.

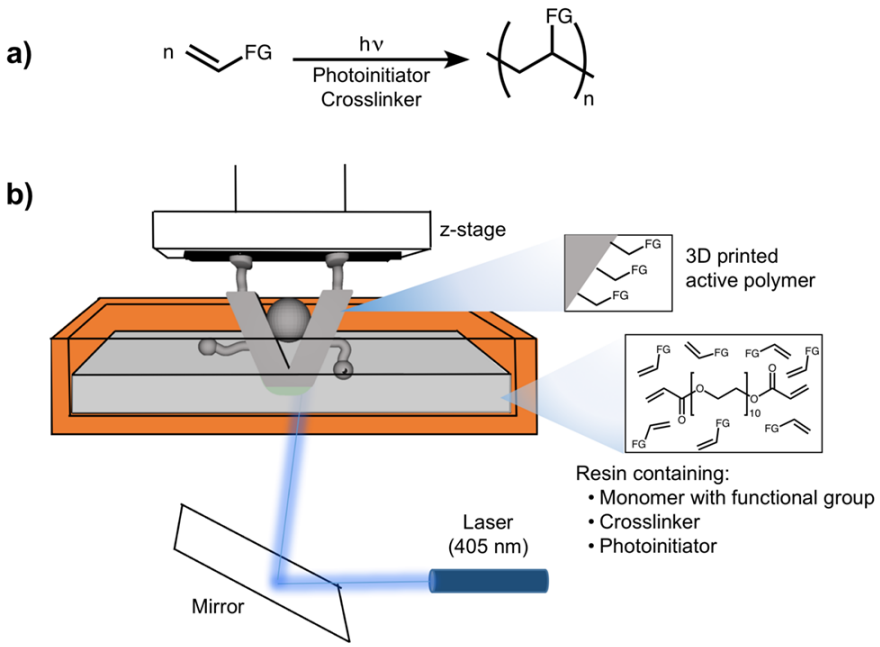

Figure 1. a) Bifunctional molecules as building blocks for 3D printing chemically active architectures: photopolymerization of an alkene bearing a functional group (FG) leads to a polymer with pendant active sites. b) 3D printing setup: a laser beam (405 nm) induces site-specific photopolymerization of the monomer inside a tank, the reaction is restricted to the irradiated area due to radical quenching by dissolved oxygen,[33] polymerization takes place on a z-stage that is elevated following completion of each layer.

Experimental

Chemicals

Acrylic acid, poly(ethylene glycol) diacrylate (PEGDA, average M_n 575), phenylbis-(2,4,6-trimethylbenzoyl)phosphine oxide (BAPO), allylamine, diallylamine, phenyl acetylene, 4-nitrobenzaldehyde, fluorescein isothiocyanate isomer I, N,N'-

Dicyclohexylcarbodiimide (DCC), ninhydrin, and aniline were purchased from Sigma-Aldrich (St. Louis, MO, USA). Cyclohexanone was purchased from Fischer Scientific (Waltham, MA, USA), and basic copper carbonate from Alfa Aesar (Tewksbury, MA, USA). All reagents were ACS grade or higher and used without further purification.

Resin formulation

Copper acrylate, $Cu(O_2CCH=CH_2)_2$. Synthesis followed a previously reported procedure.[34] Basic copper carbonate (16.1 g, 72.8 mmol) was suspended in acrylic acid (30 mL, 437 mmol) and stirred at r.t. After 1 h, acetone (20 mL) was added, and the mixture was allowed to stir overnight. A blue-green solid precipitated, and the mixture was filtered. Continuous extraction with acetone (250 mL) in a Soxhlet apparatus provided a concentrated solution. The solution was cooled to 0 °C yielding crystalline blue solid $Cu(O_2CCH=CH_2)_2$, which was isolated by filtration, washed with cold acetone, and dried overnight under vacuum. Yield 19.4 g (64.8%). IR (KBr, cm^{-1}): 1638, 1564, 1448, 1366, 1280, 1083, 1054, 992, 953, 899, 838, 676, 663, 619, 528. EA: $C_6H_6CuO_4$, calc. C, 35.04%; H, 2.94%; found C, 35.37%; H, 2.84%.

-COOH Resin

The acidic resin was prepared by mixing acrylic acid (70 mL, 1021 mmol) and PEGDA (30 mL, 58 mmol) in an Amber flask. Then, BAPO (0.350 g, 0.84 mmol) was added to the resin and the mixture was homogenized (14 000 rpm, 5 min). The solution was poured into the resin tank of a FormLabs Form 1+™ 3D printer (Somerville, MA, USA) and used for printing.

-COOH-co-NH_2/-NH Resins

The amine-modified resins were prepared by mixing acrylic acid (70 mL, 1021 mmol) and PEGDA (30 mL, 58 mmol) in an Amber flask. The flask was then set in an ice-

bath and allylamine (6.0 mL, 80 mmol) or diallylamine (6.0 mL, 49 mmol) were added dropwise into the solution controlling carefully the temperature to prevent unwanted pre-polymerization. BAPO (0.350 g, 0.84 mmol) was then added and the mixture was homogenized (14 000 rpm, 5 min). The solution was poured into the resin tank of a FormLabs Form 1+™ 3D printer (Somerville, MA, USA) and used for printing.

-$(COOH)_2$Cu Resin

The metal resin was prepared by mixing acrylic acid (70 mL, 1021 mmol) and PEGDA (30 mL, 58 mmol) in an Amber flask. Then, copper acrylate (0.70 g, 3.4 mmol) and BAPO (0.350 g, 0.84 mmol) were added to the resin and the mixture was homogenized (14 000 rpm, 5 min). The solution was poured into the resin tank of the FormLabs Form 1+™ 3D printer (Somerville, MA, USA) and used for printing.

3D printing

The CAD designs were prepared using AutoCad 2014 software and exported as STL files (Supplementary files available). 3D printing was performed via spatially resolved layer-by-layer photoinduced polymerization and cross-linking of acrylate based resins. A FormLabs Form 1+TM 3D printer (405 nm laser) was used with the clear resin settings for the laser polymerization. The selected design was an Ames Laboratory logo modified with small appendages to evaluate fine detail printing. After printing, the unreacted monomer was removed from the printed objects by immersion in toluene bath for 2 h. Final curing was performed by exposing the 3D object to UV irradiation (λ = 320 nm) in a rayonet photoreactor for 10 min.

Solvent compatibility assays

3D printed AL-COOH (0.140 g) was immersed in 10 mL of testing solvent (dichloromethane, toluene, acetone, water) inside a closed 20 mL vial. The vial was set in a

heated aluminum block on top of an orbital shaker, and was shaken at 200 rpm for 24 h at 40 °C. After that time the solvent was replaced with fresh solvent and the heated shaking was repeated for 4 additional 24 h periods. The 3D printed AL-COOH were then visually examined and the supernatants were tested for residues of polymer by ESI-MS on an Agilent QTOF 6540.

pH measurements

A 3D-printed AL-COOH (0.140 g) was immersed in 10 mL of deionized water (18 MΩ). The pH was measured with an Accumet benchtop pH meter at 20 °C every 5 min until stabilized. The pH value was stable for at least 2 weeks.

N,N'-Dicyclohexylcarbodiimide (DCC) coupling of aniline

DCC (20 mg, 0.097 mmol) was dissolved in 3 mL of dichloromethane (DCM) in a 20 mL vial. A printed AL-COOH (0.140 g) or AL-COOH-co-NH_2 was added to the mixture and shaken (300 rpm) for 1 h to activate the pendant carboxylic groups. Later, 3 mL of a solution of aniline (200 mM in DCM) was added to the solution and shaken for 16 h. The AL-COOH/AL-COOH-co-NH_2 was then washed thoroughly with DCM to remove physically adsorbed species. The DCM solvent was then evaporated from the washes under reduced pressure, and water (15 mL) was added to dissolve the residual aniline. An aliquot (40 µL) was taken and was diluted in water (1 mL) and quantified by UV-Vis spectroscopy.

Kaiser test

Ninhydrin (20 mg, 0.097) was dissolved in ethanol (15 mL). A printed AL-COOH-co-NH_2 or AL-COOH-co-NH (0.170 g) was added to the vial along with 3 mL of pure ethanol. The mixture was heated for 10 min at 100 ºC to obtain the Ruheman's purple complex. The AL-COOH-co-NH_2 was removed and washed with ethanol (5 mL) to remove

physically adsorbed species. Finally, this solution was quantified by UV-Visible spectroscopy. Hexadecylamine was used as standard to prepare a calibration curve.

Theoretical volume calculation

The Autodesk® Netfabb® software was used to calculate the volume of a 70 µm shell. In this software, the volume was calculated for a complete AL-logo, as well as for each volume reduced version, taking 600 µm steps. Finally, an interpolation was performed to find the volume at a thickness of 70 µm.

Electron microscopy

Scanning electron microscopy (SEM) and energy dispersive x-ray spectroscopy (EDS) were conducted using a FEI Teneo LoVac microscope operating at 10 kV. The 3D-printed objects were directly glued to the sample holder for analysis.

Attenuated Total Reflectance Fourier Transform Infrared (ATR-FTIR) Spectroscopy

Measurements were made on a Bruker Vertex 80 FT-IR spectrometer with OPUS software. The spectrometer was equipped with a diamond sealed high pressure clamp ATR MIRacle PIKE accessory where the 3D-printed samples were pressed against the crystal to collect the respective spectrum. 32 scans were collected for each measurement in absorbance mode with 4 cm^{-1} resolution.

Inductively Coupled Plasma-Optical Emission Spectroscopy

After performing the click reaction catalyzed by AL-$(COOH)_2$-Cu, the 3D object was removed, and the samples were concentrated under reduced pressure. Samples were calcined at 550 ºC for 6 h to remove the remaining organic material and aqua-regia was added to dissolve the metal particles. The solution was analyzed in a Perkin Elmer Optima 2100 DV Inductively Coupled Plasma-Optical Emission Spectroscope and concentration was obtained by interpolation into a freshly prepared calibration curve.

Fluorescein isothiocyanate (FITC) labeling

AL-COOH-co-NH_2 and AL-COOH-co-NH were immersed in a FITC solution in acetone (0.8 mg mL^{-1} and 1.6 mg mL^{-1} respectively). After shaking overnight, the samples were washed thoroughly with acetone to remove physically adsorbed species and dried under air. Elemental analysis was performed using a Perkin-Elmer 2400 Series II CHN/S with acetanilide as calibration standard, and combustion and reduction temperatures of 925 ºC and 640 ºC respectively.

Fluorescence microscopy

FITC-treated AL-COOH-co-NH_2/AL-COOH-co-NH were sectioned and analyzed under a Nikon eclipse Ti-U inverted microscope equipped with an AT EGFP/FITC/Cy2/Alexa Fluor 488 filter under 480 nm excitation.

Catalytic Reactions

All reactions were performed in triplicate, unless otherwise stated.

Mannich reaction

Cyclohexanone (510 µL, 4.93 mmol) was dissolved in 1 mL DCM. Then, aniline (100 µL, 1.09 mmol), benzaldehyde (102 µL, 1.00 mmol) and an AL-COOH (0.140 g, 57 µmol accessible acidic groups) or commercial poly(acrylic acid) (4 mg, 57 µmol accessible acidic groups) catalyst were added to the mixture. The solution was placed in an orbital shaker at 300 rpm and shaken for 4 h at r.t. The solution was concentrated under reduced pressure and purified by chromatography using a silica column (2 : 8, hexanes : ethyl acetate). Reaction conversions were measured by ^{1}H NMR spectroscopy using 1,4-dioxane as internal standard. NMR spectra consistent with previous reports.[35, 36] ^{1}H NMR (500 MHz, $CDCl_3$): δ(ppm) 7.45 – 7.08 (m, 7H), 6.71 – 6.63 (m, 3H), 4.90 (br, 1H), 4.75 (d, J = 6.8 Hz,

1H), 2.85 – 2.71 (m, 1H), 2.54 – 2.31 (m, 2H), 2.07 – 1.64 (m, 6H). MS (ESI): calcd. for $[M+H]^+$ 280.17, found 280.17.

Mannich reaction-Kinetics study-Step 1

50 µL of 1.0 mM solution of aniline was mixed with 50 µL of 1.0 mM solution of benzaldehyde and 2.9 mL of DCM in a 3 mL quartz cuvette (initial concentrations: 17 µM aniline, 17 µM benzaldehyde). The kinetic adaptor was added and the cuvette was set into a heated (40 ºC) cell holder of a HP 8453 UV-Visible spectrophotometer. Temperature was controlled using a thermostated circulator bath. Formation of N-benzylideneaniline was tracked at 264 nm.

Mannich reaction-Kinetics study-Step 2

500 µL of 50 mM solution of cyclohexanone was mixed with 50 µL of 1.0 mM solution of N-benzylideneaniline and 2.45 mL of DCM in a 3 mL quartz cuvette (initial concentrations: 17 µM N-benzylideneaniline, 8.3 mM cyclohexanone). The kinetic adaptor was added and the cuvette was set into a heated (40 ºC) cell holder of a HP 8453 UV-Visible spectrophotometer. Temperature was controlled using a thermostated circulator bath. Formation of the Mannich product was monitored at 250 nm.

Mannich reaction-Kinetics study-full reaction

500 µL of 50 mM solution of cyclohexanone was mixed with 50 µL of 1.0 mM solution of aniline and 50 µL of a 1.0 mM solution of benzaldehyde and 2.4 mL of DCM in a 3 mL quartz cuvette (initial concentrations: 17 µM aniline, 17 µM benzaldehyde, 8.3 mM cyclohexanone). The kinetic adaptor was added and the cuvette was set into a heated (40 ºC) cell holder of a HP 8453 UV-Visible spectrophotometer. Temperature was controlled using a thermostated circulator bath. Formation of the Mannich product was monitored at 250 nm.

3D printing millifluidic devices (MF-devices)

To 3D print the MF-devices the following parameters were changed using the OpenFL Preform software. The only parameters changed were: “otherlayerpasses” = 3, “earlylayerpasses” = 3 and “SliceHeight” = 0.2.

Aldol condensation

4-Nitrobenzaldehyde (60 mg, 0.4 mmol) was mixed with 3 mL of acetone and a AL-COOH-co-NH_2 (0.170 g, 14.6 µmol accessible groups), AL-COOH-co-NH (0.170 g, 8.0 µmol accessible groups) or poly(allyl amine) (0.0049 g, 86 µmol accessible groups). The solution was shaken at 300 rpm for 24 h at 40 ˚C. The solution was concentrated under reduced pressure and the products analyzed by ^{1}H NMR spectroscopy using dimethyl sulfone as an internal standard. ^{1}H NMR (500 MHz, $CDCl_3$): δ (ppm) aldol product: 8.20 (d, J = 8.7 Hz, 2H), 7.55 (d, J = 9.0 Hz, 2H), 5.26 (t, J = 6.1 Hz, 1H), 2.86 (d, J = 6.0 Hz, 2H), 2.21 (s, 3H); enone product, 8.29 (d, J = 9.0 Hz 2H), 7.71(d, J = 9.0 Hz 2H), 7.56 (d,1H), 6.84 (d, J = 9.0 Hz 1H), 2.42 (s, 3H). TOF was defined as mmol of products divided by mmol of accessible amine groups in the catalyst divided by 24 h. TOFs are reported as averages of three reactions and errors are reported as two standard deviations from the average.

Synthesis of Benzyl azide

Benzyl azide was prepared based on a previously reported procedure.[37] Benzyl bromide (1.2 mL, 8.6 mmol) was dissolved in 40 mL of acetone/water solution (3:1). Sodium azide (0.7 g, 10.8 mmol) was added slowly within 1 min and the solution was stirred for 2 h. Benzyl azide was extracted with DCM (40 mL) and washed with brine and then water (100 mL each). The product was concentrated from the organic layer by solvent evaporation under reduced pressure. ^{1}H NMR (500 MHz, $CDCl_3$): δ (ppm) = 7.56 – 7.28 (m, 5H), 4.36 (s, 2H). IR (KBr, cm^{-1}): 3032, 2930, 2097, 1497, 1498, 1350, 1254.

Huisgen cycloaddition

Benzyl azide (200 µL, 1.61 mmol), phenylacetylene (200 µL, 1.82 mmol) and triphenylphosphine (5.0 mg, 0.019 mmol) were mixed in a vial containing a 3D-printed AL-$(COO)_2Cu$ (0.170 g) in DCM (3 mL). The solution was shaken in an orbital shaker at 300 rpm for 24 h at 40 ˚C. The solution was concentrated under reduced pressure and the product was analyzed by ^{1}H NMR spectroscopy using dimethyl sulfone as internal standard. ^{1}H NMR (500 MHz, $CDCl_3$): δ (ppm) = 7.82 (d, J = 6.8 Hz, 2H), 7.69 (s, 1H), 7.42 – 7.26 (m, 8H), 5.53 (s, 2H). Turnover frequency for this reaction was defined as mmol of products divided by mmol of accessible copper sites (assuming a 70 µm penetration depth) in the catalyst divided by 24 h. TOFs are reported as average of three reactions and errors are reported as two standard deviations from the average.

Flow Huisgen cycloaddition

Benzyl azide (200 µL, 1.61 mmol), phenylacetylene (200 µL, 1.82 mmol) and triphenylphosphine (5.0 mg, 0.019 mmol) were mixed in DCM (5 mL). The solution was flowed through each millifluidic device at room temperature at a 5.0 mL h^{-1} rate. The collected solution was concentrated under reduced pressure and the product was analyzed by ^{1}H NMR spectroscopy using dimethyl sulfone as an internal standard. ^{1}H NMR (500 MHz, $CDCl_3$): δ (ppm) = 7.82 (d, J = 6.8 Hz, 2H), 7.69 (s, 1H), 7.42 – 7.26 (m, 8H), 5.53 (s, 2H).

Results and Discussion

3D Printing of Acid Functionalized Architectures

First, monofunctional architectures bearing acid sites were produced. To this end a 3D printing resin was prepared using acrylic acid (AA) as the bifunctional building block. Poly(ethylene glycol) diacrylate (PEGDA, M_n 575) was added as a cross-linker, and phenylbis-(2,4,6-trimethylbenzoyl)phosphine oxide (BAPO) as the photoinitiator[38] (mole

ratios 17.6/1/0.01 AA/PEGDA/BAPO). As a proof of concept, a modified Ames Lab logo (designated as AL-COOH) was printed in a commercial SLA 3D printer (Figure 2). Immersion of the 3D printed AL-COOH in organic solvents (dichloromethane, toluene and acetone) under shaking and heating (5 cycles of 24 h at 200 rpm and 40 °C) did not change the size and aspect of the prints. Electrospray ionization mass spectrometry (ESI-MS) of the supernatants revealed no traces of oligomers, suggesting AL-COOH can be used under these conditions without risk of degradation. Resolution of the prints was tested using transverse stick pile models with varying thicknesses, the smallest achievable features were 400 µm thickness and 4000 µm spacing (Figure S1).

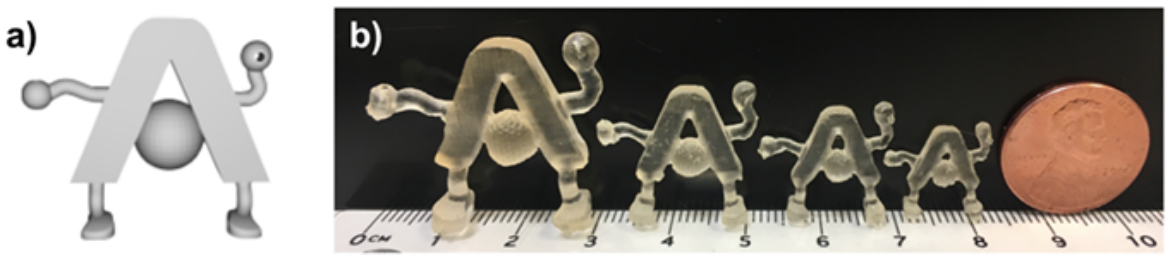

Figure 2. a) AutoCAD model of a modified Ames Laboratory logo (AL), and b) 3D-printed structures (AL-COOH) of different sizes.

The properties and accessibility of carboxylic acid functional groups in AL-COOH were characterized by a combination of infrared spectroscopy, pH measurements, and surface reactivity. ATR-FTIR spectra were collected directly by pressing the AL-COOH print against the ATR crystal and showed an asymmetric band in the carbonyl region (Figure 3, black spectrum) that was deconvoluted into three peaks centered at 1672, 1708, and 1735 cm^{-1} (Figure S2). These peaks were assigned to the C=O stretches of hydrogen-bonded and non-hydrogen bonded carboxylic acids of polyacrylic acid (PAA) and the ester groups of PEGDA, respectively.[39, 40] Immersion of the printed AL-COOH (0.140 g) in water (10 mL)

gave an acidic solution (pH 3.2). Based on the pK_a of PAA (4.5)[41] the amount of exchangeable protons was estimated at 440 ± 20 µmol g^{-1}. This number is significantly lower than what would be expected from the original resin composition (9495 µmol g^{-1}), suggesting not all of the carboxylic groups are accessible to the solvent. The accessible carboxylic acid groups were quantified by activation with N,N'-dicyclohexylcarbodiimide (DCC) followed by titration with aniline to form amide. The consumption of aniline by the DCC treated AL-COOH indicated 409 ± 6 µmol accessible sites per gram and corresponded well with the estimate from pH measurement. The FTIR spectrum of the amido product, AL-CONHPh, revealed amide I and II bands at 1686 and 1541 cm^{-1} (Figure 3, red spectrum). C=C stretching modes (1600 and 1493 cm^{-1}) characteristic of the aromatic groups were also visible in the spectrum. Deconvolution of the overlapping bands in the carbonyl region indicated a decrease in the intensity ratio between the polyacrylic acid and PEGDA bands compared to the original AL-COOH. This change in ratio further suggested that only a fraction of the carboxylates reacted with aniline, likely corresponding to surface groups while the bulk groups remained unchanged (Figure S3). It must be noted that because ATR is a surface technique and the analysis was done by directly pressing the printed AL-COOH against the crystal, signals from the surface are enhanced relative to the bulk. Further evidence of the limited accessibility to the bulk was obtained by treating the 3D-printed architecture with a copper nitrate solution. Examination of a cross-section of the treated material by light microscopy revealed a penetration depth of ca. 70 µm (Figure S4). The volume fraction of this layer with respect to the total volume of the AL-COOH print was estimated using Autodesk® Netfabb® software. The estimate (2.9 %, Figure S5) was

comparable to the fraction of accessible carboxylic groups determined by titration with DCC/aniline (4.3 %).

Catalytic Activity of 3D-Printed Architectures

The 3D-printed AL-COOH was then tested as an acid catalyst for a three-component Mannich reaction (Equation 1),[42] where protonations are proposed to promote imine formation of a non-enolizable aldehyde and enolization of a ketone. The imine and enol then react to yield the β-aminocarbonyl product (Figure S6).[43] Addition of AL-COOH to a mixture of benzaldehyde (1.0 mmol), aniline (1.1 mmol) and cyclohexanone (4.9 mmol) gave a 2.5-fold enhancement in product yield compared to the reaction in absence of the print and in presence of an AL 3D-printed using only the PEGDA cross-linker (70 ± 5 % yield, 28 % without AL-COOH and 29% with AL-PEGDA, 4 h, r.t, 2 mL dichloromethane (DCM), 5 mol % accessible COOH). The catalytic activity was comparable with that of commercial polyacrylic acid (PAA). AL-COOH was recycled without any apparent loss in catalytic activity or polymer degradation (evaluated by ESI-MS) (Figure S7).

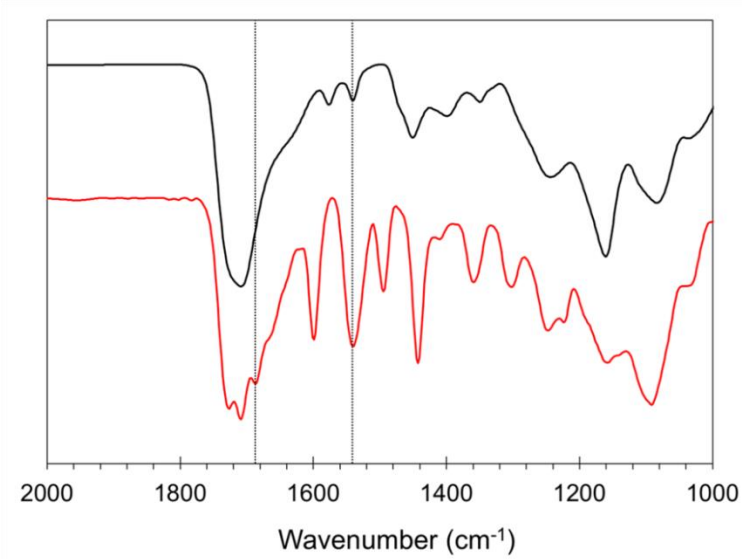

Figure 3. FTIR spectra of AL-COOH before (black) and after (red) DCC-mediated coupling with aniline. The latter shows amide I and amide II bands at 1686 cm^{-1} and 1542 cm^{-1}.

`Catalytic Activity of 3D-Printed Architectures

The 3D-printed AL-COOH was then tested as an acid catalyst for a three-component Mannich reaction (Equation 1),[42] where protonations are proposed to promote imine formation of a non-enolizable aldehyde and enolization of a ketone. The imine and enol then react to yield the β-aminocarbonyl product (Figure S6).[43] Addition of AL-COOH to a mixture of benzaldehyde (1.0 mmol), aniline (1.1 mmol) and cyclohexanone (4.9 mmol) gave a 2.5-fold enhancement in product yield compared to the reaction in absence of the print and in presence of an AL 3D-printed using only the PEGDA cross-linker (70 ± 5 % yield, 28 % without AL-COOH and 29% with AL-PEGDA, 4 h, r.t, 2 mL dichloromethane (DCM), 5 mol % accessible COOH). The catalytic activity was comparable with that of commercial polyacrylic acid (PAA). AL-COOH was recycled without any apparent loss in catalytic activity or polymer degradation (evaluated by ESI-MS) (Figure S7).

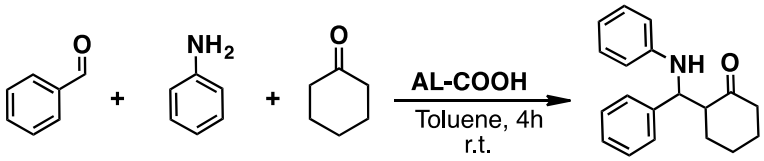

(1)

To highlight the custom manufacturing capabilities of 3D printing, the catalytic poly(acrylic acid) polymer was printed into a shape (UV-COOH) that enabled in situ monitoring the kinetics of the Mannich reaction via solution UV-Visible spectroscopy. The UV-COOH print was designed so that it could be inserted into a standard cuvette without interfering with the beam path (Figure 4a), allowing the collection of reaction spectra in real time to provide insight into the heterogeneous catalytic process. To monitor the reaction in the linear region of chromophore absorbances, the conditions were adjusted to lower reactant concentrations (17 μM aniline and benzaldehyde, 8.3 mM cyclohexanone) and higher

temperature (40 °C, continuous stirring in DCM) than those using AL-COOH. These conditions along with the use of the 3D-printed PAA allowed continuous collection of spectra as the reaction progressed. In contrast, the use of suspended polymer particles of PAA gave no distinct signals due to intense scattering (Figure S8). Under these conditions, the initial rate of the reaction catalyzed by the 3D-printed PAA was over 25 times higher than the uncatalyzed reaction (Figure 4b, Table 1).

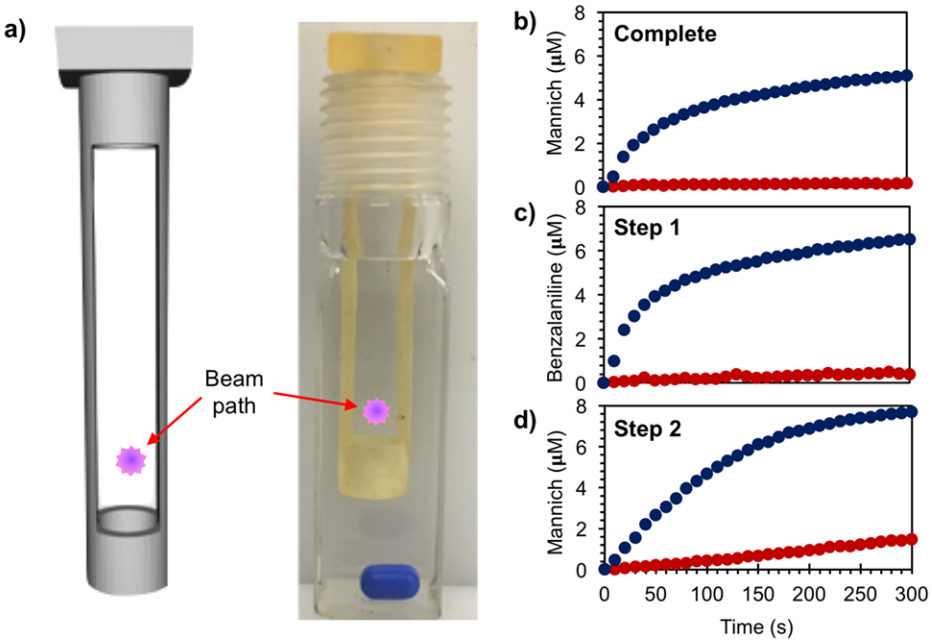

Figure 4. a) CAD model and 3D-printed catalytic cuvette adaptor to monitor the kinetics of formation of b) the Mannich product from reaction between benzaldehyde and aniline (17 μM each) and cyclohexanone (8.3 mM) and the two main steps of the reaction, namely: c) formation of N-benzylideneaniline intermediate from benzaldehyde and aniline (17 μM each), and d) formation of Mannich product by reaction between the intermediate N-benzylideneaniline (17 μM) and cyclohexanone (8.3 mM). Blue and red data points correspond to experiments with and without the 3D-printed catalytic polymer, respectively. Horizontal axis is time and has the same scale for all plots. All reactions were performed under constant stirring at 40 ºC in DCM, and monitored at 250 nm for b) and d), and 264 nm for c).

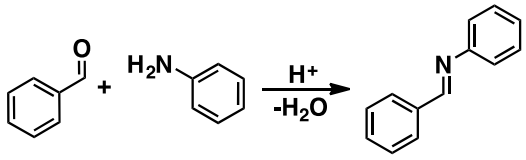

(2)

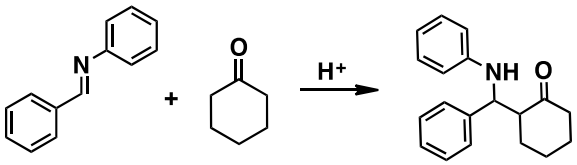

(3)

Because PAA is expected to be catalytically active for each of the two main reaction steps, the effect of the 3D-printed material was investigated separately for each of them. The kinetics of the first step (Equation 2) were investigated by reacting benzaldehyde and aniline (17 µM each, in DCM, 40 °C, constant stirring, no cyclohexanone) in presence and absence of the 3D-printed PAA. Formation of the N-benzylideneaniline product was monitored at 264 nm (Figure 4c). Comparison of the initial rates indicated a large catalytic effect of the material on the reaction (over 50 times, Table 1). The Brønsted acid has two competing effects on imine formation: on one hand it limits the equilibrium concentration of the free amine required for forming a carbinolamine intermediate, on the other it activates the aldehyde for nucleophilic attack and promotes dehydration of the carbinolamine to give the imine product.[43] The large rate enhancement observed with the 3D-printed PAA suggests that its role in aldehyde activation and carbinolamine dehydration outweighs the low equilibrium concentration of the free amine, which seems to be quickly replenished as it is consumed in the reaction. A somewhat smaller, yet fairly significant, catalytic effect of the 3D-printed PAA was also observed in the second major step of the Mannich reaction, i.e. the reaction between the isolated N-benzylideneaniline (17 µM) and excess cyclohexanone (8.3 mM) (Equation 3, ca. 10-fold initial rate increase, Table 1). This step was performed under the same conditions as the first step (DCM, 40 °C, continuous stirring) and monitored at 250 nm. The Brønsted acid is proposed to participate in this step by activating the α-carbon of cyclohexanone via enolization and protonating the imine to facilitate nucleophilic attack. In

the PAA-catalyzed conversion, this step was slower than the first step of the reaction and rate limiting. While the differences in apparent catalytic effect between the two steps could be rationalized in terms of a larger steric hindrance for the protonated N-benzylideneaniline as opposed to the protonated benzaldehyde, it is interesting to note that for the non-catalyzed process the second step is faster than the first one. This suggests that steric hindrance may not be the only or most relevant difference determining the relative rates of the two main steps of the reaction. Thus, for the non-catalyzed reaction the higher rate of the second step may be due to the reaction proceeding mainly via direct substitution of the carbinolamine intermediate by the large excess of cyclohexanone with little formation of imine.[44] In contrast, for the PAA-catalyzed reaction, the capacity of the protonated imine to accommodate the positive charge (Step 2) makes it less reactive than the protonated aldehyde (Step 1).[45, 46]

Table 1. Initial rates of individual steps and complete Mannich reaction between aniline, benzaldehyde and cyclohexanone in absence and presence of 3D-printed PAA.[a]

	Step 1 ($\times 10^{-3}$ µM s^{-1})	**Step 2** ($\times 10^{-3}$ µM s^{-1})	**Complete** ($\times 10^{-3}$ µM s^{-1})
Non-catalyzed	1.35 ± 0.10	5.08 ± 0.06	2.04 ± 0.24
Catalyzed by 3D-Printed PAA	79.6 ± 9.2	54.2 ± 1.1	54.4 ± 4.6

[a]Reaction conditions: 40 °C in DCM, constant stirring for all reactions; 17 µM aniline and 17 µM benzaldehyde for step 1; 17 µM N-benzylideneaniline and 8.3 mM cyclohexanone for step 2; 17 µM aniline, 17 µM benzaldehyde and 8.3 mM cyclohexanone for the complete reaction. Initial rates were calculated from the slope of the first 50 s of each reaction.

3D Printing of Bifunctional Materials via co-Polymerization

Copolymers containing multiple functional groups have been demonstrated to enhance catalytic conversions via cooperativity between the different types of active sites.[47] To explore this possibility on 3D-printed catalytic structures, a new resin containing allylamine and acrylic acid as co-monomers along with the PEGDA crosslinker and BAPO photoinitator was formulated (1.4/17.6/1/0.01 mole ratios, respectively). The resulting bifunctional acid/base 3D-printed structures were designated as AL-COOH-co-NH_2. The presence of chemically accessible amine groups was confirmed by the green fluorescence of fluorescein isothiocyanate (FITC)-treated 3D prints (Figure S10a, b). Fluorescence microscopy analysis of cross sections of FITC-treated AL-COOH-co-NH2 indicated that the probe penetrated about 70 μm into the printed structure (Figure S10c), which is similar to that observed for Cu^{2+} on AL-COOH (Figure S4). This result is consistent with only a fraction of the functionalities being accessible for chemical conversions and provides a visual indicator of the active domains in the 3D-printed AL-COOH-co-NH_2. In contrast, fluorescence was not detected in FITC-treated monofunctional AL-COOH under the same conditions. The amount of accessible amines in AL-COOH-co-NH_2 was quantified by reaction of the printed material with ninhydrin.[48] The resulting soluble bis-(1H-indene-1,3(2H)-dione)imine (Ruhemann's purple) was measured by UV-Vis spectroscopy indicating 86 ± 4 μmol accessible –NH_2 sites per gram of AL-COOH-co-NH_2.

ATR-FTIR analysis of AL-COOH-co-NH_2 revealed two small bands at 1630 and 1545 cm^{-1} that are consistent with asymmetric and symmetric stretching modes of ammonium, as expected for amine groups in presence of carboxylic acids (Figure S11). To investigate whether the accessible amines were located near carboxylic groups, AL-COOH-co-NH_2 samples were treated with excess DCC in DCM followed by extensive washing.

ATR-FTIR analysis of the treated prints indicated the formation of amide bonds (1635 and 1556 cm^{-1}) suggesting close proximity between the pendant –COOH and $–NH_2$ groups (Figure S11). Reaction of DCC-treated prints with ninhydrin quantified the remaining unreacted (i.e. isolated) amine sites as 21 ± 4 µmol g^{-1}. Comparison with the initial amine surface loading indicated that three quarters (about 65 µmol g^{-1}) of the accessible amine groups are in close proximity to carboxylates. The remaining accessible acidic sites were also quantified by a second sequence of activation with DCC followed by reaction with excess aniline giving 145 ± 7 µmol g^{-1}. Thus, the total accessible carboxylates in the AL-COOH-co-NH_2 prints was estimated as 210 µmol g^{-1}, and ca. 30% of surface carboxylic acids were closely associated to surface amines.

The AL-COOH-co-NH_2 prints were then tested as catalysts for the cross-aldol condensation between 4-nitrobenzaldehyde and acetone (Equation 4). It has been reported that this reaction benefits from cooperative interactions between the catalytic amine groups and neighboring weakly acidic groups.[49-54] Indeed, bifunctional AL-COOH-co-NH_2 displayed a three-fold higher turnover frequency (TOF, based on the number of accessible amine groups) than monofunctional poly(allylamine) (7.04 ± 0.35 and 2.28 ± 0.46 × 10-3 h^{-1} respectively, Figure 5), suggesting cooperativity between carboxylate and amine groups in the prints. The catalytic AL-COOH-co-NH_2 was easily recycled without any indications of polymer degradation (evaluated by ESI-MS) (Figure S12).

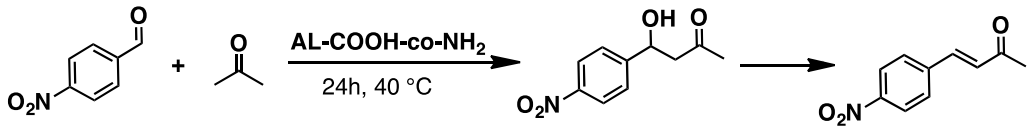

(4)

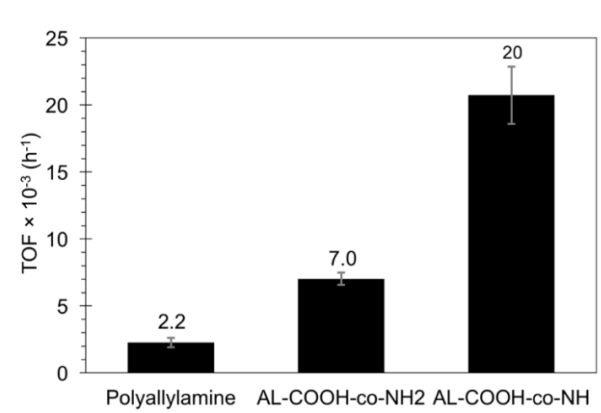

Figure 5. Catalytic activities of poly(allylamine) and 3D-printed AL-COOH-co-NH_2 and AL-COOH-co-NH in the aldol condensation between p-nitrobenzaldehyde and acetone. Reaction conditions: 0.4 mmol p-nitrobenzaldehyde, 40 ºC in 3 mL acetone.

Previous reports have indicated that the activity of primary alkylamines for this reaction may be limited by the competitive interaction of the catalyst and the non-enolizable aldehyde substrate to reversibly form an inactive imine surface species.[50] This catalyst deactivation has been solved by replacing the primary amine with a secondary amine, which cannot form imines in low polarity media.[50, 54] Based on this information, a new bifunctional material was 3D printed using diallyl amine (secondary amine) and acrylic acid as co-monomers, and was designated as AL-COOH-co-NH (diallyl amine/acrylic acid/PEGDA/BAPO 0.84/17.6/1/0.01). Treatment of the print with ninhydrin changed its color to a slight orange (Figure S13a), confirming presence of secondary amines.[55] Reaction of the print with FITC (Figure S13b) allowed quantification of accessible amine sites by determining the amount of S in the conjugate via combustion (elemental) analysis. The analysis indicated a loading of 47 ± 7 µmol of accessible secondary amines per gram of printed material. Use of AL-COOH-co-NH as a catalyst in the aldol condensation (Equation 4) led to a three-fold increase in TOF (0.0207 ± 0.0021 h^{-1}) compared to the primary amine print (AL-COOH-NH_2) (Figure 5), this catalyst also retained its activity upon recycling (Figure S14). The dramatic enhancement of catalytic activity of the new print illustrates the

advantage of being able to select functional monomers for 3D printing of chemically active materials.

3D Printing of Catalytic Transition Metal Complexes

The range of potential catalytic applications of 3D-printed structures can be even wider if the functional monomers also include reactive metal centers. For example copper(II) acetate and derivatives are used as catalysts for Huisgen cycloaddition reactions,[56] as well as in oxidative conversions.[57] To evaluate this possibility a resin containing copper acrylate was produced by dissolving the salt into the original resin formulation (copper acrylate/acrylic acid/PEGDA/BAPO 0.06/17.6/1/0.01). The resolution of the Cu-containing 3D prints improved compared to that of the original Cu-free resin (Figure S15). The minimum printable features determined with transverse stick pile models were 300 µm thick layers and 2000 µm inter-layer spacings. Possible reasons for the improved resolution include a potential decrease in the concentration of free radical either by quenching by Cu(II) or by absorption of the complex at the laser wavelength (ε_{405nm} of Cu acrylate in acrylic acid = 43 M^{-1} cm^{-1}). The resulting AL-$(COO)_2$Cu architectures had a uniform cyan color throughout the entire print suggesting successful incorporation and homogeneous dispersion of the metal centers (Figure 6a). SEM-EDS mapping of the 3D print confirmed the presence of Cu and suggested the metal was also homogeneously dispersed at the microscopic level (Figure 6b,c).

ATR-FTIR analysis of the AL-$(COO)_2$Cu 3D prints revealed three bands assigned to C=O stretches (Figure 7). The highest frequency band centered at 1720 cm^{-1} matched the composite band previously observed in AL-COOH and was thus assigned to carboxylic and ester groups resulting from the acrylic acid and PEGDA components of the resin. The additional bands at 1618 and 1447 cm^{-1} likely correspond to the antisymmetric and

symmetric stretches of the Cu(II)-coordinated carboxylate group,[58] based on comparison with the spectrum of copper(II) acetate. The blue shift of these bands compared to the corresponding stretches in the original copper acrylate suggests successful polymerization of the monomer during 3D printing.

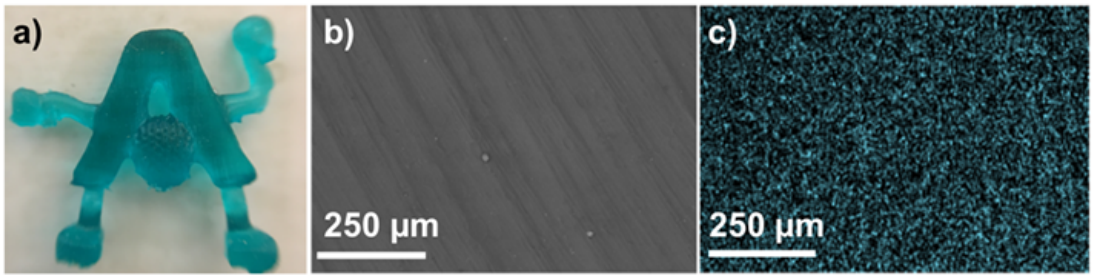

Figure 6. a) 3D-printed AL-$(COO)_2Cu$, b) SEM image of a cross section and c) its corresponding Cu-K SEM-EDS map showing homogeneous distribution of the metal.

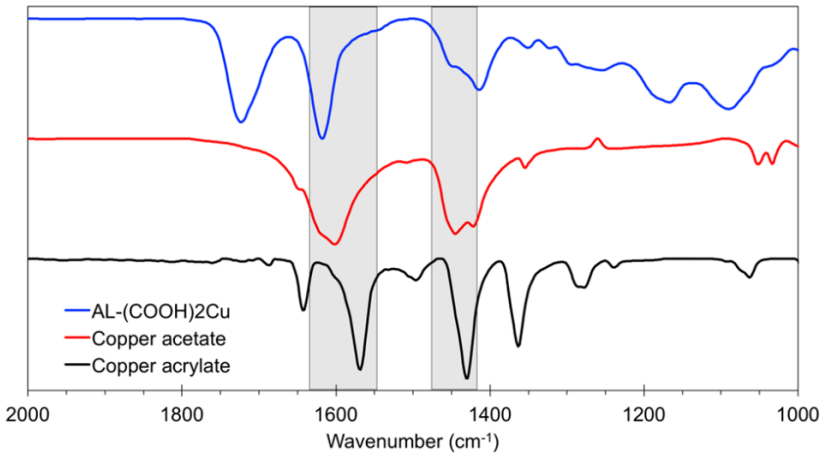

Figure 7. ATR-FTIR spectra of the 3D-printed AL-$(COO)_2Cu$ polymer (blue), copper acetate (red), and copper acrylate (black).

The AL-$(COO)_2Cu$ print was catalytically active for the 'click' Huisgen cycloaddition reaction between phenylacetylene and benzyl azide (Equation 5). Based on the homogeneity of Cu distribution suggested by EDS mapping and the penetration depth of approximately 70 µm observed with the AL-COOH and AL-COOH-co-NH_2 prints (corresponding to about 4 %

of the print volume), the number of accessible Cu sites was estimated at ca. 2 μmol per gram of material. Based on this estimate, the TOF was approximately 4.8 ± 0.97 h^{-1} (1.8 mmol phenylacetylene, 1.6 mmol benzyl azide, 0.019 mmol triphenylphosphine, 3 mL DCM, 40 ºC), which is comparable to previous reports.[37] The catalytic AL-$(COO)_2Cu$ prints were recyclable (Figure S16) without any indications of polymer degradation (evaluated by ESI-MS). In addition, ICP-OES analysis of the solvent after reaction revealed that Cu was not leached from the material. Only starting materials were observed under the same reaction conditions in absence of the print or using the original Cu-free AL-COOH 3D prints, indicating that the copper sites in the material are key to catalytic activity.

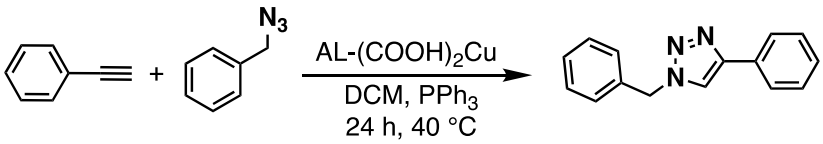

(5)

To illustrate the benefits of using computer aided design to produce custom tools for synthetic chemistry, a millifluidic catalytically active device was 3D printed using the copper acrylate resin. To further demonstrate the convenience of this approach, the design of the millifluidic device was later modified to improve its performance and footprint. Milli- and micro-fluidic continuous flow reactors are typically designed with intricate flow paths to control turbulence, maximize contact with the surface and thereby affect the performance of chemical conversions.[12, 14, 59] An important challenge in the design of fluidic devices involves controlling the integration of active species (e.g. catalysts) so that they are homogeneously dispersed along the channel walls, maximize their contact with the flowing chemicals, and prevent clog formation that can happen if sites are deposited by precipitation.[60-62] Furthermore, recent works have demonstrated the use of the Huisgen cycloaddition in

microfluidic devices, however, the catalytic Cu species was not immobilized in the reactor walls but added to the flowing reaction mixture.[63, 64] Such an approach limits catalyst recyclability and complicates the entire process because Cu needs to be separated from the products after the reaction. Here, incorporation of the active sites directly during 3D printing proved a facile way to overcome these challenges.

First, a linear millifluidic device (4 mm wide and 135 mm long channel) was 3D printed using the copper acrylate resin (Figure 8a), and tested for the Cu(II)-catalyzed cycloaddition reaction described above. A mixture of benzyl azide (322 mM), phenylacetylene (364 mM) and triphenylphosphine (38 mM) in DCM was flowed with a syringe pump through the printed device at room temperature and a 5.0 mL h^{-1} rate (Figure 8b). Formation of the triazole product was observed at a rate of 21.9 ± 5.3 µmol h^{-1}, confirming the millifluidic device was catalytically active. In contrast, no conversion was observed when flowing the same reaction mixture under the same conditions through a 3D-printed PAA millifluidic device lacking Cu. The reactor design was then modified to 3D print a more compact device with the same channel width and total path length (4 mm and 135 mm, respectively) but incorporating segments connected by 180º turns (7 segments, Figure 8c). Upon flowing the benzyl azide, phenylacetylene and triphenylphosphine reaction mixture with the same concentrations and under the same conditions a significantly higher conversion rate was obtained (35.1 ± 5.7 µmol h^{-1}). The 1.6-fold increase in conversion rate can be attributed to the change in path architecture, specifically to the incorporation of the 180º turns, which likely improved reactant mixing and enhanced probability of the reactants reaching the catalyst on the walls of the reactor. This result is consistent with previous reports that have shown tortuosity can increase conversion in flow reactors.[26] This result

demonstrates that 3D printing of chemically active materials is a facile and convenient way of controlling the performance of catalytic conversions.

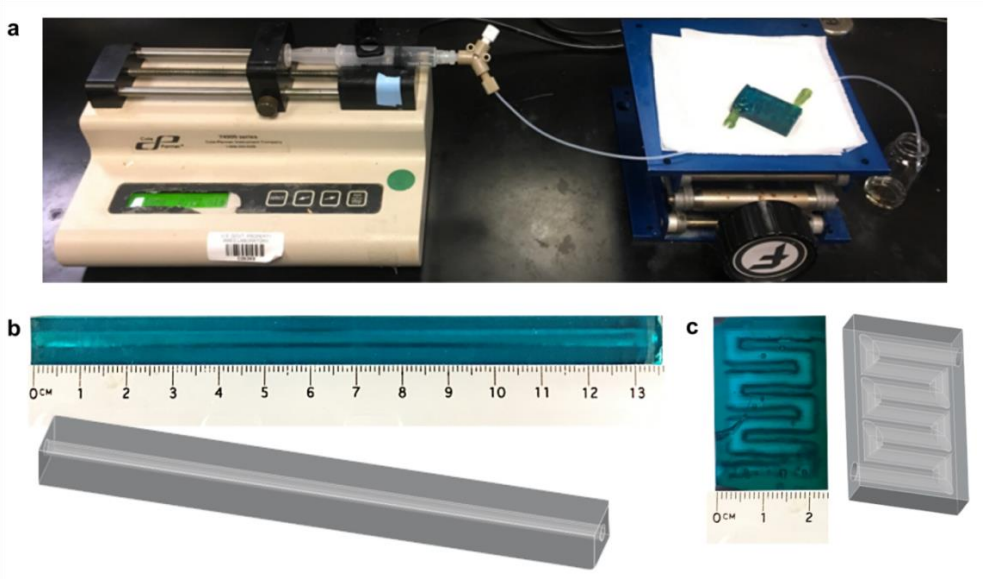

Figure 8. Millifluidic devices used for Cu-catalyzed azide-alkyne cycloaddition. a) Flow reaction setup. 3D printed devices and their models in b) linear and c) compact curved configurations (channel dimensions for both: 4 mm wide, 135 mm long).

Conclusions

This work demonstrates a general concept for 3D printing of polymers with intrinsic chemical activity. The design is based on using bifunctional molecules as building blocks, where a polymerizable double bond assembles the 3D structure via photopolymerization while the second functionality provides the chemical activity. The approach was exemplified by 3D printing an acrylic acid-based resin, where the printed objects possessed accessible carboxylic groups on the order of hundreds of μmol g^{-1} located in a 70 μm thick surface layer.

The 3D-printed materials can be further modified post-printing by transformations of the accessible functional groups on the surface. This was illustrated by reacting accessible carboxylic groups with aniline to yield surface anilides and by derivatizing surface amines

with FITC to give fluorescent surfaces. The chemical properties of the 3D-printed architectures can also be controlled by co-polymerization of multiple monomers, as shown by 3D printing resins containing mixtures of acrylic acid with allyl amine, di-allyl amine or Cu(II) acrylate. Each of these mixtures was effectively co-polymerized as evidenced by their chemical and spectroscopic properties.

The 3D-printed materials are active catalysts for different types of reactions, including a three-component Mannich reaction catalyzed by acid terminated architectures, an aldol condensation cooperatively catalyzed by bifunctional acid-base 3D-printed objects (with primary or secondary amines), and an azide-alkyne Huisgen cycloaddition catalyzed by a copper acrylate based material. Covalent binding of the active sites in the printed structure prevented catalyst leaching and allowed efficient recycling.

Ultimately, the combination of chemical control attained with this approach with the architectural control offered by 3D printing allows facile production and customization of tools for studying chemical processes in convenient ways. This was exemplified by producing a cuvette adaptor for studying the kinetics of individual steps of the heterogeneously catalyzed Mannich reaction. The adaptor allowed bypassing the limitations of conventional equipment (scattering by solids typically prevents use of solution UV-Visible spectrophotometer for monitoring heterogeneous reactions) providing insight into the mechanistic step where the catalytic effect is most relevant to the conversion (i.e. imine formation), and how the presence of catalyst determines which is the rate limiting step of the reaction. In addition, this approach is useful to directly produce systems with catalytic sites homogeneously dispersed in locations that are difficult to access by other means, as proved by 3D printing Cu-acrylate based millifluidic devices able to catalyze alkyne-azide

cycloadditions in continuous flow mode. Finally, the facile modification of flow reactor architectures allowed controlling the performance of catalytic reactions. Further developments are aimed towards increasing the number and kinds of printable active species, enhancing the penetration depth to increase the amount of accessible catalytic sites, and developing strategies to locate structural molecules in the bulk and active species exclusively on the accessible surface of the printed architectures. Ultimately, this new approach for producing chemically active architectures should be applicable to the production of complex functional devices capable of advanced tasks such as chemical synthesis, sensing, controlled release, or reactive separations.

Acknowledgements

This research was supported at the Ames Laboratory by the Laboratory Directed Research and Development (LDRD) Program. The Ames Laboratory is operated for the U.S. Department of Energy by Iowa State University under Contract No. DE-AC02-07CH11358.

Supplemental figures

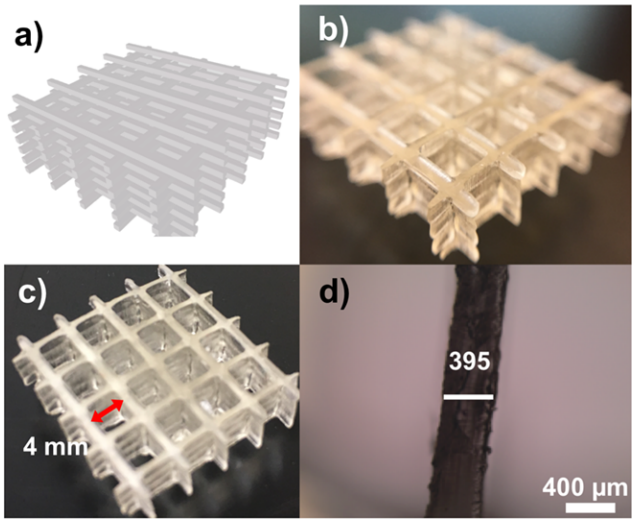

Figure S1. Resolution test for the chemically active resin. a) CAD model, b) photographs of the 3D printed object showing c) minimum inter-feature space achievable, and d) minimum printable feature size (programmed = 400 µm, printed ~ 395 µm).

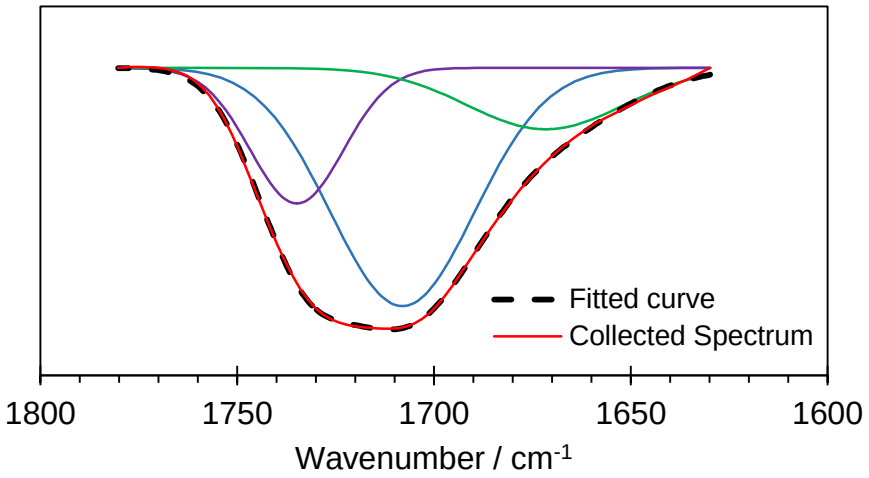

Figure S2. Deconvolution of the carbonyl region for the 3D printed AL-COOH. Bands corresponding to hydrogen bonded (green trace) and non-hydrogen bonded poly(acrylic acid) (blue trace) carbonyls are centered at 1672 and 1708 cm^{-1} respectively, while the PEGDA carbonyl appears at 1735 cm^{-1} (purple trace).

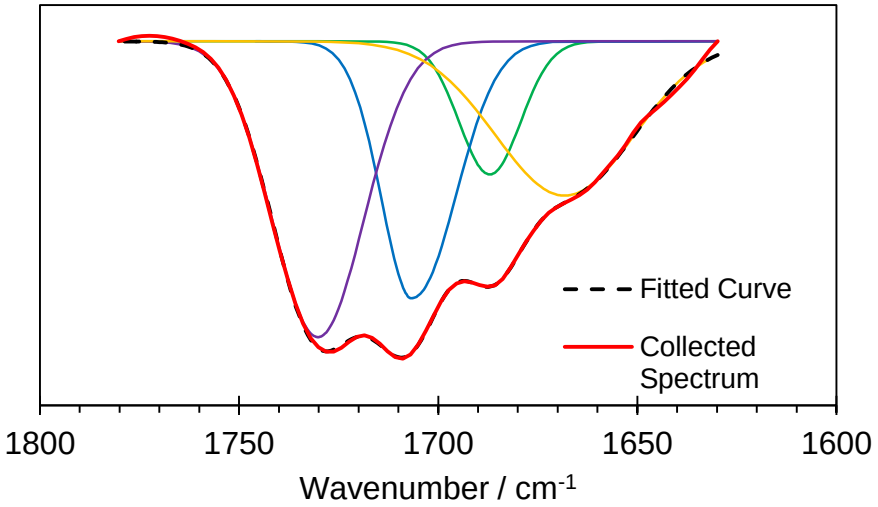

Figure S3. Deconvolution of the carbonyl region for the 3D printed AL-COOH after coupling the accessible acidic sites with aniline. Bands corresponding to poly(acrylic acid) are centered at 1669 and 1708 cm^{-1} (green and blue traces) while the PEGDA carbonyl appears at 1735 cm^{-1} (purple trace). Emergence of a new band corresponding to the amide carbonyl (1686 cm^{-1}, yellow trace) concurs with a decrease in the relative intensity of the band assigned to the poly(acrylic acid) carbonyl (compare to Figure S2).

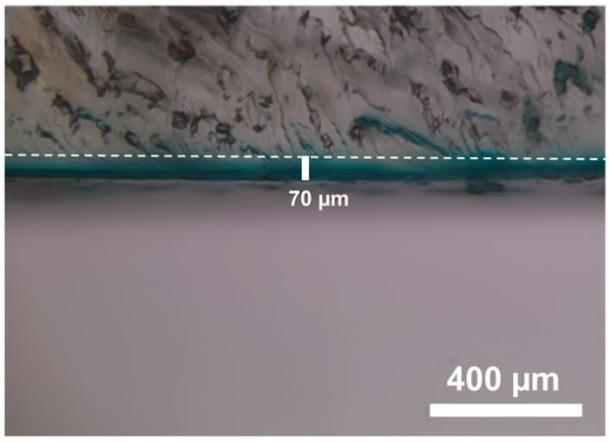

Figure S4. Cross-section of AL-COOH pretreated with aqueous $Cu(NO_3)_2$ solution, showing the penetration depth of the adsorbed metal.

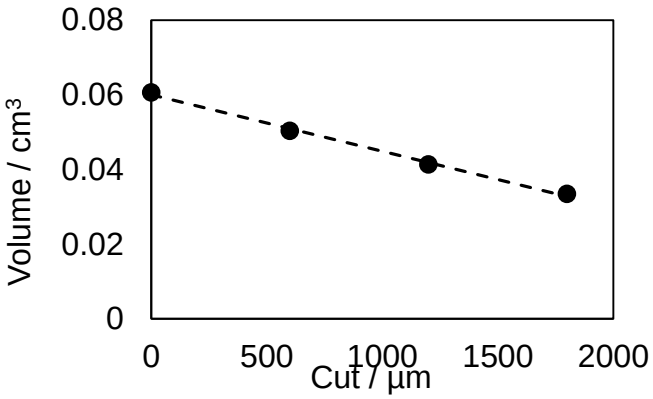

Figure S5. Volume estimation of a 70 µm shell. The 3D printed object was scaled down in 600 µm steps and the volume of each size was calculated using the Autodesk® NetFabb® software.

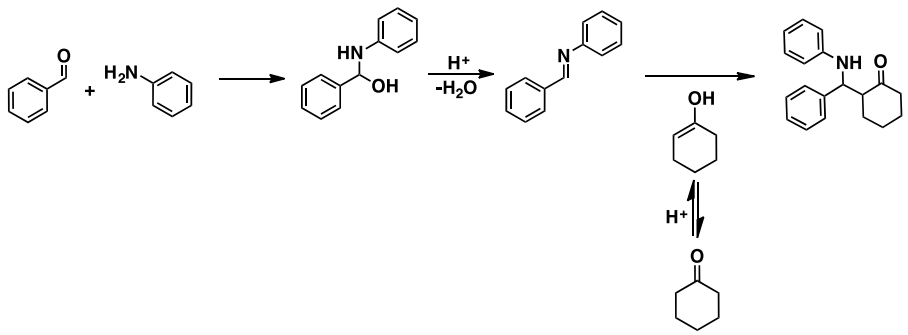

Figure S6. Steps of the three-component Mannich reaction. Two of the steps are acid catalyzed.

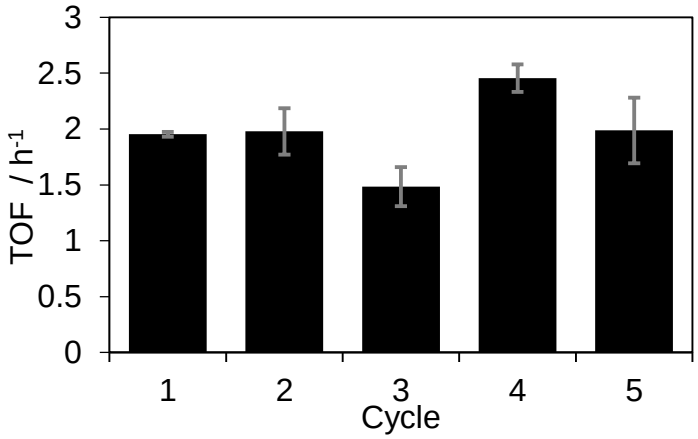

Figure S7. Recyclability of AL-COOH in the acid catalyzed three component Mannich reaction.

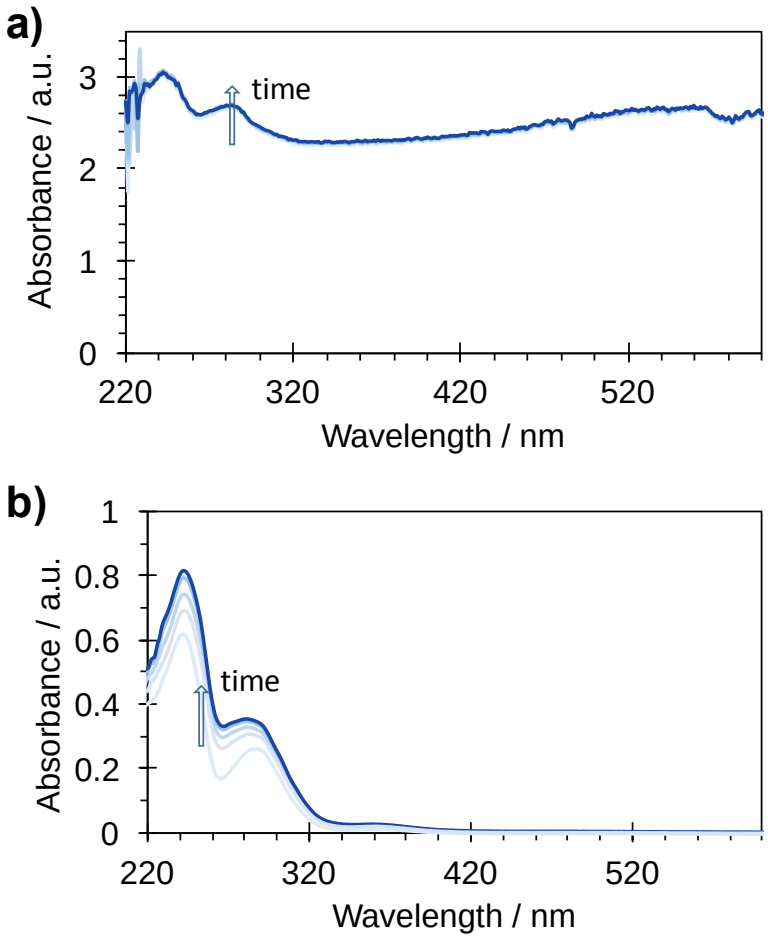

Figure S8. UV-Visible spectra of the reaction between benzaldehyde and aniline catalyzed by a) commercial poly(acrylic acid) and b) 3D-printed adaptor, recorded at increasing times.

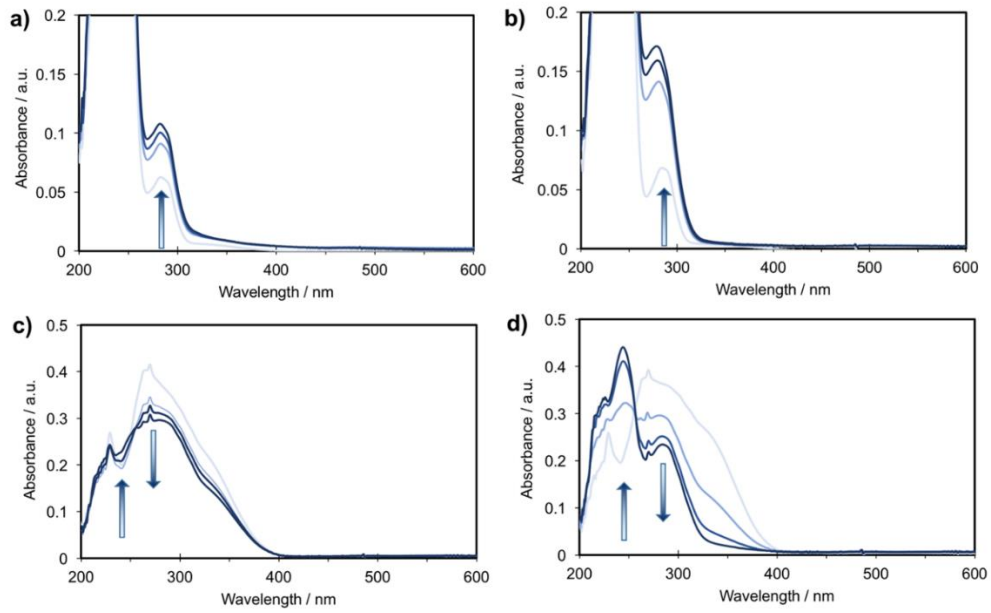

Figure S9. UV-Visible spectra of the uncatalyzed (a,c) and catalyzed by the 3D-printed adaptor (b,d) steps of the Mannich reaction as a function of time. Changes in color from light to dark blue correspond to spectra collected at 100 s intervals. The first step corresponds to the reaction between benzaldehyde and aniline (a,b) and the second step between isolated and purified *N*-benzylideneaniline and cyclohexanone (c,d).

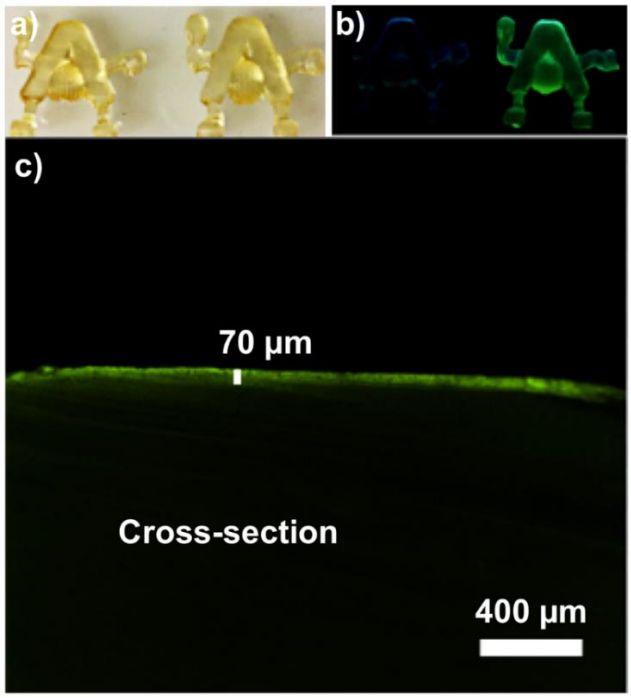

Figure S10. AL-COOH-*co*-NH_2 before (left) and after (right) treatment with FITC under a) visible light and b) a UV lamp. c) Micrograph of the cross section of the FITC treated AL-COOH-co-NH_2 shows a probe penetration of approximately 70 µm.

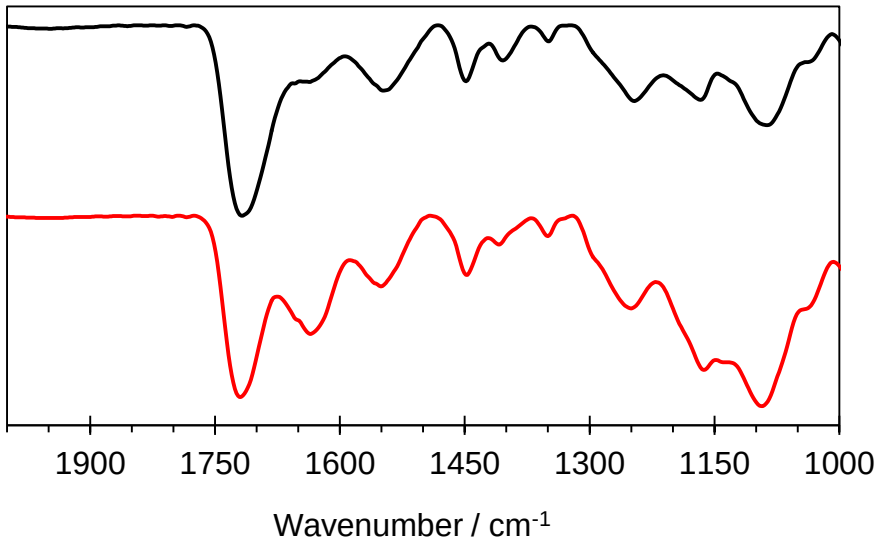

Figure S11. FTIR spectra of AL-COOH-NH_2 before (black) and after (red) DCC treatment. The band at 1545 cm^{-1} in the untreated AL-COOH-NH_2 (black trace) is indicative of ammonium in the zwitterion. Bands in the treated AL-COOH-NH_2 (red) at 1635 cm^{-1} and 1556 cm^{-1} are assigned to amide I and II absorptions.

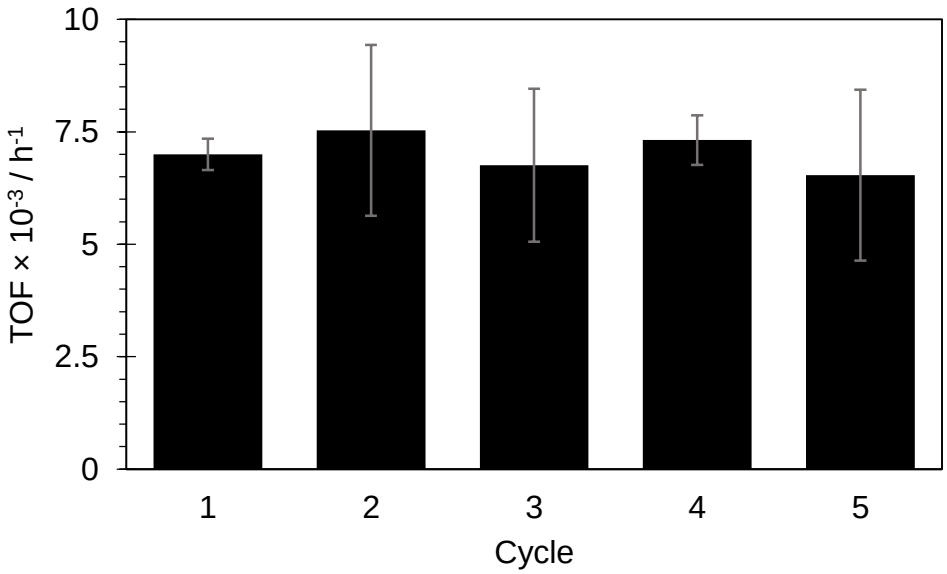

Figure S12. Recyclability of AL-COOH-co-NH_2 during the aldol condensation reaction between p-nitrobenzaldehyde and acetone. Reaction conditions: 0.4 mmol of p-nitrobenzaldehyde, 40 ºC in 3 mL of acetone.

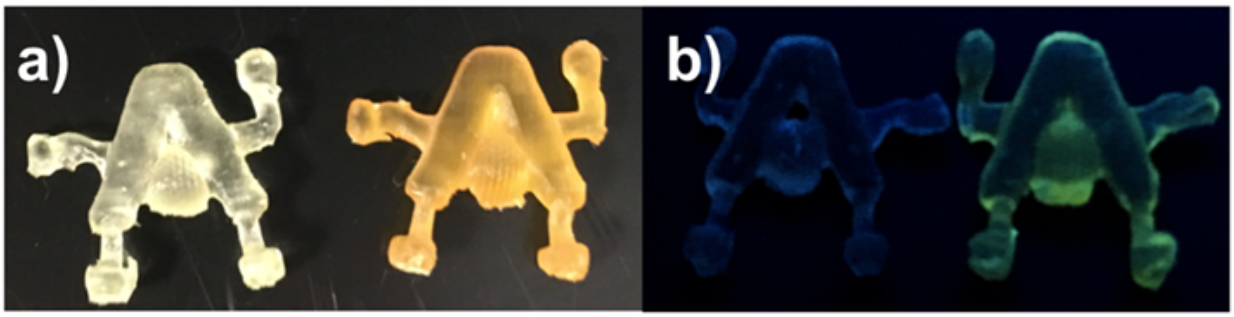

Figure S13. AL-COOH-*co*-NH before (left) and after (right) reaction with a) ninhydrin, and b) FITC.

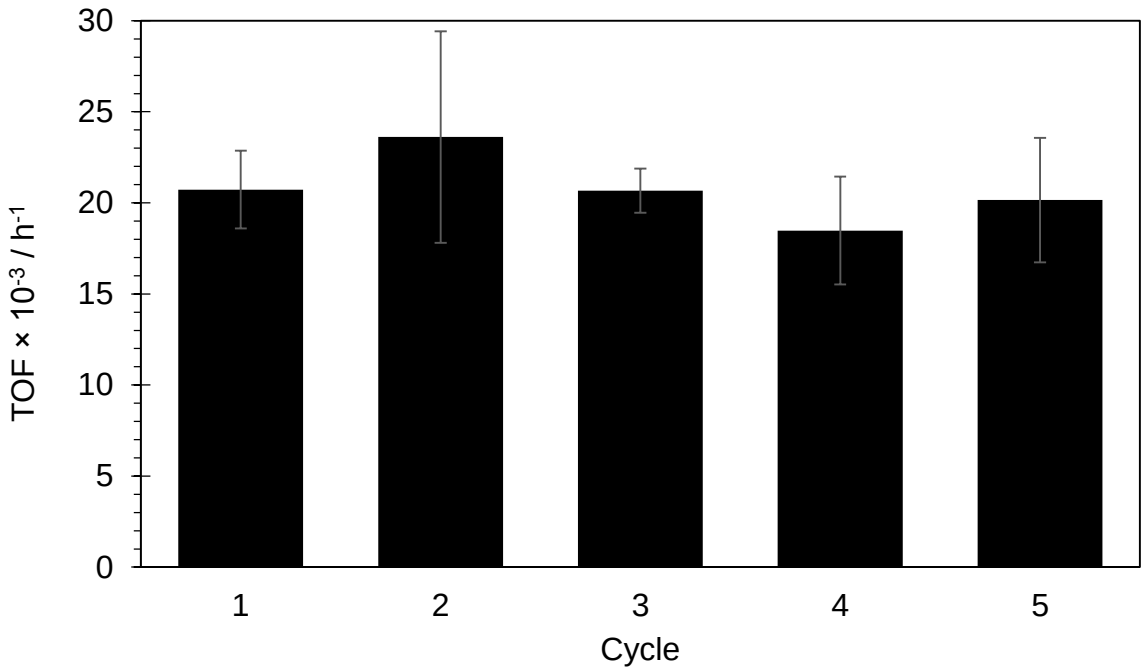

Figure S14. Recyclability of AL-COOH-*co*-NH during the aldol condensation reaction between p-nitrobenzaldehyde and acetone. Reaction conditions: 0.4 mmol of p-nitrobenzaldehyde, 40 ◦C in 3 mL of acetone.

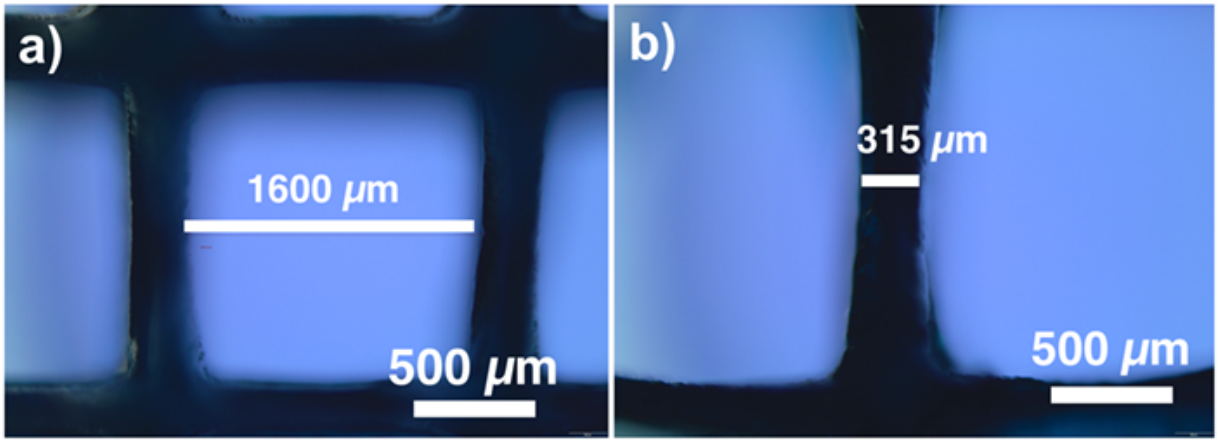

Figure S15. Resolution test using the chemically active resin AL-$(COO)_2Cu$. a) minimum space between features (programmed = 2000 μm), and b) minimum printable feature size (programmed = 300 μm).

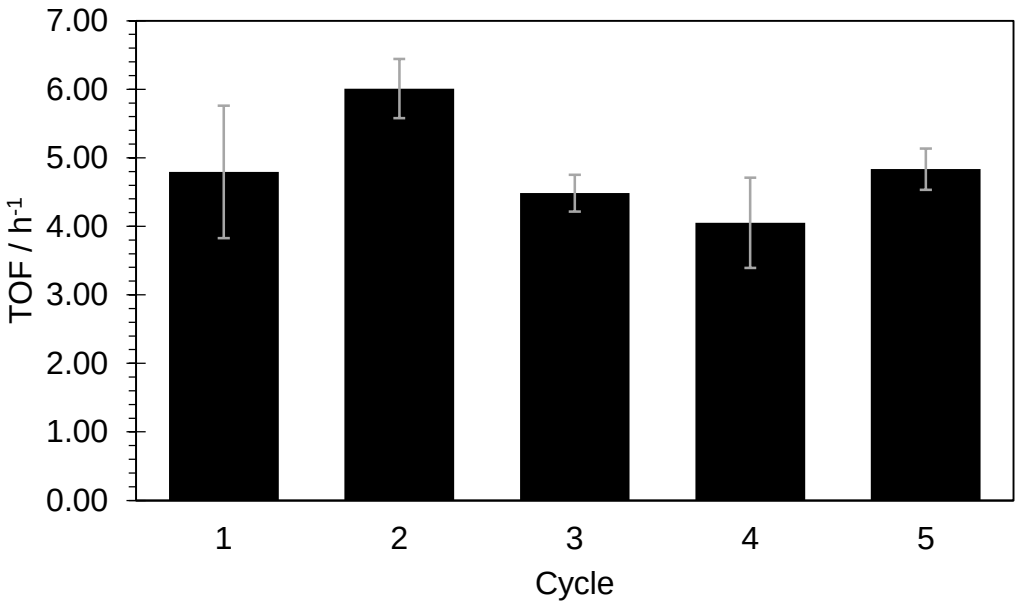

Figure S16. Recyclability of AL-$(COO)_2Cu$ catalyst in the click reaction between benzyl azide and phenyl acetylene. Reaction conditions: 1.6 mmol benzylazide, 1.8 mmol phenylacetylene, 40 °C in 3 mL DCM.

References

1. Bartolo, P., *Stereolithography Materials, Processes and Applications*. Springer: 2011; p 340.

2. Dimitrov, D.; Schreve, K.; Beer, N. d., Advances in three dimensional printing – state of the art and future perspectives. *Rapid Prototyp. J.* **2006,** *12* (3), 136-147.

3. Barry, R. A.; Shepherd, R. F.; Hanson, J. N.; Nuzzo, R. G.; Wiltzius, P.; Lewis, J. A., Direct-Write Assembly of 3D Hydrogel Scaffolds for Guided Cell Growth. *Adv. Mater.* **2009,** *21* (23), 2407-2410.

4. Boland, T.; Xu, T.; Damon, B.; Cui, X., Application of inkjet printing to tissue engineering. *Biotechnol. J.* **2006,** *1* (9), 910-917.

5. Mohanty, S.; Larsen, L. B.; Trifol, J.; Szabo, P.; Burri, H. V. R.; Canali, C.; Dufva, M.; Emnéus, J.; Wolff, A., Fabrication of scalable and structured tissue engineering scaffolds using water dissolvable sacrificial 3D printed moulds. *Mater. Sci. Eng. C* **2015,** *55*, 569-578.

6. Habibovic, P.; Gbureck, U.; Doillon, C. J.; Bassett, D. C.; van Blitterswijk, C. A.; Barralet, J. E., Osteoconduction and osteoinduction of low-temperature 3D printed bioceramic implants. *Biomater.* **2008,** *29* (7), 944-953.

7. Ahn, B. Y.; Duoss, E. B.; Motala, M. J.; Guo, X.; Park, S.-I.; Xiong, Y.; Yoon, J.; Nuzzo, R. G.; Rogers, J. A.; Lewis, J. A., Omnidirectional Printing of Flexible, Stretchable, and Spanning Silver Microelectrodes. *Science* **2009,** *323* (5921), 1590-1593.

8. Au, A. K.; Huynh, W.; Horowitz, L. F.; Folch, A., 3D-Printed Microfluidics. *Angew. Chem. Int. Ed.* **2016,** *55* (12), 3862-3881.

9. Ho, C. M. B.; Ng, S. H.; Li, K. H. H.; Yoon, Y.-J., 3D printed microfluidics for biological applications. *Lab Chip* **2015,** *15* (18), 3627-3637.

10. Waheed, S.; Cabot, J. M.; Macdonald, N. P.; Lewis, T.; Guijt, R. M.; Paull, B.; Breadmore, M. C., 3D printed microfluidic devices: enablers and barriers. *Lab Chip* **2016,** *16* (11), 1993-2013.

11. Bhattacharjee, N.; Urrios, A.; Kang, S.; Folch, A., The upcoming 3D-printing revolution in microfluidics. *Lab Chip* **2016,** *16* (10), 1720-1742.

12. Kitson, P. J.; Rosnes, M. H.; Sans, V.; Dragone, V.; Cronin, L., Configurable 3D-Printed millifluidic and microfluidic 'lab on a chip' reactionware devices. *Lab Chip* **2012,** *12* (18), 3267-3271.

13. Chisholm, G.; Kitson, P. J.; Kirkaldy, N. D.; Bloor, L. G.; Cronin, L., 3D printed flow plates for the electrolysis of water: an economic and adaptable approach to device manufacture. *Energ. Environ. Sci.* **2014,** *7* (9), 3026-3032.

14. Dragone, V.; Sans, V.; Rosnes, M. H.; Kitson, P. J.; Cronin, L., 3D-printed devices for continuous-flow organic chemistry. *Beilstein J. Org. Chem.* **2013,** *9*, 951−959

15. Ilievski, F.; Mazzeo, A. D.; Shepherd, R. F.; Chen, X.; Whitesides, G. M., Soft Robotics for Chemists. *Angew. Chem.* **2011,** *123* (8), 1930-1935.

16. Morin, S. A.; Shepherd, R. F.; Kwok, S. W.; Stokes, A. A.; Nemiroski, A.; Whitesides, G. M., Camouflage and Display for Soft Machines. *Science* **2012,** *337* (6096), 828-832.

17. Smay, J. E.; Gratson, G. M.; Shepherd, R. F.; Cesarano, J.; Lewis, J. A., Directed Colloidal Assembly of 3D Periodic Structures. *Adv. Mater.* **2002,** *14* (18), 1279-1283.

18. Compton, B. G.; Lewis, J. A., 3D-Printing of Lightweight Cellular Composites. *Adv. Mater.* **2014,** *26* (34), 5930-5935.

19. Tubío, C. R.; Guitián, F.; Gil, A., Fabrication of ZnO periodic structures by 3D printing. *J. Eur. Ceram. Soc.* **2016,** *36* (14), 3409-3415.

20. Cai, K.; Román-Manso, B.; Smay, J. E.; Zhou, J.; Osendi, M. I.; Belmonte, M.; Miranzo, P., Geometrically Complex Silicon Carbide Structures Fabricated by Robocasting. *J. Am. Ceram. Soc.* **2012,** *95* (8), 2660-2666.

21. Rao, R. B.; Krafcik, K. L.; Morales, A. M.; Lewis, J. A., Microfabricated Deposition Nozzles for Direct-Write Assembly of Three-Dimensional Periodic Structures. *Adv. Mater.* **2005,** *17* (3), 289-293.

22. Lewis, J. A., Colloidal Processing of Ceramics. *J. Am. Ceram. Soc.* **2000,** *83* (10), 2341-2359.

23. Symes, M. D.; Kitson, P. J.; Yan, J.; Richmond, C. J.; Cooper, G. J. T.; Bowman, R. W.; Vilbrandt, T.; Cronin, L., Integrated 3D-printed reactionware for chemical synthesis and analysis. *Nat. Chem.* **2012,** *4* (5), 349-354.

24. Kitson, P. J.; Marshall, R. J.; Long, D.; Forgan, R. S.; Cronin, L., 3D Printed High-Throughput Hydrothermal Reactionware for Discovery, Optimization, and Scale-Up. *Angew. Chem. Int. Ed.* **2014,** *53* (47), 12723-12728.

25. Kitson, P. J.; Symes, M. D.; Dragone, V.; Cronin, L., Combining 3D printing and liquid handling to produce user-friendly reactionware for chemical synthesis and purification. *Chem. Sci.* **2013,** *4* (8), 3099-3103.

26. Lefevere, J.; Gysen, M.; Mullens, S.; Meynen, V.; Van Noyen, J., The benefit of design of support architectures for zeolite coated structured catalysts for methanol-to-olefin conversion. *Catal. Today* **2013,** *216*, 18-23.

27. Wang, X.; Cai, X.; Guo, Q.; Zhang, T.; Kobe, B.; Yang, J., i3DP, a robust 3D printing approach enabling genetic post-printing surface modification. *Chem. Commun.* **2013,** *49* (86), 10064-10066.

28. Sullivan, K. T.; Zhu, C.; Duoss, E. B.; Gash, A. E.; Kolesky, D. B.; Kuntz, J. D.; Lewis, J. A.; Spadaccini, C. M., Controlling Material Reactivity Using Architecture. *Adv. Mater.* **2016,** *28* (10), 1934-1939.

29. Skorski, M. R.; Esenther, J. M.; Ahmed, Z.; Miller, A. E.; Hartings, M. R., The chemical, mechanical, and physical properties of 3D printed materials composed of TiO2-ABS nanocomposites. *Sci. Technol. Adv. Mater.* **2016,** *17* (1), 89-97.

30. Tubío, C. R.; Azuaje, J.; Escalante, L.; Coelho, A.; Guitián, F.; Sotelo, E.; Gil, A., 3D printing of a heterogeneous copper-based catalyst. *J. Catal.* **2016,** *334*, 110-115.

31. Azuaje, J.; Tubío, C. R.; Escalante, L.; Gómez, M.; Guitián, F.; Coelho, A.; Caamaño, O.; Gil, A.; Sotelo, E., An efficient and recyclable 3D printed α-Al2O3 catalyst for the multicomponent assembly of bioactive heterocycles. *Appl. Catal. A* **2017,** *530*, 203-210.

32. Tumbleston, J. R.; Shirvanyants, D.; Ermoshkin, N.; Janusziewicz, R.; Johnson, A. R.; Kelly, D.; Chen, K.; Pinschmidt, R.; Rolland, J. P.; Ermoshkin, A.; Samulski, E. T.; DeSimone, J. M., Continuous liquid interface production of 3D objects. *Science* **2015,** *347* (6228), 1349.

33. Yagci, Y.; Jockusch, S.; Turro, N. J., Photoinitiated Polymerization: Advances, Challenges, and Opportunities. *Macromolecules* **2010,** *43* (15), 6245-6260.

34. Gronowski, A.; Wojtczak, Z., The thermal decompositions of some transition metal acrylates and polyacrylates. *J. Therm. Anal.* **1983,** *26* (2), 233-244.

35. Zhang, Y.; Han, J.; Liu, Z.-J., Diaryliodonium salts as efficient Lewis acid catalysts for direct three component Mannich reactions. *RSC Adv.* **2015,** *5* (32), 25485-25488.

36. Movassagh, B.; Tahershamsi, L.; Mobaraki, A., A magnetic solid sulfonic acid modified with hydrophobic regulators: an efficient recyclable heterogeneous catalyst for one-pot aza-Michael-type and Mannich-type reactions of aldehydes, ketones, and amines. *Tetrahedron Lett.* **2015,** *56* (14), 1851-1854.

37. Gonda, Z.; Novak, Z., Highly active copper-catalysts for azide-alkyne cycloaddition. *Dalton Trans.* **2010,** *39* (3), 726-729.

38. Kolczak, U.; Rist, G.; Dietliker, K.; Wirz, J., Reaction Mechanism of Monoacyl- and Bisacylphosphine Oxide Photoinitiators Studied by 31P-, 13C-, and 1H-CIDNP and ESR. *J. Am. Chem. Soc.* **1996,** *118* (27), 6477-6489.

39. Dong, J.; Ozaki, Y.; Nakashima, K., Infrared, Raman, and Near-Infrared Spectroscopic Evidence for the Coexistence of Various Hydrogen-Bond Forms in Poly(acrylic acid). *Macromolecules* **1997,** *30* (4), 1111-1117.

40. Xiao, Y.; He, L.; Che, J., An effective approach for the fabrication of reinforced composite hydrogel engineered with SWNTs, polypyrrole and PEGDA hydrogel. *J. Mater. Chem.* **2012,** *22* (16), 8076-8082.

41. Michaels, A. S.; Morelos, O., Polyelectrolyte Adsorption by Kaolinite. *Ind. Eng. Chem.* **1955,** *47* (9), 1801-1809.

42. Chen, X.; Sun, H.; Luo, Y.; Jian, Y.; Wu, Y.; Zhang, W.; Gao, Z., Polyelectrolyte Bronsted acid catalyzed three-component Mannich reactions accelerated by emulsion. *RSC Adv.* **2016,** *6* (45), 39343-39347.

43. Cummings, T. F.; Shelton, J. R., Mannich Reaction Mechanisms. *J. Org. Chem.* **1960,** *25* (3), 419-423.

44. Benkovic, S. J.; Benkovic, P. A.; Comfort, D. R., Kinetic detection of the imminium cation in formaldehyde-amine condensations in neutral aqueous solution. *J. Am. Chem. Soc.* **1969,** *91* (7), 1860-1861.

45. Olah, G. A.; Kreienbuehl, P., Stable carbonium ions. L. Protonated imines. *J. Am. Chem. Soc.* **1967,** *89* (18), 4756-4759.

46. Olah, G. A.; O'Brien, D. H.; Calin, M., Stable carbonium ions. XLII. Protonated aliphatic aldehydes. *J. Am. Chem. Soc.* **1967,** *89* (14), 3582-3586.

47. Hoyt, C. B.; Lee, L. C.; Cohen, A. E.; Weck, M.; Jones, C. W., Bifunctional Polymer Architectures for Cooperative Catalysis: Tunable Acid–Base Polymers for Aldol Condensation. *ChemCatChem* **2017,** *9* (1), 137-143.

48. Kaiser, E.; Colescott, R. L.; Bossinger, C. D.; Cook, P. I., Color test for detection of free terminal amino groups in the solid-phase synthesis of peptides. *Anal. Biochem.* **1970,** *34* (2), 595-598.

49. Margelefsky, E. L.; Zeidan, R. K.; Davis, M. E., Cooperative catalysis by silica-supported organic functional groups. *Chem. Soc. Rev.* **2008,** *37* (6), 1118-1126.

50. Kandel, K.; Althaus, S. M.; Peeraphatdit, C.; Kobayashi, T.; Trewyn, B. G.; Pruski, M.; Slowing, I. I., Substrate inhibition in the heterogeneous catalyzed aldol condensation: A mechanistic study of supported organocatalysts. *J. Catal.* **2012,** *291* (0), 63-68.

51. Brunelli, N. A.; Venkatasubbaiah, K.; Jones, C. W., Cooperative Catalysis with Acid–Base Bifunctional Mesoporous Silica: Impact of Grafting and Co-condensation Synthesis Methods on Material Structure and Catalytic Properties. *Chem. Mater.* **2012,** *24* (13), 2433-2442.

52. Lauwaert, J.; De Canck, E.; Esquivel, D.; Thybaut, J. W.; Van Der Voort, P.; Marin, G. B., Silanol-Assisted Aldol Condensation on Aminated Silica: Understanding the Arrangement of Functional Groups. *ChemCatChem* **2014,** *6* (1), 255-264.

53. de Lima Batista, A. P.; Zahariev, F.; Slowing, I. I.; Braga, A. A. C.; Ornellas, F. R.; Gordon, M. S., Silanol-Assisted Carbinolamine Formation in an Amine-Functionalized Mesoporous Silica Surface: Theoretical Investigation by Fragmentation Methods. *J. Phys. Chem. B* **2016,** *120* (8), 1660-1669.

54. Kandel, K.; Althaus, S. M.; Peeraphatdit, C.; Kobayashi, T.; Trewyn, B. G.; Pruski, M.; Slowing, I. I., Solvent-Induced Reversal of Activities between Two Closely Related Heterogeneous Catalysts in the Aldol Reaction. *ACS Catal.* **2013,** *3* (2), 265-271.

55. Bottom, C. B.; Hanna, S. S.; Siehr, D. J., Mechanism of the ninhydrin reaction. *Biochem. Educ.* **1978,** *6* (1), 4-5.

56. Kuang, G.-C.; Michaels, H. A.; Simmons, J. T.; Clark, R. J.; Zhu, L., Chelation-Assisted, Copper(II)-Acetate-Accelerated Azide−Alkyne Cycloaddition. *J. Org. Chem.* **2010,** *75* (19), 6540-6548.

57. Wendlandt, A. E.; Suess, A. M.; Stahl, S. S., Copper-Catalyzed Aerobic Oxidative C-H Functionalizations: Trends and Mechanistic Insights. *Angew. Chem. Int. Ed.* **2011,** *50* (47), 11062-11087.

58. Sexton, B. A., The structure of acetate species on copper (100). *Chem. Phys. Lett.* **1979,** *65* (3), 469-471.

59. Illg, T.; Löb, P.; Hessel, V., Flow chemistry using milli- and microstructured reactors—From conventional to novel process windows. *Bioorg. Med. Chem.* **2010,** *18* (11), 3707-3719.

60. Navin, C. V.; Krishna, K. S.; Theegala, C. S.; Kumar, C. S. S. R., Space and time-resolved probing of heterogeneous catalysis reactions using lab-on-a-chip. *Nanoscale* **2016,** *8* (10), 5546-5551.

61. Amii, H.; Nagaki, A.; Yoshida, J.-i., Flow microreactor synthesis in organo-fluorine chemistry. *Beilstein J. Org. Chem.* **2013,** *9*, 2793-2802.

62. Kobayashi, J.; Mori, Y.; Okamoto, K.; Akiyama, R.; Ueno, M.; Kitamori, T.; Kobayashi, S., A Microfluidic Device for Conducting Gas-Liquid-Solid Hydrogenation Reactions. *Science* **2004,** *304* (5675), 1305-1308.

63. Wang, J.; Sui, G.; Mocharla, V. P.; Lin, R. J.; Phelps, M. E.; Kolb, H. C.; Tseng, H.-R., Integrated Microfluidics for Parallel Screening of an In Situ Click Chemistry Library. *Angew. Chem. Int. Ed.* **2006,** *45* (32), 5276-5281.

64. Wang, Y.; Lin, W.-Y.; Liu, K.; Lin, R. J.; Selke, M.; Kolb, H. C.; Zhang, N.; Zhao, X.-Z.; Phelps, M. E.; Shen, C. K. F.; Faull, K. F.; Tseng, H.-R., An integrated microfluidic device for large-scale in situ click chemistry screening. *Lab Chip* **2009,** *9* (16), 2281-2285.

CHAPTER 3. MACROSCALE CONTROL OF REACTIVITY USING 3D PRINTED MATERIALS WITH INTRINSIC CATALYTIC PROPERTIES

J. Sebastián Manzano[1,2], Hsin Wang[1,2], Igor I. Slowing[1,2]

[1]US DOE Ames Laboratory, Ames, Iowa 50011, United States

[2]Department of Chemistry, Iowa State University, Ames, Iowa 50011, United States

Abstract

The macroscopic morphology of heterogeneous catalysts can impact their performance by determining active site accessibility and heat transfer efficiency. However, standard manufacturing methods such as extrusion or pelleting offer little options for optimizing catalyst shape. Herein, we demonstrate how stereolithographic (SLA) 3D printing can directly produce catalysts with controlled architectures that dramatically affect their performance. We 3D printed a series of chemically active magnetic stir-bar compartments (SBC) of varying geometries and used them as catalysts for sucrose hydrolysis. The SBCs were made up of acrylic acid (AA) and 1,6-hexanediol diacrylate (HDDA) which provided acid sites and hydrophobic crosslinking domains, respectively. Fixing the surface area and the number of accessible catalytic sites of the 3D printed SBC allowed exploring the effect of subtle changes in morphology on the fluid dynamics of the reaction systems, and consequently on the efficiency of catalytic conversion. Moreover, varying the AA:HDDA ratios in SBC allowed tuning cooperativity between acidic sites and hydrophobic domains to control the rate of sucrose hydrolysis. This work demonstrates that 3D printing catalytic materials enables optimizing catalyst performance by simultaneously controlling macroscopic and molecular properties.

Introduction

The macroscopic structure of solid catalysts can affect the efficiency of heat and mass transfer in chemical conversions.[1-5] Solid catalysts are usually manufactured by pelleting or extruding composites of pre-catalysts, promoters and binders.[6-10] Although these methods can yield different catalyst shapes such as beads, rods, hollow cylinders or foams, these topologies are not necessarily optimal for all types of reactor and process.[11-16] Unfortunately, standard manufacturing methods can hardly go beyond these very simple shapes.[9] This limitation hinders the development and adoption of structures that could further enhance catalyst performance by influencing reactant flow dynamics. Therefore, it is desirable to explore alternative catalyst manufacturing methods that allow for a better control of topology.

3D printing is a manufacturing technique that uses digital designs to direct the assembly of materials in a layer by layer fashion with minimal waste of precursors. This technology has been applied to the production of biomaterials,[17-20] electrochemical devices,[21-22] microfluidic devices,[23-27] ceramics,[28-35] and heterogeneous catalysts.[28-29, 36] Recently Sun et al.[37] 3D printed catalytic impellers by fused deposition of iron-containing poly(lactic acid) (PLA) filament. The impellers were activated by etching with aqueous NaOH and H_2O_2 and used as catalysts for the Fenton reaction. They observed changes in the rate of methylene blue degradation as a function of the number of blades in the impellers and attributed these variations to the efficiency of reaction mixing. However, the harsh activation conditions damaged the printed surfaces to expose an unknown amount of active sites, defeating in part the purpose of 3D printing and complicating the assignment of activity to morphology alone. A way to overcome these limitations is by 3D printing morphologies that already expose

known amounts of homogeneously dispersed and well-defined active sites, without applying pretreatments that may disrupt their surface structure and chemistry.

We have recently introduced a method to directly 3D print functional catalysts that do not require any preactivation.[36] The approach is based on stereolithographic (SLA) photo-polymerization of substituted olefins, where the substituents are the target catalytic function. This method enabled the direct manufacturing of bespoke active devices (e.g. millifluidic reactors, UV-Vis adaptors) with customizable catalytic properties (e.g. acid, base, metal complexes). Herein we employed this 3D printing method to manufacture a series of devices with acid active sites, and explored the effects of topology, surface area and chemical composition on their catalytic performance for the hydrolysis of sucrose. The 3D design consisted of a magnetic stir-bar compartment (SBC) attached to different polyhedra or rotors of varying surface areas (Figure 1). We tailored the materials to expose hydrophobic domains and acid catalytic sites by using 1,6-hexanediol diacrylate and acrylic acid as cross-linker and monomer respectively and investigated the cooperative role of hydrophobic interactions on the activity of the catalytic sites.

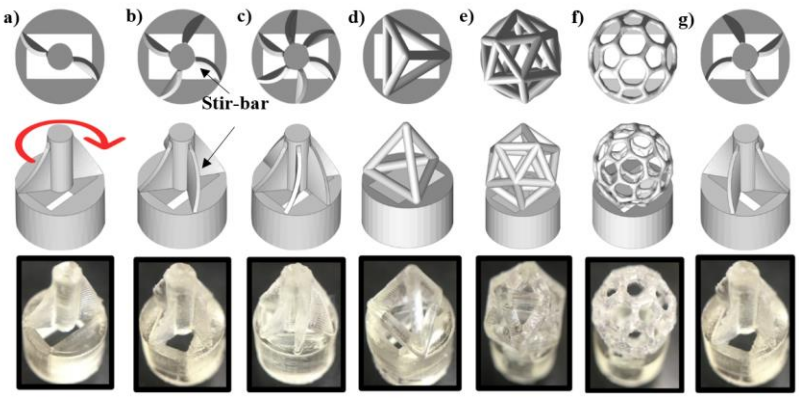

Figure 1. Top- and side-view of CAD models and optical image of 3D printed magnetic stir bar compartments (SBC). A 3 x 5 mm magnetic stir bar fits in the rectangular base of the SBC. a) SBC-2, b) SBC-4, c) SBC-6, d) SBC-T, e) SBC-TIC, f) SBC-IC, and SBC-4-R. The direction of rotation is indicated by the curved arrow.

Experimental

Materials

Acrylic acid (AA), 1,6-hexanediol diacrylate (HDDA), poly(ethylene glycol) diacrylate Mn 575 (PEGDA), phenylbis(2,4,6-trimethylbenzoyl)phosphine oxide (BAPO), p-anisaldehyde dimethyl acetal, anhydrous sodium carbonate and potassium thiocyanate were purchased from Sigma-Aldrich (St. Louis, MO, USA). Sodium citrate, copper(II)sulfate and sucrose were purchased form Fischer Scientific (Waltham, MA, USA). Potassium ferricyanide was purchased from EM Science (Darmstadt, Germany). All reagents were used without any further purification.

Catalytic resin

Acrylic acid (7 mL, 102 mmol) was mixed with PEGDA (3 mL, 5.8 mmol) in an Amber flask. Then, BAPO (0.100 g, 0.24 mmol) was added to the resin and the mixture was sonicated for 1 min. The solution was poured into the resin tank of a FormLabs Form 1+^{TM} 3D printer (Somerville, MA, USA) and used for printing. The settings used were: *laser power*: 62 mW, *first layer passes*: 10, *other layer passes*: 4, and *early layer passes*: 5.

Water tolerant catalytic resin

Acrylic acid (7.3, 14.6, 29.1, 43.7, 72.9 or 102 mmol) was mixed with 1,6-hexanedioldiacrylate (HDDA) (31, 220 or 130 mmol) in an Amber flask. Then BAPO (0.100 g, 0.24 mmol) was added to the resin and the mixture was sonicated for 1 min. The solution was poured into the resin tank of a FormLabs Form 1+^{TM} 3D printer (Somerville, MA, USA) and used for printing. The settings used were: *laser power*: 62 mW, *first layer passes*: 10, *other layer passes*: 4, and *early layer passes*: 5.

3D printing

The CAD designs were prepared using AutoCad 2014 software and exported as STL files (Supplementary files available). A FormLabs Form 1+^{TM} 3D printer (405 nm laser) was used for the laser polymerization. After printing, the unreacted monomer was removed from the printed objects by immersion in an acetone bath for 1 h. Final curing was performed by exposing the 3D object to UV irradiation (λ = 320 nm) in a Rayonet photoreactor for 10 min.

Active sites estimation

The 3D-printed impellers were immersed in 5 mL of deionized water (18 MΩ). The pH was measured with an Accumet benchtop pH meter at 20 °C. Equation 1 was used to estimate the number of accessible sites:

$$Active\ sites\ (\mu mol\ g^{-1}) = \frac{\frac{[H^+]^2 + K_a[H^+]}{K_a} - [H^+_{water}]}{m_{SBC}} \qquad (1)$$

were $[H^+]$ is the concentration of protons (μM) in the solution containing the 3D printed SBC, Ka is the equilibrium constant for polyacrylic acid, H^+_{water} is the concentration of protons in the reference sample (no 3D printed SBC), and m_{SBC} is the mass of SBC in g.

Solvent compatibility assays

3D printed impellers were immersed in 5 mL of water inside a closed 20 mL vial. The vial was set in a heated aluminum block and stirred at 500 rpm for 24 h at 65 ºC. Then, the 3D printed impellers were visually examined, and the supernatants were tested for residues of polymer by ESI-MS on an Agilent QTOF 6540.

Attenuated Total Reflectance Fourier Transform Infrared (ATR-FTIR) Spectroscopy

Measurements were made on a Bruker Vertex 80 FT-IR spectrometer with OPUS software. The spectrometer was equipped with a diamond sealed high pressure clamp ATR MIRacle PIKE accessory where the 3D-printed samples were pressed against the crystal to

collect the respective spectrum. 32 scans were collected for each measurement in absorbance mode with 4 cm^{-1} resolution.

Deacetalization reaction.

p-anisaldehyde dimethyl acetal (20 µL, 0.12 mmol) was added to 1 mL of a 1:1 mixture of water:ethanol. A 3D printed impeller was added to the solution and it was stirred at 500 rpm for 5 min at r.t. An aliquot (10 µL) was added to 1 mL of ethanol and analyzed using an Agilent GC-MS instrument (7890A, 5975C) with a HP-5MS column. The run started at 60 °C, and the temperature was then ramped to 150 °C at 5 °C min^{-1}. Then the temperature ramped to 280 ºC at 20 ºC min^{-1} and was held for 10 min.

Benedict's solution[38]

Sodium citrate (20g, 77.5 mmol), sodium carbonate (6.5g, 61.3 mmol), and potassium thiocyanate (12.5g, 143.4 mmol) were dissolved in water (80 mL). In a separate flask, copper(II)sulfate (0.8g, 3.20 mmol) was dissolved in water (10 mL). The two solutions were mixed and potassium ferricyanide (0.026 g, 0.079 mmol) was added.

Sucrose hydrolysis reaction

Sucrose (130 mg, 0.34 mmol) was dissolved in 1 mL of water. Then, a 3D printed impeller was added to the mixture. The solution was placed in an aluminum block and stirred at 500 rpm at 65 ºC for 3 h. An aliquot (50 µL) was added to 1 mL of Benedict's solution. The solution was headed to 90 ºC for 10 min. The blue color disappearance was measured in a HP 8453 UV-Visible spectrophotometer monitoring the 730 nm wavelength. Conversion and TON were calculated based on equation 2 and 3, respectively.

$$\%Conversion = \frac{mmol_{gluocse+fructose}}{mmol_{sucrose_0}} \times 100 \qquad (2)$$

$$TON = \frac{mmol_{gluocse+fructose}}{mmol_{active\ sites}} \qquad (3)$$

Results and Discussion

We have previously shown that stereolithography (SLA) 3D printing can be used to produce custom catalytic geometries with accessible acidic, basic or metallic active sites.[36] Our first generation of photo-curable resin used acrylic acid (AA) as monomer and source of catalytic sites, and poly(ethylene glycol) diacrylate (PEGDA) as crosslinker. However, the 3D printed materials prepared from this resin could only be used as catalysts in organic solvents because they tend to degrade when vigorously shaken in water due to the highly hydrophilic nature of PEGDA. To overcome this limitation, we developed a second generation photo-curable resin by replacing PEGDA crosslinker with the more hydrophobic 1,6-hexanediol diacrylate (HDDA).[39] We tested the chemical compatibility of the HDDA cross-linked architectures by immersing and shaking them in water. Visual inspection of the HDDA printed object did not show any appreciable degradation of the material after 24 h of treatment (Figure S1a, b). ESI-MS analysis of the supernatant did not show any monomer or oligomer peaks, further suggesting there was no degradation of the material (Figure S2a). In contrast, the objects 3D printed using PEGDA as crosslinker were severely damaged upon shaking in water (Figure S1c-d). ESI-MS analysis of the supernatant showed characteristic oligomer peaks with m/z 44.02 assigned to the ethyleneoxy repeating units of PEGDA, confirming degradation of the 3D printed object (Figure S2b).

The active site accessibility of the HDDA-crosslinked 3D printed architectures was assessed by treatment with an aqueous solution of copper (II) nitrate.[36] Examination of a cross section of the 3D printed object revealed an accessibility (~ 50 μm penetration depth, Figure S3) comparable to that of catalysts 3D printed with PEGDA as crosslinker. Therefore, upgrading the water compatibility of the 3D printed catalysts enables their application in greener catalytic conversions without sacrificing site accessibility.

To evaluate the effects of macrostructure and surface on catalytic performance we designed, and 3D printed a set of magnetic stir bar compartments (SBC) with varying topologies using the AA and HDDA based resin. The SBC consisted of a base that fit a magnetic stir bar and a top of variable architecture. The architectures investigated included rotors with 2, 4 and 6 curved blades of the same size and curvature and the face-free frameworks of three regular polyhedra (tetrahedron, icosahedron and truncated icosahedron) with surface areas comparable to the blades. The structures were designated as SBC-X where X stands for the number of blades or the initials of the polyhedra (Figure 1).

We have shown before that the number of accessible acidic sites in 3D printed AA-based materials can be obtained by immersing the objects in water and measuring the solution's pH.[36] Using this approach we estimated the amount of catalytic sites in each of the 3D printed SBC, and observed that this number was proportional to their calculated surface areas (Table 1). The result suggested a homogeneous dispersion of active sites in the 3D printed objects regardless of their shape. All the SBC were catalytically active for the hydrolysis of the dimethyl acetal of *p*-anisaldehyde further confirming the active site accessibility in the 3D printed architectures (>99 % conversion, 0.12 M in 1:1 water:ethanol, after 5 min r.t.).

Table 1. Number of accessible acidic sites present in the 3D printed SBC-X materials.

Sample	SBC-2	SBC-4	SBC-6	SBC-T	SBC-IC	SBC-TIC	SBC-4-R
Surface area (mm^2)[a]	271	299	328	276	441	346	299
Acidic sites (μmol g^{-1})	17.3	21.3	35.6	20.7	37.7	31.7	19.7
Sucrose Hydrolysis (% Conversion)	14.8 ± 1.2	17.3 ± 0.47	28.2 ± 2.4	9.01 ± 1.3	11.9 ± 1.1	9.86 ± 1.1	28.1 ± 1.3

[a] Calculated from STL model using 3-D Tool™

To study the effects of 3D printed material morphology on reactivity we used the SBC as catalysts for the acid hydrolysis of sucrose to D-glucose and D-fructose. This reaction is commonly used as a model to study polysaccharide deconstruction and proceeds through initial protonation of the glycosidic oxygen followed by slow decomposition of the intermediate (Scheme 1).[40-41] When the reaction is catalyzed by strong mineral acids, the first step is fast and rate depends mainly on sugar concentration. However, for weak acids such as carboxylic groups, the protonation pre-equilibrium becomes kinetically relevant and the rate shows a stronger dependence on the acid concentration.[41-42] To follow the reaction we measured the amount of D-glucose and D-fructose produced using Benedict's test.[38]

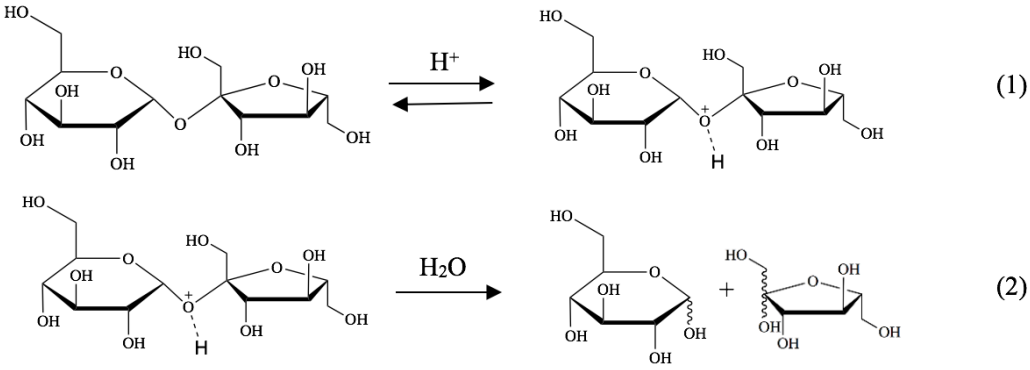

Scheme 1. Acid catalyzed hydrolysis of sucrose.

First, we compared the activities of the SBC containing different numbers of blades. We observed an increase of conversion with the number of blades (Figure S4). Since the number of blades is proportional to the surface area of the SBC (Table 1) the result could be attributed to an increase in the number of active sites. Indeed, a good linear correlation was observed between the number of active sites and conversion (Figure 2a, R^2 0.99). However, a slight drop in the activity per acidic site (turnover number, TON) was observed with increasing number of blades (Figure 2b). This result suggested that the catalytic activity of

the 3D printed SBC could be affected by an additional property, perhaps related to changes in the flow dynamics that result from the differences in the number of blades between the SBC. The relevance of flow dynamics was more evident when considering the lower conversion, sensitivity to changes in surface area, and TON observed when using the SBC with polyhedral framework tops as catalysts (Figure 2a, S5). These significant decreases in apparent activity indicated that the wireframe topology of these SBC cannot enhance mass transport in the same measure as the blades.

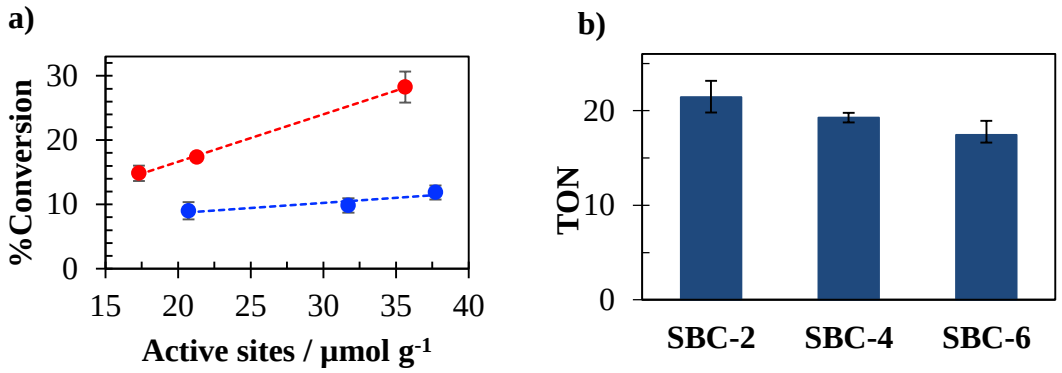

Figure 2. a) Correlation between conversion and accessible sites of SBC with blade tops (red) and polyhedral framework tops (blue). b) TON of SBC with different number of blades.

To further explore the effect of flow dynamics on the apparent activity of the catalytic architectures we produced a new SBC-4 with the blades in reversed orientation. The new print was designated as SBC-4-R and was printed as the mirror image of SBC-4. Because of the blade twist direction relative to the rotation of the magnetic stir bar SBC-4 tends to push the liquid away from its rotation axis (similar to a propeller in a forward moving boat) and SBC-4-R tends to pull liquid towards its rotation axis (similar to a propeller in a backward moving boat) (Figure S6). To visualize differences in flow dynamics we examined the effect of SBC-4, SBC-4-R and SBC-T stirring (1050 rpm) on the dispersion of Methylene Blue in

water. These three SBC had similar surface areas, thus any difference in their effects on flow should be due exclusively to their morphology. A set of photographs taken at the early stages of mixing revealed remarkable differences between the three SBC (Figure S7). While the dye started (0.12 s) as a concentrated blot on the upper part of the vial using SBC-4 and SBC-T, the vial containing SBC-4-R formed a thin funnel spanning from the liquid surface to the 3D printed object. The blot observed for SBC-4 and SBC-T appeared to eventually spread sideways and gradually diffuse to fill the solution. In contrast, the funnel observed in SBC-4-R remained in place and diffusion appeared to start from dye accumulating at the bottom to the rest of the vial. This observation suggested that rotating SBC-4 and SBC-T tend to actively push solvent away from them and that solvent reaches their surface by passive diffusion. To the contrary, SBC-4-R appeared to pull the solution towards itself, forcing the solvent in contact with its surface to diffuse away. In addition, measurement of the kinetics of dye dispersion over a longer timescale by UV-visible spectroscopy revealed significant differences between the three SBC, with SBC-4-R displaying the fastest rate of diffusion, followed by SBC-4 and SBC-T (Figure S8). Because these SBC had similar surface areas and number of active sites, any difference between their apparent activities should be mainly due to differences in mass transport, which should be related to the observed mode and kinetics of diffusion. Indeed, glucose conversion was significantly higher for SBC-4-R than SBC-4 and was the lowest for SBC-T (Figure 3). Importantly, the remarkable difference between SBC-4-R and SBC-4 should not be solely considered in terms of diffusion rates, but on the tendency of the former to pull the solution towards its own active surface as opposed to the tendency of the latter to push solution away from itself. These results clearly

demonstrate that catalytic performance can be controlled by suitable design of macroscopic architecture.

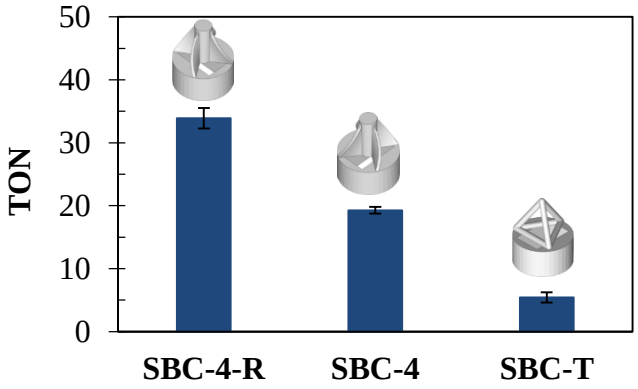

Figure 3. TON of 3D printed SBC with similar surface areas and number of active sites.

Monosaccharides are a common feedstock in downstream biorefinery and are typically produced by enzymatic hydrolysis of complex sugars.[43-46] To break down polysaccharides the enzymes use hydrophobic domains that bind the substrates via van der Waals interactions. This binding assumes most of the entropic cost of the activation step and thereby facilitates glycosidic bond cleavage by the acid active sites.[47] A similar type of synergy between hydrophobic domains and active sites is exploited when using activated carbons as catalysts for cellulose deconstruction, the abundance of hydrophobic regions in these materials allows even weakly acidic phenols to catalyze the hydrolysis.[48-51] Based on this information we decided to explore the effect of varying the amounts of hydrophobic HDDA crosslinker on the catalytic performance of 3D printed SBC for the hydrolysis of sucrose. To this end, we prepared a series of photoactive resins with varying ratios of AA to HDDA and printed a set of SBC-6 with each of them. The materials were designated as SBC-6-x, where x corresponded to the volume percent of AA used in the resins (5, 10, 20, 30, 50 and 70 %). The 3D printed SBC-6 did not show any obvious variations in texture,

mechanical strength or print resolution (Figure S9). Active site quantification via pH measurement confirmed that the number of accessible acid sites was proportional to the mole ratios of AA to HDDA in the resins (Table S1). ATR FTIR analysis of the SBC-6-x showed a red-shift in the carbonyl band with increasing AA:HDDA mole ratios (Figure 4). The shift was consistent with an increase of carboxylic acid moieties on the surface of the 3D printed SBC-6. The bands at 1708 and 1672 cm^{-1} are characteristic of non-hydrogen bonded and hydrogen bonded carboxylic acids in polyacrylic acid, while the band at higher wavenumbers (1726 cm^{-1}) is characteristic of the ester carbonyls of HDDA.[52-53] The carbonyl peaks were deconvoluted into the AA and HDAA components (Figure S10-S15 Table S1) and the ratios of their peak areas correlated well with the mole ratios of the precursors in the corresponding resins (R^2 0.96). Therefore, these ratios provided a measure of the proportion of hydrophobic domains to active sites in each SBC-6-x. To examine the distribution of hydrophobic domains, we immersed the samples in a Nile Red solution. The fluorescence of Nile Red increases with the hydrophobicity of its environment.[54-55] Analysis of fluorescence microscopy images confirmed the homogenous distribution of the hydrophobic groups (Figure S16). Furthermore, the intensity of the fluorescence emission correlated with the increment of HDDA (hydrophobic sites) in the 3D printed polymers (Figure S17).

The SBC-6-x were then evaluated as catalysts for the hydrolysis of sucrose. We observed an increase in conversion as a function of the amount of accessible active sites. However, rather than linear, the relationship appeared logarithmic with the activity tending to plateau at high acid site densities (Figure 5a). Correspondingly, the TON showed a logarithmic decay with increasing number of acid sites (Figure 5b).

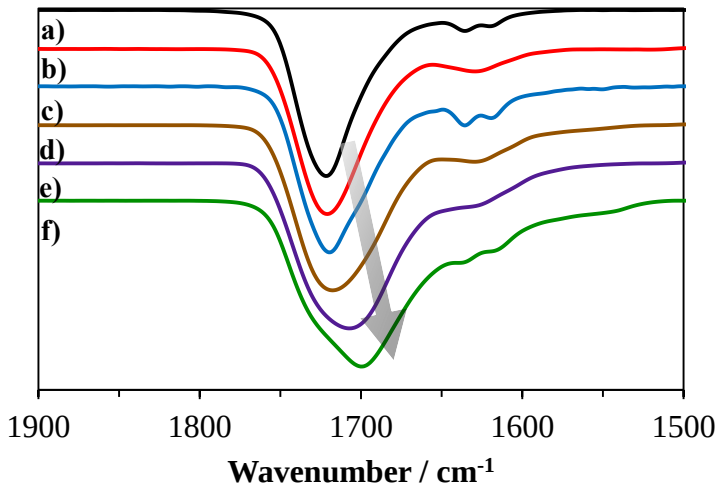

Figure 4. ATR FTIR of SBC-6-x prepared from resins having: a) 5, b) 10, c) 20, d) 30, e) 50 and f) 70 volume % of AA.

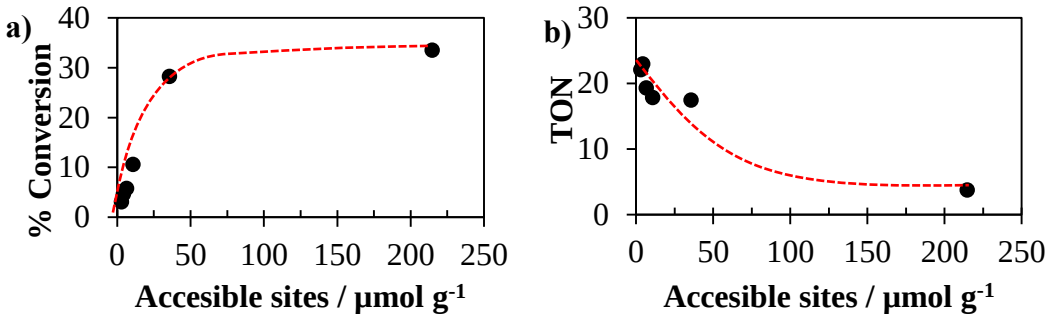

Figure 5. Correlation of a) conversion and b) TON with the number of accessible sites present on the surface of the 3D printed SBC.

These results indicated that increasing acid sites is favorable only in the low surface density regime but has negligible effects at high surface densities. This behavior could be understood as a co-dependence of activity on two types of site, in this case on the number of acid sites and hydrophobic domains provided by AA and HDDA respectively. This dependence is consistent with prior reports on the cooperativity between hydrophobic domains and acid sites in hydrolase enzymes and activated carbons.[47, 56-58] Interestingly, a plot of the dependence of conversion on the AA:HDDA mole ratios of the SBC-6-x displayed a sigmoidal behavior (Figure 6a), which is a signature of cooperative catalysis.[59-63]

These results suggested that the hydrolysis of sucrose catalyzed by the 3D printed SBC took place via van der Waals mediated adsorption of the pyranose and/or furanose rings on the HDDA hydrophobic domains of the materials in concert with acid activation of the glycosidic bonds by the AA groups on the surface (Figure 6b), akin to the behavior of hydrolase enzymes.

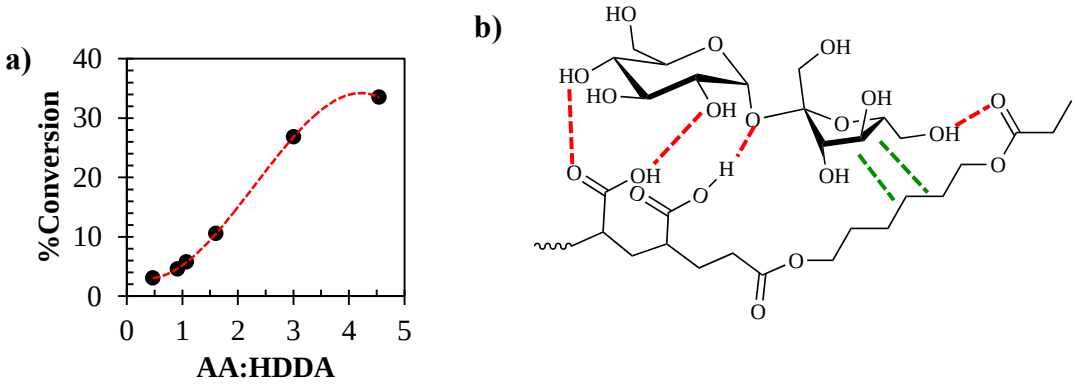

Figure 6. a) Dependence of sucrose conversion on the ratio of acrylic acid (active sites) to crosslinker (hydrophobic domains), the sigmoidal relationship is characteristic of cooperative catalysis. b) Proposed interactions between sucrose and the surface of the 3D printed polymer.

Conclusions

This work demonstrated the simultaneous control of morphology, chemical and physical properties of 3D printed catalytic materials. The approach is based on the design of a new water tolerant resin using 1,6-hexanedioldiacrylate as a crosslinker. The improvement of the physical properties of the 3D printed materials did not disrupt their catalytic properties, but provided them with a new complex chemical behavior, namely: cooperativity between acidic sites and hydrophobic domains.

The 3D printed SBC displayed varying efficiencies as catalysts for the hydrolysis of sucrose as a function of their morphology. The dependence of apparent catalytic activity on morphology, evidenced by differences in TON, originated in the different capacities of the

SBC to control the flow dynamics (mass transport) of the reaction systems. SBC with blades twisted in the direction of the magnetic bar rotation tended to push solution away from their active surfaces, resulting in TON that decreased with increasing number of blades. SBC with blades twisted in the opposite direction of magnetic bar rotation tended to drive the solution towards their surface maximizing interaction of reactants with the active sites, thereby increasing apparent activity and TON. This demonstrates that small yet precise changes in the morphology of the 3D printed objects, easily accessible with our methodology, can have dramatic effects in catalyst performance. In addition, controlling the chemical composition of the 3D printed materials induced cooperativity of vicinal weak acid sites and hydrophobic domains, indicating that catalyst design at the molecular level is compatible with this methodology. Therefore, this new approach for 3D printing active materials offers control of catalytic properties all the way from the molecular to the macroscale, which enables its application to advanced tasks in heterogeneous catalysis.

Acknowledgements

This research is supported by the U.S. Department of Energy, Office of Basic Energy Sciences, Division of Chemical Sciences, Geosciences, and Biosciences through the Ames Laboratory. The Ames Laboratory is operated for the U.S. Department of Energy by Iowa State University under Contract No. DE-AC02-07CH11358.

Supplemental Figures

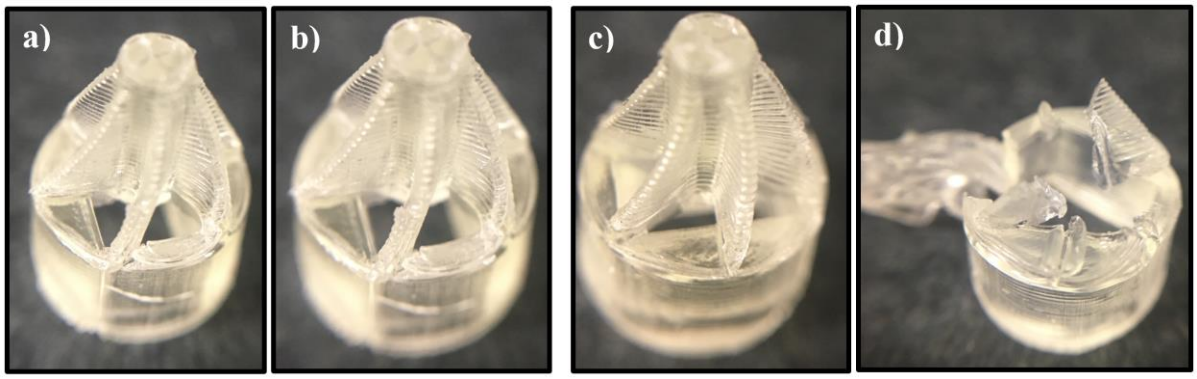

Figure S1. Optical images of 3D printed polymers: HDDA a) before, b) after and PEGDA c) before d) after immersing and shaking in water for 24 h

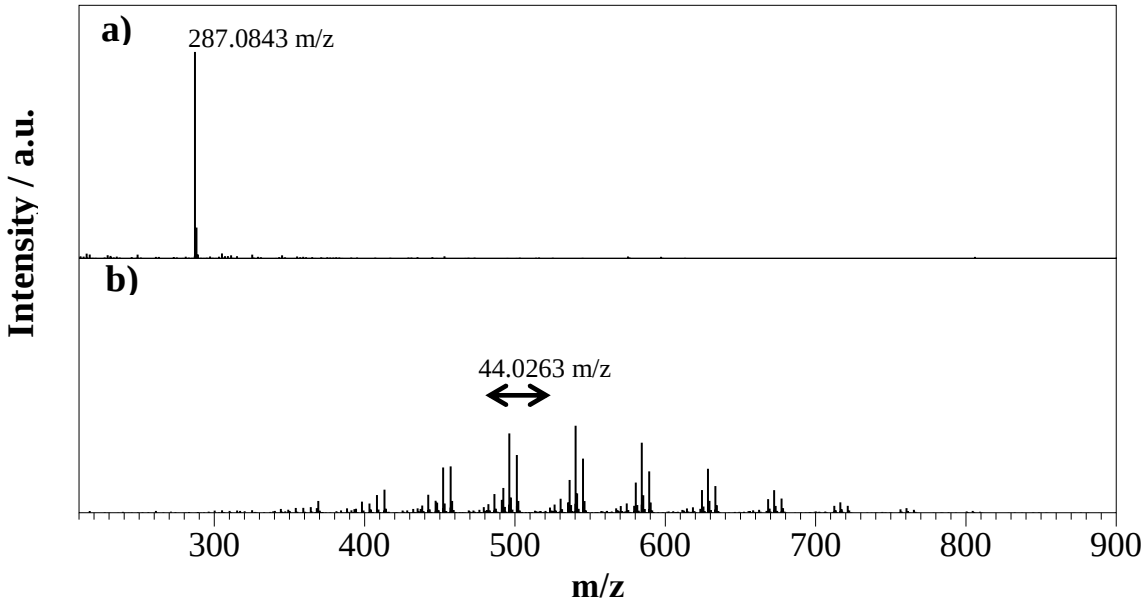

Figure S2. ESI-MS spectra of supernatants obtained after shaking 3D printed objects in water for 24 h. a) The HDDA-crosslinked object presented mainly a peak corresponding to the spent photoinitiator, b) the PEGDA-crosslinked object presented ethylenoxy repeating units characteristic of crosslinker oligomers.

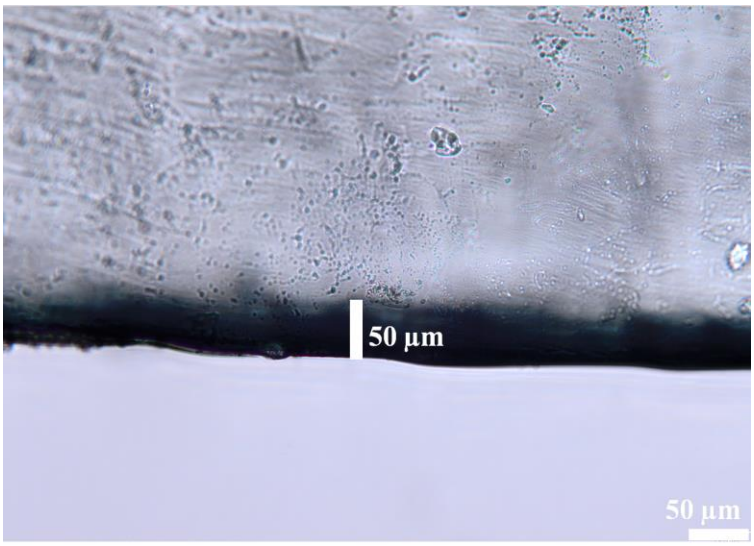

Figure S3. Microscope image of a cross-section of the 3D printed polymer treated with copper (II) nitrate. The 3D printed object has a penetration depth of 50 µm.

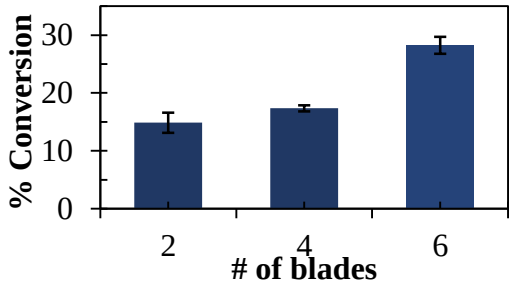

Figure S4. Increase of conversion with number of blades in the 3D printed SBC.

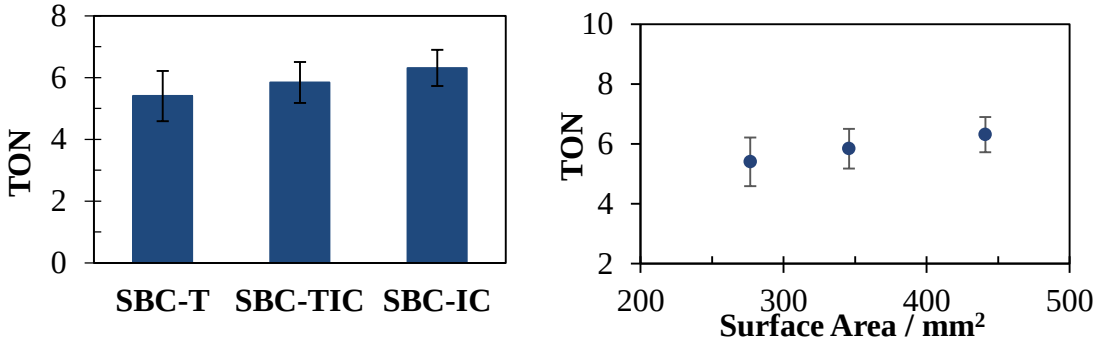

Figure S5. Correlation of activity and surface area of the SBC-polyhedra 3D printed samples.

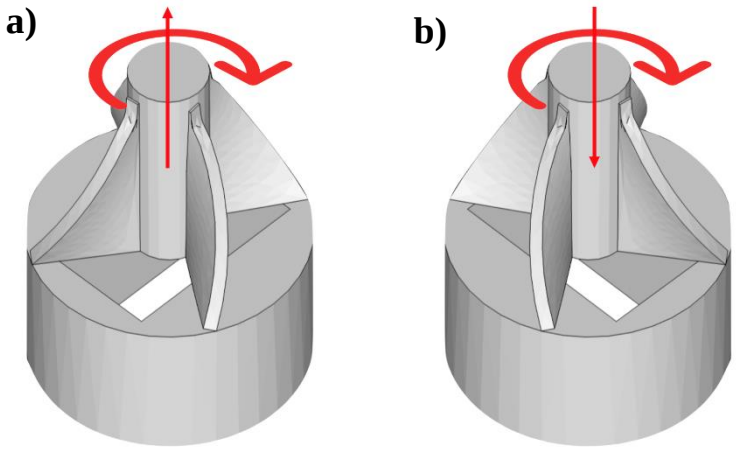

Figure S6. Clockwise rotation of the stir-bar (curved arrow) and flow direction (straight arrows) controlled by the orientation of the blades in a) SBC-4, and b) SBC-4-R.

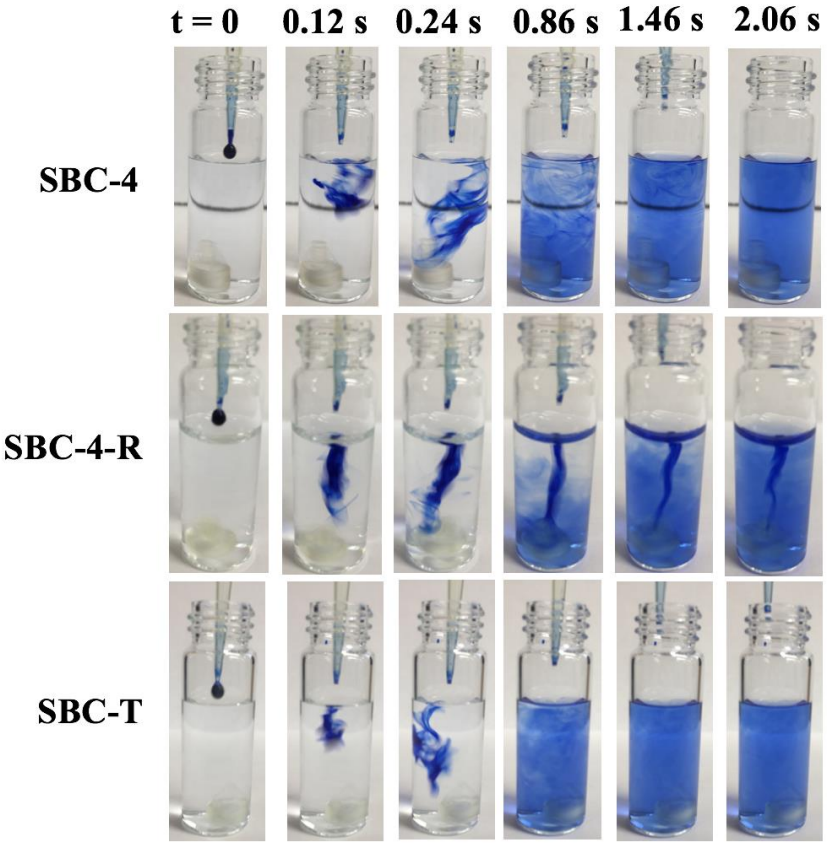

Figure S7. Optical pictures of the dissolution of Methylene Blue in water demonstrating how the flow dynamics can be tuned with subtle changes in the 3D printed morphology.

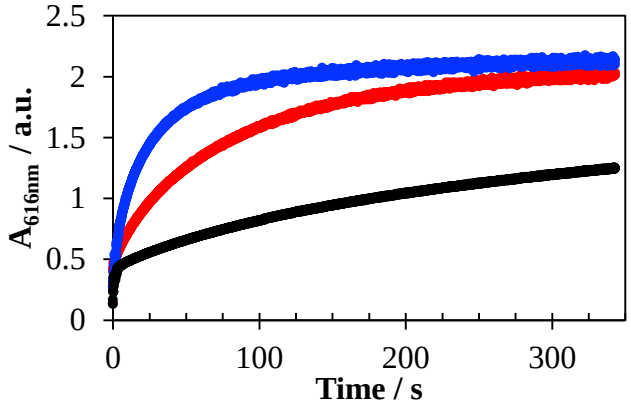

Figure S8. Kinetics of Methylene Blue dispersion in water using SBC-4-R (blue trace), SBC-4 (red trace), and SBC-T (black trace) to control the flow dynamics.

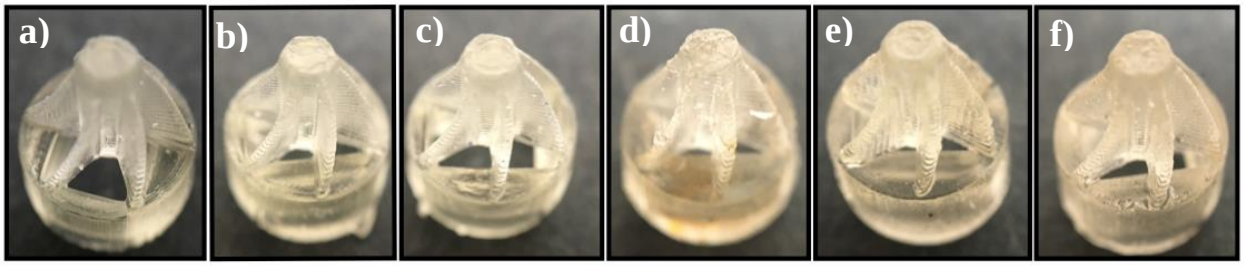

Figure S9. Optical images of the catalytic SBC with different densities of acidic groups. a) SBC-6-5, b) SBC-6-10, c) SBC-6-20, d) SBC-6-30, e) SBC-6-50, and f) SBC-6-70. The last number corresponds to the volume percent of AA used in the 3D printing resin precursor.

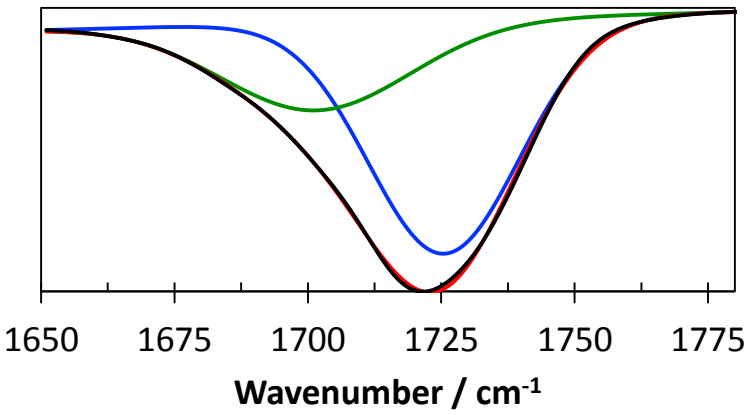

Figure S10. Deconvolution of the carbonyl peak for the 3D printed SBC-6-5. Bands corresponding to poly(acrylic acid) (green trace) carbonyls are centered at 1700 cm^{-1}, while the HDDA carbonyl appears at 1730 cm^{-1} (blue trace).

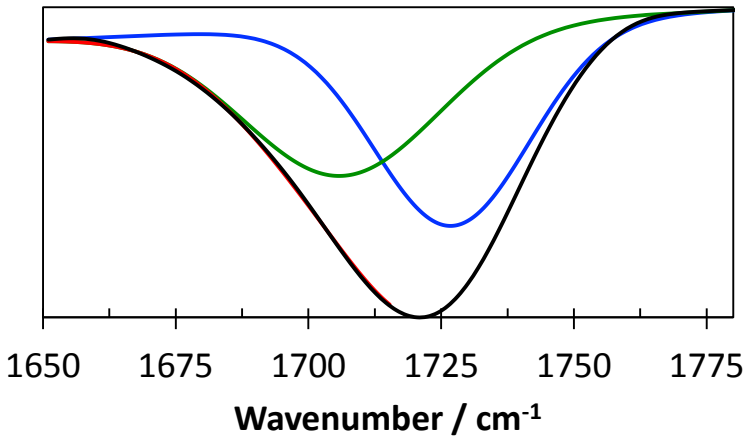

Figure S11. Deconvolution of the carbonyl peak for the 3D printed SBC-6-10. Bands corresponding to poly(acrylic acid) (green trace) carbonyls are centered at 1700 cm^{-1}, while the HDDA carbonyl appears at 1730 cm^{-1} (blue trace).

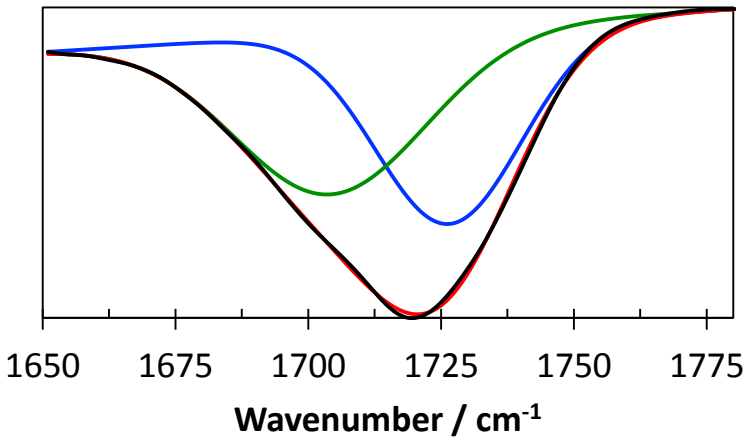

Figure S12. Deconvolution of the carbonyl peak for the 3D printed SBC-6-20. Bands corresponding to poly(acrylic acid) (green trace) carbonyls are centered at 1700 cm^{-1}, while the HDDA carbonyl appears at 1730 cm^{-1} (blue trace).

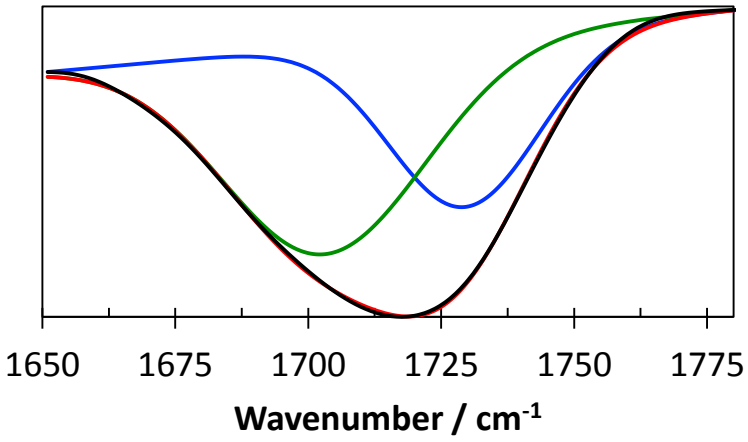

Figure S13. Deconvolution of the carbonyl peak for the 3D printed SBC-6-30. Bands corresponding to poly(acrylic acid) (green trace) carbonyls are centered at 1700 cm^{-1}, while the HDDA carbonyl appears at 1730 cm^{-1} (blue trace).

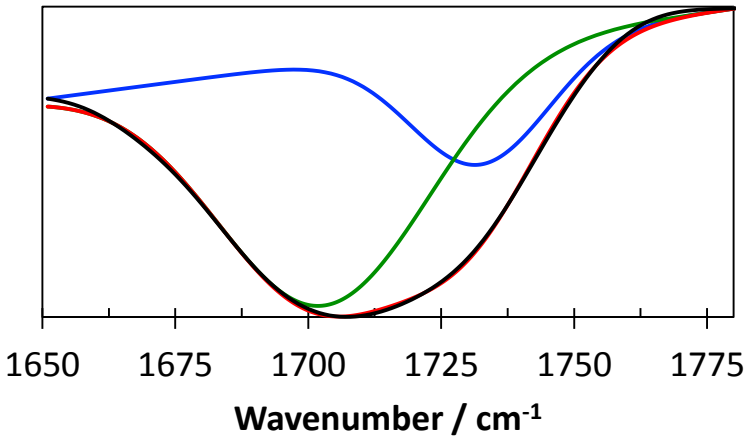

Figure S14. Deconvolution of the carbonyl peak for the 3D printed SBC-6-50. Bands corresponding to poly(acrylic acid) (green trace) carbonyls are centered at 1700 cm^{-1}, while the HDDA carbonyl appears at 1730 cm^{-1} (blue trace).

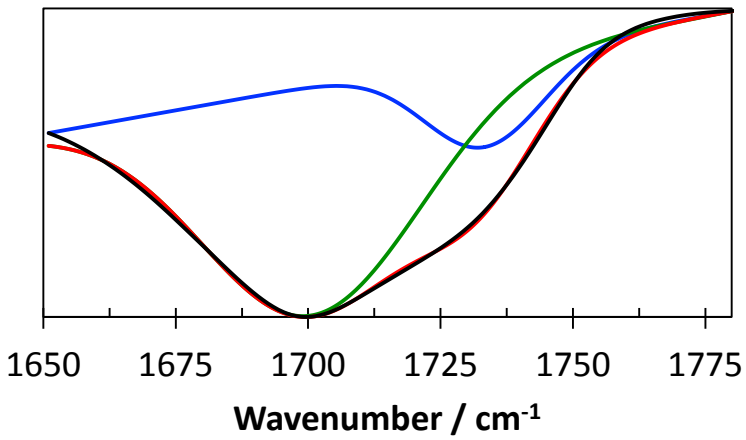

Figure S15. Deconvolution of the carbonyl peak for the 3D printed SBC-6-70. Bands corresponding to poly(acrylic acid) (green trace) carbonyls are centered at 1700 cm^{-1}, while the HDDA carbonyl appears at 1730 cm^{-1} (blue trace).

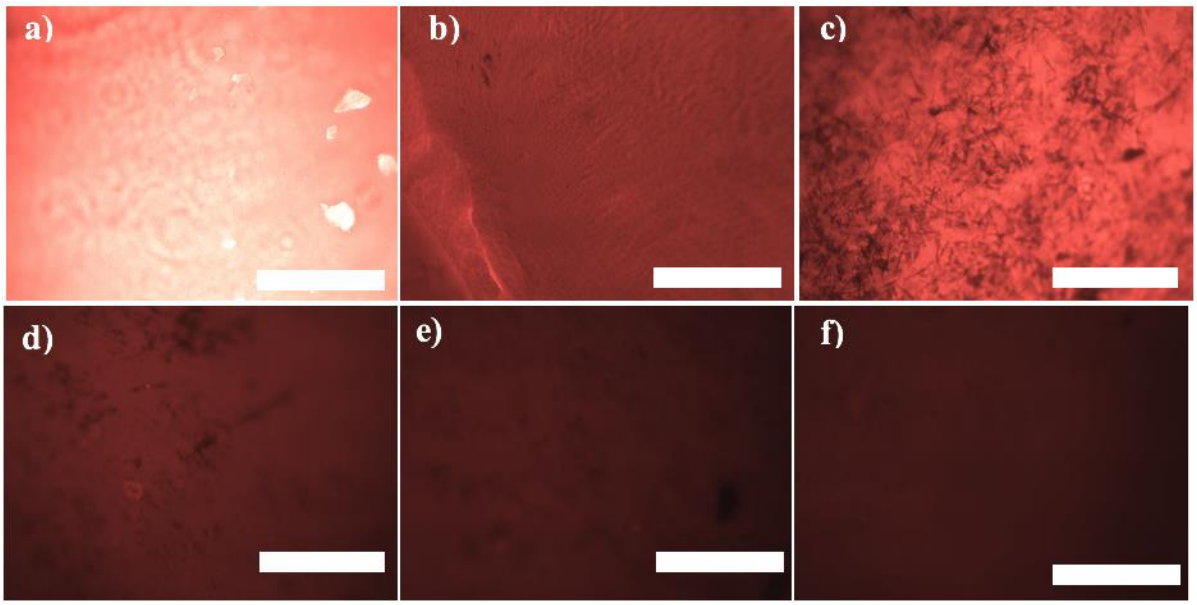

Figure S16. Fluorescence microscopy images of 3D printed samples treated with Nile Red. The polymers contained a) 5 v/v%, b) 10 v/v%, c) 20 v/v%, d) 30 v/v%, e) 50 v/v%, and f) 70 v/v% of acrylic acid. The fluorescence intensity of Nile Red decreases with increasing polarity. Scale bar is 100 µm.

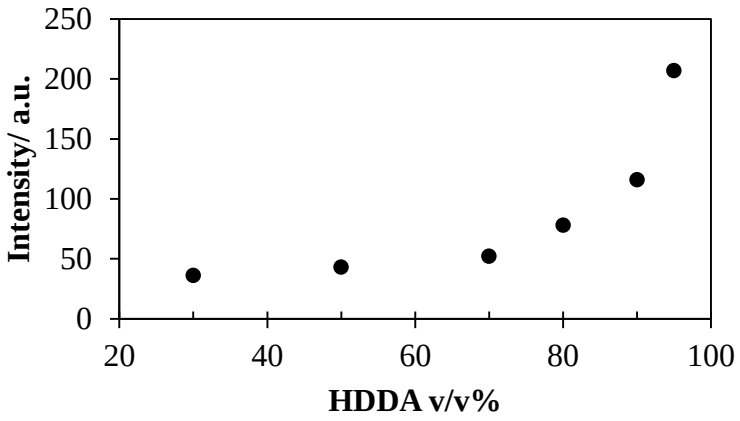

Figure S17. Correlation between fluorescence intensity and the HDD v/v% used in the resin.

Table S1. Accessible acid sites on the surface of SBC-6-x, x represents the v/v% of acrylic acid.

Acrylic Acid (v/v%)	Accessible sites (μmol g^{-1})	AA:HDDA Mole Ratio
5	3.08	0.17
10	4.39	0.36
20	6.57	0.81
30	10.74	1.42
50	35.63	3.31
70	214.81	7.84

Table S2. % Integration of the deconvoluted peaks of the carbonyl signal obtained from ATR FT-IR. The peaks centered at ca. 1700 cm^{-1} and 1730 cm^{-1} corresponded to acrylic acid (AA) and HDDA, respectively.

AA %	HDDA %	Volume Ratio AA:HDDA	Mole ratio AA:HDDA
82.0	18.0	4.55	0.17
75.0	25.0	3.01	0.36
61.6	38.4	1.61	0.81
51.7	48.3	1.07	1.42
47.8	52.2	0.91	3.31
31.9	68.1	0.47	7.84

References

1. Bond, G. C.; Sing, K. S. W.; Everett, D. H.; Haul, R. A. W.; Moscou, L.; Pierotti, R. A.; Rouquerol, J.; Siemieniewska, T., Annexes. In *Handbook of Heterogeneous Catalysis*; Wiley-VCH, Weinheim, **2008**.

2. LePage, J. F.; Schlögl, R.; Wainwright, M. S.; Schü, F.; Unger, K.; Ko, E. I.; Jacobsen, H.; Kleinschmit, P.; Menon, R. G.; Delmon, B.; Lee, K. Y.; Misino, M.; Oyama, S. T., Preparation of Solid Catalysts: Sections 2.0 and 2.1. In *Handbook of Heterogeneous Catalysis*; Wiley-VCH, Weinheim, **2008**.

3. Johnson, D. L.; Verykios, X. E., Effects of radially nonuniform distributions of catalytic activity on performance of spherical catalyst pellets. *AIChE Journal* **1984,** *30*, 44-50.

4. Bai, P. T.; Manokaran, V.; Saiprasad, P. S.; Srinath, S., Studies on Heat and Mass Transfer Limitations in Oxidative Dehydrogenation of Ethane Over Cr2O3 /Al2O3 Catalyst. *Procedia Eng.* **2015,** *127*, 1338-1345.

5. Hibbe, F.; Caro, J.; Chmelik, C.; Huang, A.; Kirchner, T.; Ruthven, D.; Valiullin, R.; Kärger, J., Monitoring Molecular Mass Transfer in Cation-Free Nanoporous Host Crystals of Type AlPO-LTA. *J. Am. Chem. Soc.* **2012,** *134*, 7725-7732.

6. Sachtler, W. M. H.; Schulz-Ekloff, G.; Ernst, S.; Friplat, J. J.; Tanabe, K.; Hattori, H.; Le Page, J. F.; Baerns, M.; Körting, E., Preparation of Solid Catalysts: Sections 2.3.4 – 2.6. *Handbook of Heterogeneous Catalysis*; Wiley-VCH, Weinheim, **2008**.

7. Baldovino-Medrano, V. G.; Le, M. T.; Van Driessche, I.; Bruneel, E.; Alcázar, C.; Colomer, M. T.; Moreno, R.; Florencie, A.; Farin, B.; Gaigneaux, E. M., Role of shaping in the preparation of heterogeneous catalysts: Tableting and slip-casting of oxidation catalysts. *Catal. Today* **2015,** *246*, 81-91.

8. Devyatkov, S. Y.; Zinnurova, A. A.; Aho, A.; Kronlund, D.; Peltonen, J.; Kuzichkin, N. V.; Lisitsyn, N. V.; Murzin, D. Y., Shaping of Sulfated Zirconia Catalysts by Extrusion: Understanding the Role of Binders. *Ind. Eng. Chem. Res.* **2016,** *55*, 6595-6606.

9. Hagen, J. Catalyst Shapes and Production of Heterogeneous Catalysts. In *Industrial Catalysis:A practical approach;* Wiley-VCH, Weinheim, **2015**.

10. Li, Y. Y.; Perera, S. P.; Crittenden, B. D.; Bridgwater, J., The effect of the binder on the manufacture of a 5A zeolite monolith. *Powder Technol.* **2001,** *116*, 85-96.

11. Richardson, J. T.; Remue, D.; Hung, J. K., Properties of ceramic foam catalyst supports: mass and heat transfer. *Appl. Catal. A* **2003,** *250*, 319-329.

12. Liu, Y.; Podila, S.; Nguyen, D. L.; Edouard, D.; Nguyen, P.; Pham, C.; Ledoux, M. J.; Pham-Huu, C., Methanol dehydration to dimethyl ether in a platelet milli-reactor filled with H-ZSM5/SiC foam catalyst. *Appl. Catal. A* **2011,** *409-410*, 113-121.

13. Incera Garrido, G.; Patcas, F. C.; Lang, S.; Kraushaar-Czarnetzki, B., Mass transfer and pressure drop in ceramic foams: A description for different pore sizes and porosities. *Chem. Eng. Sci.* **2008,** *63*, 5202-5217.

14. Lacroix, M.; Nguyen, P.; Schweich, D.; Pham Huu, C.; Savin-Poncet, S.; Edouard, D., Pressure drop measurements and modeling on SiC foams. *Chem. Eng. Sci.* **2007,** *62*, 3259-3267.

15. Patcas, F. C.; Garrido, G. I.; Kraushaar-Czarnetzki, B., CO oxidation over structured carriers: A comparison of ceramic foams, honeycombs and beads. *Chem. Eng. Sci.* **2007,** *62*, 3984-3990.

16. Ludwig, T.; Seckendorff, J.; Troll, C.; Fischer, R.; Tonigold, M.; Rieger, B.; Hinrichsen, O., Additive Manufacturing of Al2O3-Based Carriers for Heterogeneous Catalysis. *Chem. Ing. Tech.* **2018,** *90*, 703-707.

17. Barry, R. A.; Shepherd, R. F.; Hanson, J. N.; Nuzzo, R. G.; Wiltzius, P.; Lewis, J. A., Direct-Write Assembly of 3D Hydrogel Scaffolds for Guided Cell Growth. *Adv. Mater.* **2009,** *21*, 2407-2410.

18. Boland, T.; Xu, T.; Damon, B.; Cui, X., Application of inkjet printing to tissue engineering. *Biotechnol. J.* **2006,** *1*, 910-917.

19. Mohanty, S.; Larsen, L. B.; Trifol, J.; Szabo, P.; Burri, H. V. R.; Canali, C.; Dufva, M.; Emnéus, J.; Wolff, A., Fabrication of scalable and structured tissue engineering scaffolds using water dissolvable sacrificial 3D printed moulds. *Mater. Sci. Eng. C* **2015,** *55*, 569-578.

20. Kelly, C. N.; Miller, A. T.; Hollister, S. J.; Guldberg, R. E.; Gall, K., Design and Structure–Function Characterization of 3D Printed Synthetic Porous Biomaterials for Tissue Engineering. *Adv. Healthc. Mater.* **2018,** *7*, 1701095.

21. Ahn, B. Y.; Duoss, E. B.; Motala, M. J.; Guo, X.; Park, S.-I.; Xiong, Y.; Yoon, J.; Nuzzo, R. G.; Rogers, J. A.; Lewis, J. A., Omnidirectional Printing of Flexible, Stretchable, and Spanning Silver Microelectrodes. *Science* **2009,** *323*, 1590-1593.

22. Zhang, B.; Li, S.; Hingorani, H.; Serjouei, A.; Larush, L.; Pawar, A. A.; Goh, W. H.; Sakhaei, A. H.; Hashimoto, M.; Kowsari, K.; Magdassi, S.; Ge, Q., Highly stretchable hydrogels for UV curing based high-resolution multimaterial 3D printing. *J. Mate. Chem. B* **2018,** *6*, 3246-3253.

23. Alizadehgiashi, M.; Gevorkian, A.; Tebbe, M.; Seo, M.; Prince, E.; Kumacheva, E., 3D-Printed Microfluidic Devices for Materials Science. *Adv. Mater. Tech.* **2018,** *3*, 1800068.

24. Dragone, V.; Sans, V.; Rosnes, M. H.; Kitson, P. J.; Cronin, L., 3D-printed devices for continuous-flow organic chemistry. *Beilstein J. Org. Chem.* **2013,** *9*, 951−959

25. Kitson, P. J.; Rosnes, M. H.; Sans, V.; Dragone, V.; Cronin, L., Configurable 3D-Printed millifluidic and microfluidic 'lab on a chip' reactionware devices. *Lab Chip* **2012,** *12*, 3267-3271.

26. Lee, W.; Kwon, D.; Choi, W.; Jung, G. Y.; Jeon, S., 3D-Printed Microfluidic Device for the Detection of Pathogenic Bacteria Using Size-based Separation in Helical Channel with Trapezoid Cross-Section. *Sci. Rep.* **2015,** *5*, 7717.

27. Au, A. K.; Huynh, W.; Horowitz, L. F.; Folch, A., 3D-Printed Microfluidics. *Angew. Chem., Int. Ed.* **2016,** *55*, 3862-3881.

28. Díaz-Marta, A. S.; Tubío, C. R.; Carbajales, C.; Fernández, C.; Escalante, L.; Sotelo, E.; Guitián, F.; Barrio, V. L.; Gil, A.; Coelho, A., Three-Dimensional Printing in Catalysis: Combining 3D Heterogeneous Copper and Palladium Catalysts for Multicatalytic Multicomponent Reactions. *ACS Catal.* **2018,** *8*, 392-404.

29. Tubío, C. R.; Azuaje, J.; Escalante, L.; Coelho, A.; Guitián, F.; Sotelo, E.; Gil, A., 3D printing of a heterogeneous copper-based catalyst. *J. Catal.* **2016,** *334*, 110-115.

30. Tubío, C. R.; Guitián, F.; Gil, A., Fabrication of ZnO periodic structures by 3D printing. *J. Eur. Ceram. Soc.* **2016,** *36*, 3409-3415.

31. Lewis, J. A., Colloidal Processing of Ceramics. *J. Am. Ceram. Soc.* **2000,** *83*, 2341-2359.

32. Compton, B. G.; Lewis, J. A., 3D-Printing of Lightweight Cellular Composites. *Adv. Mater.* **2014,** *26*, 5930-5935.

33. Rao, R. B.; Krafcik, K. L.; Morales, A. M.; Lewis, J. A., Microfabricated Deposition Nozzles for Direct-Write Assembly of Three-Dimensional Periodic Structures. *Adv. Mater.* **2005,** *17*, 289-293.

34. Varghese, G.; Moral, M.; Castro-García, M.; López-López, J. J.; Marín-Rueda, J. R.; Yagüe-Alcaraz, V.; Hernández-Afonso, L.; Ruiz-Morales, J. C.; Canales-Vázquez, J., Fabrication and characterisation of ceramics via low-cost DLP 3D printing. *Bol. Soc. Esp. Ceram. V.* **2018,** *57*, 9-18.

35. Kotz, F.; Arnold, K.; Bauer, W.; Schild, D.; Keller, N.; Sachsenheimer, K.; Nargang, T. M.; Richter, C.; Helmer, D.; Rapp, B. E., Three-dimensional printing of transparent fused silica glass. *Nature* **2017,** *544*, 337.

36. Manzano, J. S.; Weinstein, Z. B.; Sadow, A. D.; Slowing, I. I., Direct 3D Printing of Catalytically Active Structures. *ACS Catal.* **2017,** *7*, 7567-7577.

37. Sun, X.; Yan, Y.; Zhang, L.; Ma, G.; Liu, Y.; Yu, Y.; An, Q.; Tao, S., Direct 3D Printing of Reactive Agitating Impellers for the Convenient Treatment of Various Pollutants in Water. *Adv. Mater. Interf.* **2018,** *5*.

38. Kumar, V.; Gill, K. D., Quantitative Analysis of Reducing Sugars in Urine. In *Basic Concepts in Clinical Biochemistry: A Practical Guide*, Springer Singapore: Singapore, 2018; pp 53-55.

39. Lee, H.; Lee, S. G.; Doyle, P. S., Photopatterned oil-reservoir micromodels with tailored wetting properties. *Lab Chip* **2015,** *15*, 3047-3055.

40. Yamabe, S.; Guan, W.; Sakaki, S., Three Competitive Transition States at the Glycosidic Bond of Sucrose in Its Acid-Catalyzed Hydrolysis. *J. Org. Chem.* **2013,** *78*, 2527-2533.

41. Rinaldi, R.; Schüth, F., Acid Hydrolysis of Cellulose as the Entry Point into Biorefinery Schemes. *ChemSusChem* **2009,** *2*, 1096-1107.

42. Mosier, N. S.; Sarikaya, A.; Ladisch, C. M.; Ladisch, M. R., Characterization of Dicarboxylic Acids for Cellulose Hydrolysis. *Biotechnol. Prog.* **2001,** *17*, 474-480.

43. Huber, G. W.; Corma, A., Synergies between Bio- and Oil Refineries for the Production of Fuels from Biomass. *Angew. Chem., Int. Ed.* **2007,** *46*, 7184-7201.

44. Sun, Y.; Cheng, J., Hydrolysis of lignocellulosic materials for ethanol production: a review. *Bioresour. Technol.* **2002,** *83*, 1-11.

45. Zhang, Y.-H. P.; Lynd, L. R., Toward an aggregated understanding of enzymatic hydrolysis of cellulose: Noncomplexed cellulase systems. *Biotechnol. Bioeng.* **2004,** *88*, 797-824.

46. Hammerer, F.; Loots, L.; Do, J.-L.; Therien, J. P. D.; Nickels, C. W.; Friščić, T.; Auclair, K., Solvent-Free Enzyme Activity: Quick, High-Yielding Mechanoenzymatic Hydrolysis of Cellulose into Glucose. *Angew. Chem., Int. Ed.* **2018,** *57*, 2621-2624.

47. Chen, W.; Enck, S.; Price, J. L.; Powers, D. L.; Powers, E. T.; Wong, C.-H.; Dyson, H. J.; Kelly, J. W., Structural and Energetic Basis of Carbohydrate–Aromatic Packing Interactions in Proteins. *J. Am. Chem. Soc.* **2013,** *135*, 9877-9884.

48. Shrotri, A.; Kobayashi, H.; Fukuoka, A., Air Oxidation of Activated Carbon to Synthesize a Biomimetic Catalyst for Hydrolysis of Cellulose. *ChemSusChem* **2016,** *9*, 1299-1303.

49. Kobayashi, H.; Yabushita, M.; Komanoya, T.; Hara, K.; Fujita, I.; Fukuoka, A., High-Yielding One-Pot Synthesis of Glucose from Cellulose Using Simple Activated Carbons and Trace Hydrochloric Acid. *ACS Catal.* **2013,** *3*, 581-587.

50. To, A. T.; Chung, P. W.; Katz, A., Weak-Acid Sites Catalyze the Hydrolysis of Crystalline Cellulose to Glucose in Water: Importance of Post-Synthetic Functionalization of the Carbon Surface. *Angew. Chem.* **2015,** *127*, 11202-11205.

51. Foo, G. S.; Sievers, C., Synergistic Effect between Defect Sites and Functional Groups on the Hydrolysis of Cellulose over Activated Carbon. *ChemSusChem* **2015,** *8*, 534-543.

52. Dong, J.; Ozaki, Y.; Nakashima, K., Infrared, Raman, and Near-Infrared Spectroscopic Evidence for the Coexistence of Various Hydrogen-Bond Forms in Poly(acrylic acid). *Macromolecules* **1997,** *30*, 1111-1117.

53. Choi, N.-S.; Lee, Y. M.; Park, J. H.; Park, J.-K., Interfacial enhancement between lithium electrode and polymer electrolytes. *J. Power Sourc.* **2003,** *119-121*, 610-616.

54. Singappuli-Arachchige, D.; Manzano, J. S.; Sherman, L. M.; Slowing, I. I., Polarity Control at Interfaces: Quantifying Pseudo-solvent Effects in Nano-confined Systems. *ChemPhysChem* **2016,** *17*, 2982-2986.

55. Sarkar, N.; Das, K.; Nath, D. N.; Bhattacharyya, K., Twisted charge transfer processes of nile red in homogeneous solutions and in faujasite zeolite. *Langmuir* **1994,** *10*, 326-329.

56. Kitano, M.; Yamaguchi, D.; Suganuma, S.; Nakajima, K.; Kato, H.; Hayashi, S.; Hara, M., Adsorption-Enhanced Hydrolysis of β-1,4-Glucan on Graphene-Based Amorphous Carbon Bearing SO3H, COOH, and OH Groups. *Langmuir* **2009,** *25*, 5068-5075.

57. Onda, A.; Ochi, T.; Yanagisawa, K., Selective hydrolysis of cellulose into glucose over solid acid catalysts. *Green Chem.* **2008,** *10*, 1033-1037.

58. Zolotnitsky, G.; Cogan, U.; Adir, N.; Solomon, V.; Shoham, G.; Shoham, Y., Mapping glycoside hydrolase substrate subsites by isothermal titration calorimetry. *Proc. Natl. Acad. Sci. U. S. A.* **2004,** *101*, 11275.

59. Chen, Z.; Ji, H.; Liu, C.; Bing, W.; Wang, Z.; Qu, X., A Multinuclear Metal Complex Based DNase-Mimetic Artificial Enzyme: Matrix Cleavage for Combating Bacterial Biofilms. *Angew. Chem., Int. Ed.* **2016,** *55*, 10732-10736.

60. Bonomi, R.; Scrimin, P.; Mancin, F., Phosphate diesters cleavage mediated by Ce(iv) complexes self-assembled on gold nanoparticles. *Org. Biomol. Chem.* **2010,** *8*, 2622-2626.

61. Yi, C. S.; Zeczycki, T. N.; Lindeman, S. V., Kinetic, Spectroscopic, and X-Ray Crystallographic Evidence for the Cooperative Mechanism of the Hydration of Nitriles Catalyzed by a Tetranuclear Ruthenium-μ-oxo-μ-hydroxo Complex. *Organometallics* **2008,** *27*, 2030-2035.

62. Yi, C. S.; Zeczycki, T. N.; Guzei, I. A., Highly Cooperative Tetrametallic Ruthenium-μ-Oxo-μ-Hydroxo Catalyst for the Alcohol Oxidation Reaction. *Organometallics* **2006,** *25*, 1047-1051.

63. Perutz, M. F., Mechanisms of cooperativity and allosteric regulation in proteins. *Q. Rev. Biophys.* **1989,** *22*, 139-237.

CHAPTER 4. HIGH THROUGHPUT SCREENING OF 3D PRINTABLE RESINS: CONTROLLING SURFACE AND CATALYTIC PROPERTIES

J. Sebastián Manzano,[1,2] Hsin Wang, [1,2] Igor I. Slowing[1,2]

[1]US DOE Ames Laboratory, Ames, Iowa 50011, United States

[2]Department of Chemistry, Iowa State University, Ames, Iowa 50011, United States

Abstract

Identification of new 3D printable materials is crucial to expand the breadth of physical and chemical properties attainable for 3D architectures. Stereolithography (SLA), a popular 3D printing approach based on the photo-polymerization of liquid resins, is ideally suited for exploring a wide variety of functional monomers that may be printed into solids of diverse physical and chemical properties. However, for most of the commercially available SLA 3D printers screening printable monomers and resin compositions requires large volumes (~150 mL) in each printing cycle, which makes the process costly and inefficient. Herein, a high throughput block (HTB) adaptor was developed to screen arrays of monomers and resin compositions, consuming low volumes (> 2 mL) and less time per print (<1/16 based on a 4 × 4 matrix). Using this approach, a family of materials with different surface hydrophobicities were 3D printed by including long chain acrylates in the resin composition. In addition, several metal salts were dissolved in an acrylic acid-based resin, 3D printed and screened as heterogeneous catalysts for the aerobic oxidation of benzyl alcohol to benzaldehyde. Cu(II)-based resins were identified as those giving the most active 3D printed structures. Combinations of Cu(II) and long chain acrylate monomers were used to 3D print architectures with varying degrees of hydrophobicity and investigated as means to further enhance catalytic activity for the aerobic oxidation of benzyl alcohol. The HTB enables fast

screening of resins for 3D printing architectures with intrinsic catalytic activity, tunable surface properties and minimal waste.

Introduction

Currently, mass production of goods is the main process in the industry, where standardized products are manufactured in large scales at low-cost. However, to meet the customer's needs, a mass customization approach is needed, where personalized products are manufactured preserving the low-cost production. This implementation implies a changing of tools or molds in between production runs, which reduces the efficiency of the process and makes it unsustainable. 3D printing is a technology based on the production of 3D objects in a layer-by-layer fashion using digital designs. The use of a digital configuration can allow the customers to upload the desired product, making mass customization sustainable. This emerging technology has been already used in tissue engineering,[1-4] electronics,[5] ceramics,[6-11] mechanical devices,[12-17] pharmaceuticals,[18, 19] periodic microstructures[6, 20] and more recently in catalysis.[21-24]

3D printing methods based on photo-polymerization, such as stereolithography (SLA) and continuous liquid interface production, yield high quality materials, with high resolution (140 μm), and within a smaller time frame than other 3D printing methods, and hence are among the most used methods for additive manufacturing.[25] Recently, our group demonstrated the use of SLA to produce 3D architectures with intrinsic catalytic activity by introducing active functionalities in the printing monomers.[21] This approach allowed the fabrication of custom devices with tunable chemical properties. For example, we 3D printed a catalyst adaptor to enable in situ kinetic studies of heterogeneous reactions in conventional UV-Vis spectrometers. We also manufactured a heterogeneous catalyst in the form of a

millifluidic device whose length and macroscopic shape controlled the efficiency of conversion in flow reactions.

Nonetheless, developing resin compositions that produce 3D objects with target catalytic or surface properties can be expensive and time-consuming. These limitations are due to the conventional hardware set up of most SLA printers, which are commonly designed to use a single resin per printing cycle in a relatively large volume tank (150 mL). Recently, Louzao et al. presented a high throughput screening method for printable resins, however the printability was not screened directly using a 3D printer but an UV-initiated inkjet printing apporach.[26] Consequently, a screening method that evaluates printing in three dimensions may be a more direct way to discover and expand the family of materials available for 3D printing. Herein, we report a high throughput screening method based on compartmentalizing the build platforms and resin tanks of commercial SLA printers and its application to directly identify resins for 3D printing functional materials. The applicability of the method was demonstrated by producing a library of 3D printed materials with diverse hydrophobicities and a library of 3D printed metal acrylates. The metal acrylate library was then screened to identify 3D printed catalysts for the aerobic selective oxidation of benzyl alcohol. Combination of the hydrophobic resins with the metal-containing resins was then investigated to 3D print bifunctional architectures with enhanced performance for benzyl alcohol oxidation.

Experimental

Materials

Acetonitrile, cerium(III) nitrate, chromium(III) nitrate, cobalt(II) nitrate, iron(III) acetylacetonate, palladium chloride, gold(III) chloride, erbium(III) nitrate, iridium(III) chloride, allylamine, diallylamine, butyl acrylate, isodecyl acrylate, octadecyl acrylate, 2-

ethylhexyl acrylate, lauryl acrylate, hexyl acrylate, isobutyl acrylate, acrylic acid, phenylbis(2,4,6-trimethyl)phosphine oxide (BAPO), 2,2,6,6-Tetramethyl-1-piperidinyloxy (TEMPO), benzyl alcohol, propionitrile, heptyl cyanide (caprylonitrile), butyronitrile, and poly(ethylene glycol)diacrylate (PEGDA) were purchased from Sigma-Aldrich (St. Louis, MO, USA). Antimony(III) chloride, nickel(II) nitrate, magnesium iodide, bismuth(III) nitrate and cobalt(II) nitrate were purchased from Fischer Scientific (Waltham, MA, USA), and basic copper carbonate from Alfa Aesar (Tewksbury, MA, USA). All reagents were used without further purification.

Parent resin preparation

Acrylic acid (70 mL, 1021 mmol) and PEGDA (30 mL, 58 mmol) were mixed in an Amber flask. Then, BAPO (1.0 g, 2.39 mmol) was added to the resin and the mixture was homogenized (14 000 rpm, 5 min). This was used as a stock solution to prepare the respective hydrophobic and metal salt containing resins. The solution was poured into the low volume resin tanks adapted to a FormLabs Form 1+^{TM} 3D printer (Somerville, MA, USA) and used for printing.

Metal-containing resins

5 mL of the parent resin was mixed with 0.11 mmol of the respective metal salt. The mixture was sonicated until the metal salts was completely dissolved.

FDM 3D printing

The CAD designs were prepared using OnShape software (Cambridge, MA, USA) and exported as STL files (Supplementary files available). A dissolvable filament (High Impact Polystyrene (HIPS)) with the Makerbot Replicator 2x^{TM} (New York City, NY, USA) 3D printer were used to produce the resin tanks and platform matrix (4×4).

Polydimethylsiloxane (PDMS) layer

To help the peeling process during printing, a layer of PDMS was added to the compartmentalized resin tanks. Following the manufacturer recommended ratios, 40 g of 10:1 ratio of the Sylgard®184 two-part solution was prepared and 2 mL from this mixture were added to each resin tank. The resin tanks containing PDMS were cured for 24 h in an oven at 40 ºC

SLA 3D printing

The CAD designs were prepared using OnShape software and exported as STL files (Supplementary files available). 3D printing was performed via spatially resolved layer-by-layer photo-induced polymerization and cross-linking of acrylate-based resins. A FormLabs Form 1+™ 3D printer (405 nm laser) was used with the settings for the laser polymerization: The settings used were: *laser power*: 62 mW, *first layer passes*: 10, *other layer passes*: 5, and *early layer passes*: 5. After printing, the unreacted species were removed from the 3D printed objects by immersion in an acetone bath for 5 min. Final curing was performed by exposing the 3D object to UV irradiation (λ = 320 nm) in a Rayonet photo-reactor for 10 min.

Oxidation of benzyl alcohol screening

To a solution of benzyl alcohol (20 µL, 0.19 mmol) and 2,2,6,6-Tetramethyl-1-piperidinyloxy (TEMPO, 12 mg, 0.076 mmol) in acetonitrile (1 mL) a 3D printed hollow cube containing the respective metal site was added. The reaction was stirred at 100 ºC and 200 rpm for 6 h. A 10 µL aliquot was diluted in 1 mL of ethanol and analyzed by using an Agilent GC-MS instrument (7890A, 5975C) with a HP-5MS column. The run started at 60 °C, and the temperature was then ramped to 150 °C at a rate of 5 °C min^{-1}. Then the

temperature ramped to 280 ºC at a rate of 20 ºC min^{-1} and was held for 10 min. The reactions were run in parallel using an aluminum heating block reactor.

Contact angle measurement

Were performed with a Ramé-Hart 200 (p/n 200-U1) goniometer using 2 μL of deionized water. Contact angle images were collected with a high-resolution camera and analyzed with Image J software.

Results and Discussion

Design of High Throughput Block (HTB) for the FormLabs Form 1+™

Herein, we designed and 3D printed a high throughput adaptor set consisting of a 4×4 matrix of build platforms that connect to the z-stage of a Formlabs 1+™ 3D printer, and a fitting matrix of 4×4 low volume (2 mL) resin tanks (Figure 1a,b). This configuration was chosen to maximize the number of resin tanks within the dimensions of the 3D printer, however, if a larger number of resins need to be screened or larger 3D objects are desired, the dimensions and distribution of the tanks and platforms can be adapted to the target configuration (Figure S1). The adaptors were produced using either a polypropelene (PP) or acrylonitrile/butadiene/styrene (ABS) filament in a Makerbot Replicator 2x™ 3D printer. The 4×4 matrix resin tanks were designed to be 25 × 25 × 6 mm each and were fixed onto a Z-vat resin tank using hot melt adhesives from Ad Tech™. To facilitate peeling of the printed layers, the tanks were coated with a 3 mm polydimethylsiloxane (PDMS) layer (Sylgard®184 silicone elastomer. To complete the HTB, an aluminum metal plate was added to the 4×4 matrix containing the build platforms to ensure adhesion of the 3D printed objects (Figure 1c).

Tuning the hydrophobicity of 3D printed materials of 3D printed resins

To tailor the hydrophobicity of the 3D printed architectures, we produced a library of resins that included acrylate esters of varying chain lengths and branching, and mono- and di-allylamines in different mole ratios with respect to acrylic acid in the range 0.05 to 0.7. Screening was performed by 3D printing hollow cubes (7 mm sides, Figure S11) of the test resins in the 4×4 HTB array (add picture of an array having the cubes). The hydrophobicity was assessed by measuring the water contact angles on the 3D printed cubes (Figure S2-S10). The parent resin contained only acrylic acid and PEGDA had a water contact angle of 42º, characteristic of a hydrophilic surface.

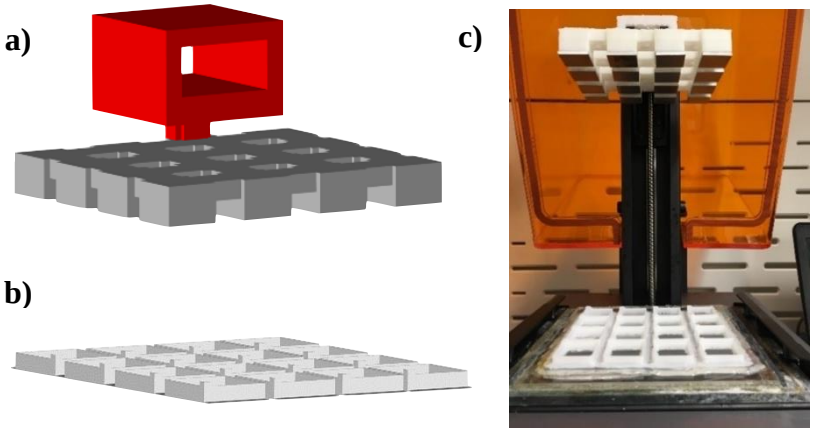

Figure 1. STL design of a) build platform, b) resin tanks and c) complete set up for high throughput screening

Tuning the hydrophobicity of 3D printed materials of 3D printed resins

To tailor the hydrophobicity of the 3D printed architectures, we produced a library of resins that included acrylate esters of varying chain lengths and branching, and mono- and di-allylamines in different mole ratios with respect to acrylic acid in the range 0.05 to 0.7. Screening was performed by 3D printing hollow cubes (7 mm sides, Figure S11) of the test resins in the 4×4 HTB array (add picture of an array having the cubes). The hydrophobicity

was assessed by measuring the water contact angles on the 3D printed cubes (Figure S2-S10). The parent resin contained only acrylic acid and PEGDA had a water contact angle of 42º, characteristic of a hydrophilic surface.

The incorporation of linear acrylate esters resulted in a moderate increase in the contact angles (about 60 ° at about 0.1 molar ratios), While little variations were observed in the contact angles of esters with chains in the C_4 to C_{12} range, a significant increase (about 80 ° at 0.1 molar ratio) was observed when using a C_{18} ester (Figure 2a). In general, the water contact angles of the 3D printed materials displayed a linear dependence on the amount of ester included in the resin. This dependence can be understood in terms of surface density of hydrophobic groups. Assuming a homogeneous distribution of groups, the longer the hydrocarbon is, the more surface it should cover, while short chains can leave unprotect carboxylates exposed to create more hydrophilic domains. Interestingly, analysis of the ratio slopes of the different C_n over C_4 revealed a correlation in C_4:C_6, C_4:C_{12}, C_4:C_{18}. For instance, the ratio between the carbon length is 1.5, 3, and 4.5 respectively, while the ratio of the slopes is 1.5, 4.5 and 11. This non-linear increment in the ratio suggests that the increasing hydrophobicity within the 3D printed sample is not only controlled by the length of the alkyl chain, but also by the density of alkyl groups. These differences in group densities might be attributed to the formation of micelles, which is more favorable at lower concentrations for longer alkyl chains.

Analysis of the water contact angles of the cubes 3D printed with branched acrylate monomers indicates a more dramatic effect on surface hydrophobicity. First, much higher water contact angles were achieved: isobutyl acrylate, 2-ethylhexyl acrylate and isodecyl acrylate reaching maximum contact angles of 93°, 102° and 117° respectively. Second, no

plateauing was observed: hydrophobicity kept increasing until the solubility limit of the ester precursors was reached (0.4 to 0.6 mole ratios). Following the idea of micelles formation when linear alkyl acrylates are used, it has been shown by Nave et al. that the critical micelle concentration (CMC) of branched monomers is lowered compared to their linear analoges.[27] The formation of micelles can affect the distribution of hydrophobic groups, having a bigger impact on the hydrophobicity of the surface.

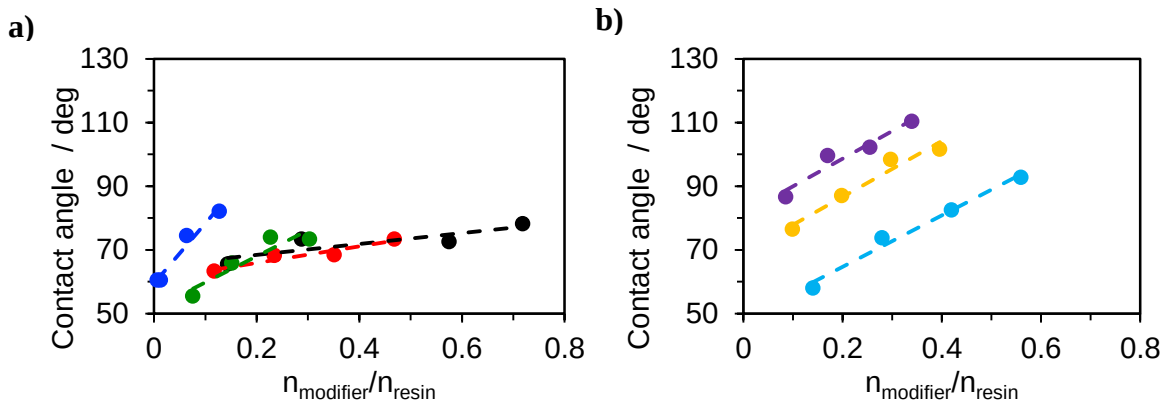

Figure 2. Change in contact angle depending on the number of moles of non-polar acrylates used in the resin composition for a) linear chains (black = butyl acrylate, red = hexyl acrylate, green = lauryl acrylate, and blue = octadecyl acrylate) and b) branched chains (light blue = isobutyl acrylate, yellow = 2-ethylhexyl acrylate, and purple = isodecyl acrylate)

While incorporation of acrylate esters to the resin resulted in more hydrophobic surfaces of the 3D printed objects, the use of allyl and diallylamine increased the hydrophilicity of the parent resin producing water contact angles of 21º and 24º respectively. This enhancement in the hydrophilicity of the 3D printed cubes can be understood in terms of the capacity of the co-polymerized amine groups to undergo acid-base reactions with the acrylic acid co-monomers resulting in a zwitterionic surface (Figure 3). The small difference in contact angles should be due to the higher carbon content and lower polarity of diallylamine than allylamine.

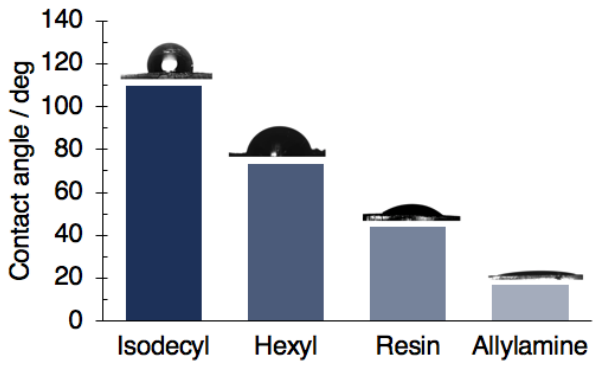

Figure 3. Variations in the wetting properties of 3D printed resins as a function of the co-monomer included in its composition.

An alternate approach to modify the surface hydrophobicity of a 3D printed AA resin is by reacting the pendant carboxylic acids with alcohols or amines. We evaluated this post-printing modification approach via carbodiimide coupling with isopropyl, *tert*-butyl and oleyl amines. The coupling was confirmed by FTIR (Figure 4a), were the characteristic amide I and amide II peaks were observed at 1550 cm^{-1} and 1630 cm^{-1}, respectively. Even though the same amounts of amine were added to the 3D printed cubes, FTIR showed large differences between the relative peak intensities of the samples. For instance, when no groups were reacted the ratio between the peak at 1720 cm^{-1} (corresponding to the carbonyl peaks from acrylic acid and PEGDA) and 1550 cm^{-1} (amide I) was ca. 125. While in the case of *tert*-butylamine and isopropylamine the ratio went down to ca. 0.01. Nonetheless, for oleylamine the ratio decreased to ca. 4.7. This suggest that the grafting of oleylamine is less efficient than the short chain amines. Nevertheless, the oleylamine modified cubes produced a significantly larger water contact angle (120º) than those modified with isopropylamine and *tert*-butylamine (89º and 72º, respectively). The hydrophobicity achieved through these methods is higher compared to the surface from the linear alkyl chain analogue (C_{18}). This

difference can be rationalized with a variation in group distribution. Considering that the main component of the 3D printed material is acrylic acid and that we are using those pendant groups, the amount of hydrophobic domains should increase using the post-printing modification. In this method, the surface coverage would be limited by the amount of acrylic acid present in the resin and not by the solubility or printability of the hydrophobic monomers.

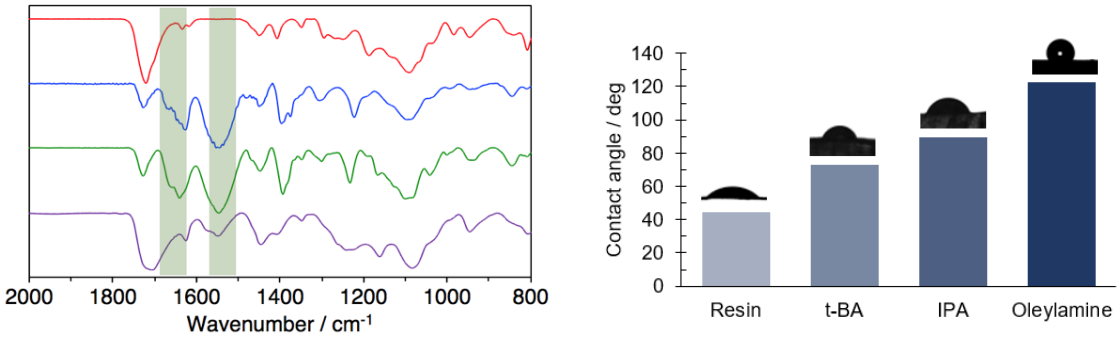

Figure 4. a) ATR-FTIR of 3D printed samples before (red) and after grafting with *tert*-butylamine (blue), isopropylamine (green) and oleylamine (purple). b) Effect on the water contact angle with the post-printing modification of 3D printed surfaces with non-polar groups. t-BA = t-butylamine, IPA = isopropylamine

High throughput 3D printing of metal catalysts of 3D printed resins

We have recently demonstrated that 3D printing can be used to produce architectures with intrinsic catalytic activity. Here, we explored 21 metal salts as potential precursors for 3D printed catalysts. First, we dissolved the salts (0.11 mmol) in a PEGDA and acrylic acid resin (5 mL resin, 11.6 and 204 mmol respectively). The resins were then 3D printed to form hollow cubes (7 mm with 1 mm wall thickness) using the HTB adaptor. The products designated as M-HC, were M represents the metal used. The hollow cubes were intended to provide a large surface to bulk ratio for the 3D printed catalysts. This would maximize

catalyst exposure because the polymeric matrix has low porosity and a penetration depth limited to ca. 70 µm.[28, 29] Of the metal salts tested, only 16 were soluble in the resin and could be 3D printed (Table 1, Figure S12). 3D printing of the metal-containing resins required optimization of printing parameters due to the varying optical properties resulting from the UV-visible absorbance of the metals. In general, optimized parameters included a laser power of 62 mW, and 5 laser passes per layer (compared to 2 laser passes for the normal resin). Interestingly, heating of the 3D printed Ag-HC and Au-HC at 40 ˚C for 1h led to a change in their colors from clear to brown and purple, respectively. These changes in color can be attributed to the formation of nanoparticles, as previously reported by Fantino et al.[30-32] and Chibac et al.[33] No changes in appearance were observed for the remaining M-HC.

Table 1. Screening of 3D printable resins and their catalytic activity in the oxidation of benzyl alcohol to benzaldehyde.

Metal Salts	Soluble	Active in oxidation	Metal Salts	Soluble	Active in oxidation	Metal Salts	Soluble	Active in oxidation
$AuCl_3$	Yes	No	$Er(NO_3)_3$	Yes	**Yes**	$Mn(OAc)_2$	Yes	No
$Ag(OAc)_2$	Yes	No	$Fe(C_5H_7O_2)_3$	Yes	No	$Ni(NO_3)_2$	Yes	**Yes**
$Bi(NO_3)_3$	Yes	No	GaP	No	No	$Nd(NO_3)_3$	No	No
$Ce(NO_3)_3$	Yes	**Yes**	GdCl3	No	No	$PdCl_3$	Yes	No
$Co(NO_3)_2$	Yes	No	$In(OAc)_2$	No	No	$SbCl_3$	Yes	No
$CrCl_3$	Yes	No	$IrCl_3$	Yes	No	$Yb(NO_3)_3$	No	No
$Cu(OAc)_2$	Yes	**Yes**	MgI_2	Yes	No	$Zn(NO_3)_2$	Yes	**Yes**

The M-HC were then screened for catalytic activity in the aerobic oxidation of benzyl alcohol. The selective oxidation of alcohols to carbonyls is an important reaction due to the ubiquity of these functionalities in active principles common in the pharmaceutical, perfume, dye, and agrochemical industries. Nonetheless, these oxidation reactions are usually catalyzed by toxic oxidizing agents (e.g. DMSO coupled reagents, hypervalent iodine

complexes or heavy metal reagents) and large amounts of organic solvents.[28, 29] Consequently, supported transition metals have been investigated as potential catalysts for this transformation with the aim of conducting a greener process.

To screen for potential catalytic activity in the selective aerobic oxidation of alcohols the M-HC were added to a solution of benzyl alcohol (20 µL, 0.38 mmol) and TEMPO (12 mg, 0.076 mmol) in acetonitrile (1 mL) and heated to 100 °C for 6 h in a parallel reaction block (200 rpm). The screening indicated small activity of nickel(II), antimony(III) and zinc(II) M-HC as they gave detectable albeit low levels of product. Differently, copper(II), zinc(II), and erbium(III) H-MC produced benzaldehyde in quantitative amounts. The remaining M-HC did not show any catalytic activity under these reaction conditions. Since Cu-HC produced the highest levels of benzaldehyde in the screening, we used this metal for further 3D printing studies.

We then explored the production of complex geometries of Cu-based 3D printed catalysts and their performance in the oxidation reaction. To this end, we 3D printed in parallel a series of minimal surface constructs occupying the same space. The 3D printed structures were: Chmutov Octic, diamond-1, diamond-3, Gyroid, Schoen-I-6, Schoen-manta and a hyper cube (Figure 6). While these intricate geometries are too difficult to produce by conventional methods, 3D printing allows even to produce and modify them at any desired scale. The 3D surfaces were designed and scaled to an 8×8×8 mm cubic volume that fit a test tube leaving space for a magnetic stir bar. The oxidation of benzyl alcohol was carried out for 21 h at 100 °C and revealed differences in conversion between the 3D printed catalyst architectures. Plotting conversion versus the surface area of the structures (calculated with 3Dtool software™) indicated that all the structures had the same intrinsic activity (Figure 7),

and the differences in performance were mainly due to the amount of surface provided by the specific topology.

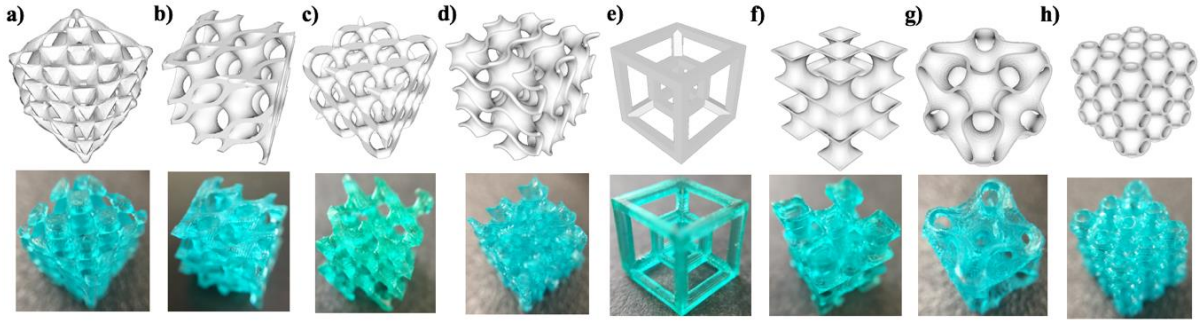

Figure 6. STL designs and optical images of the 3D printed intricate geometries. a) Chmutov Octic, b) diamond-1, c) diamond-3, d) Gyroid, e) Hyper cube, f) Schoen-I-6 g) Schoen-manta, and h) Schwarz P (primitive) minimal surfaces. All cubes are designed to have a 8 mm side

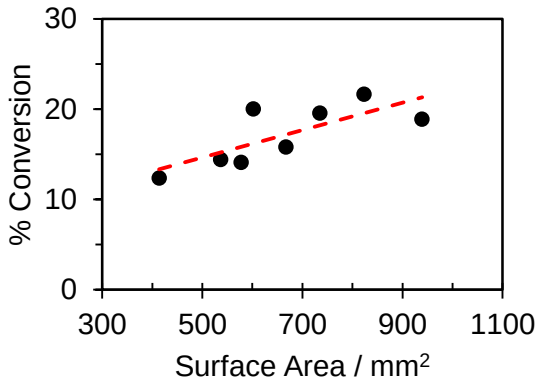

Figure 7. Correlation between surface are and catalytic activity using the Cu-containing complex geometries.

The metal-catalyzed aerobic oxidation of alcohols can be affected by the polarity of the solvent, in many cases non polar media has been shown to favor conversion.[34-36] Testing the performance of the intricate geometry with the highest activity Cu-Schoen-I-6 catalyst in three solvents of different polarities confirmed an inverse relationship between dielectric constant and benzyl alcohol conversion (Figure 8a). This dependence of conversion on polarity suggested that the performance of Cu-Schoen-I-6 could be improved by increasing

the hydrophobicity of the 3D printed material using the approaches described before. To this end, we prepared Cu-Schoen's-I-6 containing different type of alkyl acrylates to cover a wide range of hydrophobicity. To achieve contact angles of ca. 60, 80, 100, and 120, we used a $n_{modifier}/n_{resin}$ ratio of 0.14 for butyl acrylate, 0.12 octadecyl acrylate, 0.30 for 2-ethylhexyl acrylate and 0.33 for isodecyl acrylate, respectively.

The Cu-Schoen-I-6-materials were tested in the same benzyl alcohol oxidation reaction using acetonitrile as the reference solvent. This resulted in a similar trend observed with solvents with different dielectric constants (Figure 8b).

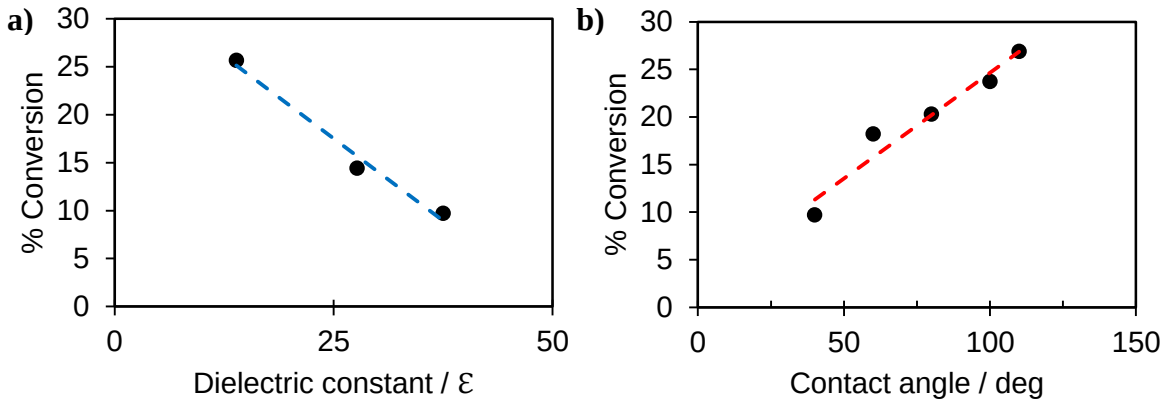

Figure 8. Catalytic activity of 3D printed geometries in a) solvents with increasing polarity, and b) using non-polar groups on the surface of the 3D objects. Reaction conditions: 2 mL acetonitrile, 0.15 mmol of TEMPO, and 0.38 mmol of benzyl alcohol stirred at 100 ºC for 21h.

Conclusions

This work presents a method to increase the throughput of commercial SLA 3D printers and enable screening of functional 3D printable resins. The high-throughput block (HTB) adaptors consisting of arrays of miniaturized build platforms and resin tanks can be custom designed and 3D printed to suit the needs of any target application. The approach proved useful for producing a series of 3D printed materials with varying surface hydrophobicites and allowed establishing structure-activity relationships to understand the

dependence of hydrophobicity on the molecular structure of monomers. While the hydrocarbon chain length of the acrylate esters increased the hydrophobicity of the 3D printed surfaces, chain branching resulted in a much larger effect. The difference between the influence of linear and branched chains can be rationalized in difference in solubility and micelle formation in the resin composition. The HTB was also useful to produce a series of 3D printed metal-organic composites that were screened as potential catalysts for the selective aerobic oxidation of benzyl alcohol. In addition, we used the HTB to 3D print a series of Cu-containing complex surfaces occupying a cubic space and demonstrated the dependence of catalytic conversion on the amount of surface that can be efficiently packed in a given volume. The Schoen-I-6 geometry gave the best catalytic activity, consistent with its highest surface area. Finally, because the activity of Cu-Schoen-I-6 for the aerobic oxidation of benzyl alcohol to benzaldehyde increases with decreasing solvent polarity, we modified the surface hydrophobicity of Cu-Schoen-I-6 with butyl acrylate, octadecyl acrylate, 2-ethylhexyl acrylate, isodecyl acrylate and tested their catalytic performance. Consistent with the reactivity trend observed in solvents of different polarity, the activity of Cu-Schoen-I-6 increased as the hydrophobicity of the material was enhanced. This result suggests that the surface properties of 3D printed catalysts can ultimately determine the behavior of the active sites, and therefore it is key to develop methods to control the surface chemistry of 3D printed materials.

Acknowledgements

This research is supported by the U.S. Department of Energy, Office of Basic Energy Sciences, Division of Chemical Sciences, Geosciences, and Biosciences, through the Ames Laboratory Catalysis Science program. The Ames Laboratory is operated for the U.S. Department of Energy by Iowa State University under Contract No. DE-AC02-07CH11358.

Supplemental Figures

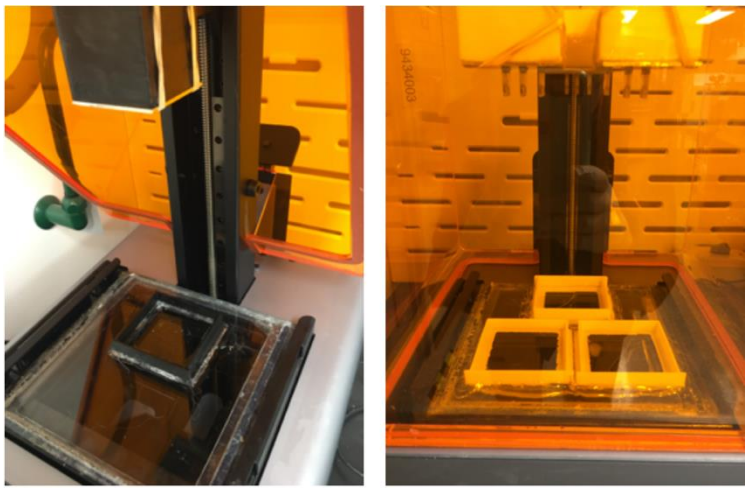

Figure S1. Different configurations for the miniaturized resin tanks. a) one 10 mL resin tank and b) 3 10 mL resin tanks.

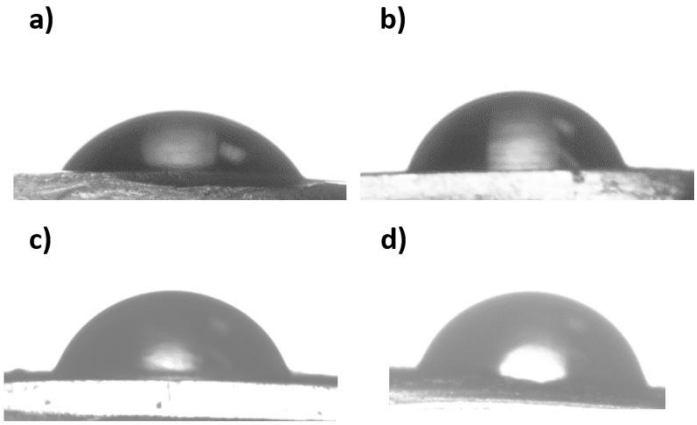

Figure S2. Water contact angle of 3D printed cubes using butyl acrylate as hydrophobic monomer. a) $n_{modifier}/n_{resin}$ = 0.14, b) $n_{modifier}/n_{resin}$ = 0.28, c) $n_{modifier}/n_{resin}$ = 0.57, and d) $n_{modifier}/n_{resin}$ = 0.72.

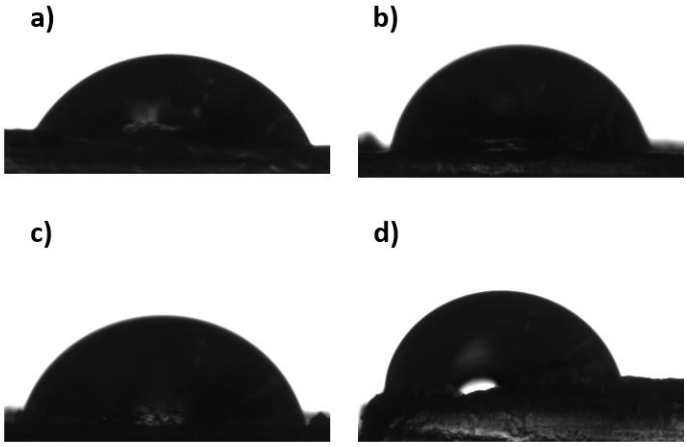

Figure S3. Water contact angle of 3D printed cubes using hexyl acrylate as hydrophobic monomer. a) $n_{modifier}/n_{resin}$ = 0.12, b) $n_{modifier}/n_{resin}$ = 0.23, c) $n_{modifier}/n_{resin}$ = 0.35, and d) $n_{modifier}/n_{resin}$ = 0.47.

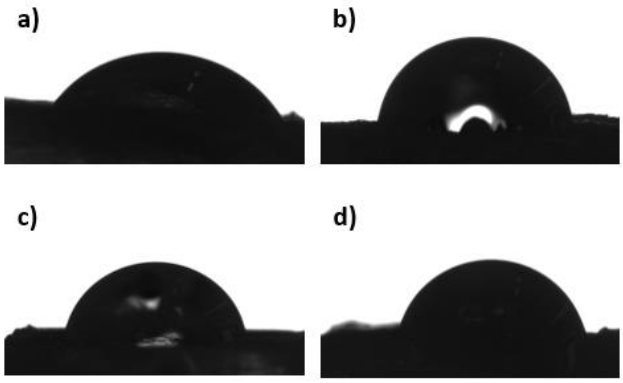

Figure S4. Water contact angle of 3D printed cubes using lauryl acrylate as hydrophobic monomer. a) $n_{modifier}/n_{resin}$ = 0.08, b) $n_{modifier}/n_{resin}$ = 0.15, c) $n_{modifier}/n_{resin}$ = 0.22, and d) $n_{modifier}/n_{resin}$ = 0.30.

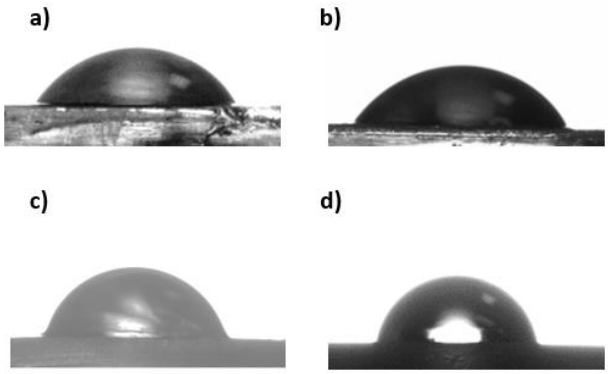

Figure S5. Water contact angle of 3D printed cubes using octadecyl acrylate as hydrophobic monomer. a) $n_{modifier}/n_{resin}$ = 0.08, b) $n_{modifier}/n_{resin}$ = 0.15, c) $n_{modifier}/n_{resin}$ = 0.22, and d) $n_{modifier}/n_{resin}$ = 0.30.

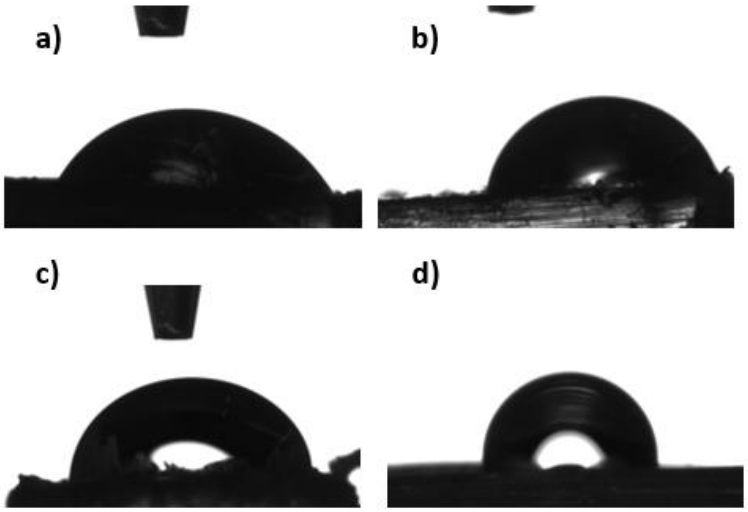

Figure S6. Water contact angle of 3D printed cubes using isobutyl acrylate as hydrophobic monomer. a) $n_{modifier}/n_{resin}$ = 0.08, b) $n_{modifier}/n_{resin}$ = 0.15, c) $n_{modifier}/n_{resin}$ = 0.22, and d) $n_{modifier}/n_{resin}$ = 0.30.

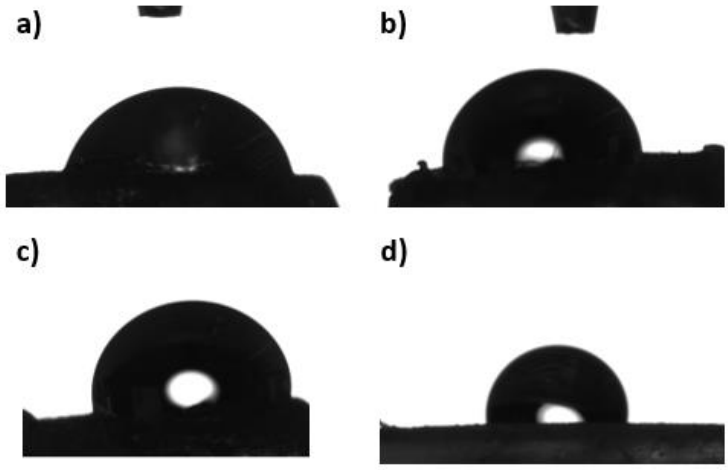

Figure S7. Water contact angle of 3D printed cubes using 2-ethylhexyl acrylate as hydrophobic monomer. a) $n_{modifier}/n_{resin}$ = 0.08, b) $n_{modifier}/n_{resin}$ = 0.15, c) $n_{modifier}/n_{resin}$ = 0.22, and d) $n_{modifier}/n_{resin}$ = 0.30.

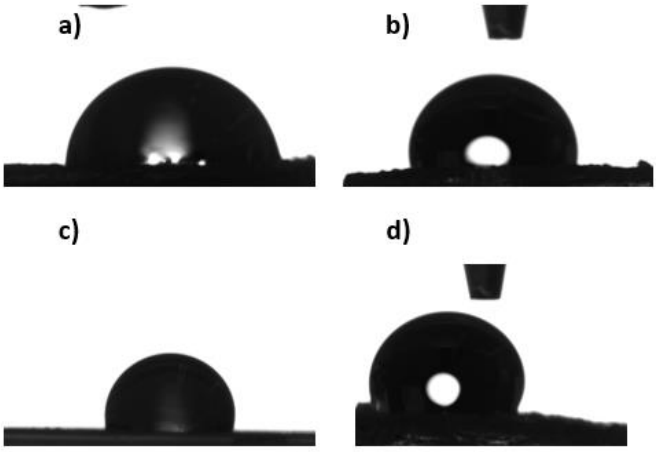

Figure S8. Water contact angle of 3D printed cubes using 2-ethylhexyl acrylate as hydrophobic monomer. a) $n_{modifier}/n_{resin}$ = 0.08, b) $n_{modifier}/n_{resin}$ = 0.15, c) $n_{modifier}/n_{resin}$ = 0.22, and d) $n_{modifier}/n_{resin}$ = 0.30.

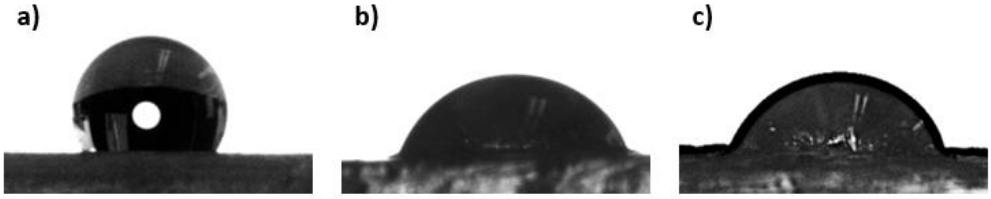

Figure S9. Water contact angle of 3D printed cubes grafted with a) oleylamine, b) isopropyl amine, and c) *tert*-butylamine.

Figure S10. Water contact angle of hydrophilic 3D printed cubes. a) parent resin, b) with allylamine, and c) with diallylamine.

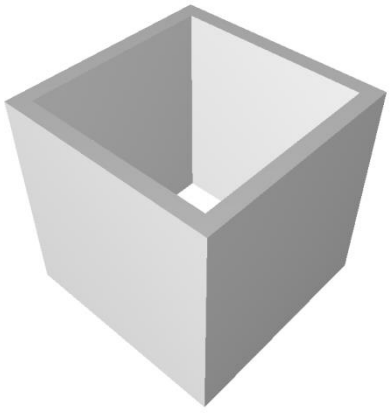

Figure S11. STL design of a 7 mm hollow cube use for screening surface and catalytic properties.

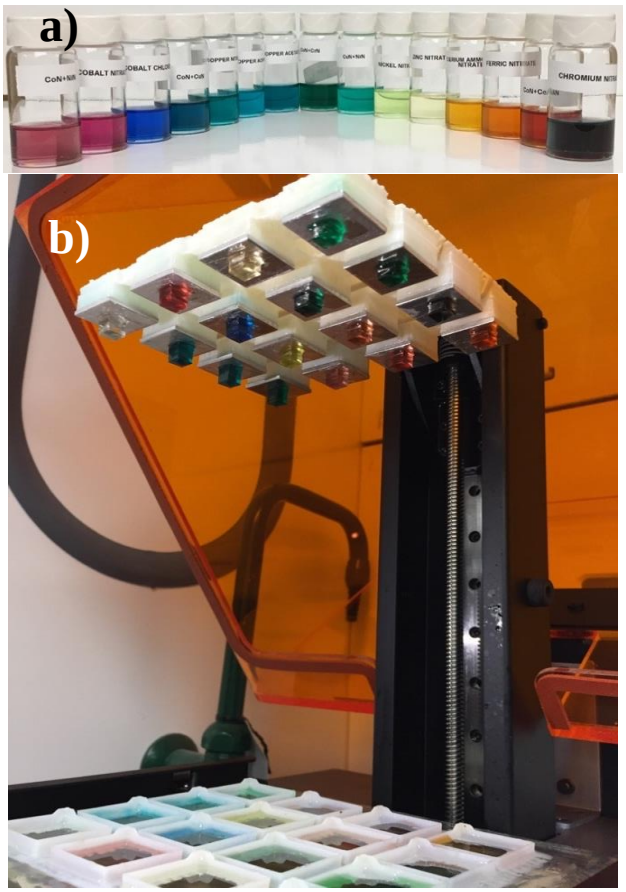

Figure S12. a) preparation and b) 3D printing of 16 different catalytic materials simultaneously.

References

1. Barry, R. A.; Shepherd, R. F.; Hanson, J. N.; Nuzzo, R. G.; Wiltzius, P.; Lewis, J. A., Direct-Write Assembly of 3D Hydrogel Scaffolds for Guided Cell Growth. *Advanced Materials* **2009,** *21* (23), 2407-2410.

2. Boland, T.; Xu, T.; Damon, B.; Cui, X., Application of inkjet printing to tissue engineering. *Biotechnology Journal* **2006,** *1* (9), 910-917.

3. Mohanty, S.; Larsen, L. B.; Trifol, J.; Szabo, P.; Burri, H. V. R.; Canali, C.; Dufva, M.; Emnéus, J.; Wolff, A., Fabrication of scalable and structured tissue engineering scaffolds using water dissolvable sacrificial 3D printed moulds. *Materials Science and Engineering: C* **2015,** *55*, 569-578.

4. Habibovic, P.; Gbureck, U.; Doillon, C. J.; Bassett, D. C.; van Blitterswijk, C. A.; Barralet, J. E., Osteoconduction and osteoinduction of low-temperature 3D printed bioceramic implants. *Biomaterials* **2008,** *29* (7), 944-953.

5. Ahn, B. Y.; Duoss, E. B.; Motala, M. J.; Guo, X.; Park, S.-I.; Xiong, Y.; Yoon, J.; Nuzzo, R. G.; Rogers, J. A.; Lewis, J. A., Omnidirectional Printing of Flexible, Stretchable, and Spanning Silver Microelectrodes. *Science* **2009,** *323* (5921), 1590-1593.

6. Smay, J. E.; Gratson, G. M.; Shepherd, R. F.; Cesarano, J.; Lewis, J. A., Directed Colloidal Assembly of 3D Periodic Structures. *Advanced Materials* **2002,** *14* (18), 1279-1283.

7. Tubío, C. R.; Azuaje, J.; Escalante, L.; Coelho, A.; Guitián, F.; Sotelo, E.; Gil, A., 3D printing of a heterogeneous copper-based catalyst. *Journal of Catalysis* **2016,** *334*, 110-115.

8. Tubío, C. R.; Guitián, F.; Gil, A., Fabrication of ZnO periodic structures by 3D printing. *Journal of the European Ceramic Society* **2016,** *36* (14), 3409-3415.

9. Cai, K.; Román-Manso, B.; Smay, J. E.; Zhou, J.; Osendi, M. I.; Belmonte, M.; Miranzo, P., Geometrically Complex Silicon Carbide Structures Fabricated by Robocasting. *Journal of the American Ceramic Society* **2012,** *95* (8), 2660-2666.

10. Rao, R. B.; Krafcik, K. L.; Morales, A. M.; Lewis, J. A., Microfabricated Deposition Nozzles for Direct-Write Assembly of Three-Dimensional Periodic Structures. *Advanced Materials* **2005,** *17* (3), 289-293.

11. Lewis, J. A., Direct Ink Writing of 3D Functional Materials. *Advanced Functional Materials* **2006,** *16* (17), 2193-2204.

12. Au, A. K.; Huynh, W.; Horowitz, L. F.; Folch, A., 3D-Printed Microfluidics. *Angewandte Chemie International Edition* **2016,** *55* (12), 3862-3881.

13. Ho, C. M. B.; Ng, S. H.; Li, K. H. H.; Yoon, Y.-J., 3D printed microfluidics for biological applications. *Lab on a Chip* **2015,** *15* (18), 3627-3637.

14. Waheed, S.; Cabot, J. M.; Macdonald, N. P.; Lewis, T.; Guijt, R. M.; Paull, B.; Breadmore, M. C., 3D printed microfluidic devices: enablers and barriers. *Lab on a Chip* **2016,** *16* (11), 1993-2013.

15. Kitson, P. J.; Rosnes, M. H.; Sans, V.; Dragone, V.; Cronin, L., Configurable 3D-Printed millifluidic and microfluidic 'lab on a chip' reactionware devices. *Lab on a Chip* **2012,** *12* (18), 3267-3271.

16. Dragone, V.; Sans, V.; Rosnes, M. H.; Kitson, P. J.; Cronin, L., 3D-printed devices for continuous-flow organic chemistry. *Beilstein J. Org. Chem.* **2013,** *9*, 951−959

17. Morin, S. A.; Shepherd, R. F.; Kwok, S. W.; Stokes, A. A.; Nemiroski, A.; Whitesides, G. M., Camouflage and Display for Soft Machines. *Science* **2012,** *337* (6096), 828-832.

18. Gross, B. C.; Erkal, J. L.; Lockwood, S. Y.; Chen, C.; Spence, D. M., Evaluation of 3D Printing and Its Potential Impact on Biotechnology and the Chemical Sciences. *Analytical Chemistry* **2014,** *86* (7), 3240-3253.

19. Goyanes, A.; Wang, J.; Buanz, A.; Martínez-Pacheco, R.; Telford, R.; Gaisford, S.; Basit, A. W., 3D Printing of Medicines: Engineering Novel Oral Devices with Unique Design and Drug Release Characteristics. *Molecular Pharmaceutics* **2015,** *12* (11), 4077-4084.

20. Compton, B. G.; Lewis, J. A., 3D-Printing of Lightweight Cellular Composites. *Advanced Materials* **2014,** *26* (34), 5930-5935.

21. Manzano, J. S.; Weinstein, Z. B.; Sadow, A. D.; Slowing, I. I., Direct 3D Printing of Catalytically Active Structures. *ACS Catalysis* **2017,** *7* (11), 7567-7577.

22. Díaz-Marta, A. S.; Tubío, C. R.; Carbajales, C.; Fernández, C.; Escalante, L.; Sotelo, E.; Guitián, F.; Barrio, V. L.; Gil, A.; Coelho, A., Three-Dimensional Printing in Catalysis: Combining 3D Heterogeneous Copper and Palladium Catalysts for Multicatalytic Multicomponent Reactions. *ACS Catalysis* **2018,** *8* (1), 392-404.

23. Konarova, M.; Aslam, W.; Ge, L.; Ma, Q.; Tang, F.; Rudolph, V.; Beltramini, J. N., Enabling Process Intensification by 3 D Printing of Catalytic Structures. *ChemCatChem* **2017,** *9* (21), 4132-4138.

24. Zhou, X.; Liu, C.-j. C., Three-dimensional Printing for Catalytic Applications: Current Status and Perspectives. *Advanced Functional Materials* **2017,** *27* (30), 1701134-n/a.

25. Bartolo, P., *Stereolithography Materials, Processes and Applications*. Springer: 2011.

26. Louzao, I.; Koch, B.; Taresco, V.; Ruiz-Cantu, L.; Irvine, D. J.; Roberts, C. J.; Tuck, C.; Alexander, C.; Hague, R.; Wildman, R.; Alexander, M. R., Identification of Novel "Inks" for 3D Printing Using High-Throughput Screening: Bioresorbable Photocurable Polymers for Controlled Drug Delivery. *ACS Applied Materials & Interfaces* **2018**.

27. Nave, S.; Eastoe, J.; Penfold, J., What Is So Special about Aerosol-OT? 1. Aqueous Systems. *Langmuir* **2000,** *16* (23), 8733-8740.

28. Uyanik, M.; Ishihara, K., Hypervalent iodine-mediated oxidation of alcohols. *Chemical Communications* **2009,** (16), 2086-2099.

29. Ciriminna, R.; Pandarus, V.; Béland, F.; Xu, Y.-J.; Pagliaro, M., Heterogeneously Catalyzed Alcohol Oxidation for the Fine Chemical Industry. *Organic Process Research & Development* **2015,** *19* (11), 1554-1558.

30. Fantino, E.; Chiappone, A.; Calignano, F.; Fontana, M.; Pirri, F.; Roppolo, I., In Situ Thermal Generation of Silver Nanoparticles in 3D Printed Polymeric Structures. *Materials* **2016,** *9* (7), 589.

31. Taormina, G.; Sciancalepore, C.; Bondioli, F.; Messori, M., Special Resins for Stereolithography: In Situ Generation of Silver Nanoparticles. *Polymers* **2018,** *10* (2), 212.

32. Sciancalepore, C.; Moroni, F.; Messori, M.; Bondioli, F., Acrylate-based silver nanocomposite by simultaneous polymerization–reduction approach via 3D stereolithography. *Composites Communications* **2017,** *6*, 11-16.

33. Chibac, A. L.; Melinte, V.; Buruiana, T.; Mangalagiu, I.; Buruiana, E. C., Preparation of photocrosslinked sol-gel composites based on urethane-acrylic matrix, silsesquioxane sequences, TiO2, and Ag/Au Nanoparticles for use in photocatalytic applications. *Journal of Polymer Science Part A: Polymer Chemistry* **2015,** *53* (10), 1189-1204.

34. Singappuli-Arachchige, D.; Manzano, J. S.; Sherman, L. M.; Slowing, I. I., Polarity Control at Interfaces: Quantifying Pseudo-solvent Effects in Nano-confined Systems. *ChemPhysChem* **2016,** *17* (19), 2982-2986.

35. Chen, Y. X.; Qian, L. F.; Zhang, W.; Han, B., Efficient Aerobic Oxidative Synthesis of 2-Substituted Benzoxazoles, Benzothiazoles, and Benzimidazoles Catalyzed by 4-Methoxy-TEMPO. *Angewandte Chemie* **2008,** *120* (48), 9470-9473.

36. Shi, S.; Liu, M.; Zhao, L.; Wang, M.; Chen, C.; Gao, J.; Xu, J., Catalytic Oxidation of Alcohol to Carboxylic Acid with a Hydrophobic Cobalt Catalyst in Hydrocarbon Solvent. *Chemistry – An Asian Journal* **2017,** *12* (18), 2404-2409.

CHAPTER 5. KINETICS OF THE FUNCTIONALIZATION OF MESOPOROUS SILICA NANOPARTICLES WITH ORGANOTRIALKOXYSILANES

J. Sebastián Manzano[1,2], Hsin Wang[1,2], Takeshi Kobayashi[1,2], Marek Pruski[1,2], Igor I. Slowing[1,2]

[1]US DOE Ames Laboratory, Ames, Iowa 50011, United States

[2]Department of Chemistry, Iowa State University, Ames, Iowa 50011, United States

ABSTRACT

Mesoporous silica nanoparticles (MSN) are materials with high surface areas, and controllable pore sizes and particle morphologies. Functionalizing the surface of MSN with organic moieties enables their use in a wide range of applications (e.g. catalysis, drug delivery, adsorption, etc.). Controlling and understanding the functionalization process is critical for the rational design of hierarchical MSN-based hybrid materials. In this work, we study the post-synthesis modification (grafting) of MSN with organotrimethoxysilanes (R-TMS) via *in situ* ^{1}H NMR spectroscopy. Grafting involves an adsorption/desorption equilibrium prior to the reaction of R-TMS with the surface silanols. A concentration dependence study of 3-aminopropyltrimethoxysilane (AP-TMS) grafting reveals a behavior akin to substrate-inhibition. Analysis of methanol production rates shows a significantly higher grafting rate in AP-TMS compared to other R-TMS, due to a catalytic effect of the amino group. This effect was used to control the grafting rates of other R-TMS by adding amines with different pK_a. Solid-state NMR (SSNMR) studies revealed that use of amine additives can also control the distribution of the grafted species on the surface of MSN.

Introduction

Mesoporous silica nanoparticles (MSN) are versatile platform materials that combine high surface areas (~ 1000 m^2 g^{-1}) and accessible pores (controllable widths in the 2-30 nm

range) with a highly tunable surface chemistry. Modification of their surface is performed using organosilanes either during synthesis by *co-condensation*,[1, 2] or post-synthesis via *grafting* i.e. reaction of silazanes, halo- or alkoxy-silanes with the surface silanols.[3-5] Post-synthesis *grafting* is the most commonly used method to produce hybrid organic/inorganic materials.

The facile functionalization of MSN surface has proven key to their application in several areas including adsorption,[6-8] drug delivery[9-15] and catalysis.[16-21] For example, the grafted organic groups can tune the adsorption/desorption equilibria of molecular guests by establishing specific interactions, act as molecular machines that regulate the release of active molecules stored inside the pores, modulate interfacial polarity in MSN suspensions, or tune the activity of supported catalysts by inducing cooperativity.[22-27] To maximize the performance of the grafted groups in these applications it is crucial to regulate their surface distribution.[28-31] Such regulation could be facilitated by controlling the kinetics of grafting. Surprisingly, to the best of our knowledge, there are no studies of the grafting kinetics of organosilanes on MSN, and of how the nature of the organic groups affects the rates of functionalization. Obtaining kinetic information of this process would be critical to better understand its mechanism and enable a rational design of increasingly complex hybrid organic-inorganic mesoporous materials.

In this work, we used solution ^{1}H NMR spectroscopy to study the grafting kinetics of a series of organotrialkoxysilanes and assessed the role of organic functionalities on the grafting process. We determined the limitations imposed by adsorption and desorption on the reaction kinetics, and how they determine its mechanism, and used this understanding to explain how catalytic species can regulate the surface distribution of grafted groups.

Experimental

Materials

Hexadecyltrimethylammonium bromide (CTAB), Tetrakis(trimethylsilyl)silane (TMSS), methyl isothiocyanate, pyrrolidine, morpholine, and aniline were purchased from Sigma-Aldrich. Tetraethyl orthosilicate (TEOS), hexyltrimethoxysilane (H-TMS), 3-mercaptopropyltrimethoxysilane (MP-TMS), 3-aminopropyltrimethoxysilane (AP-TMS), 3-methoxypropyltrimethoxysilane (MeOP-TMS), and 3-cyanopropyltrimethoxysilane (CP-TMS) were purchased from Gelest, Inc. Sodium hydroxide (NaOH) and pyridine were purchased from Fisher Scientific. Benzene–d_6 (99.5 % D) was purchased from Cambridge Isotope Laboratories.

Synthesis of Mesoporous Silica Nanoparticles (MSN)

CTAB (5.10 g, 13.5 mmol) was dissolved in deionized water (2400 mL, 17.6 MΩ cm) in a 3-necked 5 L round bottom flask followed by addition of 2.0 M NaOH (17.5 mL, 35.0 mmol). The solution was stirred at 500 rpm for 1 h at 80 °C. TEOS (25.0 mL, 115 mmol) was then added drop wise using a syringe pump with a control rate of 150 mL h^{-1}. Overhead stirring was continued for another 2 h at 80 °C. The solution was filtered, washed with abundant water and methanol, and vacuum dried overnight. CTAB was removed by calcination at 550 °C for 6 h at a 2 °C min^{-1} rate. The prepared materials were stored under vacuum to minimize water exposure. XRD (Cu Kα radiation): 2θ (degrees) 2.37 (100), 4.27 (110) and 4.91(200). BET surface area: 1193 m^2 g^{-1}. BJH Pore volume: 0.97 cm^3 g^{-1}. BJH Pore size: 2.8 nm (distribution 2.12 - 3.40 nm) FTIR (KBr): 1082, 1627, 3741, 3643, 3435 cm^{-1} (Figure S1-S2). Surface silanol concentration: 4.56 mmol g^{-1}, determined by measuring the concentration of toluene produced in a titration with $Mg(CH_2Ph)_2(O_2C_4H_8)_2$[32, 33]

Characterization

The XRD pattern was recorded on a Bruker X–ray diffractometer using Cu Kα radiation (40 kV, 44 mA) over the range of 1–10 2θ degrees. Nitrogen sorption isotherms were measured in a Micromeritics Tristar surface area and porosity analyzer. The surface area and pore size distribution were calculated by the Brunauer Emmett Teller (BET) and Barrett Joyner Halenda (BJH) methods respectively. Transmission mode FTIR measurements were made on a Bruker Vertex80 FT-IR spectrometer equipped with a HeNe laser and photovoltaic MCT detector and OPUS software. Samples were mixed at ca. 2 wt% with KBr and pressed into pellets for analysis.

Blocking of amine groups

3-Aminopropyltrimethoxysilane (AP-TMS, 1.0 mL, 5.7 mmol) was mixed with methyl isothiocyanate (0.42 g, 5.7 mmol) and stirred at room temperature for 3 h resulting in a yellow solution. ^{1}H NMR (500 MHz, $CDCl_3$): δ (ppm) 0.55 (t, 2H), 1.60 (q, 2H), 2.59 (s, 3H), 3.26 (br, 2H), 3.40 (s, 9H).

Reaction kinetics

10.0 mg of MSN were added to a NMR tube. To this, 400 µL of a 9.97 mM solution of TMSS (internal standard) in benzene-d_6 was added. Then 400 µL of a 133 mM solution of the organotrimethoxysilane (AP-TMS, MP-TMS, CP-TMS, MeO-TMS, H-TMS or blocked AP-TMS, in general abbreviated as R-TMS) was added to the NMR tube, vortexed for 2 s and immediately inserted in the NMR. To explore effects of concentrations on rate, additional experiments were performed changing the concentrations of MP-TMS and AP-TMS in a range of 8 mM to 190 mM.

NMR measurements were performed using a Bruker 500MHz DRX FT-NMR spectrometer. The^{1}H NMR spectra were collected using 16 scans per kinetic data point. Data

points were collected every 5 min for 1 h. Ethylene glycol was used as a temperature probe. The temperature was calculated using the equation T = (4.637 - Δppm)/ 0.009967, where Δppm is the difference between the C**H**$_2$ and O**H** peaks (Bruker Instruments, Inc. VT-calibration manual).[34-36] The signal tracked for the consumption of R-TMS corresponds to the C**H**$_2$ next to the terminal functional group with a chemical shift of 1.54 ~ 2.54 ppm depending on the group, while the production of MeOH was tracked at 3.05 ppm.

Catalyzed grafting of 3-mercaptopropyltrimethoxysilane (MP-TMS)

For the catalyzed grafting of MP-TMS, 100 µL of a 52.8 mM solution of the respective amine (pyrrolidine, butylamine, morpholine, aniline, pyridine) were mixed with 300 µL of a 9.97 mM solution of TMSS in benzene-D6. Then 400 µL of a 133 mM solution of MP-TMS was added to the NMR tube, vortexed for 2 s and immediately inserted in the NMR.

Computational methods

All calculations were performed using the dispersion-corrected B3LYP-D3[37] method implemented in the GAMESS[38] package using the 6-311G(d,p) basis set. The different surfaces were optimized using the MCM-41 model developed by Ugliengo and collaborators.[39, 40] All of the models were optimized using the QM/MM SIMMOM[41] method implement in GAMESS.

Solid-state NMR

The ^{1}H SSNMR experiments were performed on a Varian NMR spectrometer, equipped with a 1.6 mm triple-resonance MAS probe and operated at 14.1 T. All experiments were performed under fast MAS at a rate of 36 kHz. The T_2^0 relaxation times of ^{1}H nuclei were measured using a spin-echo sequence without ^{1}H–^{1}H radio-frequency (RF) homonuclear decoupling.

Results and Discussion

Grafting of MSN is usually performed by reacting their surface silanols with organosubstituted silazanes, alkoxy- or chlorosilanes.[4, 6] Alkoxysilanes are the most common reactants for this process and yield alcohols as by-products. The produced alcohols can be used to monitor the reaction progress. For R-trimethoxysilanes (R-TMS, where R is the organic functionality of interest) each mole of reacted silane can yield between 1 and 3 equivalents of methanol (Scheme 1). This stoichiometry should translate into rate ratios of R-TMS disappearance to methanol formation ($r_{R\text{-}TMS}$:r_{MeOH}) ranging from 0.33 to 1 depending on the final podality of the organosilane on the surface.

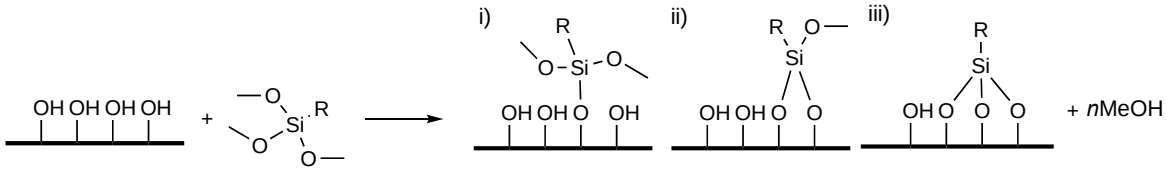

Scheme 1. Grafting of a R-TMS molecule onto the silica surface producing: i) monopodal, ii) bipodal or iii) tripodal organosilanes. Each alternative implies production of one, two or three equivalents of methanol, respectively.

Table 1. Initial rates of R-TMS consumption and MeOH production.[a]

	Observed			Corrected	
Organosilane	$r_{R\text{-}TMS}$ (mM min^{-1})	r_{MeOH} (mM min^{-1})	$r_{R\text{-}TMS}$: r_{MeOH}	$r_{0\text{-}MeOH}$ (mM min^{-1})	$r_{R\text{-}TMS}$: r_{MeOH}
AP-TMS	-0.7 ± 0.1	0.77 ± 0.09	0.87	1.95 ± 0.08	0.34
MP-TMS	-0.12 ± 0.01	0.017 ± 0.001	6.7	0.064 ± 0.002	1.9
CP-TMS	-0.075 ± 0.005	0.015 ± 0.001	5	0.057 ± 0.005	1.3
MeOP-TMS	-0.11± 0.007	0.0071 ± 0.0002	15	0.026 ± 0.002	4.2
Hex-TMS	-0.11± 0.02	0.003 ± 0.0001	32	0.013 ± 0.001	8.5

[a] Conditions: 10 mg MSN, 400 µL 133 mM of R-TMS in C_6D_6, 400 µL of 9.97 mM of TTMS in C_6D_6. The reaction was performed for 1h at 50 ºC.

First, we monitored the grafting of five different R-TMS (R: aminopropyl (AP), hexyl (Hex), methoxypropyl (MeO), cyanopropyl (CP), and mercaptopropyl (MP)) onto MSN by tracking the disappearance of the CH_2 peak in R (1.55-2.8 ppm) and the growth of the methyl peak of the produced methanol (3.05 ppm) in solution ^{1}H NMR (52.8 µmol R-TMS, 10.0 mg MSN, 800 µL C_6D_6, 50 °C, Figure S3-S7). Whereas the observed initial rates of R-TMS consumption ($r_{R\text{-}TMS}$) were very similar for four of the organic groups (Hex, MeO, CP, MP), their initial rates of MeOH production (r_{MeOH}) varied with the type of functionality. Furthermore, the $r_{R\text{-}TMS}$: r_{MeOH} ratios of all these R-TMS were much larger than one (Table 1), which is far off the expected from stoichiometry. In sharp contrast to these silanes, AP-TMS showed a significantly faster $r_{R\text{-}TMS}$ and a $r_{R\text{-}TMS}$: r_{MeOH} within the expected range.

(1) $\text{R-Si-(OMe)}_3 + \text{(HO)}_m\text{-(SiO}_2)_n \underset{k_{-1}}{\overset{k_1}{\rightleftharpoons}} \text{R-Si-(OMe)}_3\text{*}$

(2) $\text{R-Si-(OMe)}_3\text{*} + \text{(HO)}_m\text{-(SiO}_2)_n \xrightarrow{k_2} \text{R-Si-(O)}_3\text{(OH)}_{m-1}\text{(SiO}_2)_n + \text{MeOH*}$

(3) $\text{MeOH*} \underset{k_{-3}}{\overset{k_3}{\rightleftharpoons}} \text{MeOH} + \text{*}$

Scheme 2. Steps for the functionalization of mesoporous silica. * = adsorbed

Because of its heterogeneous nature, the grafting reaction is preceded by the adsorption of R-TMS on the MSN surface (step (1), Scheme 2). If R-TMS adsorption is slow it could potentially limit the reaction rate. However, since $r_{R\text{-}TMS}$: r_{MeOH} >> 1 for all R-TMS other than AP-TMS, the adsorption step is not rate limiting but likely a fast equilibrium that precedes the actual grafting reaction (step (2), Scheme 2). Thus, the large $r_{R\text{-}TMS}$: r_{MeOH} ratios can be explained by the R-TMS adsorption being much faster than the reaction between the adsorbed silane and the surface silanols. This assumption should be true as long as the methanol by-product is desorbed from the surface (step (3), Scheme 2) at a rate significantly

higher than the rate of the grafting reaction. In fact, addition of C_6D_6 to an NMR tube containing MeOH pre-adsorbed onto MSN (5.4 mg MeOH in 10.2 mg MSN and 800 mL C_6D_6) resulted in a burst release of 50 % of methanol to the solvent just 3 min after mixing (acquisition of the first NMR datapoint). Furthermore, the concentration of methanol did not change significantly over time, (Figure S8) indicating the equilibrium was reached quickly and the methanol desorption rate is greater or equal than 35.5 mM min^{-1}. Thus, the methanol desorption rate is at least 18 times larger than the r_{MeOH} observed during the grafting reactions. We can therefore conclude that the reaction rate is not limited by the R-TMS adsorption or methanol desorption rates, and that r_{MeOH} can be used as a measure of the reaction kinetics (step (2), Scheme 2).

However, since only part of the produced methanol is desorbed from MSN, the rate calculations need to be corrected to account for the fraction that remains adsorbed in equilibrium. To this end we measured methanol adsorption isotherms on MSN and fitted them to the Langmuir model[42] (equation 2) (10 mg of MSN in 800 µL C_6D_6).

$$q_{ads} = \frac{Q_M K_{eq}[MeOH]_{eq}}{1+K_{eq}[MeOH]_{eq}} \qquad (2)$$

Where Q_M is the maximum adsorption in mmol g^{-1}, K_{eq} is the equilibrium constant for the adsorption and $[MeOH]_{eq}$ is the equilibrium concentration of methanol. Analysis of the isotherm (Figure S9) allows calculating the amount of MeOH that remains adsorbed on the surface ($[MeOH]_{ads}$) as a function of the $[MeOH]_{eq}$ in solution, which is directly measured by ^{1}H NMR. Therefore, the total amount of methanol produced in the grafting reaction can be calculated using equation 3. It must be noted that at concentrations corresponding to those used in the grafting reactions (ca. 66 mM) most of the MeOH remains adsorbed on the surface of MSN.

$$[MeOH]_T = [MeOH]_{eq} + \frac{Q_M K_{eq}[MeOH]_{eq} m_{MSN}}{(1+K_{eq}[MeOH]_{eq})V} \quad (3)$$

Applying this correction to r_{MeOH} (Table 1) resulted in a $r_{R\text{-}TMS}$: r_{MeOH} of 0.34 for AP-TMS, which suggests most of the grafted molecules should be tripodal. In a scaled up experiment a 100 mg sample of MSN was reacted with 66 mM AP-TMS (10 mL in toluene at 50 °C, 1h). NMR analysis of the solution including the correction for the adsorbed methanol indicated the grafting of 2.38, 4.78 or 7.16 mmol g of AP-TMS depending on the podality of the groups. Elemental analysis of the washed and dried solid indicated a 3.84 % content of nitrogen, corresponding to a total of 2.74 mmol g^{-1} of AP grafted in the sample. This is consistent with groups grafted in a bipodal or tripodal fashion. The results are also consistent with the ^{29}Si CPMAS SS-NMR analysis of the material, which after 5 min of reaction already displayed only T^2 and T^3 sites (Figure S10).

Whereas the $r_{R\text{-}TMS}$: r_{MeOH} of MP-, CP-, MeOP- and H-TMS decreased when correcting for the adsorbed methanol, they all remained larger than one (Table 1). This result suggests that only a fraction of the adsorbed silane reacts at a given time. In other words, the rate of silane adsorption is larger than the rate of grafting. Because the $r_{R\text{-}TMS}$ were very similar for all R-TMS except for AP-TMS, the adsorption rates of these silanes must depend mainly on TMS rather than on the organic groups. Indeed, adsorption experiments of TMS-free organic molecules with the same functional groups (except for AP) at the same concentrations used in the grafting (66 mM in C_6D_6, 10 mg MSN) revealed less than 5 % adsorption over 15 min, suggesting that adsorption is controlled mainly by H-bond interactions between the C-O-Si moieties of TMS and the surface silanols.

Analysis of the corrected initial reaction rates (r'_{MeOH}, Table 1) and their kinetic traces (Figure 1) indicates a clear dependence of reactivity on the nature of the functional

groups. Whereas the r'_{MeOH} of AP-TMS is two orders of magnitude higher than the rest of the silanes, the differences between the rates of all the other groups are much smaller and decrease in the order MP-TMS > CP-TMS > MeOP-TMS > Hex-TMS. These rate differences suggest that secondary interactions between the functional groups and the silica surface may affect the reactivity between the adsorbed silane and the silanol groups. One possible interaction is the formation of H-bonds between an acceptor in the organic group and a silanol.

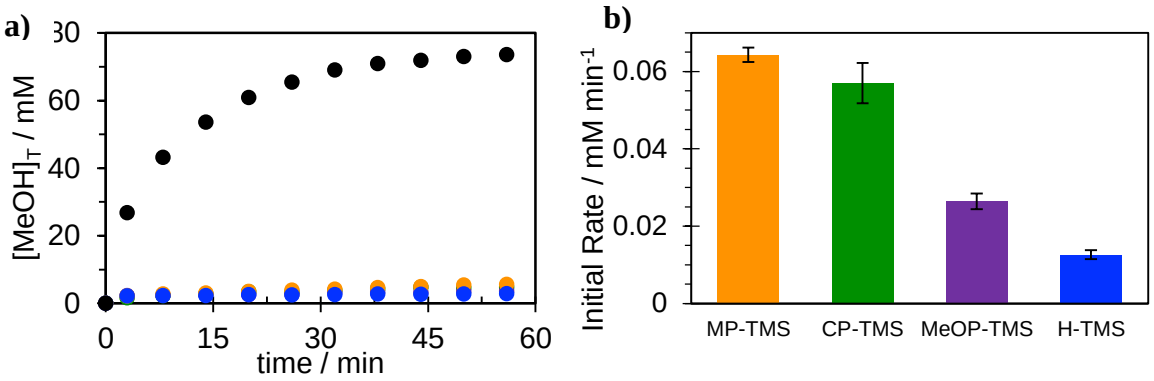

Figure 1. Plots of R-TMS over time respect to a) production of MeOH at 50 ºC b) Rate of R-TMS.

We performed DFT calculations to explore the potential interactions between the R-TMS and the silica surface. The surface was modeled using a silica slab developed by Ugliengo and collaborators,[39, 40, 43] and was optimized using the QM/MM SIMOMM[41] method implemented in GAMESS.[38] Interestingly, the same group suggested that London-dispersion forces can play an important role in the interaction of molecules with the surfaces of MSNs, therefore dispersion terms were included in the calculations.[43, 44] The calculated binding energies for the R-TMS correlated well with the observed r'_{MeOH}.(Figure 2).

Significant differences in the ratios of $r_{AP\text{-}TMS}$:r_{MeOH} are observed, suggesting that grafting of MeO-TMS and Hex-TMS is not as efficient as of CP-TMS or MP-TMS. Based on

the DFT calculations, these differences can be attributed to the contribution of dispersion forces to the silane-surface interaction, controlling the effectiveness of the grafting process.

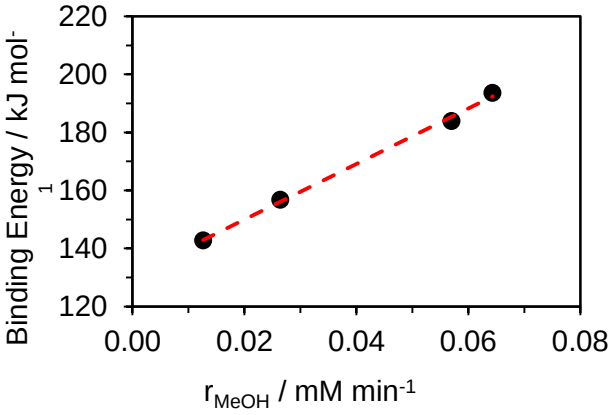

Figure 2. Correlation of DFT calculated binding energies with the initial rate of methanol evolution (r_{MeOH})

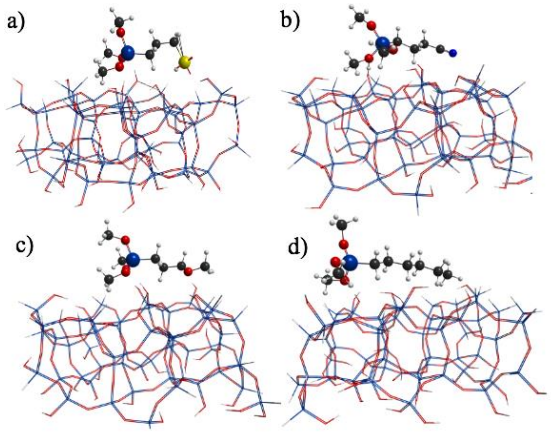

Figure 3. Optimized structures using the SIMOMM method for a) MP-TMS, b) CP-TMS, c) MeOP-TMS and d) H-TMS. The silica surface is shown as a wireframe structure for clarity.

A separate study revealed a non-linear dependence of initial reaction rate (r'_{MeOH}) on AP-TMS concentration (Figure 4a). Whereas r'_{MeOH} increased with the amount of AP-TMS in the low concentration regime (2.20 mM to 33.2 mM), higher concentrations resulted in a steady drop of r'_{MeOH}. The behavior can be described using a substrate-inhibition model.[45] Increasing concentrations of AP-TMS result in an increasingly saturated surface, where

molecular crowding in the adsorbed layer thwarts the alignment of the Si centers of the silane with the surface silanols, causing a decrease of the reaction rate. The mechanism can be described as in Scheme 3 and by the equation 4:

$$r_{MeOH} = \frac{V_{max}[\text{AP-TMS}]}{K_{eff}+[\text{AP-TMS}]\left(1+\frac{[\text{AP-TMS}]^n}{K_i}\right)} \quad (4)$$

Where V_{max} is the maximum r'_{MeOH}, K_{eff} represents the binding affinity of AP-TMS for MSN at concentrations below saturation and is analogous to the Michaelis-Menten constant, K_i is the binding affinity when an excess of AP-TMS is adsorbed to the surface, and n is the number of substrate molecules competing for a binding site during inhibition. The best fitting was obtained for n = 3 (Figure 4a).

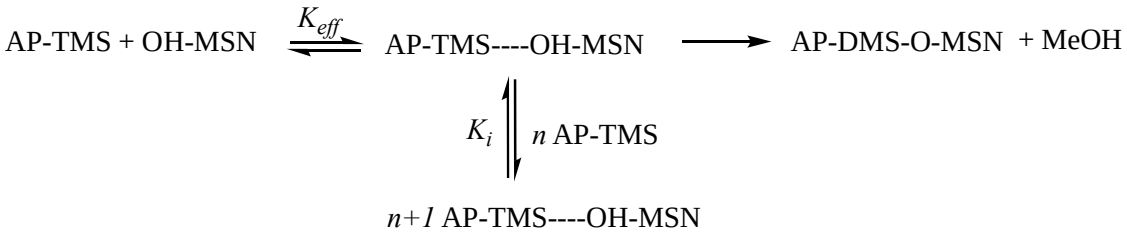

Scheme 3. Substrate inhibition mechanism for the grafting process of AP-TMS on MSN. AP-DMS (3-aminopropyldimethoxysilane grafted on the silica surface).

For reactions under flooding conditions (i.e. when the amount of Si-OH is 10 or more times larger than the amount of AP-TMS) the dependence of r'_{MeOH} on [AP-TMS] is linear (R^2 0.98). The log([AP-TMS])-log(r'_{MeOH}) plot of the linear range indicates a second-order dependence on [AP-TMS] (Figure 4b). The Eyring plot of the temperature dependence study (Figure 4c) indicates a negative $\Delta S^{\ddagger}$ (-238 ± 180 J K^{-1} mol^{-1}) further confirming the reaction takes place through an associative mechanism, where two AP-TMS molecules participate in the transition state.

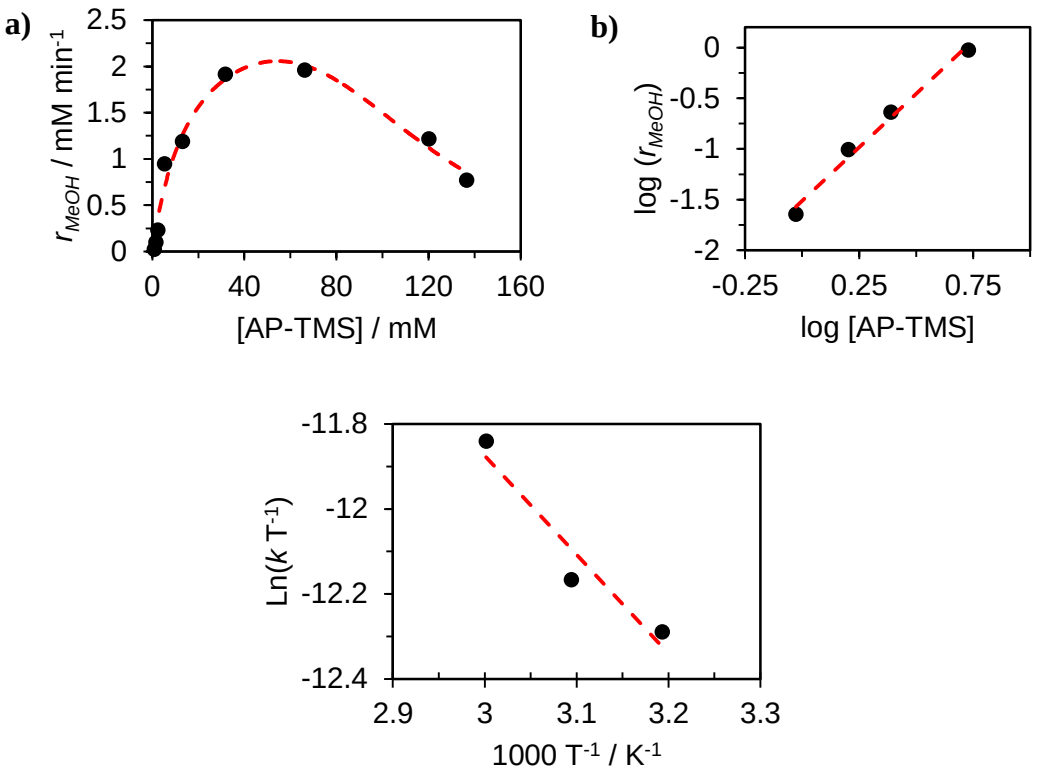

Figure 4. a) Rate of MeOH production vs [AP-TMS], b) log-log plot of the linear region of a), and c) Eyring plot of the AP-TMS grafting reaction.

The second order dependence of r'_{MeOH} on [AP-TMS] may be explained as one AP-TMS molecule activating the other AP-TMS for the reaction. The amine groups in the activating AP-TMS could behave either as Brønsted bases assisting the deprotonation of a surface silanol to enhance its nucleophilicity, or as Lewis bases binding the Si center in the grafting AP-TMS molecule to enhance its electrophilicity. Both of these proposed mechanisms require significant molecular organization on the MSN surface, which explains the strong negative effect of surface saturation on r'_{MeOH} (i.e. the substrate inhibition behavior).

Because the catalytic action of the amine groups is hypothesized to depend on their basic character, one can expect that blocking them should decrease reaction rates. We tested this hypothesis by reacting AP-TMS with methyl isothiocyanate to produce the

corresponding thiourea-modified silane. Grafting of the blocked AP-TMS onto MSN resulted in a r'_{MeOH} 47 times slower than the parent AP-TMS (0.041 mM min^{-1}, 50 ºC, 66 mM). In fact, the r'_{MeOH} of the blocked silane is comparable to that of other MP-TMS, which further supports the idea that the amino groups are responsible for the higher grafting rates of AP-TMS. Conversely, addition of catalytic amounts of butylamine increases five times the r'_{MeOH} of MP-TMS. Furthermore, grafting MP-TMS in presence of different amines reveals a linear relationship between the log(r'_{MeOH}) and the pK_a of the amines, strongly suggesting the catalytic action of the amines is due to their basicity (Figure 5a).

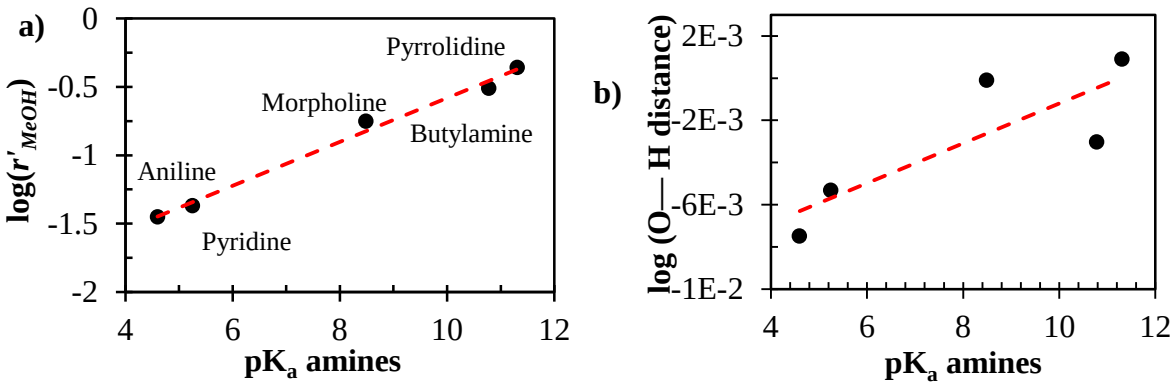

Figure 5. Effect of amine additives in the grafting rate of MP-TMS. a) correlation between the observed rate and the pK_a of the respective additives. b) correlation between the calculated O—H distance (in silanols) and the pK_a of the amines.

DFT models of the amines adsorbed on the silica surface also indicate that the O—H distances in silica increase with the pK_a of the amines (Figures 5b, S12-S16). As the O—H distance increases, the O is more prone to perform a nucleophilic attack on R-TMS. Similar behaviors have been observed in a homogenous analogue for the silylation of alcohols.[46-48]

Nevertheless, rather than increasing r'_{MeOH} aniline and pyridine lead to a drop in the grafting rate of MP-TMS. Because the pK_a of these amines is lower than that of silanol groups (4.9 – 8.5),[49, 50] they are not able to activate the O—H bonds and may instead

compete with MP-TMS for adsorption sites. If this is the case, the presence of these amines in the reaction media should affect the distribution of grafted MP-TMS. To test this hypothesis, we studied the spatial distribution of MP-TMS grafted on MSN using double-quantum/single-quantum (DQ/SQ) homonuclear ^{1}H solid-state NMR correlations. Analysis of the 2D correlation spectra of materials grafted using aniline, morpholine and pyrrolidine as additives revealed significant differences between the intensities of the thiol proton cross peaks (Figure 6). The intensities of the thiol proton cross peaks relative to their corresponding α protons (which are more intense due to the self-correlation of the two equivalent protons attached to the α C) serves as an indicator of the average distance between two thiol groups.[51] The observed drop in intensities aniline > morpholine > pyrrolidine indicates that the slower reactions result in more isolated groups and the faster grafting rates lead to silane clustering. Whether this behavior is due to competitive adsorption between MP-TMS and the weaker amine bases or to the reaction kinetics remains unknown.

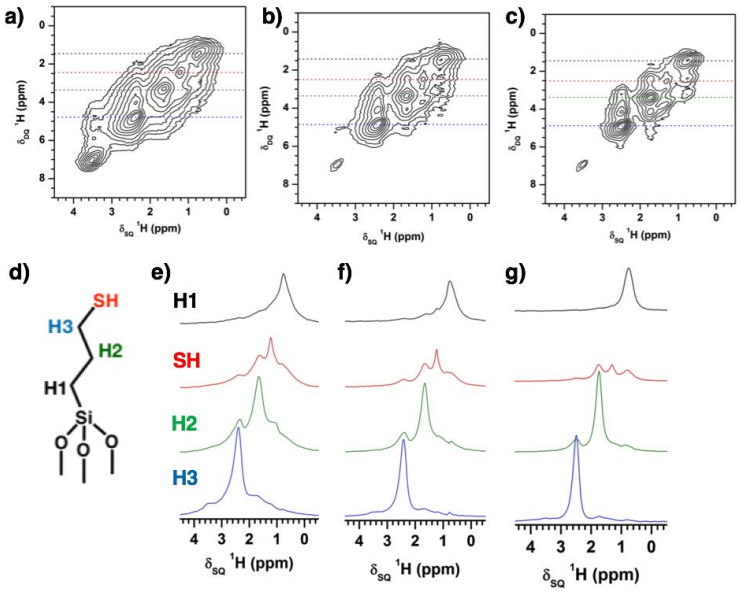

Figure 6. 2D 1H DQ experiments for a) pyrrolidine, b) morpholine, c) aniline. d) signal labeling for MP-TMS. Proton slices for e) pyrrolidine, f) morpholine and g) aniline.

Conclusion

In summary, the kinetics of surface modification of mesoporous silica nanoparticles is presented. The nature of the organic groups controls the rate of reaction, where the more polar groups (e.g. CP-TMS and MP-TMS) react faster that non-polar groups (e.g. MeO-TMS and Hex-TMS). Differently, AP-TMS revealed a reaction rate 30 times higher than the other R-TMS groups. This behavior was studied by performing a concentration dependence study, where a substrate inhibition like behavior was observed at concentrations higher than 32 mM. A log-log plot of the linear portion of this graph revealed a second-order mechanism. The participation of two molecules of AP-TMS can be attributed to a catalytic effect in the deprotonation of the surface silanols. This catalytic property was used to increase the rate of reaction of MP-TMS using different amines with various pKa values. This showed a linear correlation between the rate and the pKa of the respective amines. These results were analyzed using DFT methods, where it was observed that the distance between the O—H of the surface silanols correlates with basicity of the catalytic amines. This "deprotonated" state of the surface silanol makes the O more prone to perform a nucleophilic attack to the upcoming silane. Controlling the rate of grafting lead to controlling the group distribution on the surface of the silicas, as revealed by SSNMR studies. These results demonstrate that the famous grafting procedure can be tuned not only based on the nature of the organic groups but also based on the addition of organo-catalysts.

Acknowledgements

This research is supported by the U.S. Department of Energy, Office of Basic Energy Sciences, Division of Chemical Sciences, Geosciences, and Biosciences, through the Ames Laboratory Catalysis Science pro-gram. The Ames Laboratory is operated for the U.S. Department of Energy by Iowa State University under Contract No. DE-AC02-07CH11358.

Supplemental Figures

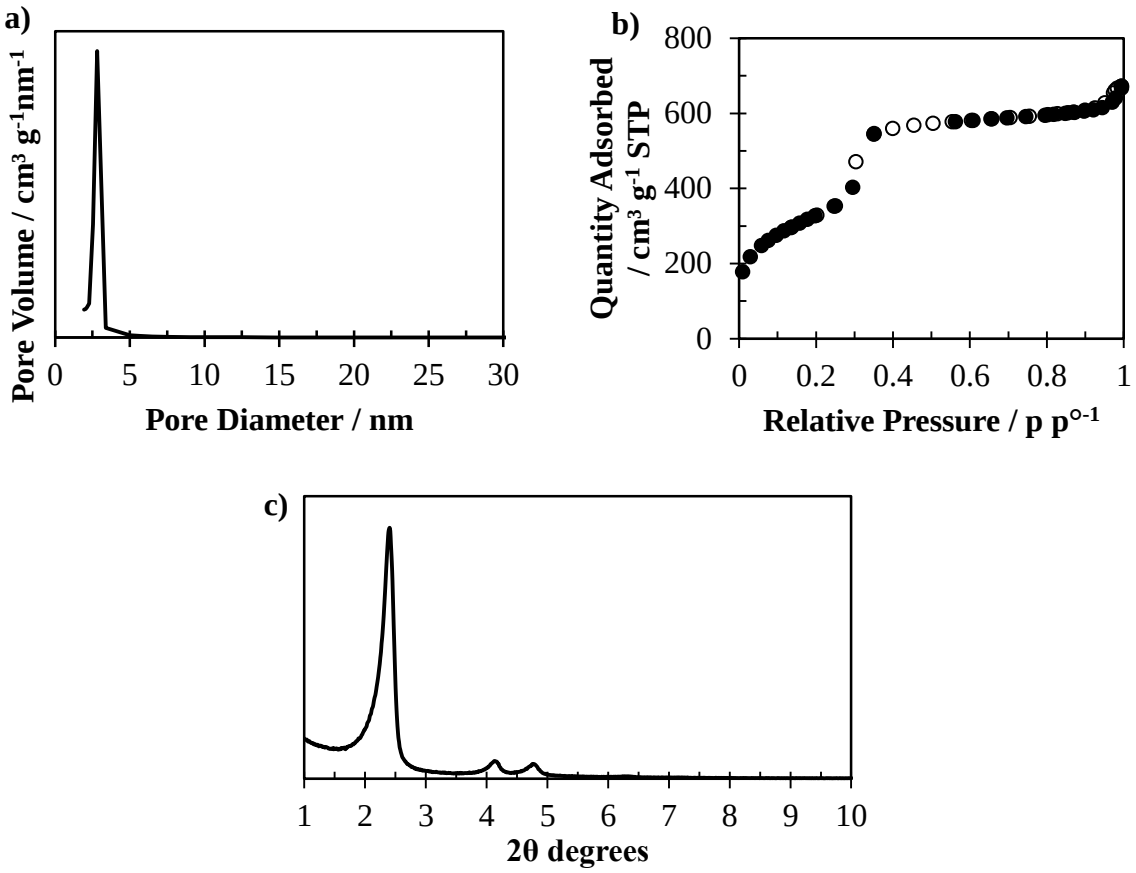

Figure S1. a) pore size distribution centered at 2.8 nm, b) N_2 adsorption isotherm, and c) XRD pattern (peaks centered at 2.42º, 4.18º and 4.85º) of synthesized Mesoporous Silica Nanoparticles.

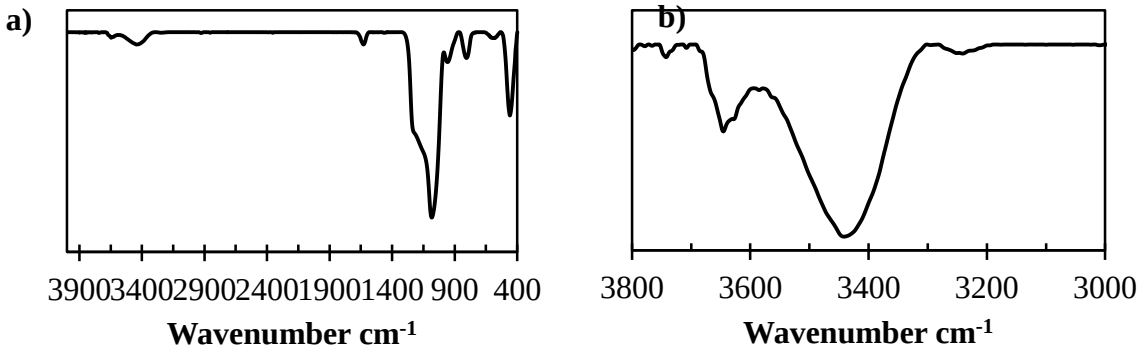

Figure S2. FT-IR of as-synthetized Mesoporous Silica Nanoparticles. a) Full spectrum and b) silanol region

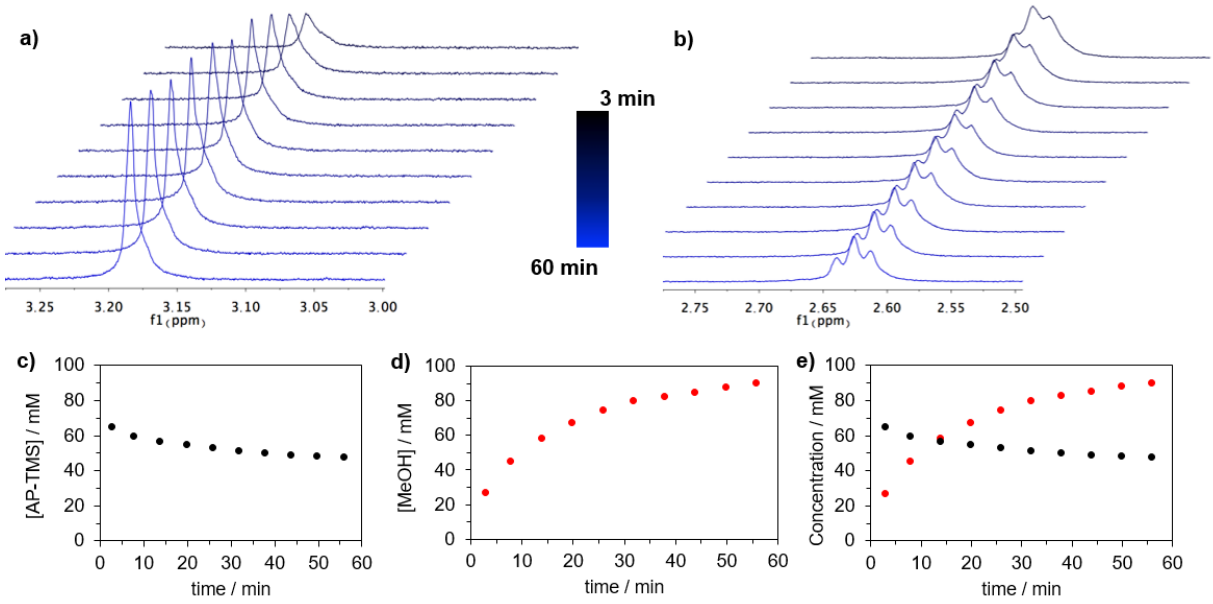

Figure S3. Solution ^{1}H NMR for a) production of MeOH and b) the consumption of AP-TMS. Kinetic trace for c) the consumption of AP-TMS, d) production of MeOH and e) combination of both (red trace = MeOH production, black = AP-TMS consumption). Reaction conditions: 66 mM AP-TMS, 50 ^{o}C, 1h.

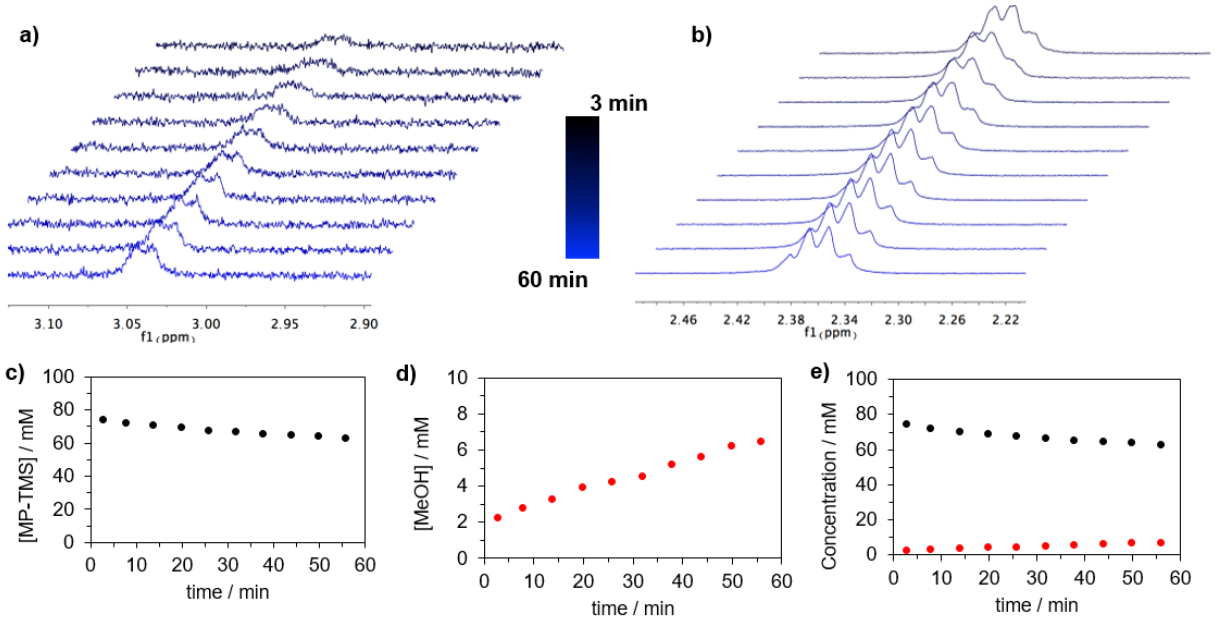

Figure S4. Solution ^{1}H NMR for a) production of MeOH and b) the consumption of MP-TMS. Kinetic trace for c) the consumption of MP-TMS, d) production of MeOH and e) combination of both (red trace = MeOH production, black = MP-TMS consumption). Reaction conditions: 66 mM MP-TMS, 50 ^{o}C, 1h.

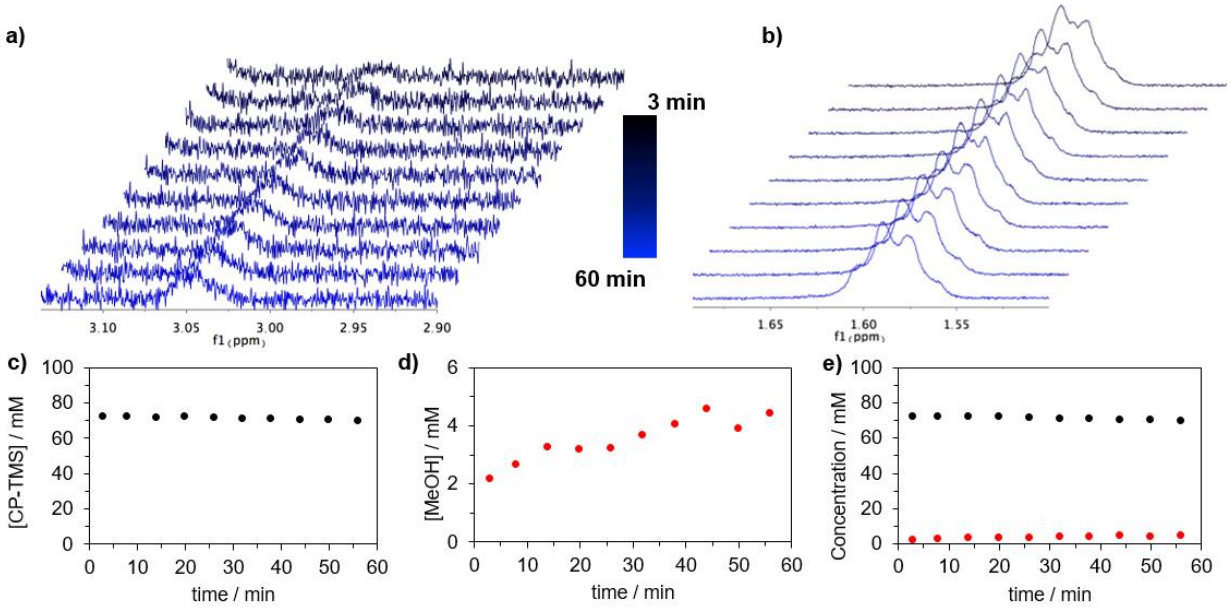

Figure S5. Solution ^{1}H NMR for a) production of MeOH and b) the consumption of CP-TMS. Kinetic trace for c) the consumption of CP-TMS, d) production of MeOH and e) combination of both (red trace = MeOH production, black = CP-TMS consumption). Reaction conditions: 66 mM CP-TMS, 50 ^{o}C, 1h.

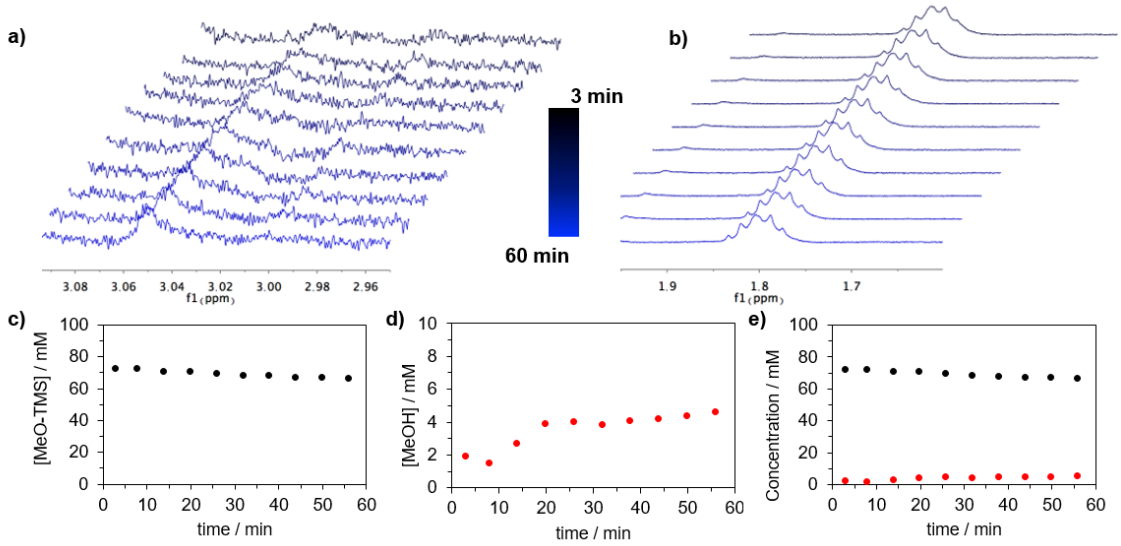

Figure S6. Solution ^{1}H NMR for a) production of MeOH and b) the consumption of MeO-TMS. Kinetic trace for c) the consumption of MeO-TMS, d) production of MeOH and e) combination of both (red trace = MeOH production, black = MeO-TMS consumption). Reaction conditions: 66 mM MeO-TMS, 50 ^{o}C, 1h.

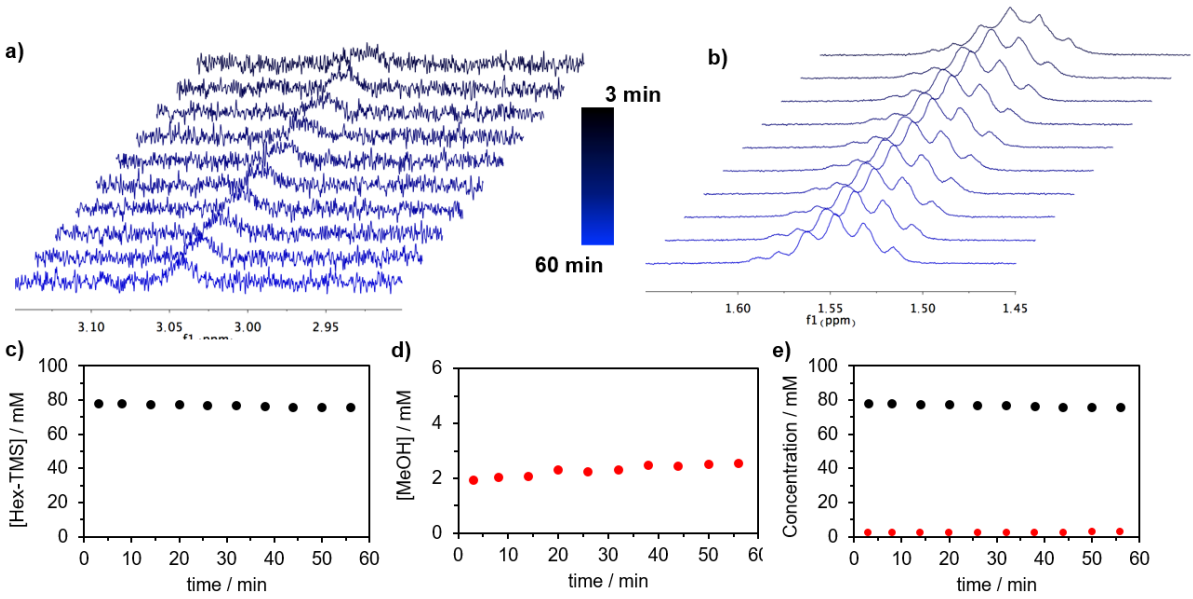

Figure S7. Solution ^{1}H NMR for a) production of MeOH and b) the consumption of Hex-TMS. Kinetic trace for c) the consumption of Hex-TMS, d) production of MeOH and e) combination of both (red trace = MeOH production, black = Hex-TMS consumption). Reaction conditions: 66 mM Hex-TMS, 50 ^{o}C, 1h.

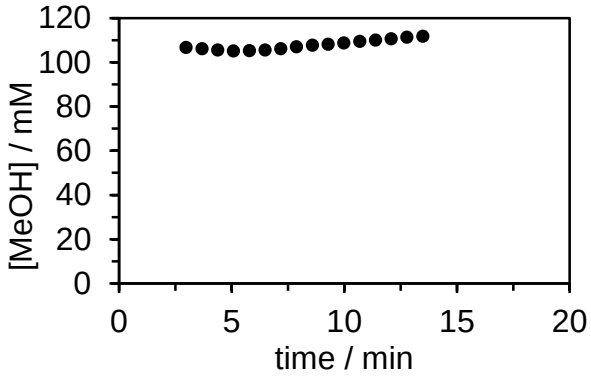

Figure S8. Solution ^{1}H NMR for the desorption of MeOH at 50 ^{o}C

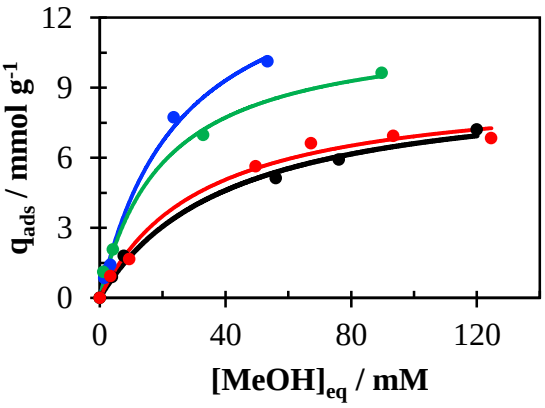

Figure S9. MeOH adsorption isotherms on MSN (10.0 mg MSN in 800 µL C_6D_6) at 30 ºC (blue), 40 ºC (green), 50 ºC (black), 60 ºC (red). Data-points were fitted to the Langmuir model.

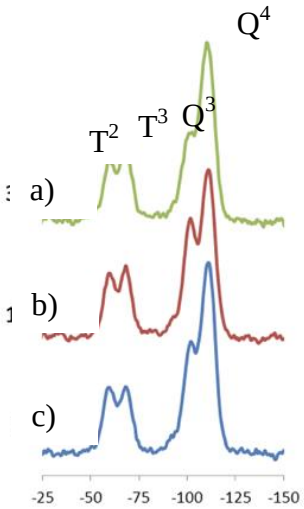

Figure S10. ^{29}Si CPMAS NMR of an MSN sample after a) 15 min, b) 15 min and c) 30 min of grafting with AP-TMS. The spectra show that the amino groups grafted in a bipodal or tripodal fashion.

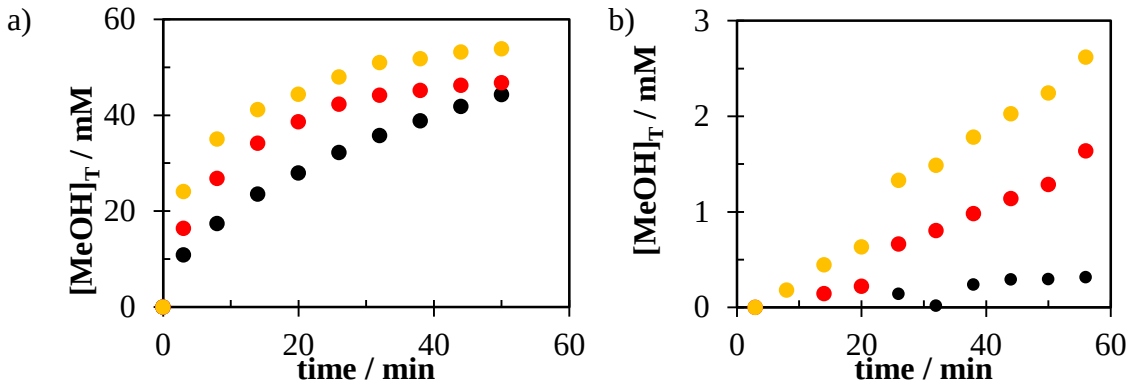

Figure S11. Rate of methanol production upon a) MP-TMS b) AP-TMS grafting on MSN at 30 ºC (black), 50 ºC (red), and 60 ºC (yellow).

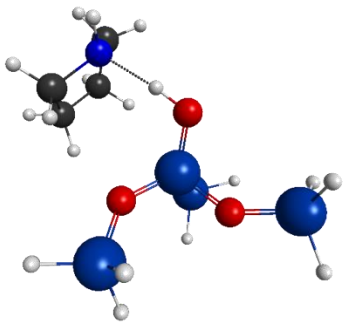

Figure S12. Optimized structure of the interaction of pyrrolidine with a surface silanol.

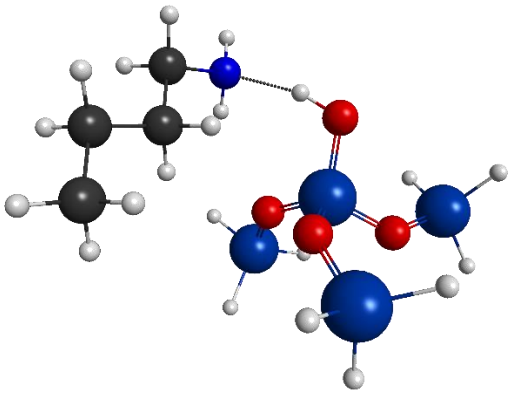

Figure S13. Optimized structure of the interaction of butylamine with a surface silanol.

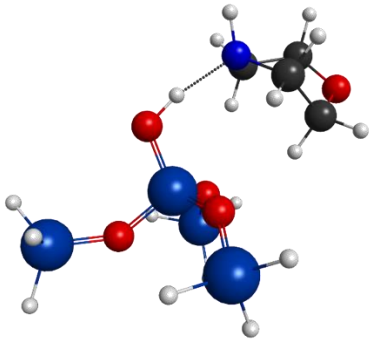

Figure S14. Optimized structure of the interaction of morpholine with a surface silanol.

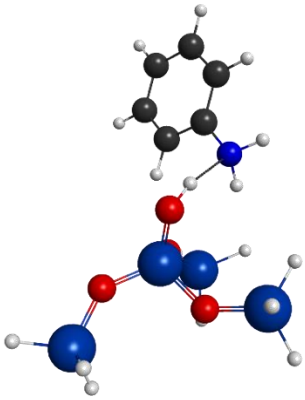

Figure S15. Optimized structure of the interaction of aniline with a surface silanol.

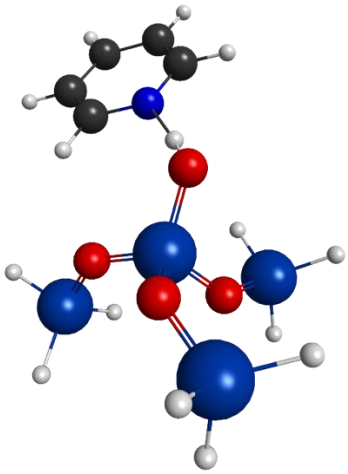

Figure S16. Optimized structure of the interaction of pyridine with a surface silanol.

References

1. Burkett, S. L.; Sims, S. D.; Mann, S., Synthesis of hybrid inorganic-organic mesoporous silica by co-condensation of siloxane and organosiloxane precursors. *Chemical Communications* **1996,** (11), 1367-1368.

2. Huh, S.; Wiench, J. W.; Yoo, J.-C.; Pruski, M.; Lin, V. S. Y., Organic Functionalization and Morphology Control of Mesoporous Silicas via a Co-Condensation Synthesis Method. *Chem. Mater.* **2003,** *15* (22), 4247-4256.

3. Bruhwiler, D., Postsynthetic functionalization of mesoporous silica. *Nanoscale* **2010,** *2* (6), 887-892.

4. Hoffmann, F.; Cornelius, M.; Morell, J.; Fröba, M., Silica-Based Mesoporous Organic–Inorganic Hybrid Materials. *Angew. Chem., Int. Ed.* **2006,** *45* (20), 3216-3251.

5. Cauvel, A.; Renard, G.; Brunel, D., Monoglyceride Synthesis by Heterogeneous Catalysis Using MCM-41 Type Silicas Functionalized with Amino Groups. *J. Org. Chem.* **1997,** *62* (3), 749-751.

6. Slowing, I. I.; Vivero-Escoto, J. L.; Trewyn, B. G.; Lin, V. S. Y., Mesoporous silica nanoparticles: structural design and applications. *J. Mater. Chem.* **2010,** *20* (37), 7924-7937.

7. Chen, J.; Sheng, Y.; Song, Y.; Chang, M.; Zhang, X.; Cui, L.; Meng, D.; Zhu, H.; Shi, Z.; Zou, H., Multimorphology Mesoporous Silica Nanoparticles for Dye Adsorption and Multicolor Luminescence Applications. *ACS Sustainable Chem. Eng.* **2018,** *6* (3), 3533-3545.

8. Huang, C.-H.; Chang, K.-P.; Ou, H.-D.; Chiang, Y.-C.; Wang, C.-F., Adsorption of cationic dyes onto mesoporous silica. *Microporous Mesoporous Mater.* **2011,** *141* (1), 102-109.

9. Aznar, E.; Oroval, M.; Pascual, L.; Murguía, J. R.; Martínez-Máñez, R.; Sancenón, F., Gated Materials for On-Command Release of Guest Molecules. *Chemical Reviews* **2016,** *116* (2), 561-718.

10. Tarn, D.; Ashley, C. E.; Xue, M.; Carnes, E. C.; Zink, J. I.; Brinker, C. J., Mesoporous Silica Nanoparticle Nanocarriers: Biofunctionality and Biocompatibility. *Accounts of Chemical Research* **2013,** *46* (3), 792-801.

11. Slowing, I. I.; Vivero-Escoto, J. L.; Wu, C.-W.; Lin, V. S. Y., Mesoporous silica nanoparticles as controlled release drug delivery and gene transfection carriers. *Adv. Drug Deliv. Rev.* **2008,** *60* (11), 1278-1288.

12. Vallet-Regí, M.; Balas, F.; Arcos, D., Mesoporous Materials for Drug Delivery. *Angew. Chem., Int. Ed.* **2007,** *46* (40), 7548-7558.

13. Yang, P.; Gai, S.; Lin, J., Functionalized mesoporous silica materials for controlled drug delivery. *Chem. Soc. Rev.* **2012,** *41* (9), 3679-3698.

14. Trewyn, B. G.; Slowing, I. I.; Giri, S.; Chen, H.-T.; Lin, V. S. Y., Synthesis and Functionalization of a Mesoporous Silica Nanoparticle Based on the Sol–Gel Process and Applications in Controlled Release. *Acc. Chem. Res.* **2007,** *40* (9), 846-853.

15. Zhao, T.; Chen, L.; Li, Q.; Li, X., Near-infrared light triggered drug release from mesoporous silica nanoparticles. *Journal of Materials Chemistry B* **2018**.

16. Nelson, N. C.; Chaudhary, U.; Kandel, K.; Slowing, I. I., Heterogeneous Multicatalytic System for Single-Pot Oxidation and C–C Coupling Reaction Sequences. *Top. Catal.* **2014,** *57* (10), 1000-1006.

17. Kandel, K.; Chaudhary, U.; Nelson, N. C.; Slowing, I. I., Synergistic Interaction between Oxides of Copper and Iron for Production of Fatty Alcohols from Fatty Acids. *ACS Catal.* **2015,** *5* (11), 6719-6723.

18. Sun, M.-H.; Huang, S.-Z.; Chen, L.-H.; Li, Y.; Yang, X.-Y.; Yuan, Z.-Y.; Su, B.-L., Applications of hierarchically structured porous materials from energy storage and conversion, catalysis, photocatalysis, adsorption, separation, and sensing to biomedicine. *Chem. Soc. Rev.* **2016,** *45* (12), 3479-3563.

19. Sun, L.-B.; Liu, X.-Q.; Zhou, H.-C., Design and fabrication of mesoporous heterogeneous basic catalysts. *Chem. Soc. Rev.* **2015,** *44* (15), 5092-5147.

20. Zhu, J.; Wang, T.; Xu, X.; Xiao, P.; Li, J., Pt nanoparticles supported on SBA-15: Synthesis, characterization and applications in heterogeneous catalysis. *Applied Catalysis B: Environmental* **2013,** *130-131*, 197-217.

21. Corma, A., From Microporous to Mesoporous Molecular Sieve Materials and Their Use in Catalysis. *Chem. Rev.* **1997,** *97* (6), 2373-2420.

22. Singappuli-Arachchige, D.; Manzano, J. S.; Sherman, L. M.; Slowing, I. I., Polarity Control at Interfaces: Quantifying Pseudo-solvent Effects in Nano-confined Systems. *ChemPhysChem* **2016,** *17* (19), 2982-2986.

23. Doadrio, J. C.; Sousa, E. M. B.; Izquierdo-Barba, I.; Doadrio, A. L.; Perez-Pariente, J.; Vallet-Regí, M., Functionalization of mesoporous materials with long alkyl chains as a strategy for controlling drug delivery pattern. *J. Mater. Chem.* **2006,** *16* (5), 462-466.

24. Santos-Figueroa, L. E.; Giménez, C.; Agostini, A.; Aznar, E.; Marcos, M. D.; Sancenón, F.; Martínez-Máñez, R.; Amorós, P., Selective and Sensitive Chromofluorogenic Detection of the Sulfite Anion in Water Using Hydrophobic Hybrid Organic–Inorganic Silica Nanoparticles. *Angew. Chem., Int. Ed.* **2013,** *52* (51), 13712-13716.

25. Karimi, B.; Khorasani, M., Selectivity Adjustment of SBA-15 Based Tungstate Catalyst in Oxidation of Sulfides by Incorporating a Hydrophobic Organic Group inside the Mesochannels. *ACS Catal.* **2013,** *3* (7), 1657-1664.

26. Bass, J. D.; Solovyov, A.; Pascall, A. J.; Katz, A., Acid−Base Bifunctional and Dielectric Outer-Sphere Effects in Heterogeneous Catalysis: A Comparative Investigation of

Model Primary Amine Catalysts. *Journal of the American Chemical Society* **2006,** *128* (11), 3737-3747.

27. Sebastián Manzano, J.; Singappuli-Arachchige, D.; Parikh, B. L.; Slowing, I. I., Fine-tuning the release of molecular guests from mesoporous silicas by controlling the orientation and mobility of surface phenyl substituents. *Chem. Eng. J.* **2018,** *340*, 73-80.

28. Nakazawa, J.; Smith, B. J.; Stack, T. D. P., Discrete Complexes Immobilized onto Click-SBA-15 Silica: Controllable Loadings and the Impact of Surface Coverage on Catalysis. *J. Am. Chem. Soc.* **2012,** *134* (5), 2750-2759.

29. Sharma, K. K.; Asefa, T., Efficient Bifunctional Nanocatalysts by Simple Postgrafting of Spatially Isolated Catalytic Groups on Mesoporous Materials. *Angewandte Chemie International Edition* **2007,** *46* (16), 2879-2882.

30. Hicks, J. C.; Dabestani, R.; Buchanan, A. C.; Jones, C. W., Spacing and Site Isolation of Amine Groups in 3-Aminopropyl-Grafted Silica Materials: The Role of Protecting Groups. *Chem. Mater.* **2006,** *18* (21), 5022-5032.

31. Nakazawa, J.; Stack, T. D. P., Controlled Loadings in a Mesoporous Material: Click-on Silica. *J. Am. Chem. Soc.* **2008,** *130* (44), 14360-14361.

32. Eedugurala, N.; Wang, Z.; Chaudhary, U.; Nelson, N.; Kandel, K.; Kobayashi, T.; Slowing, I. I.; Pruski, M.; Sadow, A. D., Mesoporous Silica-Supported Amidozirconium-Catalyzed Carbonyl Hydroboration. *ACS Catalysis* **2015,** *5* (12), 7399-7414.

33. Fujdala, K. L.; Tilley, T. D., An Efficient, Single-Source Molecular Precursor to Silicoaluminophosphates. *J. Am. Chem. Soc.* **2001,** *123* (41), 10133-10134.

34. Fortier-McGill, B.; Toader, V.; Reven, L., 1H Solid State NMR Study of Poly(methacrylic acid) Hydrogen-Bonded Complexes. *Macromolecules* **2012,** *45* (15), 6015-6026.

35. Wiester, M. J.; Braunschweig, A. B.; Yoo, H.; Mirkin, C. A., Solvent and Temperature Induced Switching Between Structural Isomers of RhI Phosphinoalkyl Thioether (PS) Complexes. *Inorg. Chem.* **2010,** *49* (15), 7188-7196.

36. Milkovic, N. M.; Catazaro, J.; Lin, J.; Halouska, S.; Kizziah, J. L.; Basiaga, S.; Cerny, R. L.; Powers, R.; Wilson, M. A., Transient sampling of aggregation-prone conformations causes pathogenic instability of a parkinsonian mutant of DJ-1 at physiological temperature. *Protein Science* **2015,** *24* (10), 1671-1685.

37. Grimme, S.; Antony, J.; Ehrlich, S.; Krieg, H., A consistent and accurate ab initio parametrization of density functional dispersion correction (DFT-D) for the 94 elements H-Pu. *The Journal of Chemical Physics* **2010,** *132* (15), 154104.

38. Schmidt, M. W.; Baldridge, K. K.; Boatz, J. A.; Elbert, S. T.; Gordon, M. S.; Jensen, J. H.; Koseki, S.; Matsunaga, N.; Nguyen, K. A.; Su, S.; Windus, T. L.; Dupuis, M.; Montgomery, J. A., General atomic and molecular electronic structure system. *Journal of Computational Chemistry* **1993,** *14* (11), 1347-1363.

39. Coasne, B.; Ugliengo, P., Atomistic Model of Micelle-Templated Mesoporous Silicas: Structural, Morphological, and Adsorption Properties. *Langmuir* **2012,** *28* (30), 11131-11141.

40. Ugliengo, P.; Sodupe, M.; Musso, F.; Bush, I. J.; Orlando, R.; Dovesi, R., Realistic Models of Hydroxylated Amorphous Silica Surfaces and MCM-41 Mesoporous Material Simulated by Large-scale Periodic B3LYP Calculations. *Adv. Mater.* **2008,** *20* (23), 4579-4583.

41. Shoemaker, J. R.; Gordon, M. S., SIMOMM: An Integrated Molecular Orbital/Molecular Mechanics Optimization Scheme for Surfaces. *J. Phys. Chem. A* **1999,** *103* (17), 3245-3251.

42. Jordan, R., *Reaction Mechanisms of Inorganic and Organometallic Systems*. Third Edition ed.; Oxford University Press: 2007.

43. Delle Piane, M.; Corno, M.; Pedone, A.; Dovesi, R.; Ugliengo, P., Large-Scale B3LYP Simulations of Ibuprofen Adsorbed in MCM-41 Mesoporous Silica as Drug Delivery System. *J. Phys. Chem. C* **2014,** *118* (46), 26737-26749.

44. Delle Piane, M.; Corno, M.; Ugliengo, P., Does Dispersion Dominate over H-Bonds in Drug–Surface Interactions? The Case of Silica-Based Materials As Excipients and Drug-Delivery Agents. *Journal of Chemical Theory and Computation* **2013,** *9* (5), 2404-2415.

45. Bapiro, T. E.; Sykes, A.; Martin, S.; Davies, M.; Yates, J. W. T.; Hoch, M.; Rollison, H. E.; Jones, B., Complete Substrate Inhibition of Cytochrome P450 2C8 by AZD9496, an Oral Selective Estrogen Receptor Degrader. *Drug Metabolism and Disposition* **2018,** *46* (9), 1268.

46. Marin-Luna, M.; Patschinski, P.; Zipse, H., Substituent Effects in the Silylation of Secondary Alcohols: A Mechanistic Study. *Chem. Eur. J.* **2018**.

47. Patschinski, P.; Zhang, C.; Zipse, H., The Lewis Base-Catalyzed Silylation of Alcohols—A Mechanistic Analysis. *J. Org. Chem.* **2014,** *79* (17), 8348-8357.

48. Docherty, S. R.; Estes, D. P.; Copéret, C., Facile Synthesis of Unsymmetrical Trialkoxysilanols: (RO)2(R′O)SiOH. *Helvetica Chimica Acta* **2018,** *101* (3).

49. Ong, S.; Zhao, X.; Eisenthal, K. B., Polarization of water molecules at a charged interface: second harmonic studies of the silica/water interface. *Chem. Phys. Lett.* **1992,** *191* (3,Äì4), 327-335.

50. Sulpizi, M.; Gaigeot, M.-P.; Sprik, M., The Silica–Water Interface: How the Silanols Determine the Surface Acidity and Modulate the Water Properties. *Journal of Chemical Theory and Computation* **2012,** *8* (3), 1037-1047.

51. Kobayashi, T.; Singappuli-Arachchige, D.; Slowing, I. I.; Pruski, M., Spatial distribution of organic functional groups supported on mesoporous silica nanoparticles (2): a study by 1H triple-quantum fast-MAS solid-state NMR. *Physical Chemistry Chemical Physics* **2018,** *20* (34), 22203-22209.

CHAPTER 6. FINE-TUNING THE RELEASE OF MOLECULAR GUESTS FROM MESOPOROUS SILICAS BY CONTROLLING THE ORIENTATION AND MOBILITY OF SURFACE PHENYL SUBSTITUENTS

This work was published in *Chem. Eng. J.*, **2018**, *340*,75-80.

J. Sebastián Manzano,[1,2,†] Dilini Singappuli-Arachchige, [1,2,†] Bosky L. Parikh[1,2], Igor I. Slowing[1,2]

[1]US DOE Ames Laboratory, Ames, Iowa 50011, United States

[2]Department of Chemistry, Iowa State University, Ames, Iowa 50011, United States

[†]These authors contributed equally to this study.

Abstract

Phenyl-functionalized mesoporous silica materials were used to explore the effect of non-covalent interactions on the release of Ibuprofen into simulated body fluid. Variations in orientation and conformational mobility of the surface phenyl groups were introduced by selecting different structural precursors: 1) a rigid upright orientation was obtained using phenyl groups directly bound to surface Si atoms (Ph-MSN), 2) mobile groups were produced by using ethylene linkers to connect phenyl groups to the surface (PhEt-MSN), and 3) groups co-planar to the surface were obtained synthesizing a phenylene-bridged periodic mesoporous organosilica (Ph-PMO). The Ibuprofen release profiles from these materials and non-functionalized mesoporous silica nanoparticles (MSN) were analyzed using an adsorption-diffusion model. The model provided kinetic and thermodynamic parameters that evidenced fundamental differences in drug-surface interactions between the materials. All phenyl-bearing materials show lower Ibuprofen initial release rates than bare MSN. The conformationally locked Ph-MSN and Ph-PMO have stronger interactions with the drug (negative ΔG of adsorption) than the flexible PhEt-MSN and bare MSN (positive ΔG of

adsorption). These differences in strength of adsorption are consistent with differences between interaction geometries obtained from DFT calculations. B3LYP-D3-optimized models show that π-π interactions contribute more to drug adsorption than H-bonding with silanol groups. The results suggest that the type and geometry of interactions control the kinetics and extent of drug release, and should therefore serve as a guide to design new drug delivery systems with precise release behaviors customized to any desired target.

Introduction

Advancements in drug delivery systems (DDS) are of utmost importance to the development of the pharmaceutical and biomedical fields. One of the key properties of advanced DDS is the ability of releasing drug molecules in a controlled fashion. In this respect, mesoporous silicas have been extensively studied as promising DDS because in addition to their biocompatibility, controllable pore structure, large pore volumes and surface areas, they can be functionalized with a wide variety of moieties.[1-5] These properties have enabled the design of gated DDS that release their cargo upon application of specific stimuli like radiation, changes in pH, temperature, redox potentials, magnetic fields, or signaling molecules.[6-12] Furthermore, these materials have also been modified with receptors, antibodies, or aptamers to provide targeting capabilities, and with reactive moieties to control cell internalization and endo/lysosomal escape.[13-18]

In spite of all these sophisticated designs and their successful *in vitro* and *in vivo* applications,[19-21] little attention has been paid to the influence of drug-surface interactions on the extent and kinetics of release. Moreover, our understanding of the role of organic moieties on surface-solvent partition equilibria and diffusion rates of the loaded drugs is fairly limited and often overlooked. This is surprising given the importance usually attributed to the high surface area and the ability to tailor the surface chemistry of these materials.

Initial efforts to determine the effects of surface groups on the performance of mesoporous silica DDS were conducted by Vallet-Regí and co-workers when studying Erythromycin release as a function of alkyl substitution.[22] Their results showed that release was affected by surface hydrophobicity, and suggested that partition equilibria between the surface and the media controlled drug discharge. More recently, Berger and collaborators investigated the effects of group functionalities on the release of Metoprolol from mesoporous silica.[23] They observed a correlation between functional group pK_a and the amount of drug released, suggesting that electrostatic interactions controlled release rates. Interestingly, computational studies by Ugliengo and co-workers suggested that even weak interactions can determine drug release. Their simulations showed that London dispersion forces play a more important role than H-bonding in the adsorption of Ibuprofen on the silica surface.[24, 25] However, NMR and relaxation dielectric spectroscopy studies have shown that the interaction of Ibuprofen with the silica surface is so weak that only a fraction of the drug is adsorbed to the pore walls and the rest exists as highly mobile species.[26-31] Thus, one can expect that producing gradual enhancements of the drug-silica interactions may allow fine-tuning drug release.

Herein, with the aim of enabling precise control of drug release rates, we explore the potential role of non-covalent interactions on the behavior of mesoporous silica-based DDS. Specifically, we investigate the effect of π-π interactions between Ibuprofen and surface-immobilized phenyl groups on its release kinetics from silica carriers. To this end, we produced phenyl-functionalized mesoporous silicas with different structural features, namely: 1) mesoporous silica nanoparticles (MSN) with phenyl groups directly bound to silicon atoms (Ph-MSN) where groups are rigid and upright, 2) MSN with phenyl groups attached via flexible ethylene linkers (PhEt-MSN) where groups have conformational mobility, and 3)

phenylene-bridged periodic mesoporous organosilica (Ph-PMO) where the phenyl group is co-planar to the pore surface (Scheme 1). We compared the Ibuprofen release profiles from these materials and non-functionalized MSN to assess the effects of orientation (perpendicular versus co-planar to the pore walls) and conformational flexibility on the strength of interactions and release kinetics of the drug. By fitting the release profiles to a three-parameter kinetic model developed by Zeng and Wu, we characterized the thermodynamics of surface-solvent partition and the diffusion kinetics of the desorbed molecules from the pores to the bulk media.[32, 33] Finally, we pursued an atomistic level understanding of the interactions via computational modeling of drug-surface complexes using a silica surface model developed by Ugliengo and co-workers.[34, 35]

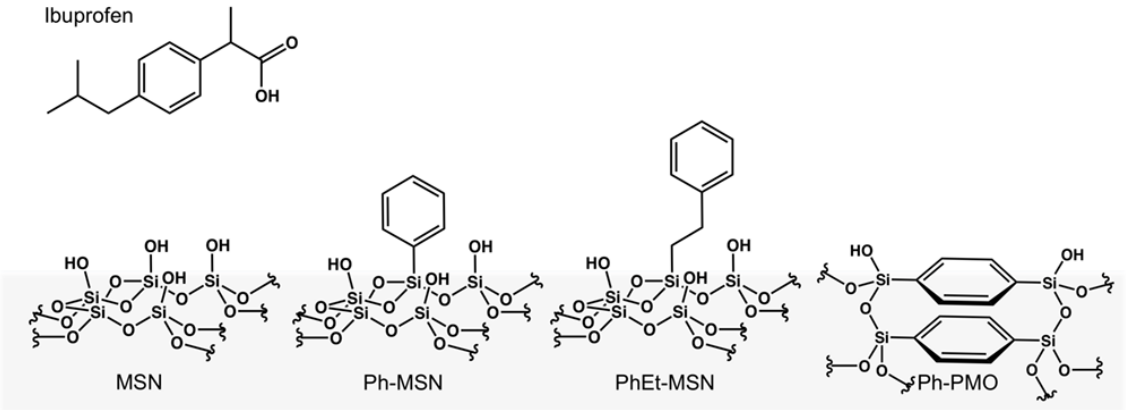

Scheme 1. Structure of Ibuprofen and surface functionalities of the four mesoporous silica based DDS.

Experimental

Chemicals

Hexadecyltrimethylammonium bromide (CTAB), Brij 76 ($C_{18}EO_{10}$) and Ibuprofen were purchased from Aldrich. Tetraethylorthosilicate (TEOS), phenyltrimethoxysilane, phenethyltrimethoxysilane and 1,4-bis(triethoxysilyl) benzene were purchased from Gelest,

Inc. NaOH, NaCl, KCl, K_2HPO_4, $MgCl_2 \cdot 6H_2O$, $CaCl_2$, Na_2SO_4, Tris(hydroxymethyl)aminomethane, conc. HCl and acetone were purchased from Fisher Scientific. $NaHCO_3$ was from Alfa Aesar, and Prodan from Anapec, Inc. All chemicals were used as received without any further purification.

Synthesis of MSN

CTAB (1.0 g, 2.74 mmol) was dissolved in deionized water (480 ml) in a round bottom flask followed by addition of 2 M NaOH (3.5 mL, 7.0 mmol). The solution was stirred for 1 h at 80 °C. TEOS (5.0 mL, 22.6 mmol) was then added drop wise over 5 min to the CTAB solution. Magnetic stirring was continued for another 2 h at 80 °C. The solution was filtered, washed with abundant water and methanol, and vacuum dried overnight. CTAB was removed by refluxing 1.0 g of dry solid with 100 mL of methanol and conc. HCl (0.8 mL, 9.7 mmol) at 60 °C for 6 h. The surfactant removal step was repeated. The surfactant-removed sample was then filtered, washed with abundant methanol and vacuum dried overnight.

Synthesis of Phenyl (Ph-MSN) and Phenethyl (PhEt-MSN) substituted MSN

CTAB (1.0 g, 2.74 mmol) was dissolved in deionized water (480 ml) in a round bottom flask followed by addition of 2 M NaOH (3.5 mL, 7.0 mmol). The solution was stirred for 1 h at 80 °C. TEOS (5.0 mL, 22.6 mmol) and phenyltrimethoxysilane (0.19 mL, 1.0 mmol) for Ph-MSN or phenethyltrimethoxysilane (0.22 mL, 1.0 mmol) for PhEt-MSN were then added drop wise over 7 min to the CTAB solution. Magnetic stirring was continued for another 2 h at 80 °C. The solution was filtered, washed with abundant water and methanol respectively, and vacuum dried overnight. CTAB template was removed by refluxing 1.0 g of dry solid with 100 mL of methanol and conc. HCl (0.8 mL, 9.7 mmol) at

60 °C for 6 h. The surfactant removal step was repeated. The surfactant-removed samples were then filtered, washed with abundant methanol and vacuum dried overnight.

Synthesis of Phenyl bridged Periodic Mesoporous Organosilica (Ph-PMO)

Brij 76 (0.5 g, 0.703 mmol) was dissolved in 2 M HCl (12.5 mL, 25.0 mmol) and distilled water (2.5 mL) in a round bottom flask with continuous magnetic stirring for 30 min at 50 °C. 1,4-Bis(triethoxysilyl) benzene (1.04 mL, 2.63 mmol) was then added to the mixture and the stirring was continued for another 20 h at 50 °C. The solid product was collected via filtration and was air-dried for 24 h. The surfactant template was removed by refluxing 1.0 g of dry solid with 150 ml of ethanol and conc. HCl (1.69 mL, 20.3 mmol) at 50 °C for 5 h. The surfactant removal step was repeated one more time. The final product was filtered, air-dried, and further dried under vacuum overnight.

Characterization

XRD patterns were recorded on a Bruker X–ray diffractometer using Cu Kα radiation (40 kV, 44 mA) over the range of 1–50 2θ degrees. Nitrogen sorption isotherms were measured on a Micromeritics Tristar surface area and porosity analyzer. The surface area and pore size distribution were calculated by the Brunauer Emmett Teller (BET) and Barrett Joyner Halenda (BJH) methods respectively. Elemental analyses of the dry samples were done by triplicate on a Perkin Elmer 2100 series II CHNS analyzer, using acetanilide as calibration standard and combustion and reduction temperatures of 925 °C and 640 °C respectively. Transmission Electron Microscopy (TEM) images were obtained using a FEI Tecnai G2 F20 scanning transmission electron microscope operating at 200 kV. TEM samples were prepared by placing 2-3 drops of dilute methanol suspensions onto a carbon-coated copper grid. Transmission mode FTIR measurements were made on a Bruker Vertex 80 FT-IR spectrometer equipped with a HeNe laser and photovoltaic MCT detector and

OPUS software. Samples were mixed at ca. 2 wt% with KBr and pressed into pellets for analysis.

Relative polarity measurements of samples were done according to a previously published method.[36] A solution of Prodan in acetone (10 µL, 1.0 mM) was added to the samples (10.0 mg each), grinded, let dry, and suspended in water (2.0 mL). Fluorescence measurements of the suspensions were recorded in a Cary Eclipse Fluorescence Spectrophotometer. Excitation wavelength was set at 337 nm and both excitation and emission slit widths were set at 5 nm. Obtained fluorescence curves were fitted in origin pro using a Gaussian distribution model. Maximum fluorescence emission wavelength of each sample was used to assign relative polarities based on probe fluorescence in reference solvents.[36]

Impregnation of Ibuprofen into mesoporous materials

Ibuprofen was introduced into the pores via incipient wetness impregnation. In brief, the mesoporous materials (30.0 mg each) were ground to a fine powder using a pestle in an agate mortar. A fresh solution of Ibuprofen in acetone (30 µL, 0.5 M) was then added dropwise to each material, and the mixture was ground until seemingly dry. The impregnated materials were then oven-dried to remove excess acetone, and then dried overnight under vacuum.

Preparation of simulated body fluid (SBF) solution.

This solution was prepared following the literature.[37] NaCl (7.996 g, 0.14 mmol), $NaHCO_3$ (0.350 g, 0.0042 mmol), KCl (0.224 g, 0.0030 mmol), K_2HPO_4 (0.174 g, 0.001 mmol), $MgCl_2{\bullet}6H_2O$ (0.305 g, 0.0015 mmol), 1M HCl (40.0 mL, 0.04 mmol), $CaCl_2$ (0.278 g, 0.0025 mmol), Na_2SO_4 (0.071 g, 0.0050 mmol), and tris(hydroxymethyl) aminomethane (6.057 g, 0.05 mmol) were dissolved in deionized water (500 mL) one by one in the above

mentioned order in a 1L polyethylene bottle while stirring at 36.5 ºC. The pH of the solution was adjusted to 7.40 using a 1M HCl solution. The total volume of the solution was then adjusted to 1L by adding deionized water and shaking at 20 °C. The prepared SBF solution was stored in a refrigerator at 5 °C.

Ibuprofen release experiments

The Ibuprofen-loaded samples (30.0 mg each) were introduced into a dialysis membrane (Spectrum Labs, MW cutoff = 12-14 kDa) and immersed into SBF (10.0 mL). The intact SBF solution was continuously circulated through a quartz flow cuvette, and the absorption band at 263 nm was monitored for 20 h via UV-vis spectroscopy, taking scans every 5 min. Three separate release experiments were performed for each material, and the results were averaged.

Computational methods.

All calculations were performed using the dispersion-corrected B3LYP-D3[38] method implemented in the GAMESS[39] package using the 6-311G(d,p) basis set. Three different surfaces were optimized using the MCM-41 model developed by Ugliengo and collaborators.[34] The surfaces consisted of bare MCM-41 silica, and MCM-41 silica substituted with a phenyl group and with a phenethyl group. Ph-PMO was modeled based on previous work by Martinez and Pacchioni.[40] The structure corresponds to a sequence of six and four membered rings of organosilica tetrahedra with T3:T2 ratio of 2:1, based on the solid state NMR study by Comotti *et al*.[41] All of the models were optimized using the QM/MM SIMMOM[42] implemented in GAMESS, using the B3LYP-D3 functional with a 6-311(d,p) basis set.

Results and Discussion

Material synthesis and characterization

To explore the effects of non-covalent interactions, group orientation and conformational flexibility on Ibuprofen release, MCM-41 type mesoporous silica nanoparticles (MSN) functionalized with phenyl (Ph-MSN) and phenethyl (PhEt-MSN) groups, and phenylene-bridged periodic mesoporous organosilica (Ph-PMO) were synthesized. Non-functionalized MSN was also prepared as a control (Scheme 1).

Characterization of the materials by nitrogen physisorption and x-ray diffraction revealed that the organic groups have no significant effects on the textural properties and pore geometry of the MSN samples. While all the MSN materials have similar surface areas (around 1200 m^2 g^{-1}), the surface of Ph-PMO is about 30% lower (807 m^2 g^{-1}) (Table 1, Fig. S1). However, the pore width distributions of all materials are very similar (centered at 2.6 – 3.0 nm), and all of them have 2D hexagonal arrays of pores as evidenced by XRD patterns and TEM images (Fig. S2, S3). While the loadings of phenyl groups are very similar for Ph-MSN and PhEt-MSN based on CHN elemental analysis, Ph-PMO has a much higher number of groups because its only precursor is the bis-siloxy-benzene.

The relative polarities of the pore surfaces were measured to determine if material hydrophobicity controls Ibuprofen release. Pore polarities were assessed via fluorescence spectroscopy of the impregnated molecular probe Prodan, as reported before (Table 1, Fig. 1, S4).[36] Because of the lack of organic moieties, the silanol-rich non-functionalized MSN has a much higher interfacial polarity than the other materials. Interestingly, Ph-MSN has a higher polarity than PhEt-MSN, likely due to the differences in flexibility of the two surface groups. While the rigid Ph groups in Ph-MSN expose the surface silanols allowing their contribution to the interfacial polarity, the flexible PhEt can bend over the surface and mask some of the

polar silanols to decrease their contribution.[43] Interestingly, in spite of the larger amount of phenyl groups in Ph-PMO, its relative polarity is very similar to that of PhEt-MSN. This result supports the idea that the phenyl groups in PhEt-MSN may lay flat on the surface covering a fraction of silanols thus giving a balance of hydrophobic-hydrophilic groups comparable to that of Ph-PMO.

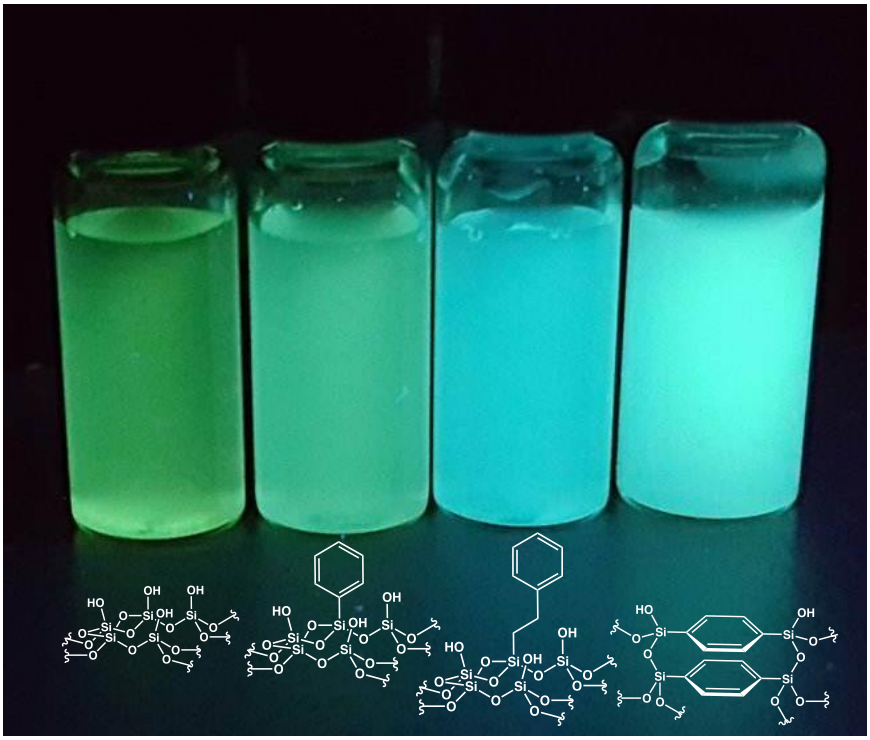

Figure 1 Photograph of aqueous suspensions of (left to right) MSN, Ph-MSN, PhEt-MSN, and Ph-PMO loaded with the solvatochromic fluorophore Prodan. Interfacial polarity is proportional to the wavelength of emission (i.e. green and blue indicate high and low polarity respectively).[36]

FTIR analysis of the materials (Fig. S5) evidenced features common to all of them, including the characteristic intense peaks centered at ca. 1090 cm^{-1} and 3400 cm^{-1} assigned to Si–O–Si and –O–H stretching vibrations respectively, the latter corresponding to H-bonding silanols and physisorbed water. Presence of water in all the materials is confirmed by a clear signal of the scissor bending vibration at 1630 cm^{-1}. The organic groups are characterized in

Ph-MSN, PhEt-MSN and Ph-PMO by peaks in the 3000 – 3100 cm^{-1} region corresponding to aromatic C–H stretching vibrations, and 1380 – 1420 cm^{-1} region attributed to aromatic ring vibrations and Si–C stretching. These signals are much better defined in Ph-PMO due to the larger number of organic groups in the material. Additional absorption between 2900 and 3000 cm^{-1} is visible for PhEt-MSN corresponding to the aliphatic C–H bonds of the ethylene groups.

Table 1. Physicochemical properties of the materials.

	S_{BET} (m^2 g^{-1})	W_{BJH} (nm)	Relative polarity[a]	Phenyl groups (mmol g^{-1})[b]
MSN	1262	3.0	1.00 ± 0.01	--
Ph-MSN	1221	2.6	0.84 ± 0.02	1.2
PhEt-MSN	1196	2.6	0.69 ± 0.01	1.0
Ph-PMO	807	2.8	0.72 ± 0.01	3.2[c]

[a]Determined by fluorescence measurement of solvatochromic probe Prodan.[36] [b]Determined by CHN elemental analysis. [c]Estimated from the surface area of the material and its structural model.[44]

Ibuprofen loading

Ibuprofen was loaded into the materials via incipient wetness impregnation to facilitate drug penetration into the pores by capillary action.[45] The amount loaded (0.5 mmol g^{-1}) was selected to ensure there were plenty of phenyl groups in the materials to interact with the drug. Drug loading is confirmed by FTIR analysis of the impregnated materials which show a clear absorption band at 1710 cm^{-1} corresponding to the C=O stretching of Ibuprofen (Fig 2). This signal is red-shifted by ca. 14 cm^{-1} in all of the loaded materials with respect to the pure drug suggesting interaction of the group with the surface, likely via hydrogen bonding with silanol groups.[26] Smaller blue shifts in ring vibration bands (1462 to 1467 cm^{-1} and 1508 to 1514 cm^{-1}) suggest that the aromatic group is either interacting with the surface

or its mobility is significantly restricted likely due to confinement in the porous materials.[46-48] Wide angle XRD analysis of the drug-loaded materials does not show crystalline Ibuprofen reflections in any of the materials (Fig. S6), which is consistent with previous reports and has also been attributed to confinement of the drug into the pores.[26]

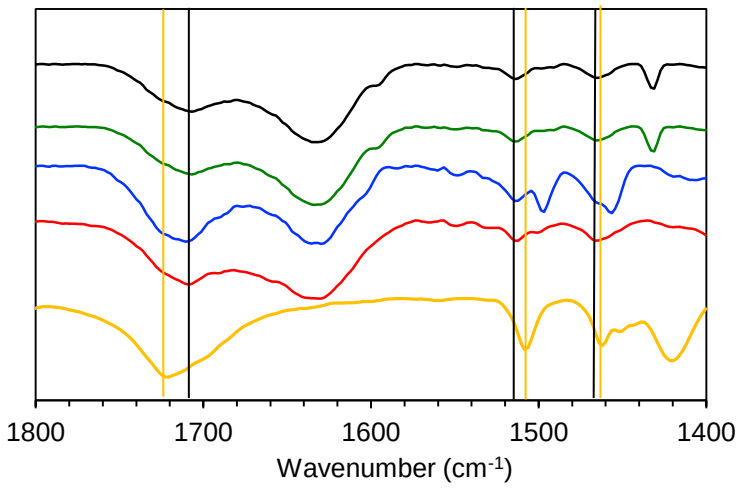

Figure 2 FTIR spectra of Ibuprofen-loaded MSN (black), Ph-MSN (green), PhEt-MSN (blue) and Ph-PMO (red). Spectrum of the free drug (KBr pellet) is in yellow.

Ibuprofen release from different MSN

The release of Ibuprofen from the materials to simulated body fluid (SBF) was monitored via UV-visible spectroscopy (λ = 263 nm). The drug-loaded materials were set in a dialysis bag (MW cutoff = 12–14 kDa) and immersed in SBF (Fig. S7). The solution was continuously circulated through a quartz flow cuvette and spectra were acquired every 5 min for 20 h.

The average Ibuprofen release profiles indicate a clear dependence on the functionality of the silica materials (Fig. 3, Table 2). Some of the most relevant differences between the profiles include: 1) only MSN and PhEt-MSN reach a plateau within the experimental timeframe (less than 1% change after 12 and 16 h, respectively), 2) MSN and

Ph-MSN show the largest cumulative release after 20 h (ca. 82 ± 3% and 81 ± 4%, respectively), 3) MSN presents a higher initial release rate than the other materials, all of which present the same values (0.44 versus 0.25 mM h^{-1} respectively), 4) while all the phenyl-bearing materials give the same initial rates, PhEt-MSN sustains it for a longer time (2 h) than Ph-MSN (1.5 h) and Ph-PMO (0.5 h). These differences indicate that the phenyl groups indeed have an effect on the adsorption and retention of Ibuprofen, and are consistent with the phenyl-bearing materials having lower polarity (i.e. more hydrophobicity) than the non-functionalized MSN. However, the differences observed between the drug release profiles of all the phenyl-functionalized materials cannot be explained by hydrophobicity alone. The different release profiles from these materials must be due to significant variations in the drug-surface interactions at the molecular level, which are likely regulated by the relative orientation and flexibility of binding sites on the surface.

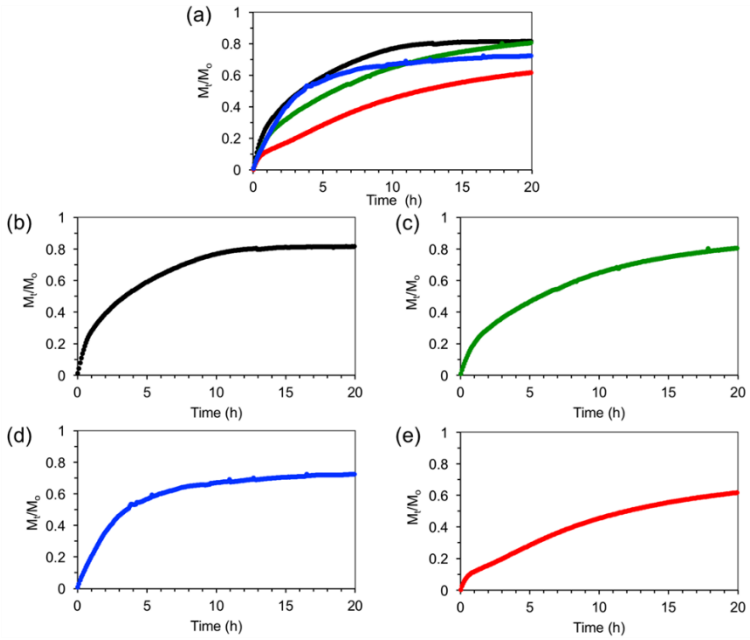

Figure 3. Average release profiles of Ibuprofen from the DDS. M_t/M_o is the fraction of Ibuprofen released at a given time t. (a) Overlaid profiles of all materials. (b-e) Individual profiles: (b) MSN (black), (c) Ph-MSN (green), (d) PhEt-MSN (blue), (e) Ph-PMO (red). The colors in (a) correspond to those in (b-e).

Table 2. Descriptors of Ibuprofen release from the mesoporous materials.

Material	20 h release (%)	Initial rate (mM h^{-1})	Initial rate regime (h)
MSN	82 ± 3	0.44	0.8
Ph-MSN	81 ± 4	0.25	1.5
PhEt-MSN	73 ± 2	0.25	2.0
Ph-PMO	62 ± 4	0.25	0.5

Kinetic and thermodynamic analysis of Ibuprofen release

To better understand the differences between the materials the drug release data were fitted to a kinetic model developed by Wu and co-workers.[49] The model deconvolutes the contributions of pore diffusion and drug-support interactions from the release profiles, and is defined by three fundamental parameters: the diffusion/convection rate constant (k_s), and the rate constants for adsorption (k_{on}) and desorption (k_{off}) of the drug from the support. The experimental release profiles are fitted to the model equation:

$$\frac{M_t}{M_0} = \frac{k_{off}}{k_{on}+k_{off}}(1 - e^{-k_s t}) + \frac{k_{on}}{k_{on}+k_{off}}(1 - e^{-k_{off} t}) \qquad (1)$$

where M_t and M_0 are the cumulative drug release at time t and the initial drug amount, respectively, and the kinetic constants k_s, k_{on}, and k_{off} are defined as above. In addition, the partition equilibrium between the surface and the solvent is defined by the ratio k_{on}/k_{off}, and the associated free energy change that controls the burst-release phase is related to this ratio by:

$$\Delta G = -k_B\, T\, ln(\frac{k_{on}}{k_{off}}) \qquad (2)$$

where k_B is the Boltzmann constant and T the absolute temperature. Fitting of the average release profiles to equation (1) gives high correlation coefficients ($R^2 > 0.98$ for each

profile, Fig. S8), and provides kinetic constants for Ibuprofen release from each material (Table 3).

Table 3. Kinetic and thermodynamic parameters for the release of Ibuprofen from all of the materials.

	k_s (h^{-1})	k_{on} (h^{-1})	k_{off} (h^{-1})	$\Delta G \times 10^{21}$ (J)
MSN	0.377 ± 0.012	0.019 ± 0.003	0.037 ± 0.003	2.80 ± 1.44
Ph-MSN	0.836 ± 0.031	0.227 ± 0.007	0.074 ± 0.0005	-4.63 ± 0.04
PhEt-MSN	0.376 ± 0.003	0.005 ± 0.0004	0.010 ± 0.0006	2.71 ± 0.72
Ph-PMO	0.242 ± 0.019	0.104 ± 0.016	0.035 ± 0.001	-4.47 ± 0.22

The sign of ΔG is indicative of the strength of interaction between the surface and the drug. The positive ΔG for MSN and PhEt-MSN indicates that desorption of the drug from the surface is favored ($k_{off} > k_{on}$) leading to the burst type release observed in Fig. 3b,d. To the contrary, ΔG for Ph-MSN and Ph-PMO is negative, indicating strong interactions with the drug that hinder desorption ($k_{off} < k_{on}$), and is reflected by a more sustained type of release (Fig. 3c,e). While ΔG of Ibuprofen with Ph-MSN indicates a strong adsorption, its cumulative release after 20 h is the same as MSN and higher than PhEt-MSN, both of which have weaker interactions with the drug. The magnitude of the cumulative release is proportional to the rate of diffusion from the pores to the SBF media (k_s), which is also higher for Ph-MSN than for MSN and PhEt-MSN. This apparent contradiction between the difference in strength of interaction and the diffusion kinetics and cumulative drug release from these materials is explained by examining the magnitudes of k_{on} and k_{off}. While the ratio of these two parameters favors adsorption for Ph-MSN, both k_{on} and k_{off} are significantly higher indicating that the drug exchanges quickly between adsorbed and desorbed state in this material, which leads to a higher probability of reaching the end of the pores and escape

to the surrounding SBF solution. This also explains why PhEt-MSN, despite having the same k_s and ΔG as MSN, gives a lower cumulative 20 h release: the much lower adsorption and desorption rate constants decrease the probabilities of the drug reaching the end of the pores for discharge into SBF.

Computational modeling of Ibuprofen-surface interactions

DFT calculations were performed to understand the differences between the interaction of Ibuprofen with the mesoporous materials. For the functionalized MSNs, the models used were based on a silica slab reported by Ugliengo and collaborators.[34, 35] The different surfaces were modified with the respective organic groups and optimized using the hybrid QM/MM SIMOMM method.[42] The Ph-PMO structure was produced based on the model developed by Martinez and Pacchioni.[40]

The possible interactions of Ibuprofen with the materials' surfaces are H-bonding between –COOH and silanol groups, and π-π interactions between the phenyl rings in the drug and the rings on the surface. The optimized structures showed a significant difference in the O-H distances corresponding to H-bonds between the non-functionalized MSN (1.97 Å) and phenyl-bearing materials (Ph-MSN 1.76 Å and PhEt 1.72Å) (Fig. 4, S9). This suggests a weaker interaction of the former with the surface, a result that is consistent with the highest experimental rate and extent of release observed for MSN.

While the slightly shorter O-H distance in PhEt-MSN than Ph-MSN would suggest a stronger interaction of the drug with the former, the ΔG of adsorption derived from their release profiles indicate the opposite behavior. However, as pointed out by Ugliengo *et al.*, H-bonding is not the dominant interaction between Ibuprofen and a silica surface.[24] Thus, it is likely that the experimental differences observed between the release profiles of Ibuprofen from these two materials are due to π-π interactions between the aromatic rings. Further

analysis of the optimized complexes reveals differences in the relative positions of the phenyl groups in the drug with respect to the surface phenyl groups (Fig. S10). While there are clear deviations from ideal stacking in all of the interacting pairs, the misalignment with the ring in Ibuprofen is larger in PhEt-MSN: the average distances between aromatic carbons of the rings are longer (4.89 Å versus 4.56 Å) and the diverging angle is wider (39° versus 28°) than in Ph-MSN (Fig. S10). These differences in interaction geometries are likely the main reason for the more favorable ΔG of adsorption of the drug with Ph-MSN, and for the observed differences in drug release profiles between the materials.

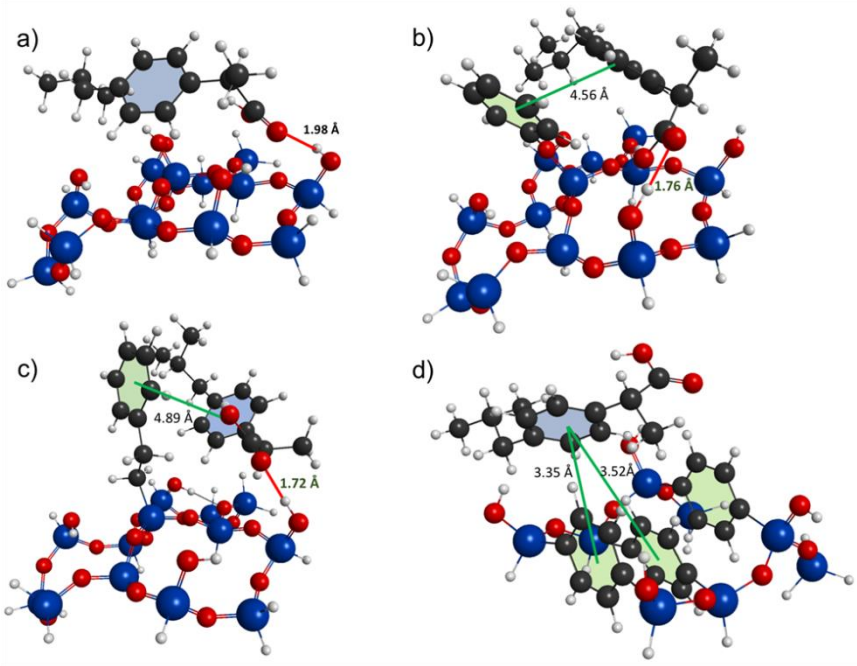

Figure 4. QM section of the optimized structures of Ibuprofen interacting with (a) MSN, (b) Ph-MSN, (c) PhEt-MSN, and (d) Ph-PMO. For clarity, the surface phenyl rings are shaded green and the Ibuprofen phenyl rings are shaded blue.

While the slightly shorter O-H distance in PhEt-MSN than Ph-MSN would suggest a stronger interaction of the drug with the former, the ΔG of adsorption derived from their release profiles indicate the opposite behavior. However, as pointed out by Ugliengo *et al.*, H-bonding is not the dominant interaction between Ibuprofen and a silica surface.[24] Thus, it

is likely that the experimental differences observed between the release profiles of Ibuprofen from these two materials are due to π-π interactions between the aromatic rings. Further analysis of the optimized complexes reveals differences in the relative positions of the phenyl groups in the drug with respect to the surface phenyl groups (Fig. S10). While there are clear deviations from ideal stacking in all of the interacting pairs, the misalignment with the ring in Ibuprofen is larger in PhEt-MSN: the average distances between aromatic carbons of the rings are longer (4.89 Å versus 4.56 Å) and the diverging angle is wider (39° versus 28°) than in Ph-MSN (Fig. S10). These differences in interaction geometries are likely the main reason for the more favorable ΔG of adsorption of the drug with Ph-MSN, and for the observed differences in drug release profiles between the materials.

Analysis of Ph-PMO indicates much shorter distances between its phenyl rings and those of the drug (3.35 and 3.52 Å). In addition, while the π-π interactions of Ibuprofen with Ph-MSN and PhEt-MSN tend to be face-to-face, the relative orientation of the rings in the drug-Ph-PMO model indicates the interaction is edge-to-face. Because of the quadrupolar nature of phenyl rings, edge-to-face interactions are generally stronger than face-to-face.[50] These results suggest that the interaction of the drug with Ph-PMO must be stronger than with Ph-MSN and PhEt-MSN, and are in agreement with the negative ΔG and lowest rate and extent of Ibuprofen release observed for this material.

Conclusions

In summary, the kinetics and cumulative release of Ibuprofen from mesoporous silica DDS can be controlled by modification of the carrier's surface with phenyl groups. The presence of phenyl groups on the surface decreases the initial rate of release, in principle due to a decrease in interfacial polarity that affects the partition equilibrium between the surface and the aqueous SBF. Controlling the orientation and conformational flexibility of the

surface phenyl groups uncovers subtle differences in intermolecular interactions that allow further fine-tuning the drug release profiles. At the molecular level, incorporation of phenyl groups on silica surfaces results in stronger drug-surface interactions arising from cooperativity between COOH-silanol H-bonding and π-π interactions with the surface phenyl groups. The negative ΔG of Ph-MSN and positive ΔG of PhEt-MSN suggest that π-π interactions contribute more to Ibuprofen adsorption than H-bonding, because the former has closer and better phenyl ring alignment but longer O-H distances than the latter. While these two systems possess silanols and phenyl rings, it appears that the locked conformation of phenyl groups in Ph-MSN provides a better fit for Ibuprofen docking than the phenyl groups with mobile ethylene linkers in PhEt-MSN. This conformational rigidity of Ph-MSN appears to facilitate a rapid drug adsorption/desorption equilibrium evidenced by the large k_{on} and k_{off} values that eventually lead to a high cumulative release after long contact times. In contrast to Ph-MSN and PhEt-MSN where the phenyl rings of Ibuprofen tend to interact face-to-face, the π-π interaction of the drug with Ph-PMO seems to be edge-to-face. This type of interaction in Ph-PMO is stronger than the face-to-face and explains the slower kinetics and cumulative release of Ibuprofen observed for this material. These results demonstrate that careful selection and design of drug-surface interactions can be a valuable tool to precisely tune the sustained release of drugs for custom therapeutic applications.

Acknowledgements

This research is supported by the U.S. Department of Energy, Office of Basic Energy Sciences, Division of Chemical Sciences, Geosciences, and Biosciences, through the Ames Laboratory Catalysis Science program. The Ames Laboratory is operated for the U.S. Department of Energy by Iowa State University under Contract No. DE-AC02-07CH11358.

Supplemental Figures

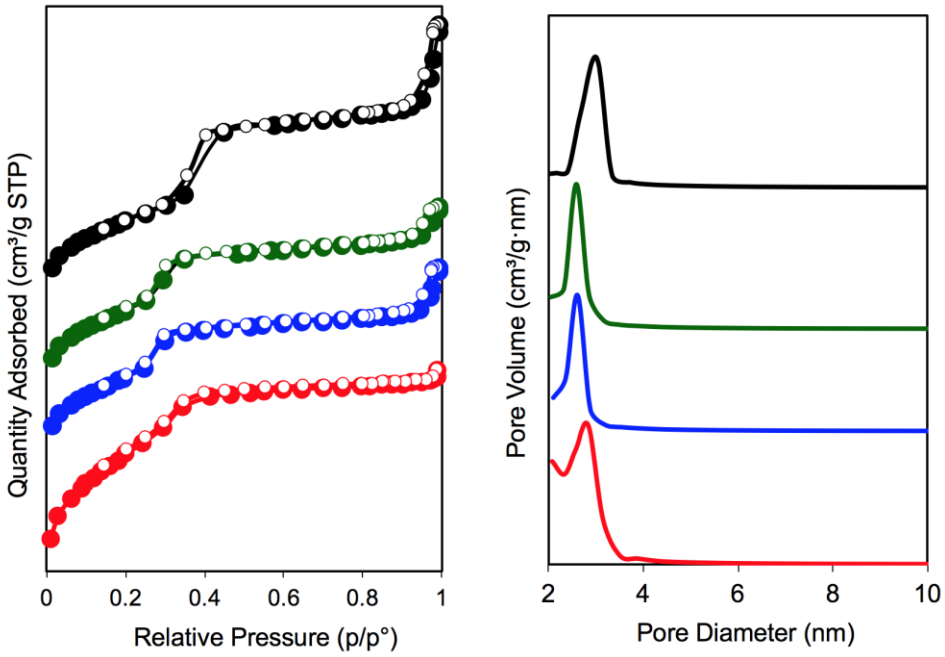

Figure S1. (a) N_2 sorption isotherms and (b) pore size distributions of MSN (black), Ph-MSN (green), PhEt-MSN (blue) and Ph-PMO (red). Figures are shifted for clarity.

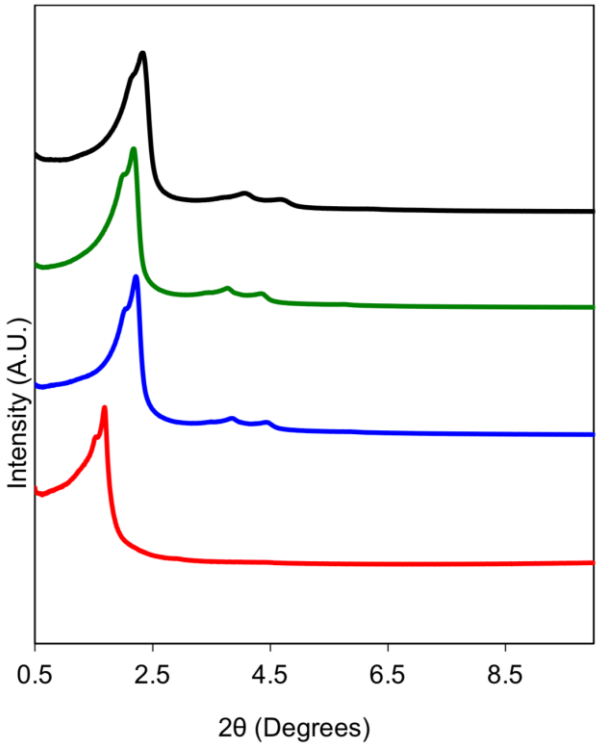

Figure S2. XRD patterns of MSN (black), Ph-MSN (green), PhEt-MSN (blue) and Ph-PMO (red). Figures are shifted for clarity.

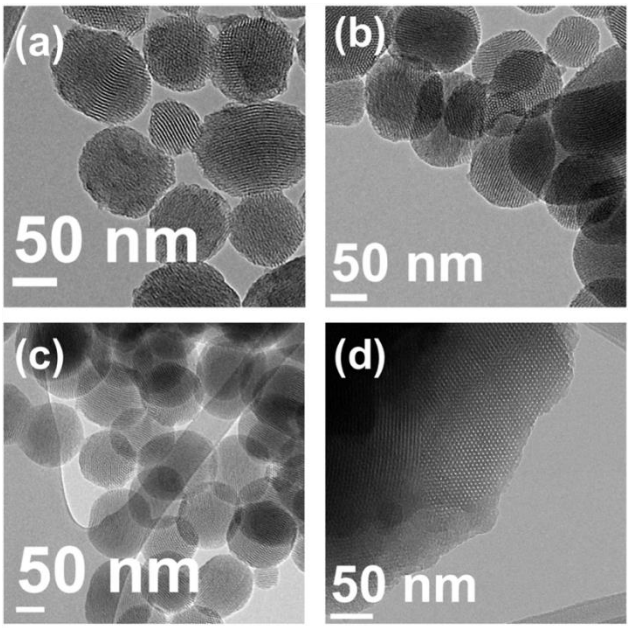

Figure S3. Transmission electron micrographs of (a) MSN, (b) Ph-MSN, (c) PhEt-MSN and (d) Ph-PMO.

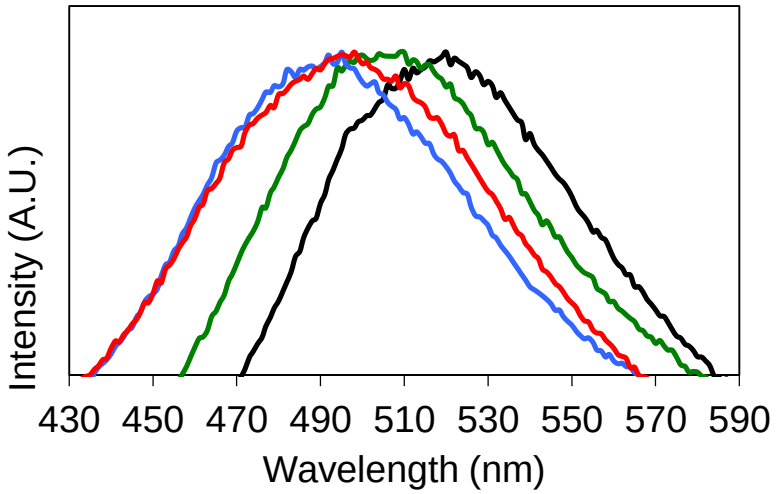

Figure S4. Fluorescence emission spectra of aqueous suspensions of Prodan-loaded MSN (black), Ph-MSN (green), PhEt-MSN (blue) and Ph-PMO (red). Excitation wavelength: 337 nm.

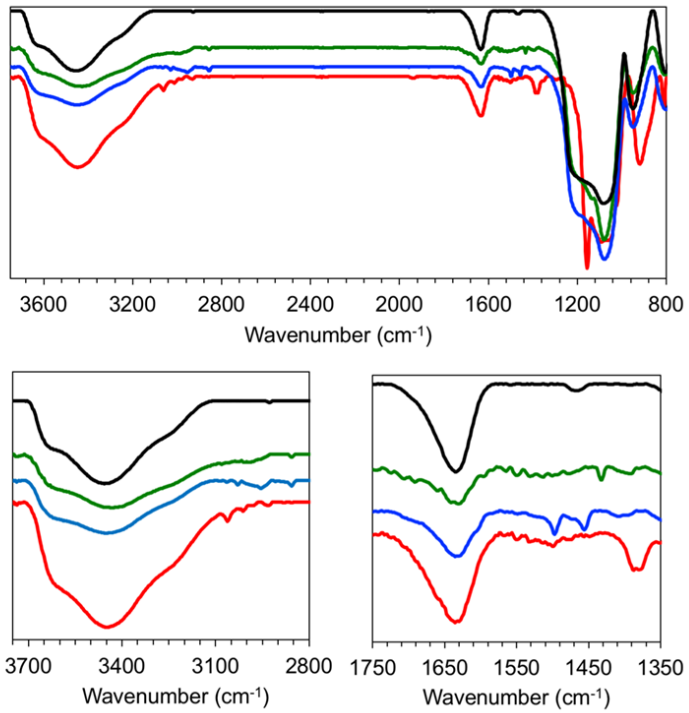

Fig. S5. Different regions of the FT-IR spectra of MSN (black), Ph-MSN (green), PhEt-MSN (blue) and Ph-PMO (red).

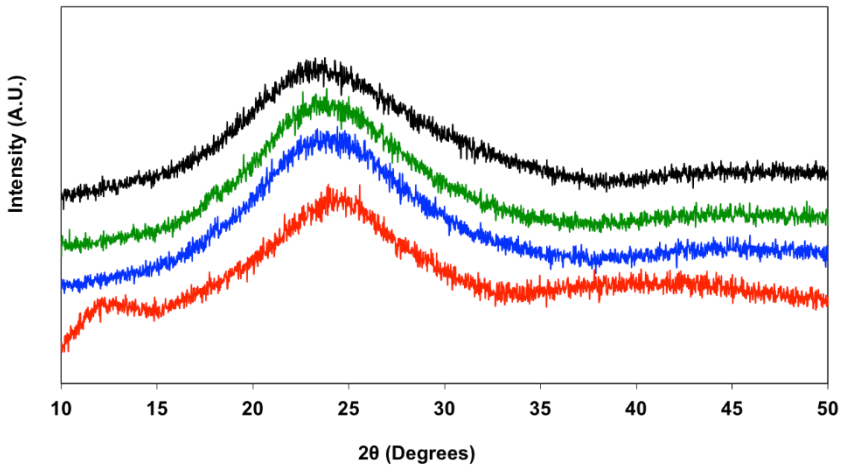

Figure S6. Wide angle XRD patterns of Ibuprofen(0.5 mmol/g) loaded MSN (black), Ph-MSN (green), PhEt-MSN (blue) and Ph-PMO (red).

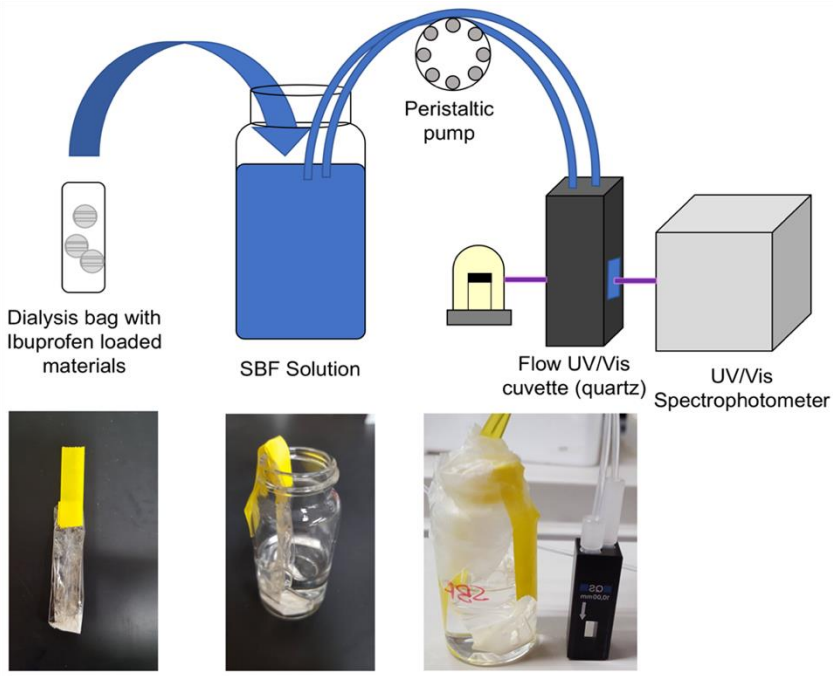

Figure S7. Experimental setup for Ibuprofen release experiments.

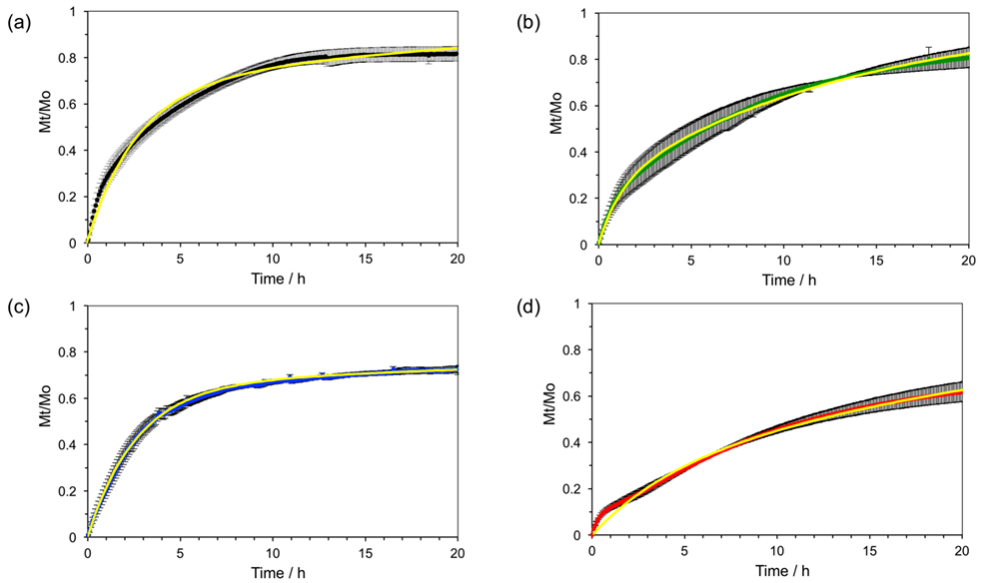

Figure S8. Fitting of the Ibuprofen release profiles from (a) MSN (black), (b) Ph-MSN(green), (c) PhEt-MSN(blue) and (d) Ph-PMO(red) to the 3-parameter thermodynamic model. Fittings are the yellow lines, black lines around each colored datapoint are the error bars consisting of 2 standard deviations from three separate release experiments from each material.

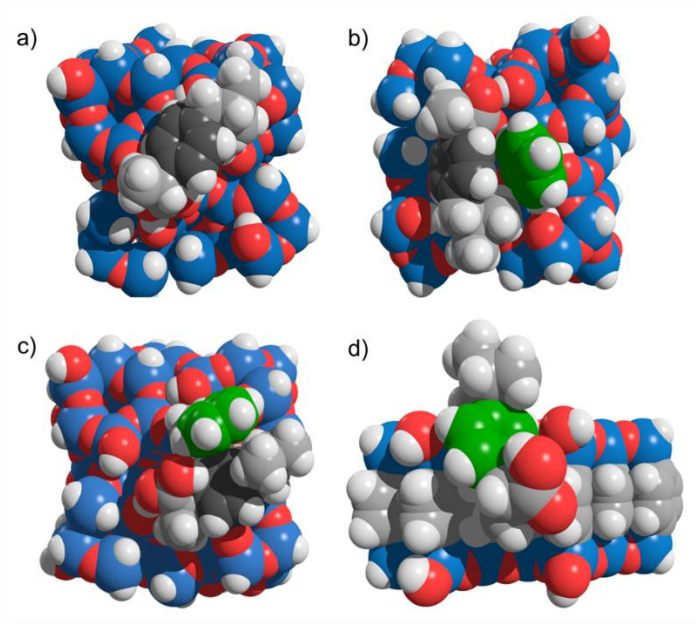

Figure S9. Optimized structures of Ibuprofen adsorbed on the surfaces of (a) MSN, (b) Ph-MSN, (c) PhEt-MSN, and (d) Ph-PMO.

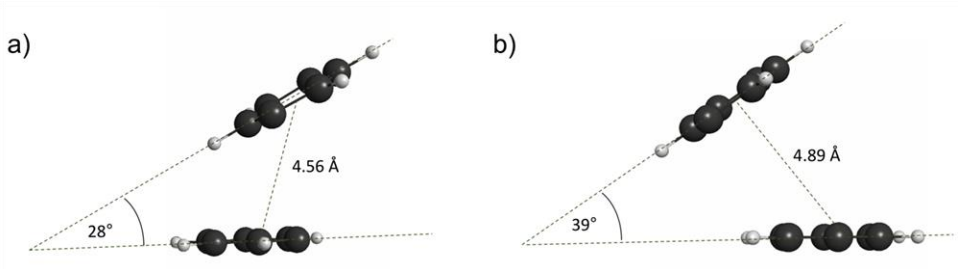

Figure S10. Relative positions of the aromatic ring of Ibuprofen with respect to the interacting aromatic ring in (a) Ph-MSN, (b) PhEt-MSN

References

1. Slowing, I. I.; Vivero-Escoto, J. L.; Trewyn, B. G.; Lin, V. S.-Y., Mesoporous silica nanoparticles: structural design and applications. *J. Mater. Chem.* **2010,** *20* (37), 7924 - 7937.

2. Aznar, E.; Oroval, M.; Pascual, L.; Murguía, J. R.; Martínez-Máñez, R.; Sancenón, F., Gated Materials for On-Command Release of Guest Molecules. *Chem. Rev.* **2016,** *116* (2), 561-718.

3. Tarn, D.; Ashley, C. E.; Xue, M.; Carnes, E. C.; Zink, J. I.; Brinker, C. J.,

Mesoporous Silica Nanoparticle Nanocarriers: Biofunctionality and Biocompatibility. *Acc. Chem. Res.* **2013,** *46* (3), 792-801.

4. Slowing, I. I.; Vivero-Escoto, J. L.; Wu, C.-W.; Lin, V. S. Y., Mesoporous silica nanoparticles as controlled release drug delivery and gene transfection carriers. *Adv. Drug Deliv. Rev.* **2008,** *60* (11), 1278-1288.

5. Vallet-Regí, M.; Balas, F.; Arcos, D., Mesoporous Materials for Drug Delivery. *Angew. Chem., Int. Ed.* **2007,** *46* (40), 7548-7558.

6. Argyo, C.; Weiss, V.; Bräuchle, C.; Bein, T., Multifunctional Mesoporous Silica Nanoparticles as a Universal Platform for Drug Delivery. *Chem. Mater.* **2013,** *26* (1), 435-451.

7. Gao, W.; Chan, J. M.; Farokhzad, O. C., pH-Responsive Nanoparticles for Drug Delivery. *Molecular Pharmaceutics* **2010,** *7* (6), 1913-1920**.**

8. Tukappa, A.; Ultimo, A.; de la Torre, C.; Pardo, T.; Sancenón, F.; Martínez-Máñez, R., Polyglutamic Acid-Gated Mesoporous Silica Nanoparticles for Enzyme-Controlled Drug Delivery. *Langmuir* **2016,** *32* (33), 8507-8515.

9. Zhao, Y.; Trewyn, B. G.; Slowing, I. I.; Lin, V. S. Y., Mesoporous Silica Nanoparticle-Based Double Drug Delivery System for Glucose-Responsive Controlled Release of Insulin and Cyclic AMP. *J. Am. Chem. Soc.* **2009,** *131* (24), 8398-+.

10. Mortera, R.; Vivero-Escoto, J.; Slowing, II; Garrone, E.; Onida, B.; Lin, V. S. Y., Cell-induced intracellular controlled release of membrane impermeable cysteine from a mesoporous silica nanoparticle-based drug delivery system. *Chem. Commun.* **2009,** (22), 3219-3221.

11. Vivero-Escoto, J. L.; Slowing, I. I.; Wu, C.-W.; Lin, V. S.-Y., Photoinduced Intracellular Controlled Release Drug Delivery in Human Cells by Gold-Capped Mesoporous Silica Nanosphere. *J. Am. Chem. Soc.* **2009,** *131* (10), 3462-3463.

12. Martín-Saavedra, F. M.; Ruíz-Hernández, E.; Boré, A.; Arcos, D.; Vallet-Regí, M.; Vilaboa, N., Magnetic mesoporous silica spheres for hyperthermia therapy. *Acta Biomaterialia* **2010,** *6* (12), 4522-4531.

13. Vivero-Escoto, J. L.; Slowing, II; Lin, V. S. Y., Tuning the cellular uptake and cytotoxicity properties of oligonucleotide intercalator-functionalized mesoporous silica nanoparticles with human cervical cancer cells HeLa. *Biomater.* **2010,** *31* (6), 1325-1333.

14. Slowing, I. I.; Vivero-Escoto, J. L.; Zhao, Y.; Kandel, K.; Peeraphatdit, C.; Trewyn, B. G.; Lin, V. S. Y., Exocytosis of Mesoporous Silica Nanoparticles from Mammalian Cells: From Asymmetric Cell-to-Cell Transfer to Protein Harvesting. *Small* **2011,** *7* (11), 1526-1532.

15. Slowing, I.; Trewyn, B. G.; Lin, V. S. Y., Effect of Surface Functionalization of MCM-41-Type Mesoporous Silica Nanoparticles on the Endocytosis by Human Cancer

Cells. *J. Am. Chem. Soc.* **2006,** *128* (46), 14792-14793.

16. Pan, L.; He, Q.; Liu, J.; Chen, Y.; Ma, M.; Zhang, L.; Shi, J., Nuclear-Targeted Drug Delivery of TAT Peptide-Conjugated Monodisperse Mesoporous Silica Nanoparticles. *J. Am. Chem. Soc.* **2012,** *134* (13), 5722-5725.

17. Tsai, C.-P.; Chen, C.-Y.; Hung, Y.; Chang, F.-H.; Mou, C.-Y., Monoclonal antibody-functionalized mesoporous silica nanoparticles (MSN) for selective targeting breast cancer cells. *J. Mater. Chem.* **2009,** *19* (32), 5737-5743.

18. Tu, J.; Wang, T.; Shi, W.; Wu, G.; Tian, X.; Wang, Y.; Ge, D.; Ren, L., Multifunctional ZnPc-loaded mesoporous silica nanoparticles for enhancement of photodynamic therapy efficacy by endolysosomal escape. *Biomater.* **2012,** *33* (31), 7903-7914.

19. Lu, J.; Liong, M.; Li, Z.; Zink, J. I.; Tamanoi, F., Biocompatibility, Biodistribution, and Drug-Delivery Efficiency of Mesoporous Silica Nanoparticles for Cancer Therapy in Animals. *Small* **2010,** *6* (16), 1794-1805.

20. Chen, F.; Hong, H.; Zhang, Y.; Valdovinos, H. F.; Shi, S.; Kwon, G. S.; Theuer, C. P.; Barnhart, T. E.; Cai, W., In Vivo Tumor Targeting and Image-Guided Drug Delivery with Antibody-Conjugated, Radiolabeled Mesoporous Silica Nanoparticles. *ACS Nano* **2013,** *7* (10), 9027-9039.

21. Lee, J. E.; Lee, N.; Kim, T.; Kim, J.; Hyeon, T., Multifunctional Mesoporous Silica Nanocomposite Nanoparticles for Theranostic Applications. *Acc. Chem. Res.* **2011,** *44* (10), 893-902.

22. Doadrio, J. C.; Sousa, E. M. B.; Izquierdo-Barba, I.; Doadrio, A. L.; Perez-Pariente, J.; Vallet-Regi, M., Functionalization of mesoporous materials with long alkyl chains as a strategy for controlling drug delivery pattern. *J. Mater. Chem.* **2006,** *16* (5), 462-466.

23. Mitran, R.-A.; Matei, C.; Berger, D., Correlation of Mesoporous Silica Structural and Morphological Features with Theoretical Three-Parameter Model for Drug Release Kinetics. *J. Phys. Chem. C* **2016,** *120* (51), 29202-29209.

24. Delle Piane, M.; Corno, M.; Pedone, A.; Dovesi, R.; Ugliengo, P., Large-Scale B3LYP Simulations of Ibuprofen Adsorbed in MCM-41 Mesoporous Silica as Drug Delivery System. *J. Phys. Chem. C* **2014,** *118* (46), 26737-26749.

25. Delle Piane, M.; Vaccari, S.; Corno, M.; Ugliengo, P., Silica-Based Materials as Drug Adsorbents: First Principle Investigation on the Role of Water Microsolvation on Ibuprofen Adsorption. *J. Phys. Chem. A* **2014,** *118* (31), 5801-5807.

26. Azaïs, T.; Tourné-Péteilh, C.; Aussenac, F.; Baccile, N.; Coelho, C.; Devoisselle, J.-M.; Babonneau, F., Solid-State NMR Study of Ibuprofen Confined in MCM-41 Material. *Chem. Mater.* **2006,** *18* (26), 6382-6390.

27. Babonneau, F.; Yeung, L.; Steunou, N.; Gervais, C.; Ramila, A.; Vallet-Regi,

M., Solid State NMR Characterisation of Encapsulated Molecules in Mesoporous Silica. *Journal of Sol-Gel Science and Technology* **2004,** *31* (1), 219-223.

28. Brás, A. R.; Merino, E. G.; Neves, P. D.; Fonseca, I. M.; Dionísio, M.; Schönhals, A.; Correia, N. T., Amorphous Ibuprofen Confined in Nanostructured Silica Materials: A Dynamical Approach. *J. Phys. Chem. C* **2011,** *115* (11), 4616-4623.

29. Guenneau, F.; Panesar, K.; Nossov, A.; Springuel-Huet, M.-A.; Azais, T.; Babonneau, F.; Tourne-Peteilh, C.; Devoisselle, J.-M.; Gedeon, A., Probing the mobility of ibuprofen confined in MCM-41 materials using MAS-PFG NMR and hyperpolarised-129Xe NMR spectroscopy. *Phys. Chem. Chem. Phys.* **2013,** *15* (43), 18805-18808.

30. Brás, A. R.; Noronha, J. P.; Antunes, A. M. M.; Cardoso, M. M.; Schönhals, A.; Affouard, F.; Dionísio, M.; Correia, N. T., Molecular Motions in Amorphous Ibuprofen As Studied by Broadband Dielectric Spectroscopy. *J. Phys. Chem. B* **2008,** *112* (35), 11087-11099.

31. Brás, A. R.; Fonseca, I. M.; Dionísio, M.; Schönhals, A.; Affouard, F.; Correia, N. T., Influence of Nanoscale Confinement on the Molecular Mobility of Ibuprofen. *J. Phys. Chem. C* **2014,** *118* (25), 13857-13868.

32. Zeng, L.; An, L.; Wu, X., Modeling Drug-Carrier Interaction in the Drug Release from Nanocarriers. *J. Drug Delivery* **2011,** *2011*, 370308.

33. Zeng, L.; Wu, X., Modeling the sustained release of lipophilic drugs from liposomes. *Applied Physics Letters* **2010,** *97* (7), 073701.

34. Ugliengo, P.; Sodupe, M.; Musso, F.; Bush, I. J.; Orlando, R.; Dovesi, R., Realistic Models of Hydroxylated Amorphous Silica Surfaces and MCM-41 Mesoporous Material Simulated by Large-scale Periodic B3LYP Calculations. *Adv. Mater.* **2008,** *20* (23), 4579-4583.

35. Coasne, B.; Ugliengo, P., Atomistic Model of Micelle-Templated Mesoporous Silicas: Structural, Morphological, and Adsorption Properties. *Langmuir* **2012,** *28* (30), 11131-11141.

36. Singappuli-Arachchige, D.; Manzano, J. S.; Sherman, L. M.; Slowing, I. I., Polarity Control at Interfaces: Quantifying Pseudo-solvent Effects in Nano-confined Systems. *ChemPhysChem* **2016,** *17* (19), 2982-2986.

37. Kokubo, T.; Kushitani, H.; Sakka, S.; Kitsugi, T.; Yamamuro, T., Solutions able to reproduce in vivo surface-structure changes in bioactive glass-ceramic A-W3. *Journal of Biomedical Materials Research* **1990,** *24* (6), 721-734.

38. Grimme, S.; Antony, J.; Ehrlich, S.; Krieg, H., A consistent and accurate ab initio parametrization of density functional dispersion correction (DFT-D) for the 94 elements H-Pu. *The Journal of Chemical Physics* **2010,** *132* (15), 154104.

39. Schmidt, M. W.; Baldridge, K. K.; Boatz, J. A.; Elbert, S. T.; Gordon, M. S.; Jensen, J. H.; Koseki, S.; Matsunaga, N.; Nguyen, K. A.; Su, S.; Windus, T. L.;

Dupuis, M.; Montgomery, J. A., General atomic and molecular electronic structure system. *Journal of Computational Chemistry* **1993,** *14* (11), 1347-1363.

40. Martinez, U.; Pacchioni, G., Interaction of CO, CO2 and CH4 with mesoporous organosilica: Periodic DFT calculations with dispersion corrections. *Microporous Mesoporous Mater.* **2010,** *129* (1), 62-67.

41. Comotti, A.; Bracco, S.; Valsesia, P.; Ferretti, L.; Sozzani, P., 2D Multinuclear NMR, Hyperpolarized Xenon and Gas Storage in Organosilica Nanochannels with Crystalline Order in the Walls. *J. Am. Chem. Soc.* **2007,** *129* (27), 8566-8576.

42. Shoemaker, J. R.; Gordon, M. S., SIMOMM: An Integrated Molecular Orbital/Molecular Mechanics Optimization Scheme for Surfaces. *J. Phys. Chem. A* **1999,** *103* (17), 3245-3251.

43. Mao, K.; Kobayashi, T.; Wiench, J. W.; Chen, H.-T.; Tsai, C.-H.; Lin, V. S. Y.; Pruski, M., Conformations of Silica-Bound (Pentafluorophenyl)propyl Groups Determined by Solid-State NMR Spectroscopy and Theoretical Calculations. *J. Am. Chem. Soc.* **2010,** *132* (35), 12452-12457.

44. Inagaki, S.; Guan, S.; Ohsuna, T.; Terasaki, O., An ordered mesoporous organosilica hybrid material with a crystal-like wall structure. *Nature* **2002,** *416* (6878), 304-307.

45. Zhu, X.; Cho, H.-r.; Pasupong, M.; Regalbuto, J. R., Charge-Enhanced Dry Impregnation: A Simple Way to Improve the Preparation of Supported Metal Catalysts. *ACS Catal.* **2013,** *3* (4), 625-630.

46. Jubert, A.; Legarto, M. L.; Massa, N. E.; Tévez, L. L.; Okulik, N. B., Vibrational and theoretical studies of non-steroidal anti-inflammatory drugs Ibuprofen [2-(4-isobutylphenyl)propionic acid]; Naproxen [6-methoxy-α-methyl-2-naphthalene acetic acid] and Tolmetin acids [1-methyl-5-(4-methylbenzoyl)-1H-pyrrole-2-acetic acid]. *Journal of Molecular Structure* **2006,** *783* (1), 34-51.

47. Gordijo, C. R.; Barbosa, C. A. S.; Da Costa Ferreira, A. M.; Constantino, V. R. L.; Oliveira Silva, D. d., Immobilization of Ibuprofen and Copper-Ibuprofen Drugs on Layered Double Hydroxides. *J. Pharm. Sci.* **2005,** *94* (5), 1135-1148.

48. Kandziolka, M. V.; Kidder, M. K.; Gill, L.; Wu, Z.; Savara, A., Aromatic-hydroxyl interaction of an alpha-aryl ether lignin model-compound on SBA-15, present at pyrolysis temperatures. *Phys. Chem. Chem. Phys.* **2014,** *16* (44), 24188-24193.

49. Zeng, L.; An, L.; Wu, X., Modeling Drug-Carrier Interaction in the Drug Release from Nanocarriers. *Journal of Drug Delivery* **2011,** *2011*, 15.

50. Sinnokrot, M. O.; Valeev, E. F.; Sherrill, C. D., Estimates of the Ab Initio Limit for π–π Interactions: The Benzene Dimer. *J. Am. Chem. Soc.* **2002,** *124* (36), 10887-10893.

CHAPTER 7. SUMMARY AND OUTLOOK

Summary

The work outlined in this dissertation sought to customize heterogeneous catalysts at the macroscale by using 3D printing methods, and at the nanoscale by fine-tuning the distribution and molecular orientation of surface organic modifiers. Initially, it was demonstrated that 3D printing can be used to produce catalytically active structures without the need of any post-printing treatment. Using stereolithography (SLA) allowed us to create custom-made heterogeneous catalysts, inaccessible by conventional means. The photo-polymerization used in SLA allowed us to control the molecular properties of the curable resin to target specific catalytic properties of 3D geometries. This was demonstrated by producing unique devices and applying them in different catalytic reactions (e.g. Mannich, aldol condensation, Huisgen cycloaddition, sucrose hydrolysis, alcohol oxidation). This new method of producing heterogeneous catalysts enabled the study of macroscale morphology on catalytic activity. It was demonstrated that even minor changes in the morphology (orientation of catalytically active stirring blades) can result in improvements of the catalytic activity. Nonetheless, controlling the architecture does not limit the molecular control of catalytic sites, on the contrary, the synergy achieved between macroscopic and molecular properties provides an overall control over the experimental set up.

Developing resins with advanced properties is expensive and time consuming due to the set-up of commercially available 3D printers (i.e. large volume resin tanks). To overcome this limitation a high-throughput screening adaptor for 3D printers was designed and produced. The adaptor consists of miniaturized resin tanks and matching build platforms that increase the screening efficiency and minimize waste production. This allowed 3D printing

multiple materials with different surface (i.e. hydrophobicity or hydrophilicity) and catalytic properties (i.e. metal catalysts). Finally, an optimized 3D printed catalytic material was prepared by combining the compositions of the best surface and catalytic properties along with the best morphology.

In the outlined work, we also studied the functionalization (grafting) of mesoporous silica nanoparticles (MSN) with common organo-substituted trimethoxysilane modifiers. We showed that the grafting rates can be tuned by controlling the interaction of the organic groups in the silane with the silica surface. This process can be catalyzed by amines, where their pKa can be used to tune the reaction rate along with the group distribution on the silica surface. It was shown that the kinetics have a second order dependence on amine-bearing silanes and displays a substrate-inhibition at high trimethoxysilane concentrations. Additionally, the silica surface was modified with phenyl groups with different orientations and mobilities on the silica surface. This was used to study their effect in the drug release of Ibuprofen. It was shown that the orientation of the groups controls the drug release rate through drug-surface interactions. DFT calculations demonstrated that the dominant drug-surface interactions were π-π type.

Outlook

In recent years, 3D printing has been exploited in many different research areas. However, its application to controlling the geometry of catalytic materials is relatively new. This new research field opens the possibility to explore new methods and ways of controlling catalytic reactions. Considering the early state of this new approach, there are still many limitations that must be overcome to optimize the process. SLA is a flexible method that allows selecting the chemical composition of the printable materials, and the mechanism that triggers the printing process. Nowadays, SLA printers are limited to one type of laser (405

nm), that triggers only one type of polymerization (radical). Modification of the current hardware (e.g. laser power, wavelength) or polymerization type (cationic-, radical-, ring opening-polymerization) used in SLA 3D printing can open the possibility of a full control over the final chemical properties of the 3D printed objects. For example, in order to not waste catalyst in the wall of the reactor, the bulk part of the reactor walls can be printed with an inert material, while the surface can be arranged with catalytic sites. Nonetheless, exploration is also needed at the molecular level, where catalytic accessibility can be improved by the insertion of pores at the macro-, meso- or micro-scale. In the long run, the desirable catalyst should be a combination of the projects presented in this thesis, where a full control over the macroscopic and nanoscopoic properties can be achieved in one single process.